Design of vibration reduction measures for railway traffic by means of topology optimization

Cédric VAN HOORICKX

Examination committee:
Prof. dr. A. Bultheel, chair
Prof. dr. ir. G. Lombaert, supervisor
Prof. dr. ir.-arch. M. Schevenels, supervisor
Dr. ir. E. Deckers, secretary
Prof. dr. ir. G. Degrande
Prof. dr. ir. J. Meyers
Prof. dr. ir. P. Galvín Barrera
(Universidad de Sevilla, Spain)

Dissertation presented in partial fulfillment of the requirements for the degree of Doctor of Engineering Science (PhD)

September 2017

© 2017 KU Leuven – Faculty of Engineering Science
Uitgegeven in eigen beheer, Cédric Van hoorickx, Kasteelpark Arenberg 40 box 2448, B-3001 Leuven (Belgium)

Alle rechten voorbehouden. Niets uit deze uitgave mag worden vermenigvuldigd en/of openbaar gemaakt worden door middel van druk, fotokopie, microfilm, elektronisch of op welke andere wijze ook zonder voorafgaande schriftelijke toestemming van de uitgever.

All rights reserved. No part of the publication may be reproduced in any form by print, photoprint, microfilm, electronic or any other means without written permission from the publisher.

Voorwoord

Deze tekst vormt het sluitstuk van vier jaar onderzoek. Ik wil graag een aantal mensen bedanken voor hun aandeel in deze onderneming.

In de eerste plaats gaat mijn dank uit naar mijn promotoren Geert Lombaert en Mattias Schevenels voor hun steun, hun enthousiasme en hun kundig advies. De regelmatige vergaderingen gaven een richting aan het onderzoek en waren onmisbaar voor het slagen van dit doctoraatsproject. Ook de vele suggesties en hulp bij het schrijven van papers en het maken van presentaties waren een grote verrijking.

Naast mijn promotoren bedank ik Geert Degrande en Johan Meyers voor hun bijdrage als lid van mijn begeleidingscommissie. Geert Degrande gaf me verder de mogelijkheid om betrokken te zijn bij verschillende meetcampagnes en Johan Meyers leidde verder de werking van OPTEC werkgroep 4 in goede banen, waardoor mijn kijk op optimalisatie is verbreed.

I would also like to thank the other members of the jury, Elke Deckers and Pedro Galvín for their valuable comments and suggestions which significantly contributed to the overall quality of the manuscript. Adhemar Bultheel bedank ik voor het vervullen van de voorzitterstaak.

Het Fonds Wetenschappelijk Onderzoek - Vlaanderen (FWO) dank ik voor het ondersteunen van mijn onderzoek door middel van een vierjarig aspirantenmandaat.

I wish to express my gratitude to Ole Sigmund and Boyan Lazarov for their contribution to this work and for their hospitality during my stay as a visiting researcher at the Section of Solid Mechanics at the DTU (Denmark).

Mijn dank gaat uit naar Ann Zwarts voor het verlichten van administratieve en logistieke taken, telkens met een glimlach. Edwin Reynders wil ik bedanken voor de voortreffelijke begeleiding van mijn master thesis, wat een belangrijke invloed had op mijn beslissing om aan dit doctoraat te beginnen.

De voorbije jaren heb ik met plezier aan de afdeling bouwmechanica gewerkt. De jaarlijkse BWM uitstap, de vele middagen in Alma, de kerstversieringswedstrijd, de departementsactiviteiten waarop onze afdeling steeds talrijk aanwezig was, . . . hebben allemaal bijgedragen tot een leuke werksfeer. Ik dank in het bijzonder de volgende collega's voor het creëren van een aangename werkomgeving en voor de momenten van verstrooiing en plezier: Matthias, Ramses, Manthos, Jie, Dimitrios, Carolina, Katrien, Kristof, Jonas, Avisek, Klaus, Pengchao, Jan, Hernan, Bram, Arne, Pieter en Miche. Ann Zwarts, Guido De Roeck, Geert Degrande, Geert Lombaert, Edwin Reynders en Stijn François wil ik graag bedanken om alle activiteiten in goede banen te leiden.

Ik heb het plezier gehad om te mogen samenwerken met de afdeling Architectuur en Bouwtechniek, onder andere voor het begeleiden van masterthesissen structurele optimalisatie. Roxane, Jef, Jeroen, Wouter en Willem bedank ik voor de aangename samenwerking en alle fijne momenten in binnen- en buitenland.

Ik wil mijn vrienden bedanken voor de aangename dinertjes, de verstrooiende weekends en skireizen, en om samen talrijke activiteiten te organiseren. Verder bedank ik mijn familie voor hun steun en interesse, ook al was het voor hen niet altijd even duidelijk waar ik mee bezig was. Een speciale bedanking gaat uit naar mijn ouders voor hun onvoorwaardelijke steun en alle kansen die ze me bieden. Astrid en Harm bedank ik voor de leuke babbels en de fijne gezinsmomenten.

Cédric Van hoorickx
September 2017

Abstract

Railway induced vibrations in the built environment may lead to annoyance to people and malfunctioning of sensitive equipment, which necessitates the development of effective mitigation measures. Mitigation measures on the transmission path try to reduce the ground vibrations propagating from the railway track to, for example, nearby buildings. Because of the high computational cost of numerical simulations, mitigation measures on the transmission path are usually designed by trial and error. Only a limited number of relatively simple design geometries is explored, leaving much room for further improvement. The aim of this work is therefore to look for novel wave barrier designs with an improved performance.

As double walls are shown to be effective in reducing air-borne sound transmission, the performance of double wall barriers in reducing ground vibration transmission is investigated using the efficient two-and-a-half-dimensional finite element methodology. Double wall barriers are shown to perform hardly better than single wall barriers, except if the wall thicknesses and the spacing between the walls are tuned to optimally reflect waves.

To improve the performance of wave barriers, topology optimization is used to optimally distribute material in the soil in a domain in the vicinity of the railway track. The results demonstrate the high potential of optimized designs in terms of performance improvement and volume reduction. Topology optimization often leads to designs with small features, which are sensitive to geometric imperfections and may be hard to manufacture. A robust approach is therefore used, leading to designs which can be simplified with little deterioration of performance.

Beknopte samenvatting

Trillingen ten gevolge van treinverkeer in de bebouwde omgeving kunnen zorgen voor menselijke hinder en storing van gevoelige apparatuur, wat de ontwikkeling van effectieve trillingsreducerende maatregelen noodzakelijk maakt. Maatregelen op het transmissiepad proberen de grondtrillingen te verminderen die zich van het spoor naar bijvoorbeeld nabijgelegen gebouwen verspreiden. Vanwege de hoge rekenkost van numerieke simulaties worden trillingsreducerende maatregelen op het transmissiepad meestal door trial and error ontworpen. Slechts een beperkt aantal relatief eenvoudige geometrieën worden hierbij onderzocht, waardoor er veel ruimte is voor verdere verbetering. Het doel van dit werk is daarom om te zoeken naar nieuwe ontwerpen van trillingsreducerende schermen met een verbeterde prestatie.

Aangezien dubbele wanden effectief zijn in het reduceren van luchtgeluidstransmissie, wordt de prestatie van dubbele wandschermen bij het reduceren van de voortplanting van trillingen in de grond onderzocht met behulp van de efficiënte twee-en-een-half-dimensionale eindige elementen methodologie. Dubbele wandschermen blijken nauwelijks beter te werken dan enkele wandschermen, behalve als de wanddiktes en de afstand tussen de wanden bepaald zijn zodanig dat de golven optimaal gereflecteerd worden.

Om de prestaties van trillingsschermen te verbeteren wordt topologische optimalisatie gebruikt om materiaal optimaal te verdelen over een domein in de grond in de nabijheid van het spoor. De resultaten tonen het hoge potentieel van geoptimaliseerde ontwerpen op het vlak van prestatieverbetering en volumevermindering. Topologische optimalisatie leidt vaak tot ontwerpen die gevoelig zijn voor geometrische imperfecties en moeilijk te vervaardigen zijn. Een robuuste aanpak wordt daarom gebruikt, wat leidt tot ontwerpen die kunnen worden vereenvoudigd zonder de prestaties sterk te verslechteren.

List of Symbols

The following list gives an overview of the most commonly adopted acronyms and symbols used throughout the text.

Acronyms

1D	One-dimensional
2D	Two-dimensional
2.5D	Two-and-a-half-dimensional
3D	Three-dimensional
BE	Boundary Elements
BESO	Bi-directional Evolutionary Structural Optimization
DOF	Degree Of Freedom
EDT	ElastoDynamics Toolbox
EMU	Electric Multiple Unit
ESO	Evolutionary Structural Optimization
FE	Finite Elements
FFT	Fast Fourier Transform
IL	Insertion Loss
PML	Perfectly Matched Layers
RAMP	Rational Approximation of Material Properties
RMS	Root Mean Square
SAND	Simultaneous Analysis and Design
SAO	Sequential Approximate Optimization
SIMP	Solid Isotropic Material with Penalization
MMA	Method of Moving Asymptotes
NAND	Nested Analysis and Design
SQP	Sequential Quadratic Programming
VC	Vibration Criteria

General notational conventions

$\mathbb{R}$	Set of real numbers
$\mathbb{C}$	Set of complex numbers
x	Scalar
$\mathbf{x}$	Vector
$\mathbf{X}$	Matrix
$\hat{\square}$	Variable $\square$ in the frequency-spatial domain
$\tilde{\square}$	Variable $\square$ in the frequency-wavenumber domain
$\underline{\square}$	Discretized variable
$\mathrm{Re}\{\square\}$, $\square^{\mathrm{R}}$	Real part of $\square$
$\mathrm{Im}\{\square\}$, $\square^{\mathrm{I}}$	Imaginary part of $\square$
$\square^{\mathrm{T}}$	Transpose of a matrix $\square$
$\square^{*}$	Complex conjugate of a matrix $\square$
$\square^{\mathrm{H}}$	Hermitian (conjugate) transpose of a matrix $\square$
$\square^{-1}$	Inverse of a matrix $\square$
$\mathrm{Tr}\{\square\}$	Trace of a matrix $\square$
$\det\{\square\}$	Determinant of a matrix $\square$

Operators

$\mathcal{F}$	Fourier transform
$\mathcal{F}^{-1}$	Inverse Fourier transform
$\ln$	Natural logarithm
$\log_{\square}$	Logarithm with base $\square$
$*$	Convolution

Material properties

β_{p}	Longitudinal damping ratio
β_{s}	Shear damping ratio
λ, μ	Lamé coefficients
ν	Poisson's ratio
ρ	Mass density
C_{p}	Longitudinal wave velocity
C_{s}	Shear wave velocity
C_{R}	Rayleigh wave velocity
E	Elastic modulus (Young's modulus)
G	Shear modulus ($= \mu$)
K	Impedance ratio

Elastodynamics

f	Frequency [Hz]
ω	Circular frequency [rad/s]
(x, y, z)	Cartesian coordinates
λ_y	Longitudinal wavelength
k_y	Longitudinal wavenumber
p_y	Longitudinal slowness
Σ	Interface between design domain and surrounding domain
$\mathbf{u}$	Displacement vector
$\mathbf{u}^{\mathrm{ref}}$	Displacement vector of the original space (without barrier)
$\hat{v}^{\mathrm{RMS}}$	RMS velocity
$\boldsymbol{\epsilon}$	Strain tensor
$\boldsymbol{\sigma}$	Stress tensor
$\mathbf{t}^{\mathrm{n}}$	Tractions on the boundary with outward normal vector $\mathbf{n}$
$\mathbf{n}$	Unit outward normal vector
$\mathbf{p}$	Force vector
$\mathbf{M}$	Mass matrix
$\mathbf{K}^0$, $\mathbf{K}^1$, $\ldots$	Stiffness matrices 2.5D FE approach
$\mathbf{K}$	Dynamic stiffness matrix
t	Transmission coefficient

Topology optimization

β	Heaviside projection sharpness parameter
η	Heaviside projection threshold
$\boldsymbol{\lambda}$	Adjoint vector
$\boldsymbol{\rho}$	Design variables
$\tilde{\boldsymbol{\rho}}$	Filtered densities
$\bar{\boldsymbol{\rho}}$	(Physical) element densities
$\bar{\boldsymbol{\rho}}^{\mathrm{d}}$	Dilated element densities
$\bar{\boldsymbol{\rho}}^{\mathrm{i}}$	Intermediate element densities
$\bar{\boldsymbol{\rho}}^{\mathrm{e}}$	Eroded element densities
$f(\mathbf{x})$	Objective function
$g(\mathbf{x})$	State equation
$h(\mathbf{x})$	Constraint function
p_j	SIMP penalization parameter for material parameter j
q_j	RAMP penalization parameter for material parameter j
R	Filter radius
$V^{\max}$	Volume constraint

Contents

Voorwoord **i**

Abstract **iii**

Beknopte samenvatting **v**

List of Symbols **vii**

Contents **xi**

List of Figures **xvii**

List of Tables **xxxiii**

1 Introduction **1**

1.1 Problem outline 1

1.2 State of the art 2

1.2.1 Mitigation measures for railway induced vibration . . . 2

1.2.2 Structural optimization 5

1.3 Objectives and contributions 7

1.4 Organization of the text 8

2 Periodic wave barriers for one-dimensional elastic wave propagation 11

2.1 Introduction 11

2.2 Direct stiffness formulation 13

2.2.1 Governing equations 13

2.2.2 Element dynamic stiffness matrices 14

2.2.3 Amplification problem 16

2.3 A layer embedded in a full space 17

2.3.1 Wave reflection and transmission at an interface 18

2.3.2 Wave reflection and transmission through a layer embedded in a homogeneous full space 20

2.4 Periodic stacking of layers 22

2.4.1 Bloch waves 22

2.4.2 Stopbands 27

2.4.3 Transmission for a stacking of periodic layers 30

2.5 Conclusion 36

3 Double wall barriers for three-dimensional elastic wave propagation 37

3.1 Introduction 37

3.2 Problem description 39

3.3 Two-and-a-half dimensional finite element method 41

3.3.1 Governing equations 42

3.3.2 Discretization 45

3.3.3 Perfectly matched layers 48

3.4 Analysis of a double wall barrier 50

3.4.1 Point load 50

3.4.2 Train loading 52

3.5 Physical interpretation 55

3.5.1 The stiffness effect 55

3.5.2 Reflection . . . 58

3.6 Influence of the material parameters . . . 68

3.7 Conclusion . . . 71

4 Topology optimization for one-dimensional elastic wave propagation 73

4.1 Introduction . . . 73

4.2 Topology optimization method . . . 74

4.2.1 Density based approach . . . 74

4.2.2 Regularization techniques and continuation schemes . . 79

4.2.3 Sensitivities . . . 82

4.2.4 Optimization algorithm . . . 86

4.3 Optimization of one-dimensional wave barriers . . . 87

4.3.1 Problem description . . . 87

4.3.2 Harmonic sources . . . 89

4.3.3 Broadband sources . . . 93

4.3.4 Harmonic sources at a frequency in a given range 98

4.4 Conclusion . . . 100

5 Topology optimization for two-dimensional elastic wave propagation 103

5.1 Introduction . . . 103

5.2 Topology optimization . . . 104

5.2.1 Problem description . . . 104

5.2.2 Optimization problem . . . 108

5.2.3 Harmonic sources . . . 109

5.2.4 Broadband sources . . . 117

5.2.5 Harmonic sources at a frequency in a given range 118

5.3 Robust optimization and practical designs . . . 119

5.3.1 Geometric imperfections . . . 119

5.3.2 Robust topology optimization 122
5.3.3 Shape optimization 125
5.3.4 Discrete object layout optimization 131
5.4 Conclusion 135

6 Topology optimization for three-dimensional elastic wave propagation 139

6.1 Introduction 139
6.2 Wave barriers of infinite length 140
6.2.1 Sensitivities 141
6.2.2 Spatially harmonic line loads 142
6.2.3 Point loads 148
6.3 Wave barriers of finite length 154
6.3.1 Subdomain formulation 154
6.3.2 Spatial windowing 155
6.3.3 Sensitivities 157
6.3.4 Results 158
6.4 A case study 159
6.4.1 Problem description 163
6.4.2 A double wall barrier 169
6.4.3 Minimizing the vibration levels 170
6.4.4 Minimizing the volume 173
6.5 Conclusion 176

7 Conclusions and recommendations for further research 179

7.1 Conclusions 180
7.2 Recommendations for further research 182

A Properties of the transfer matrix $\mathbf{H}$ for a periodic stacking of layers 185

A.1 Properties of the transfer matrix 186

A.2 Derivation of the Chebyshev Identity 187

B 2.5D methodology for shell elements 189

B.1 In-plane shell deformation 190

B.2 Bending of shell elements 191

B.3 Shape functions for two-node shell elements 196

C Dispersion relations for a beam 197

C.1 Longitudinal mode 198

C.2 Bending-shear modes 201

C.3 Torsion mode 206

Bibliography 215

Curriculum vitae 233

List of Figures

1.1 Railway induced vibrations in the built environment. 2

1.2 Mitigation measures on the transmission path: (a) open trench, (b) soft wave barrier, (c) stiff wall barrier, (d) subgrade stiffening, (e) wave impeding block, and (f) heavy mass on the surface. . . 3

2.1 Waves propagating through a periodic layered elastic medium. A part of the incoming wave with amplitude I is transmitted (T), a part is reflected (R) and a part is dissipated. 12

2.2 One-dimensional (a) semi-infinite and (b) finite layer. 15

2.3 One-dimensional amplification problem. 17

2.4 Two semi-infinite halfspaces with different properties, in contact at $x = 0$. 18

2.5 The reflection (dashed-dotted line) and transmission (solid line) coefficients (r and t). 19

2.6 Real part, imaginary part and modulus of the wave field for a homogeneous full space (dotted line) and two different semi-infinite halfspaces (solid line) at (a) 50 Hz and (b) 100 Hz. . . . 20

2.7 A layer with finite thickness embedded in a homogeneous full space. 21

2.8 Modulus of the transmission coefficient $|t|$ for a layer embedded in a full space with impedance ratio $K = 1$ (dotted line), $K = 0.5$ (dashed-dotted line), and $K = 2$ (solid line). 23

2.9 Real part, imaginary part and modulus of the wave field for a homogeneous full space (dotted line) and for a layer embedded in this full space with thickness 2 m (solid solid line) at (a) 50 Hz and (b) 100 Hz. 23

2.10 Part of the infinite periodic structure. 24

2.11 The function $\cos(kL)$ (equation (2.49)) as a function of the frequency with impedance ratio $K = 1$ (dotted line), $K = 0.5$ (dashed-dotted line), and $K = 2$ (solid line). 26

2.12 (a) Real and (b) imaginary part of the wavenumber k with impedance ratio $K = 1$ (dotted line), $K = 0.5$ (dashed-dotted line), and $K = 2$ (solid line). 26

2.13 Stop bands in the $(k_{\mathrm{p1}}L_1, k_{\mathrm{p2}}L_2)$ plane for an impedance ratio (a) $K = 1.5$, (b) $K = 2$, (c) $K = 5$, and (d) $K = 10$. 27

2.14 $(k_{\mathrm{p1}}L_1, k_{\mathrm{p2}}L_2)$ pairs corresponding to the frequencies f_{cs} close to the center of the stopbands (solid lines), the frequencies f_{ns} where no stopbands are observed (dashed lines), and the frequencies f_{mc} for which the function $\cos kL$ has a maximum (plus marks). 28

2.15 The width $\Delta(k_{\mathrm{p1}}L_1) = \Delta(k_{\mathrm{p2}}L_2)$ of the stopbands as a function of the impedance ratio K. 31

2.16 Periodic stacking of layers. 31

2.17 Modulus of the transmission coefficient $|t|$ for (a) two (b) three, (c) four, and (d) ten periodic cells with $K = 1$ (dotted line), $K = 0.5$ (dashed-dotted line), and $K = 2$ (solid line). The gray areas indicate the theoretical stopbands for $K = 2$ as predicted by equations (2.52) and (2.60). 33

2.18 Modulus of the transmission coefficient $|t|$ at the center frequency of the first stopband (i.e. at 50 Hz) as a function of the number of periodic cells for $K = 2$. 34

2.19 Real part, imaginary part and modulus of the wave field for a homogeneous full space (dotted line) and for two periodic cells embedded in this full space with thicknesses $L_1 = 1$ m and $L_2 =$ 2 m (solid line) at (a) 50 Hz and (b) 100 Hz.. 34

2.20 Real part, imaginary part and modulus of the wave field for a homogeneous full space (dotted line) and for three periodic cells embedded in this full space with thicknesses $L_1 = 1\,\mathrm{m}$ and $L_2 = 2\,\mathrm{m}$ (solid line) at (a) 50 Hz and (b) 100 Hz. 35

2.21 Real part, imaginary part and modulus of the wave field for a homogeneous full space (dotted line) and for four periodic cells embedded in this full space with thicknesses $L_1 = 1\,\mathrm{m}$ and $L_2 = 2\,\mathrm{m}$ (solid line) at (a) 50 Hz and (b) 100 Hz. 35

3.1 A semi-infinite halfspace excited by a point load at the surface. A double wall barrier is introduced to reduce the wave propagation close to the surface of the halfspace. 38

3.2 The three-dimensional wave propagation problem with a double wall barrier. The mesh is added as illustration only and is not the actual finite element mesh. 40

3.3 Domain Ω with longitudinal invariant cross-section A and Dirichlet (Γ_u) and Neumann boundary (Γ_t) conditions. 42

3.4 Real part of the vertical displacement $\hat{u}_z$ at 25 Hz resulting from a unit point load for (a) the original homogeneous halfspace, (b) the single stiff wall barrier (wall thickness $2t_w = 2\,\mathrm{m}$), and (c) the double stiff wall barrier (wall thickness $t_w = 1\,\mathrm{m}$ and spacing $d = 4\,\mathrm{m}$) in sandy soil. Corresponding insertion loss $\hat{\mathrm{IL}}$ for (d) the single stiff wall barrier and (e) the double stiff wall barrier in sandy soil. 51

3.5 Real part of the vertical displacement $\hat{u}_z$ at 50 Hz resulting from a unit point load for (a) the original homogeneous halfspace, (b) the single stiff wall barrier (wall thickness $2t_w = 2\,\mathrm{m}$), and (c) the double stiff wall barrier (wall thickness $t_w = 1\,\mathrm{m}$ and spacing $d = 4\,\mathrm{m}$) in sandy soil. Corresponding insertion loss $\hat{\mathrm{IL}}$ for (d) the single stiff wall barrier and (e) the double stiff wall barrier in sandy soil. 51

3.6 Amplitude of the vertical displacement $|\hat{u}_z|$ resulting from a point load for the original halfspace (dotted line), the single stiff wall barrier (dashed line; wall thickness $2t_w = 2\,\mathrm{m}$), and the double stiff wall barrier (solid line; wall thickness $t_w = 1\,\mathrm{m}$ and spacing $d = 4\,\mathrm{m}$) in sandy soil at the different receiver points: (a) receiver 1, (c) receiver 2, and (e) receiver 3 (figure 3.2). Corresponding insertion loss $\hat{\mathrm{IL}}$ for the single stiff wall barrier (dashed line) and the double stiff wall barrier (solid line) in sandy soil at the different receiver points: (b) receiver 1, (d) receiver 2, and (f) receiver 3. 53

3.7 The axle positions of a typical four-car EMU train. 54

3.8 (a) Amplitude of the vertical displacement $\hat{u}_z$ at receiver 1 (figure 3.2) resulting from a train load for the original halfspace (dotted line), the single stiff wall barrier (dashed line; wall thickness $2t_w = 2\,\mathrm{m}$), and the double stiff wall barrier (solid line; wall thickness $t_w = 1\,\mathrm{m}$ and spacing $d = 4\,\mathrm{m}$) in sandy soil. (b) Corresponding insertion loss $\hat{\mathrm{IL}}$ for the single stiff wall barrier (dashed line) and the double stiff wall barrier (solid line) in sandy soil. 54

3.9 (a) Dispersion curves for the single stiff wall (with a width of $2\,\mathrm{m}$ and a height of $7.5\,\mathrm{m}$). Dispersion curves computed from equation (3.50) are indicated with gray dots. The analytically calculated dispersion curves are superimposed: the longitudinal mode (solid line), Timoshenko's bending mode around the x-axis (dashed line), Timoshenko's bending mode around the z-axis (dotted line), and Barr's torsion mode (dashed-dotted line). The associated modes at $f \approx 0\,\mathrm{Hz}$ (from high to low value of p_y) are displayed for (b) the shear-bending mode around the z-axis, (c) the shear-bending mode around the x-axis, (d) the torsion mode, and (e) the longitudinal mode. 56

3.10 Insertion loss $\tilde{\mathrm{IL}}(x = 15\,\mathrm{m}, k_y, z = 0\,\mathrm{m}, \omega)$ for (a) the single stiff wall barrier (wall thickness $2t_w = 2\,\mathrm{m}$) and (b) the double stiff wall barrier (wall thickness $t_w = 1\,\mathrm{m}$ and spacing $d = 4\,\mathrm{m}$) in sandy soil. Superimposed are the analytical dispersion curve for Timoshenko's bending mode around the x-axis (black dashed line), the Rayleigh wave slowness (black solid line), and the frequency-slowness curves which show the phase shift between wave fronts in the reference case and in the case of stiffening (black dotted lines). For the double wall barrier, the dispersion curves caused by the standing waves between the walls are added (gray solid lines). 57

3.11 Definition of the wavenumber components for Rayleigh waves. . 59

3.12 Amplitude of the vertical displacement $\hat{u}_z$ and insertion loss $\hat{\mathrm{IL}}$ at receiver 1 (figure 3.2) resulting from a point load for a wall thickness t_w of (a)-(b) $0.5\,\mathrm{m}$, (c)-(d) $1\,\mathrm{m}$, and (e)-(f) $2\,\mathrm{m}$ in sandy soil. For the original halfspace, the amplitude is shown with a dotted line, for the single stiff wall barrier (wall thickness $2t_w$) with a dashed line. The results are plotted for different distances d between the walls: $0.5\,\mathrm{m}$, $1\,\mathrm{m}$, $2\,\mathrm{m}$, and $4\,\mathrm{m}$ (from light gray to black solid lines). 61

3.13 Insertion loss $\tilde{\mathrm{IL}}(x = 15\,\mathrm{m}, k_y, z = 0\,\mathrm{m}, \omega)$ for (a) the single stiff wall barrier (wall thickness $2t_w = 2\,\mathrm{m}$) and (b) the double stiff wall barrier (wall thickness $t_w = 2\,\mathrm{m}$ and spacing $d = 4\,\mathrm{m}$) in sandy soil. Superimposed are the analytical dispersion curve for Timoshenko's bending mode around the x-axis (black dashed line), the Rayleigh wave slowness (black solid line), and the frequency-slowness curves which show the phase shift between wave fronts in the reference case and in the case of stiffening (black dotted lines). For the double wall barrier, the dispersion curves caused by the standing waves between the walls are added (gray solid lines). 62

3.14 Insertion loss $\hat{\mathrm{IL}}$ at receiver 1 (figure 3.2) for the single stiff wall barrier (dashed line; wall thickness $2t_w = 2\,\mathrm{m}$) and the double stiff wall barrier (solid line; wall thickness $t_w = 2\,\mathrm{m}$ and spacing $d = 4\,\mathrm{m}$) in sandy soil, for both a point load (2.5D model, black line) and line load (2D model, gray line). 63

3.15 The one-dimensional wave propagation problem with a double wall barrier. 63

3.16 Insertion loss $\hat{\mathrm{IL}}_{1\mathrm{D}}$ for the one-dimensional problem as a function of the frequency in the case of the single stiff wall barrier (dashed line; wall thickness $2t_w = 2\,\mathrm{m}$) and the double stiff wall barrier (solid line; wall thickness $t_w = 2\,\mathrm{m}$ and spacing $d = 4\,\mathrm{m}$) in air. Superimposed are the mass law (thin line with circles), the value of the resonance frequency (dotted vertical line), and the theoretical values for frequencies above this frequency (thin line with triangles). 64

3.17 Insertion loss $\hat{\mathrm{IL}}_{1\mathrm{D}}$ for the one-dimensional problem as a function of the frequency in the case of the single stiff wall barrier (dashed line; wall thickness $2t_w = 2\,\mathrm{m}$) and the double stiff wall barrier (solid line; wall thickness $t_w = 2\,\mathrm{m}$ and spacing $d = 4\,\mathrm{m}$) in sandy soil. Superimposed are the stopband frequencies in equation (2.52) (gray lines). 65

3.18 Insertion loss for the one-dimensional problem $\hat{\mathrm{IL}}_{1\mathrm{D}}$ as a function of the wall thickness t_w and the distance d between the walls in the case of the double stiff wall barrier in sandy soil at (a) 20 Hz, (b) 40 Hz, (c) 60 Hz, and (d) 80 Hz. The lines corresponding to $k_1 d + k_2 t_w = n\pi$ for $n = 1, 2, \ldots$ are superimposed. 67

3.19 (a) Amplitude of the vertical displacement $\hat{u}_z$ at receiver 1 (figure 3.2) resulting from a point load for the original halfspace (dotted line), the single concrete wall barrier (dashed line; wall thickness $2t_w = 2\,\mathrm{m}$) and the double concrete wall barrier (solid line; wall thickness $t_w = 0.5\,\mathrm{m}$ and spacing $d = 4\,\mathrm{m}$) in sandy soil. (b) Corresponding insertion loss $\hat{\mathrm{IL}}$ at receiver 1 for the single concrete wall barrier (dashed line) and the double concrete wall barrier (solid line) in sandy soil. 68

3.20 Insertion loss $\tilde{\mathrm{IL}}(x = 15\,\mathrm{m}, k_y, z = 0\,\mathrm{m}, \omega)$ for (a) the single concrete wall barrier (wall thickness $2t_w = 2\,\mathrm{m}$) and (b) the double concrete wall barrier (wall thickness $t_w = 0.5\,\mathrm{m}$ and spacing $d = 4\,\mathrm{m}$) in sandy soil. Superimposed are the analytical dispersion curve for Timoshenko's bending mode around the x-axis (black dashed line) and the Rayleigh wave slowness (black solid line). For the double wall barrier, the dispersion curves caused by the standing waves between the walls are added (gray solid lines). 69

3.21 (a) Amplitude of the vertical displacement $\hat{u}_z$ at receiver 1 (figure 3.2) resulting from a point load for the original halfspace (dotted line), the single stiff wall barrier (dashed line; wall thickness $2t_w = 2\,\mathrm{m}$) and the double stiff wall barrier (solid line; wall thickness $t_w = 1\,\mathrm{m}$ and spacing $d = 4\,\mathrm{m}$) in soft clay soil. (b) Corresponding insertion loss $\hat{\mathrm{IL}}$ at receiver 1 for the single stiff wall barrier (dashed line) and the double stiff wall barrier (solid line) in soft clay soil. 70

3.22 Insertion loss $\tilde{\mathrm{IL}}(x = 15\,\mathrm{m}, k_y, z = 0\,\mathrm{m}, \omega)$ for (a) the single stiff wall barrier (wall thickness $2t_w = 2\,\mathrm{m}$) and (b) the double stiff wall barrier (wall thickness $t_w = 1\,\mathrm{m}$ and spacing $d = 4\,\mathrm{m}$) in soft clay soil. Superimposed are the analytical dispersion curve for Timoshenko's bending mode around the x-axis (black dashed line) and the Rayleigh wave slowness (black solid line). For the double wall barrier, the dispersion curves caused by the standing waves between the walls are added (gray solid lines). 70

4.1 General problem: a harmonic wave propagating in a full space encounters the design domain. 74

4.2 Material distribution in a design domain. 75

4.3 Different material interpolations: linear interpolation (dashed line), SIMP interpolation (solid line) and classical two-material interpolation (dashed-dotted line) for a value $p = 3$ of the penalization parameter. 78

4.4 Linear conic function used for density filtering [94]. 80

4.5 Approximate Heaviside projection function based on equation (4.11) for $\eta = 0.5$ and for different values of β: 1, 2, 4, 8, 16, and 32 (light gray to dark gray lines). These are compared with the Heaviside step function from equation (4.10) (black line). 81

4.6 One-dimensional topology optimization problem. The mesh is added as illustration only and is not the actual one. 88

4.7 Fully filled design used as initial design for the one-dimensional optimization. The boundaries of the design domain are indicated with a gray dashed line. 90

4.8 Convergence of the optimization problem for the design optimized at a frequency of 40 Hz (figure 4.9c). 91

4.9 One-dimensional designs optimized at a frequency of (a) 20 Hz, (c) 40 Hz, (e) 60 Hz, and (g) 80 Hz. The boundaries of the design domain are indicated with a gray dashed line. Transmission coefficient as a function of the frequency for the reference case of a fully filled design (dashed line) and for the designs optimized at (b) 20 Hz, (d) 40 Hz, (f) 60 Hz, and (h) 80 Hz (solid line). . . 92

4.10 One-dimensional designs optimized at a frequency of (a) $10 - 30$ Hz, (c) $30 - 50$ Hz, (e) $50 - 70$ Hz, and (g) $70 - 90$ Hz. The boundaries of the design domain are indicated with a gray dashed line. Transmission coefficient as a function of the frequency for the reference case of a fully filled design (dashed line) and for the designs optimized at (b) $10 - 30$ Hz, (d) $30 - 50$ Hz, (f) $50 - 70$ Hz, and (h) $70 - 90$ Hz (solid line). . 95

4.11 (a) One-dimensional design optimized for the average transmittance over the frequency range $20 - 80$ Hz with $N_f = 61$ (local optimum). The boundaries of the design domain are indicated with a gray dashed line. (b) Transmission coefficient as a function of the frequency for the reference case of a fully filled design (dashed line) and for the optimized design (solid line). . 96

4.12 Influence of the number of frequencies N_f considered in the optimization on the value of the objective function (x-marks) and the mean transmittance, computed with $\Delta f = 0.01$ Hz (circles). In (a), four frequency ranges are considered with $f_\mathrm{u} - f_\mathrm{l} = 20$ Hz (from top to bottom): $10-30$ Hz (blue), $30-50$ Hz (red), $50 - 70$ Hz (green), and $70 - 90$ Hz (magenta). In (b), the frequency range $20 - 80$ Hz (black) is considered. 96

4.13 (a) Design optimized for the average transmittance over the frequency range $20 - 80$ Hz with $N_f = 35$ (presumed global optimum). The boundaries of the design domain are indicated with a gray dashed line. (b) Transmission coefficient as a function of the frequency for the reference case of a fully filled design (dashed line) and for the optimized design (solid line). . 97

4.14 Alternative initial design for the one-dimensional optimization. The boundaries of the design domain are indicated with a gray dashed line. 98

4.15 Influence of the number of frequencies N_f considered in the optimization on the value of the objective function (x-marks) and the mean transmittance, computed with $\Delta f = 0.01\,\mathrm{Hz}$ (circles). The frequency range $20 - 80\,\mathrm{Hz}$ is considered and the initial design of the optimization is taken to be the one in figure 4.14. 98

4.16 (a) One-dimensional design optimized for the maximum transmittance over the frequency range $20 - 80\,\mathrm{Hz}$ with $N_f = 61$. The boundaries of the design domain are indicated with a gray dashed line. (b) Transmission coefficient as a function of the frequency for the reference case of a fully filled design (dashed line) and for the optimized design (solid line). 100

4.17 Influence of the number of frequencies N_f considered in the optimization on the value of the objective function (x-marks) and the maximum transmittance, computed with $\Delta f = 0.01\,\mathrm{Hz}$ (circles). The frequency range $20 - 80\,\mathrm{Hz}$ is considered. The initial design is in (a) the fully filled design in figure 4.7 and in (b) the asymmetric design in figure 4.14. 100

5.1 General problem: a semi-infinite halfspace excited at the surface by a line load. A wave barrier reduces the wave propagation close to the surface of the halfspace. 104

5.2 The optimization problem for the two-dimensional halfspace. The mesh is added as illustration only and is not the actual finite element mesh. 105

5.3 Constraints added to the intermediate nodes of the finer mesh in the design domain for a ratio of the element size of the surrounding domain to the element size of the design domain equal to (a) 2 and (b) 3. 108

5.4 The reference design: a rectangular single wall barrier. 110

5.5 Convergence of the optimization problem for the design maximizing $\hat{\mathrm{IL}}_z$ (equation (5.11)) at $25\,\mathrm{Hz}$ (figure 5.6a). 111

5.6 (a) Optimized design maximizing $\hat{\mathrm{IL}}_z$ at $25\,\mathrm{Hz}$, and (b) resulting insertion loss $\hat{\mathrm{IL}}_z$ (Eq. (5.11)) as a function of the frequency for the reference design in figure 5.4 (dashed line) and the optimized design (solid line). 111

5.7 The insertion loss (a) $\hat{\mathrm{IL}}_x$ (equation (5.12)) and (b) $\hat{\mathrm{IL}}$ (equation (5.13)) as a function of the frequency for the reference design in figure 5.4 (dashed line) and the optimized design in figure 5.6a (solid line). 112

5.8 (a) Optimized design maximizing $\hat{\mathrm{IL}}$ at 25 Hz, and (b) resulting insertion loss $\hat{\mathrm{IL}}$ (equation (5.13)) as a function of the frequency for the reference design in figure 5.4 (dashed line) and the optimized design (solid line). 113

5.9 Real part of the displacement field $\hat{\mathbf{u}}^R$ at 25 Hz (a) for the original domain and after the introduction of (b) the reference design in figure 5.4, (c) part (1) of the optimized design, (d) parts (1) and (2) of the optimized design, and (e) the entire optimized design maximizing IL at 25 Hz (figure 5.8a). Insertion loss IL at 25 Hz after the introduction of (f) the reference design in figure 5.4, (g) part (1) of the optimized design, (h) parts (1) and (2) of the optimized design, and (i) the entire optimized design maximizing IL at 25 Hz (figure 5.8a). 114

5.10 (a) Optimized design maximizing $\hat{\mathrm{IL}}$ at 50 Hz, and (b) resulting insertion loss $\hat{\mathrm{IL}}$ (equation (5.13)) as a function of the frequency for the reference design in figure 5.4 (dashed line) and the optimized design (solid line). 115

5.11 Real part of the displacement field $\hat{\mathbf{u}}^R$ at 50 Hz (a) for the original domain and after the introduction of (b) the reference design in figure 5.4, (c) the left half of part (1) of the optimized design, (d) part (1) of the optimized design, and (e) the entire optimized design maximizing $\hat{\mathrm{IL}}$ at 50 Hz (figure 5.10a). Insertion loss $\hat{\mathrm{IL}}$ at 50 Hz after the introduction of (f) the reference design in figure 5.4, (g) the left half of part (1) of the optimized design, (h) part (1) of the optimized design, and (i) the entire optimized design maximizing $\hat{\mathrm{IL}}$ at 50 Hz (figure 5.10a). 116

5.12 (a) Optimized design maximizing $\overline{\mathrm{IL}}$ over the frequency range $20 - 80$ Hz (discretized with 10 frequencies), and (b) resulting insertion loss $\hat{\mathrm{IL}}$ (equation (5.13)) as a function of the frequency for the reference design in figure 5.4 (dashed line) and the optimized design (solid line). 118

5.13 Real part of the displacement field $\hat{\mathbf{u}}^R$ in the homogeneous halfspace for excitation at (a) 30 Hz, (b) 50 Hz, and (c) 70 Hz, with the reference design for excitation at (d) 30 Hz, (e) 50 Hz, and (f) 70 Hz, and with the design maximizing the frequency averaged insertion loss $\overline{\mathrm{IL}}$ for excitation at (g) 30 Hz, (h) 50 Hz, and (i) 70 Hz. 119

5.14 (a) Optimized design maximizing $\min_{f_n} \hat{\mathrm{IL}}(f_n)$ over the frequency range $20 - 80$ Hz (discretized with 10 frequencies), and (b) resulting insertion loss $\hat{\mathrm{IL}}$ (equation (5.13)) as a function of the frequency for the reference design in figure 5.4 (dashed line) and the optimized design (solid line). 120

5.15 The (a) dilated ($\eta = 0.25$), (b) intermediate ($\eta = 0.5$), and (c) eroded ($\eta = 0.75$) version of the optimized design maximizing the insertion loss $\hat{\mathrm{IL}}$ at a frequency of 25 Hz (figure 5.8a) and (d) the influence of the projection threshold η on the insertion loss $\hat{\mathrm{IL}}$ at 25 Hz. 121

5.16 The (a) dilated ($\eta = 0.25$), (b) intermediate ($\eta = 0.5$), and (c) eroded ($\eta = 0.75$) version of the optimized design maximizing the insertion loss $\hat{\mathrm{IL}}$ at a frequency of 50 Hz (figure 5.10a) and (d) the influence of the projection threshold η on the insertion loss $\hat{\mathrm{IL}}$ at 50 Hz. 121

5.17 The (a) dilated ($\eta = 0.25$), (b) intermediate ($\eta = 0.5$), and (c) eroded ($\eta = 0.75$) version of the optimized design maximizing the frequency averaged insertion loss $\overline{\mathrm{IL}}$ over the frequency range $20 - 80$ Hz (figure 5.12a) and (d) the influence of the projection threshold η on the frequency averaged insertion loss $\overline{\mathrm{IL}}$ in the frequency range $20 - 80$ Hz. 122

5.18 The (a) dilated ($\eta = 0.25$), (b) intermediate ($\eta = 0.5$), and (c) eroded ($\eta = 0.75$) version of the optimized design maximizing the minimal insertion loss $\min_{f_n} \hat{\mathrm{IL}}(f_n)$ over the frequency range $20 - 80$ Hz (figure 5.14a) and (d) the influence of the projection threshold η on the minimal insertion loss $\min_{f_n} \hat{\mathrm{IL}}$ in the frequency range $20 - 80$ Hz. 123

5.19 (a) Optimized design maximizing $\overline{\mathrm{IL}}$ over the frequency range $20 - 80$ Hz (discretized with 10 frequencies) using a worst case robust approach, and (b) resulting insertion loss $\hat{\mathrm{IL}}$ (equation (5.13)) as a function of the frequency for the reference design in figure 5.4 (dashed line) and the optimized (intermediate) design (solid line). 124

5.20 The (a) dilated ($\eta = 0.25$), (b) intermediate ($\eta = 0.5$), and (c) eroded ($\eta = 0.75$) version of the robust optimized design maximizing the frequency averaged insertion loss $\overline{\mathrm{IL}}$ over the frequency range $20 - 80\,\mathrm{Hz}$ (figure 5.19a) and (d) the influence of the projection threshold η on the frequency averaged insertion loss $\overline{\mathrm{IL}}$ in the frequency range $20 - 80\,\mathrm{Hz}$. 125

5.21 (a) Simplified design after manual post-processing of the optimized design maximizing $\overline{\mathrm{IL}}$ over the frequency range $20 - 80\,\mathrm{Hz}$ (discretized with 10 frequencies) using a worst case robust approach (figure 5.19a), and (b) resulting insertion loss $\hat{\mathrm{IL}}$ (Eq. (5.13)) as a function of the frequency for the reference design in figure 5.4 (dashed line), the robust optimized design in figure 5.19a (dashed-dotted line), and the post-processed design (solid line). 125

5.22 Pyramid for the construction of rectangular objects. The function μ_e^o describing this pyramid is built from the auxiliary functions A_1^o, A_2^o, A_3^o, and A_4^o. 127

5.23 Construction of the element density field for the shape optimization problem: (a) pyramid densities $\boldsymbol{\mu}^1$, (a) pyramid densities $\boldsymbol{\mu}^2$, (c) total densities $\tilde{\boldsymbol{\rho}}$, and (d) element densities $\bar{\boldsymbol{\rho}}$ for a sharpness parameter $\beta = 8$. 128

5.24 Convergence of the optimization problem for the shape optimization problem (figure 5.25). 130

5.25 (a) Shape optimized design maximizing $\overline{\mathrm{IL}}$ over the frequency range $20 - 80\,\mathrm{Hz}$ (discretized with 10 frequencies), and (b) resulting insertion loss $\hat{\mathrm{IL}}$ (Eq. (5.13)) as a function of the frequency for the reference design in figure 5.4 (dashed line), the simplified robust design in figure 5.21a (dashed-dotted line) and the parameter optimized design (solid line). 130

5.26 (a) Discrete circle layout optimized design maximizing $\overline{\mathrm{IL}}$ over the frequency range $20 - 80\,\mathrm{Hz}$ (discretized with 10 frequencies), and (b) resulting insertion loss $\hat{\mathrm{IL}}$ (Eq. (5.13)) as a function of the frequency for the reference design in figure 5.4 (dashed line) and the optimized design (solid line). 134

5.27 (a) Discrete rectangle layout optimized design maximizing $\overline{\mathrm{IL}}$ over the frequency range $20 - 80\,\mathrm{Hz}$ (discretized with 10 frequencies), and (b) resulting insertion loss $\hat{\mathrm{IL}}$ (Eq. (5.13)) as a function of the frequency for the reference design in figure 5.4 (dashed line) and the optimized design (solid line). 135

5.28 (a) Discrete rectangle layout optimized design considering only the local neighborhood and maximizing $\overline{\mathrm{IL}}$ over the frequency range $20 - 80\,\mathrm{Hz}$ (discretized with 10 frequencies), and (b) resulting insertion loss $\hat{\mathrm{IL}}$ (Eq. (5.13)) as a function of the frequency for the reference design in figure 5.4 (dashed line) and the optimized design (solid line). 136

6.1 General problem: a semi-infinite halfspace excited by a point load at the surface. A wave barrier is introduced to reduce the wave propagation close to the surface of the halfspace. 140

6.2 Designs optimized at a frequency of 25 Hz for a slowness p_y equal to (a) 0 s/m, (c) 0.0025 s/m, and (e) 0.0050 s/m. Resulting insertion loss as a function of the frequency for the reference design in figure 5.4 (dashed line) and the optimized design (solid line) at a frequency of 25 Hz for a slowness p_y equal to (b) 0 s/m, (d) 0.0025 s/m, and (f) 0.0050 s/m. 144

6.3 Real part of the displacement field $\hat{\mathbf{u}}^R$ for excitation at 25 Hz in the homogeneous halfspace for a slowness p_y equal to (a) 0 s/m, (d) 0.0025 s/m, and (g) 0.0050 s/m, with the reference design for a slowness p_y equal to (b) 0 s/m, (e) 0.0025 s/m, and (h) 0.0050 s/m, and with the designs optimized for a slowness p_y equal to (c) 0 s/m, (f) 0.0025 s/m, and (i) 0.0050 s/m. 145

6.4 Designs optimized at a frequency of 50 Hz for a slowness p_y equal to (a) 0 s/m, (c) 0.0025 s/m, and (e) 0.0050 s/m. Resulting insertion loss as a function of the frequency for the reference design in figure 5.4 (dashed line) and the optimized design (solid line) at a frequency of 50 Hz for a slowness p_y equal to (b) 0 s/m, (d) 0.0025 s/m, and (f) 0.0050 s/m. 146

6.5 Real part of the displacement field $\hat{\mathbf{u}}^R$ for excitation at 50 Hz in the homogeneous halfspace for a slowness p_y equal to (a) 0 s/m, (d) 0.0025 s/m, and (g) 0.0050 s/m, with the reference design for a slowness p_y equal to (b) 0 s/m, (e) 0.0025 s/m, and (h) 0.0050 s/m, and with the designs optimized for a slowness p_y equal to (c) 0 s/m, (f) 0.0025 s/m, and (i) 0.0050 s/m. 147

6.6 The optimization problem for the two-and-a-half-dimensional halfspace excited by a point load. The mesh is added as illustration only and is not the actual finite element mesh. . . . 148

6.7 Designs optimized for a point load (a) at a frequency of 25 Hz, (c) at a frequency of 50 Hz, and (e) for the frequency range 20−80 Hz. Resulting insertion loss as a function of the frequency for the reference design in figure 5.4 (dashed line) and the optimized design (solid line) (b) at a frequency of 25 Hz, (d) at a frequency of 50 Hz, and (f) for the frequency range 20 − 80 Hz. 150

6.8 Real part of the displacement field $\hat{\mathbf{u}}^R$ in the homogeneous halfspace at a frequency f of (a) 25 Hz, (d) 50 Hz, and (g) 70 Hz, with the reference design at a frequency f of (b) 25 Hz, (e) 50 Hz, and (h) 70 Hz, and with the designs optimized for a receiver at $(x = 15\,\mathrm{m}, y = 0\,\mathrm{m}, z = 0\,\mathrm{m})$ at a frequency of (c) 25 Hz, (f) 50 Hz, and (i) 70 Hz (design optimized for 20 − 80 Hz). 151

6.9 Designs optimizing the insertion loss $\hat{\mathrm{IL}}_{0\,\mathrm{m}}$ at a frequency of (a) 25 Hz, (d) 50 Hz, and (g) 20 − 80 Hz. Designs optimizing the averaged insertion loss $\hat{\mathrm{IL}}_{10\,\mathrm{m}}$ for a point load at a frequency of (b) 25 Hz, (e) 50 Hz, and (h) 20 − 80 Hz. Designs optimizing the averaged insertion loss $\hat{\mathrm{IL}}_{40\,\mathrm{m}}$ for a point load at a frequency of (c) 25 Hz, (f) 50 Hz, and (i) 20 − 80 Hz. 153

6.10 Decomposition of (a) the soil displacement field $\tilde{\mathbf{u}}_{\mathrm{s}}$ into (b) the wave field $\tilde{\mathbf{u}}_0$ and (c) the diffracted wave field $\tilde{\mathbf{u}}_{\mathrm{d}}$ and decomposition of (d) the wave field $\tilde{\mathbf{u}}_0$ into (e) the incident wave field $\tilde{\mathbf{u}}_{\mathrm{inc}}$ and (f) the locally diffracted wavefield $\tilde{\mathbf{u}}_{\mathrm{d}0}$. 155

6.11 (a) Discrete (gray crosses) and fitted (black solid line) mode count $N(f)$ and (b) modal overlap $M(f)$, for the reference design in figure 5.4 with a length of $L_{\mathrm{b}y} = 15\,\mathrm{m}$. 157

6.12 Designs with a finite length of $L_{\mathrm{b}y} = 15\,\mathrm{m}$ optimized for a point load (a) at a frequency of 25 Hz, (c) at a frequency of 50 Hz, and (e) for the frequency range 20 − 80 Hz. Resulting insertion loss as a function of the frequency for the reference design in figure 5.4 (dashed line) and the optimized design (solid line) (b) at a frequency of 25 Hz, (d) at a frequency of 50 Hz, and (f) for the frequency range 20 − 80 Hz. 160

6.13 Real part of the displacement field $\hat{\mathbf{u}}^R$ in the homogeneous halfspace at a frequency f of (a) 25 Hz, (d) 50 Hz, and (g) 70 Hz, with the finite reference design at a frequency f of (b) 25 Hz, (e) 50 Hz, and (h) 70 Hz, and with the finite designs optimized for a receiver at $(x = 15\,\mathrm{m}, y = 0\,\mathrm{m}, z = 0\,\mathrm{m})$ at a frequency of (c) 25 Hz, (f) 50 Hz, and (i) 70 Hz (design optimized for $20 - 80$ Hz). 161

6.14 Designs with a finite length of $L_{\mathrm{b}y} = 15\,\mathrm{m}$ optimizing the insertion loss $\hat{\mathrm{IL}}_{0\,\mathrm{m}}$ at a frequency of (a) 25 Hz, (d) 50 Hz, and (g) $20 - 80$ Hz. Designs optimizing the averaged insertion loss $\hat{\mathrm{IL}}_{10\,\mathrm{m}}$ for a point load at a frequency of (b) 25 Hz, (e) 50 Hz, and (h) $20 - 80$ Hz. Designs optimizing the averaged insertion loss $\hat{\mathrm{IL}}_{40\,\mathrm{m}}$ for a point load at a frequency of (c) 25 Hz, (f) 50 Hz, and (i) $20 - 80$ Hz. 162

6.15 The longitudinally invariant elastodynamic optimization problem. The mesh is added as illustration only and is not the actual finite element mesh. 163

6.16 Model of (a) the railway track and (b) half a wagon [122]. . . . 164

6.17 PSD function of the dynamic axle loads obtained from the dynamic train-track interaction problem with the PSD function of the rail unevenness given by equation (6.25). 166

6.18 The one-third octave band RMS spectra of the velocity for the original homogeneous halfspace at receivers (a) `R1x`, (b) `R1y`, (c) `R1z`, (d) `R2z`, (e) `R3z`. Superimposed are Gordon's generic vibration criteria for sensitive equipment [78]. 167

6.19 Modes of the clamped building floor at (a) 21 Hz, (b) 56 Hz, (c) 110 Hz, and (d) 183 Hz (values for $k_y = 0\,\mathrm{m}^{-1}$). 168

6.20 The maximum one-third octave band RMS spectra of the velocity over the different receivers for the homogeneous halfspace. Superimposed are Gordon's generic vibration criteria for sensitive equipment [78]. 169

6.21 (a) The single wall barrier, (b) the double wall barrier and (c) the maximum one-third octave band RMS spectra of the velocity at the different receivers for the original homogeneous halfspace (black), for the single wall barrier (blue), and for the double wall barrier (blue). 170

6.22 The weighting function w_m. 171

6.23 (a) The topology optimized design and (b) the maximum one-third octave band RMS spectra of the velocity at the different receivers for the original homogeneous halfspace (black), for the rectangular reference design in figure 6.21a (blue), and for the optimized design (red). 172

6.24 (a) The inclined part of the topology optimized design and (b) the maximum one-third octave band RMS spectra of the velocity at the different receivers for the original homogeneous halfspace (black), for the optimized design (red), and for the inclined part of this design (cyan). 172

6.25 The (a) dilated ($\eta = 0.25$), (b) intermediate ($\eta = 0.5$), and (c) eroded ($\eta = 0.75$) version of the optimized design and (d) the influence of the projection threshold η on the maximum one-third octave band RMS spectra of the velocity at the different receivers. 173

6.26 (a) Simplified design after a manual post-processing of the topology optimized design and (b) the maximum one-third octave band RMS spectra of the velocity at the different receivers for the original homogeneous halfspace (black), for the optimized design (red), and for the simplified design (magenta). 174

6.27 (a) The topology optimized design satisfying the VC-C for a minimum volume and (b) the maximum one-third octave band RMS spectra of the velocity at the different receivers for the original homogeneous halfspace (black), for the rectangular reference design in figure 6.21a (blue), and for the optimized design (red). 175

6.28 (a) The topology optimized design satisfying the VC-D for a minimum volume and (b) the maximum one-third octave band RMS spectra of the velocity at the different receivers for the original homogeneous halfspace (black), for the rectangular reference design in figure 6.21a (blue), and for the optimized design (red). 175

C.1 Element with longitudinal deformation. 198

C.2 Element with (a) only bending deformation, (b) only shear deformation, and (c) total bending-shear deformation (Timoshenko's Theory). 201

C.3 Element with torsion deformation. 206

List of Tables

1.1 Organization of the text. 9

3.1 Material properties of the original homogeneous halfspace and the stiff wall barrier. 40

3.2 Theoretical frequencies calculated with equation (2.52) compared with local maxima in the insertion loss for respectively the 1D, 2D, and 2.5D model. 66

4.1 Material properties used in the optimization of the one-dimensional design. 88

4.2 Thicknesses of the layers fulfilling the quarter-wave stack conditions for $C_{\mathrm{p}1} = 200$ m/s and $C_{\mathrm{p}2} = 400$ m/s. 93

5.1 Material properties of the original homogeneous halfspace and the inserted material. 105

6.1 Characteristics of the railway track [119]. 165

6.2 Characteristics of the EMU train [129]. 165

6.3 Receiver positions in the building where the vibration levels are to be reduced. 166

Chapter 1

Introduction

1.1 Problem outline

Railway induced vibrations in the built environment are a major environmental concern. These vibrations are generated at the wheel-rail interface, for example by rail or wheel unevenness, rail joints, or parametric excitation, and propagate as elastic waves in the underlying soil (figure 1.1). Interaction with buildings results in discomfort to people and malfunctioning of sensitive equipment in the frequency range between 1 and 80 Hz. At frequencies between 16 and 250 Hz, ground-borne vibrations can cause re-radiated or structure-borne noise by vibrating walls and floors [118].

The growing need for public transportation in populated areas, the construction of buildings close to railway lines, and the increasing sensitivity of equipment have necessitated the development of vibration mitigation measures. For existing tracks, mitigation measures that hinder the wave propagation in the soil have the advantage of not requiring modification or renewal of railway infrastructure. Railway operators are often not keen on modifying railway lines, as this not only leads to modification costs, but also to loss of profits due to the closure of the line.

Currently, only a limited number of simple design geometries for mitigation measures have been investigated, mostly single wall barriers with a rectangular cross section. The geometry plays an important role in the performance of mitigation measures, but only the influence of the width and the height of barriers has been assessed [65]. The depth of the mitigation measure for example determines to what extent incoming waves are reflected or refracted.

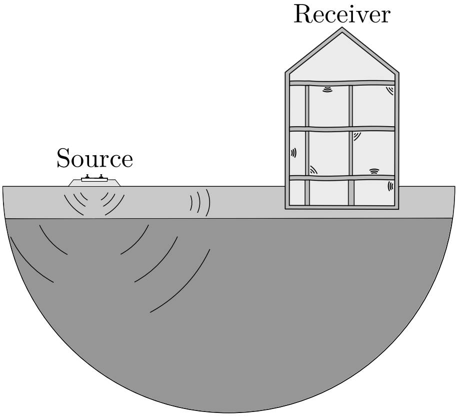

Figure 1.1: Railway induced vibrations in the built environment.

Furthermore, the geometry influences the stiffness which has proven to be important in the performance of mitigation measures in the soil [53]. This demonstrates the importance of the design geometry, indicating the potential of improved performance by exploring novel shapes.

1.2 State of the art

This section provides a state of the art of some aspects considered in this work. First, an overview is given of mitigation measures for railway induced vibration. Next, a state of the art in topology optimization is given.

1.2.1 Mitigation measures for railway induced vibration

In order to reduce environmental ground vibration due to railway traffic, mitigation measures at the source, on the transmission path and at the receiver can be applied. Mitigation measures at the source include rail grinding [131], soft railpads [88], under-sleeper pads [123], ballast mats [49] and floating slab tracks [120]. Mitigation measures at the receiver include foundation design and base isolation [159]. Mitigation measures on the transmission path aim at impeding propagation of ground vibrations from source to receiver. They are particularly appealing in situations with existing track and buildings, since these can be left unmodified.

Open trenches (figure 1.2a) can be used as mitigation measure on the transmission path [101, 174]. They start to be effective for depths larger than half the Rayleigh wavelength [74]. The effectiveness of an open trench is almost independent of the trench width [27]. Due to stability reasons and the possible presence of ground water, however, the open trenches can only be built for small depths. They can be stabilized by using sloped or walled trenches [100], which hardly effect the performance [65].

Alternatively, a soft wave barrier can be used (figure 1.2b). Soft barriers can be constructed for example using rubber chips [107, 183], gas-filled cushions [125] and polystyrene sandwich panels [74]. The barrier depth again determines the frequency range of effectiveness. The vibration reduction increases with decreasing stiffness of the in-fill material and with increasing barrier width [65].

Stiff wall barriers (figure 1.2c) can also be effective mitigation measures. Examples include concrete walls [4, 9], a row of concrete piles [102], sheet pile walls [7, 64], and jet grouting [50]. The effectiveness is influenced by both the impedance and the stiffness of the barrier. For large depths, the difference in impedance will result in reflection of incoming Rayleigh waves. The bending stiffness of the wall prevents the propagation of waves for small trace wavelengths compared to the bending wavelength of the barrier [53].

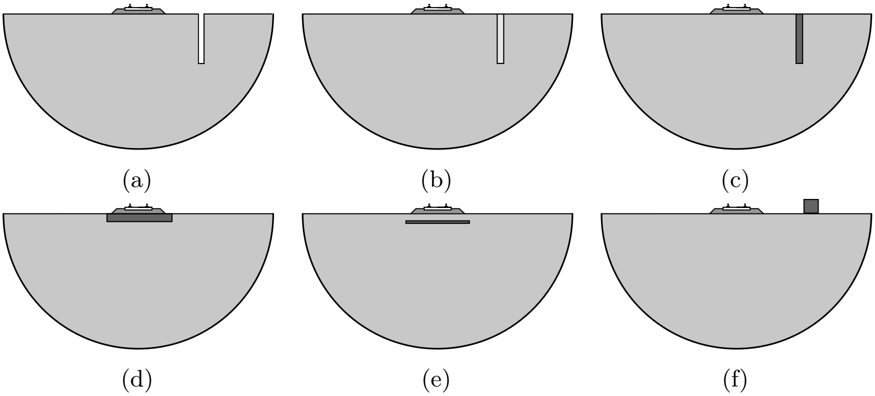
(a) (b) (c)

(d) (e) (f)

Figure 1.2: Mitigation measures on the transmission path: (a) open trench, (b) soft wave barrier, (c) stiff wall barrier, (d) subgrade stiffening, (e) wave impeding block, and (f) heavy mass on the surface.

Up to now, single wall barriers with a rectangular cross section have mostly been studied. In building acoustics, however, it is well known that double walls can reduce sound levels much better than single walls, especially between the double wall resonance frequency and the first cavity resonance frequency [70].

Double wall barriers for environmental ground vibration have, despite their potential, not been investigated.

Subgrade stiffening (figure 1.2d) is often applied in the case of soft soils to improve the soil beneath the track, including the embankment and the top layers beneath and next to the track. It can lead to an increased bearing capacity, reduction of settlements, a decrease in the risk of failure, and a better earthquake resistance [3]. Subgrade stiffening has moreover shown to be effective as mitigation measure [9, 53]. Several soil improvement techniques can be applied, such as vibro compaction and replacement [13], deep soil mixing [14], lime-cement columns [88], jet grouting [130] and vacuum consolidation [69]. There is, however, a risk for track uplifting [51], making it less suitable as vibration mitigation measure.

Wave impeding blocks (figure 1.2e) in the soil under or next to the track aim at modifying the wave propagation in the soil. Both solid [134] and honeycomb [157] structures have been studied as wave impeding blocks. For a soft layer on a rigid bedrock, it is known that a cut-on frequency exists below which the propagating waves remain evanescent [145]. Installing a sufficiently stiff wave impeding block in the soil reduces the thickness of the top layer, therefore increasing the cut-on frequency. The installing of wave impeding blocks, however, may amplify the vibration levels at higher frequencies [134]. Takemiya and Fujiwara [158] pointed out that the wave impeding block is only effective if its width is sufficiently large compared with the wavelength.

Instead of inserting material into the soil, stone baskets or concrete blocks can be placed on the surface (figure 1.2f). The incident surface waves are scattered by these wave reflectors, reducing the transmitted wave field [110]. The best performance is found for soft soils and heavy masses, as a low mass-spring resonance frequency leads to a strong vibration reduction [63]. The walls can also be used as a noise barrier, therefore reducing both airborne sound and vibration propagation in the soil.

As subgrade stiffening has the risk of track uplifting and wave impeding blocks need to be very large in order to be effective, these are not preferred as mitigation measures for existing tracks. The effectiveness of the other mitigation measures strongly depends on the soil profile, and soft soils are found to be generally beneficial [65]. Soft wave barriers have the best performance for soft fill materials, but the stiffness can be affected by the confining pressure due to the soil, the presence of groundwater, chemical components in the soil and freeze/thaw cycles, influencing their lifetime [121]. Stiff barriers have the ability to be very effective in reducing vibrations at low frequencies [50, 62]. The cost of soft and stiff barriers is expected to be larger than for heavy masses next to the track and is mainly determined by the cost of the inserted material, the installation cost (which also depends on the soil type), the cost for determining the soil properties, and the cost for evaluating the vibration levels [121]. Barriers have, however, hardly a visual impact, opposed to heavy masses next to the track [121].

Complex design geometries have rarely been considered. Because of the high computational cost of numerical simulations, mitigation measures on the transmission path are usually designed by trial and error. This leads to designs which are underperforming in cost-effectiveness. Because of its potential for finding novel, optimized designs, topology optimization can be adopted to improve the design of current mitigation measures on the transmission path. A state of the art relating to structural optimization with focus on topology optimization is therefore given next.

1.2.2 Structural optimization

In structural optimization, a design problem is formulated as a mathematical optimization problem where the total cost of a structure is minimized for a given performance. Alternatively, the performance is maximized while the cost is specified in advance. Structural optimization approaches are commonly categorized in three groups: size, shape, and topology optimization [43]. In size optimization the cross-sectional dimensions of members such as beams or plates are optimized. The layout of these members has been specified a priori [86]. Traditionally, they are considered as continuous optimization problems. In practice, however, the design variables can only take discrete values, for example when selecting a beam from a steel catalog, making the problems hard to solve [160]. Moreover, the members are often subjected to a large number of constraints, and it takes a lot of effort to take these into account [168].

In shape optimization problems, the geometry of a structure is optimized. A distinction can be made between two approaches. In the first approach, the finite element node coordinates are used as design variables [182]. This approach provides much design freedom [113], but often leads to large optimization problems which possess some numerical instabilities [85]. In the second approach, the boundary is parametrized, for example using spline functions [32], tackling these issues at the expense of modeling effort [10].

Topology optimization searches for the most efficient distribution of a given amount of material in a specified design domain. Topology optimization simultaneously optimizes not only the size and the shape of the design, but also the topology, making it possible to obtain novel, improved design geometries. Classically, the book of Bendsøe and Sigmund [23] is suggested as an introduction in topology optimization. For more recent advances in methodology and application, the review paper of Deaton and Grandhi [59] can be recommended.

Topology optimization was originally developed for static mechanical problems, but has since then been used for a variety of applications including problems governed by wave propagation [140]. A lot of research has been performed in the field of photonic crystal waveguide design. These electromagnetic waveguides are designed based on the band-gap phenomenon in periodic structures, obstructing wave propagation for specific frequencies [29, 97]. An overview of the applications within nano-photonics is given by Jensen and Sigmund [98].

Next to photonic band-gaps due to electromagnetic waves, also phononic band-gaps due to elastic and acoustic waves have been investigated. Sigmund and Jensen [149] maximize the bandwidth of phononic band-gap materials and minimize the transmitted wave amplitude of a band-gap structure subjected to harmonic loading. Jensen [96] discusses a two-dimensional problem, where an incoming plane pressure or shear wave is maximally reflected or dissipated by an optimal periodic distribution of scattering or absorbing inclusions.

Structural optimization has also been applied to acoustic design problems. Pioneering work in the application of topology optimization to acoustic problems is done by Wadbro and Berggren [171], who optimize an acoustic horn that efficiently radiates sound. In room acoustics, topology optimization has been used to optimally distribute reflecting material along the ceiling or walls of a room [67]. Christiansen et al. [44] use topology optimization to minimize the average pressure level in an acoustic cavity, which is later validated experimentally [45]. The application of noise barriers has also received some attention. Duhring et al. [67] optimize an outdoor barrier to reduce the sound power level behind the barrier. A similar problem is considered by Yoon et al. [181] who use a mixed finite element approach. Kook et al. [108] minimize the maximum main loudness. Greiner et al. [79] apply shape optimization using genetic algorithms to optimize Y-shaped noise barriers. Shape optimization is also used by Abe et al. [1] to optimize noise barriers for railway viaducts.

Topology optimized designs are often only optimal for the specific problem considered. Small variations in the physical system might result in a strongly deteriorated performance. Robust optimization techniques have been developed to take these uncertainties into account. Sources of uncertainty considered in robust optimization include load conditions [20, 35, 68], material properties [11, 39, 111], support conditions [127], and geometric imperfections. Several types of geometric imperfections have been studied: over- and underetching [111, 143, 147, 172], misplacement of material [94], and local material failure [95].

1.3 Objectives and contributions

Only simple design geometries for mitigation measures on the transmission path have been considered whose dimensions are obtained by trial and error. However, current construction methods of wave barriers provide a wider flexibility in design geometry. Improvements are expected when considering more complex and optimized designs, which will be explored in this work.

The objectives are therefore to (1) study novel design geometries which have the potential to improve the current performance and (2) develop a methodology to optimize the design of mitigation measures. Because of its potential for identifying novel design geometries, topology optimization is adopted as the main tool for design optimization.

The main contributions are:

- The performance of a double wall barrier is investigated using a 2.5D FE-PML model. A comparison is made between the single and double walls, and the influence of geometric and material parameters is assessed by examining the free vibrations of the wall structure and by analyzing an equivalent one-dimensional model. It is shown that double wall barriers only perform better than single wall barriers for specific geometries.
- It is investigated whether using topology optimization to design mitigation measures for railway induced vibration leads to geometries outperforming the simple shapes previously investigated. The results of this work demonstrate the high potential of optimized designs as they lead to a considerable performance improvement and volume reduction.

The original contributions related to the methodology include:

- The adjoint method is applied to compute the sensitivities with respect to the design variables. This allows computing the gradient by means of only one additional analysis. Analytical expressions for the sensitivities are needed and are therefore derived in this work for one-dimensional, two-dimensional, and two-and-a-half-dimensional models. These expressions are applied to multiple objective and constraint functions. The sensitivities are verified by means of the finite difference method.
- A methodology is developed to find simplified designs. By applying a robust optimization approach, designs are obtained which are less

sensitive to deviations in the design geometry. These designs can be simplified with only little deterioration. A shape optimization can further optimize the design. An alternative is presented which optimizes the layout of discrete objects. The method developed by Guest [81] considered circular shapes and is extended to rectangular shapes and convex polygons. The method is then applied for finding simple designs.

1.4 Organization of the text

The text can be divided in two main parts. In the first part (chapters 2 and 3), wave barriers are analyzed whose potential is shown by successful applications in other fields such as photonics and acoustics. In the second part (chapters 4 to 6), structural optimization is applied to discover novel design geometries. The two parts are further sub-divided according to the loading type, namely plane waves, line loads, and point loads. An overview is given in table 1.1.

Chapter 1 introduces the thesis by presenting the problem statement and the state of the art for mitigation measures for railway induced vibrations, wave propagation models, and structural optimization. The original contributions are highlighted and the organization of the text is clarified.

Chapter 2 gives an introduction of wave propagation in one-dimensional elastic media, focusing on periodic series of alternating layers as wave barrier for incoming plane waves. The existence of stopbands in infinite periodic series is shown and the influence of the number of periodic cells is studied.

Chapter 3 analyzes the performance of double wall barriers for mitigation of ground vibration transmission by 2.5D FE-PML models. A comparison is made with single wall barriers and a physical interpretation is given by studying the performance in the frequency-wavenumber domain and by comparing the behaviour with equivalent one-dimensional models. The influence of geometric and material properties is investigated.

Chapter 4 introduces the concepts of topology optimization, discusses its application to elastodynamics, and presents the adjoint method for the computation of the sensitivities. A one-dimensional optimization problem is presented where the transmission of plane waves in a full space is minimized. Multiple objective functions are considered, namely for harmonic sources at a known frequency, at a frequency in a given range, and broadband sources.

Chapter 5 discusses the application of topology optimization for designing wave barriers close to the surface of a halfspace excited by a line load. As the designs are shown to be sensitive to geometric imperfections, a robust

Table 1.1: Organization of the text.

	Analysis	Optimization
Plane waves	Chapter 2 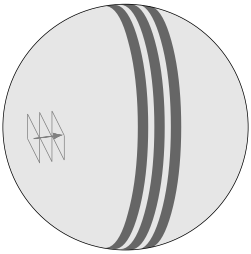	Chapter 4 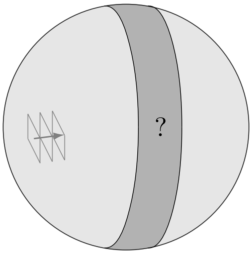
Line loads		Chapter 5 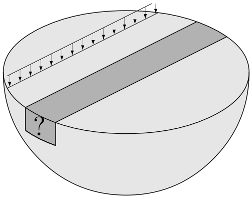
Point loads	Chapter 3 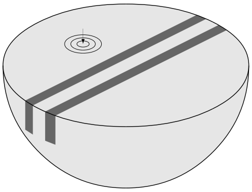	Chapter 6 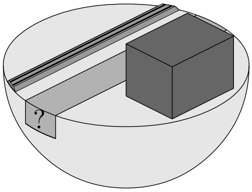

optimization approach is subsequently used. Furthermore, this chapter deals with the issue of feasibility.

Chapter 6 focuses on topology optimization taking three-dimensional wave propagation into account by using a 2.5D FE-PML model. A similar problem to the one in chapter 5 is first considered, but now for point loads exciting the surface. The influence of the barrier length on the optimized design is analyzed by applying the spatial windowing technique. To conclude, a case study is presented in which the model is expanded with a building and coupled to a track excited by the axle loads of a passing train.

Chapter 7 summarizes the main conclusions of the thesis and gives some recommendations for further research.

Chapter 2

Periodic wave barriers for one-dimensional elastic wave propagation

2.1 Introduction

This chapter investigates the wave transmission through one-dimensional periodic stacking of layers. The problem considered is shown in figure 2.1. A homogeneous elastic full space is divided in two by a periodic layered elastic medium. When an incoming wave arrives at the periodic configuration, a part of the energy is transmitted, a part is reflected and a part is dissipated in the structure. The frequency domain formulation allows for a simple analysis of harmonic wave propagation through one-dimensional media.

Wave propagation in one-dimensional media has been studied for a long time [2]. In the field of elastodynamics, the direct stiffness method [104] has been developed, considering wave propagation in linear elastic horizontally layered media. This method is similar to the Haskell-Thomson transfer matrix approach [87, 161], but the direct stiffness method has as advantages that the stiffness matrices are symmetric, they involve half as many degrees of freedom as transfer matrices, and the method is robust for thick layers and high frequency by the implementation of limiting expressions [103]. The direct stiffness method has been implemented in MATLAB in the EDT toolbox developed at the Structural Mechanics Section of KU Leuven [142].

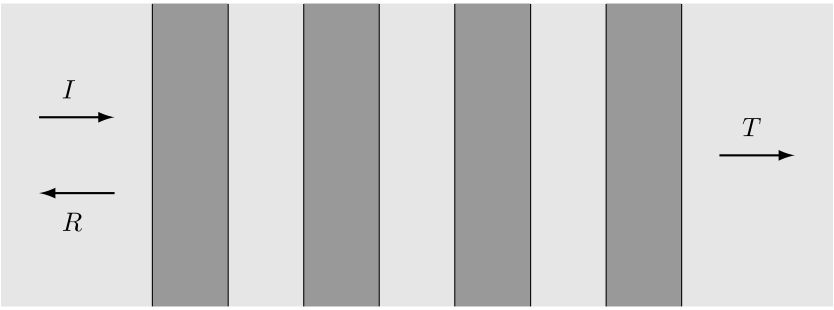

Figure 2.1: Waves propagating through a periodic layered elastic medium. A part of the incoming wave with amplitude I is transmitted (T), a part is reflected (R) and a part is dissipated.

Periodic one-dimensional media have already been extensively studied in many domains [34, 128]. The most important applications nowadays can be found in the field of photonics [141]. The periodicity leads to the well-known pass- and stopbands [99]. Yariv and Yeh [179] have calculated an expression for the dispersion relation between the wavenumber and the frequency and proposed an analytical expression for the reflectivity of a multi-periodic structure [180]. A similar expression for the transmittance is determined using the transfer matrix method [21, 152].

Next to photonics, where the governing waves are electromagnetic, research on periodic one-dimensional media has also been done in the case of elastic waves, primarily in the field of composite materials. An example are the locally resonant sonic materials developed by the group of Sheng [116]. Dispersion curves are derived using the transfer matrix method by Hussein et al. [91, 92] for both infinite and finite structures. The same authors also designed a periodic structure with the multiscale dispersive design methodology by first designing a periodic unit cell [93].

In this chapter, wave propagation through one-dimensional periodic elastic media is studied, both for a single layer and for a periodic stacking of layers. The theory discussed in this chapter will be used in the next chapter to interpret the performance of double wall barriers. In chapter 4, optimized one-dimensional designs are shown which consist of periodic stacking of layers. This chapter gives the underlying explanation of these optimization results by analyzing their performance.

The chapter is organized as follows. The direct stiffness formulation is introduced first. In section 2.3, the wave propagation through a single layer with finite thickness in a homogeneous full space is studied. Next, the wave propagation through a periodic stacking of layers is discussed and the phenomenon of stop- and passbands is addressed (section 2.4).

2.2 Direct stiffness formulation

This section introduces the governing elastodynamic equations, as can be found in for example [2] or [60], and presents the direct stiffness formulation [60, 104].

2.2.1 Governing equations

A P-wave propagates in the x-direction and causes a displacement component $u_x(x,t)$ as a function of time t. The equation of motion in the x-direction is [2]:

$$\frac{\partial \sigma_{xx}}{\partial x} + \rho b_x = \rho \frac{\partial^2 u_x}{\partial t^2} \tag{2.1}$$

In this expression, ρ is the density of the material and ρb_x is the body force in the x-direction. In the case of constrained wave propagation, the normal stress σ_{xx} in the x-direction is equal to [2]:

$$\sigma_{xx} = (\lambda + 2\mu)\epsilon_{xx} \tag{2.2}$$

where λ and μ are the Lamé coefficients and the strain ϵ_{xx} is found from the following linear strain-displacement relation [2]:

$$\epsilon_{xx} = \frac{\partial u_x}{\partial x} \tag{2.3}$$

When no body forces are present, equation (2.1) reduces to the following partial differential equation [2]:

$$\frac{\partial^2 u_x}{\partial x^2} = \frac{1}{C_{\mathrm{p}}^2}\frac{\partial^2 u_x}{\partial t^2} \tag{2.4}$$

where $C_{\mathrm{p}} = \sqrt{\dfrac{\lambda + 2\mu}{\rho}}$ is the dilatational wave velocity.

Consider now the following Fourier transform pair [71, 165]:

$$\hat{u}_x(x,\omega) = \int\limits_{-\infty}^{\infty} u_x(x,t) e^{-\mathrm{i}\omega t} \mathrm{d}t \tag{2.5}$$

$$u_x(x,t) = \frac{1}{2\pi} \int\limits_{-\infty}^{\infty} \hat{u}_x(x,\omega) e^{+\mathrm{i}\omega t} \mathrm{d}\omega \tag{2.6}$$

where a hat above a variable denotes its representation in the frequency domain and i is the imaginary unit. The forward Fourier transform of the partial differential equation (2.4) results in the following differential equation for the transformed displacement $\hat{u}_x(x,\omega)$ [60]:

$$\frac{\partial^2 \hat{u}_x}{\partial x^2} + \frac{\omega^2}{C_\mathrm{p}^2} \hat{u}_x = 0 \tag{2.7}$$

With the wavenumber given by $k_\mathrm{p} = \dfrac{\omega}{C_\mathrm{p}}$, this equation becomes [60]:

$$\frac{\partial^2 \hat{u}_x}{\partial x^2} + k_\mathrm{p}^2 \hat{u}_x = 0 \tag{2.8}$$

The solution of this differential equation is given by [60]:

$$\hat{u}_x(x,\omega) = P e^{-\mathrm{i}k_\mathrm{p}x} + N e^{+\mathrm{i}k_\mathrm{p}x} \tag{2.9}$$

where the amplitudes P and N refer to waves propagating in the positive and in the negative x-direction, respectively. The axial strain $\hat{\epsilon}_{xx}(x,\omega)$ becomes:

$$\hat{\epsilon}_{xx}(x,\omega) = \frac{\partial \hat{u}_x}{\partial x} = -\mathrm{i}k_\mathrm{p} P e^{-\mathrm{i}k_\mathrm{p}x} + \mathrm{i}k_\mathrm{p} N e^{+\mathrm{i}k_\mathrm{p}x} \tag{2.10}$$

and the normal stress $\hat{\sigma}_{xx}(x,\omega)$ is equal to:

$$\hat{\sigma}_{xx}(x,\omega) = (\lambda + 2\mu)\hat{\epsilon}_{xx}(x,\omega) \tag{2.11}$$

2.2.2 Element dynamic stiffness matrices

The direct stiffness method can be used to model one-dimensional wave propagation [104]. This method is similar to the finite element method: a layered medium is modelled as an assembly of layers, and element stiffness matrices are used to express the relation between displacements and tractions at the element boundaries. In this section, the element stiffness matrices are derived according to [60]. The stiffness matrix is then assembled from the element stiffness matrices in the same way as for the finite element method. A distinction is made between semi-infinite and finite layers.

Semi-infinite layer Consider the case of a semi-infinite layer given by figure 2.2a. In this one-dimensional semi-infinite layer, without any applied forces, waves can only propagate in the positive x-direction as Sommerfeld's radiation condition [151] should be met. The displacement $\underline{\hat{u}}_{x1}$ at the end $x = 0$ of the layer can be derived from equation (2.9):

$$\underline{\hat{u}}_{x1} = \hat{u}_x(0, \omega) = P \tag{2.12}$$

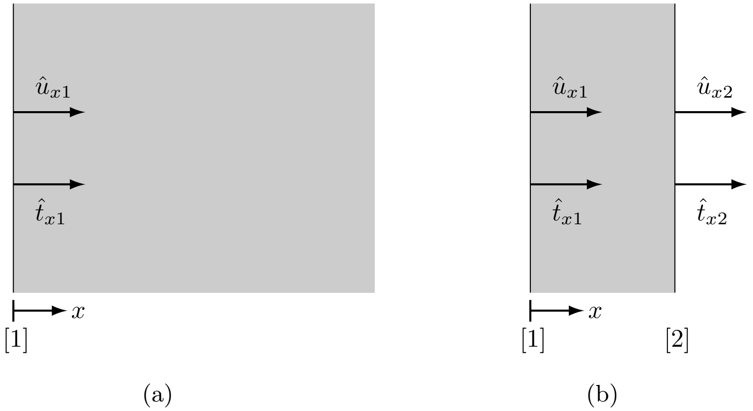

Figure 2.2: One-dimensional (a) semi-infinite and (b) finite layer.

The traction vector $\underline{\hat{t}}_{x1}$ at the end $x = 0$ of the semi-infinite layer can be derived from equations (2.10) and (2.11):

$$\begin{aligned} \underline{\hat{t}}_{x1} = \hat{t}_x(0, \omega) = -\hat{\sigma}_{xx}(0, \omega) &= -(\lambda + 2\mu)\hat{\epsilon}_{xx}(0, \omega) \\ &= (\lambda + 2\mu)\mathrm{i}k_{\mathrm{p}}P \end{aligned} \tag{2.13}$$

Elimination of the unknown amplitude P from equations (2.12) and (2.13) results in the following relation between the traction $\underline{\hat{t}}_{x1}$ and the displacement $\underline{\hat{u}}_{x1}$ [60]:

$$\underline{\hat{t}}_{x1} = \mathrm{i}k_{\mathrm{p}}(\lambda + 2\mu)\underline{\hat{u}}_{x1} = \mathrm{i}\omega\rho C_{\mathrm{p}}\underline{\hat{u}}_{x1} \tag{2.14}$$

This can be written in the form:

$$\hat{\mathbf{K}}^e \underline{\hat{\mathbf{u}}}^e = \underline{\hat{\mathbf{t}}}^e \tag{2.15}$$

Here, $\underline{\hat{\mathbf{u}}}^e = \{\underline{\hat{u}}_{x1}\}$ is the displacement vector, $\underline{\hat{\mathbf{t}}}^e = \{\underline{\hat{t}}_{x1}\}$ is the traction vector and $\hat{\mathbf{K}}^e$ is the 1×1 dynamic stiffness matrix of the one-dimensional semi-infinite layer [60]:

$$\hat{\mathbf{K}}^e = \left[\mathrm{i}\omega\rho C_{\mathrm{p}}\right] \tag{2.16}$$

Finite layer Consider now the case of a semi-infinite layer given by figure 2.2b. The displacements at both ends $z = 0$ and $z = L$ of the layer are equal to:

$$\underline{\hat{\mathbf{u}}}^e = \begin{Bmatrix} \underline{\hat{u}}_{x1} \\ \underline{\hat{u}}_{x2} \end{Bmatrix} = \begin{Bmatrix} \hat{u}_x(0,\omega) \\ \hat{u}_x(L,\omega) \end{Bmatrix} = \begin{bmatrix} 1 & 1 \\ e^{-\mathrm{i}k_\mathrm{p}L} & e^{+\mathrm{i}k_\mathrm{p}L} \end{bmatrix} \begin{Bmatrix} P \\ N \end{Bmatrix} \tag{2.17}$$

The tractions at both ends $x = 0$ and $x = L$ of the layer are equal to:

$$\begin{aligned} \underline{\hat{\mathbf{t}}}^e = \begin{Bmatrix} \underline{\hat{t}}_{x1} \\ \underline{\hat{t}}_{x2} \end{Bmatrix} &= \begin{Bmatrix} -\hat{\sigma}_{xx}(0,\omega) \\ \hat{\sigma}_{xx}(L,\omega) \end{Bmatrix} \\ &= (\lambda + 2\mu)\mathrm{i}k_\mathrm{p} \begin{bmatrix} 1 & -1 \\ -e^{-\mathrm{i}k_\mathrm{p}L} & e^{+\mathrm{i}k_\mathrm{p}L} \end{bmatrix} \begin{Bmatrix} P \\ N \end{Bmatrix} \end{aligned} \tag{2.18}$$

Elimination of the unknown amplitudes P and N from equations (2.17) and (2.18) results in the following relation between the tractions $\underline{\hat{\mathbf{t}}}^e$ and the displacements $\underline{\hat{\mathbf{u}}}^e$ [60]:

$$\begin{Bmatrix} \underline{\hat{t}}_{x1} \\ \underline{\hat{t}}_{x2} \end{Bmatrix} = \frac{\omega\rho C_\mathrm{p}}{\sin k_\mathrm{p}L} \begin{bmatrix} \cos k_\mathrm{p}L & -1 \\ -1 & \cos k_\mathrm{p}L \end{bmatrix} \begin{Bmatrix} \underline{\hat{u}}_{x1} \\ \underline{\hat{u}}_{x2} \end{Bmatrix} \tag{2.19}$$

This can be written in the general form:

$$\hat{\mathbf{K}}^e \underline{\hat{\mathbf{u}}}^e = \underline{\hat{\mathbf{t}}}^e \tag{2.20}$$

Here, $\underline{\hat{\mathbf{u}}}^e = \{\underline{\hat{u}}_{x1}, \underline{\hat{u}}_{x2}\}^T$ is the displacement vector, $\underline{\hat{\mathbf{t}}}^e = \{\underline{\hat{t}}_{x1}, \underline{\hat{t}}_{x2}\}^T$ is the traction vector and $\hat{\mathbf{K}}^e$ is the 2×2 dynamic stiffness matrix of the one-dimensional finite layer [60]:

$$\hat{\mathbf{K}}^e = \frac{\omega\rho C_\mathrm{p}}{\sin k_\mathrm{p}L} \begin{bmatrix} \cos k_\mathrm{p}L & -1 \\ -1 & \cos k_\mathrm{p}L \end{bmatrix} \tag{2.21}$$

2.2.3 Amplification problem

A one-dimensional amplification problem is considered as illustrated in figure 2.3. The first layer is a semi-infinite halfspace. In this layer, there is an incident wave with amplitude I that is partly reflected by the other layers. The displacement field in the semi-infinite layer is given by:

$$\hat{u}_x^1(x,\omega) = Ie^{-\mathrm{i}k_\mathrm{p}x} + Re^{+\mathrm{i}k_\mathrm{p}x} \tag{2.22}$$

where k_p is the wave number in the semi-infinite layer. At interface $[a]$ $(x = 0)$, the displacement is equal to:

$$\underline{\hat{u}}_{xa} = \hat{u}_x^1(0,\omega) = I + R \tag{2.23}$$

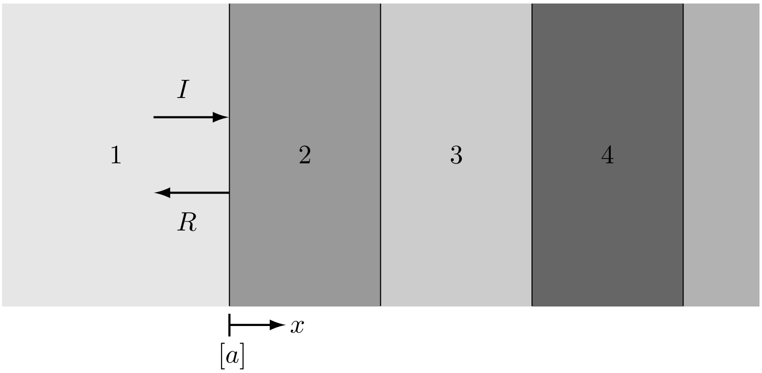

Figure 2.3: One-dimensional amplification problem.

The traction is equal to:

$$\underline{\hat{t}}_{xa} = \hat{\sigma}^1_{xx}(0,\omega) = (\lambda + 2\mu)\mathrm{i}k_\mathrm{p}(-I + R) \tag{2.24}$$

Elimination of the unknown amplitude R from these equations results in [60]:

$$\underline{\hat{t}}_{x1} = (\lambda + 2\mu)\mathrm{i}k_\mathrm{p}(\underline{\hat{u}}_{x1} - 2I) = \mathrm{i}\omega\rho C_\mathrm{p}(\underline{\hat{u}}_{x1} - 2I) \tag{2.25}$$

Recall that for a semi-infinite layer, the stiffness matrix is given by equation (2.16). The above equation can therefore be written as [60]:

$$\underline{\hat{\mathbf{t}}}^e = \hat{\mathbf{K}}^e(\underline{\hat{\mathbf{u}}}^e - 2I) \tag{2.26}$$

or:

$$\hat{\mathbf{K}}^e\underline{\hat{\mathbf{u}}}^e = \underline{\hat{\mathbf{t}}}^e + 2\hat{\mathbf{K}}^e I \tag{2.27}$$

This equation is assembled in the global equilibrium equation $\hat{\mathbf{K}}\underline{\hat{\mathbf{u}}} = \underline{\hat{\mathbf{p}}}$ where $\hat{\mathbf{K}}$ is the stiffness matrix, $\underline{\hat{\mathbf{u}}}$ the global displacement vector, and $\underline{\hat{\mathbf{p}}}$ the load vector.

2.3 A layer embedded in a full space

In this section, the propagation of dilatational waves through a layer embedded in a homogeneous full space is studied. To better understand the underlying physical mechanisms, first wave transmission at an interface between two materials is discussed.

2.3.1 Wave reflection and transmission at an interface

The reflection and transmission of waves at the interface between two materials is well known in the domain of elastodynamics. Expressions for these coefficients are for example shown in [2].

At an interface between two materials, a part of the incoming wave (with amplitude I) is reflected (R) and a part is transmitted (T) (figure 2.4). The waves travel with a speed $C_{\mathrm{p}1}$ in the first and $C_{\mathrm{p}2}$ in the second semi-infinite halfspace. The corresponding wavenumbers are $k_{\mathrm{p}1} = \omega / C_{\mathrm{p}1}$ and $k_{\mathrm{p}2} = \omega / C_{\mathrm{p}2}$. The displacement fields in the first and second halfspace are written as:

$$\begin{cases} \hat{u}_x^1(x,\omega) = I e^{-\mathrm{i}k_{\mathrm{p}1}x} + R e^{+\mathrm{i}k_{\mathrm{p}1}x} & x \leq 0 \\ \hat{u}_x^2(x,\omega) = T e^{-\mathrm{i}k_{\mathrm{p}2}x} & 0 \leq x \end{cases} \tag{2.28}$$

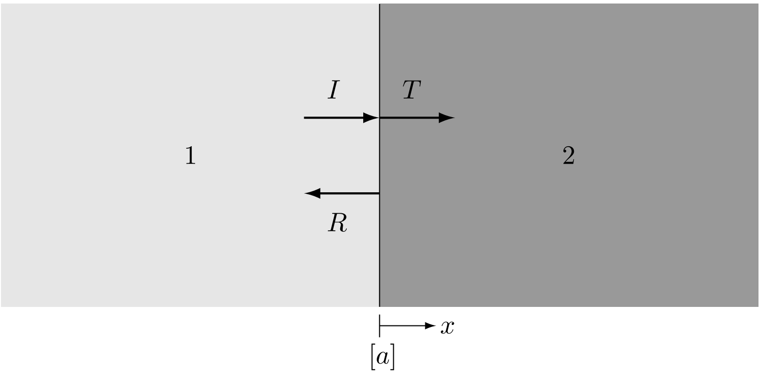

Figure 2.4: Two semi-infinite halfspaces with different properties, in contact at $x = 0$.

The displacement $\underline{\hat{u}}_{xa}$ at interface $[a]$ is obtained using the direct stiffness method. As the stiffness matrix is $\hat{\mathbf{K}} = [\mathrm{i}\omega\rho_1 C_{\mathrm{p}1} + \mathrm{i}\omega\rho_2 C_{\mathrm{p}2}]$ and the load vector is $\underline{\hat{\mathbf{p}}} = [2\mathrm{i}\omega\rho_1 C_{\mathrm{p}1} I]$, this displacement is equal to:

$$\underline{\hat{u}}_{xa} = \frac{2}{1+K} \tag{2.29}$$

where K is the ratio of the impedances $Z_{\mathrm{p}1}$ and $Z_{\mathrm{p}2}$ of the two materials:

$$K = \frac{Z_{\mathrm{p}2}}{Z_{\mathrm{p}1}} = \frac{\rho_2 C_{\mathrm{p}2}}{\rho_1 C_{\mathrm{p}1}} \tag{2.30}$$

As $\underline{\hat{u}}_{xa} = \hat{u}_x^1(0,\omega) = I + R = \hat{u}_x^2(0,\omega) = T$, the amplitude of the reflected and transmitted wave are given by [2]:

$$R = \frac{1-K}{1+K} I = rI \tag{2.31}$$

$$T = \frac{2}{1+K} I = tI \tag{2.32}$$

In these expressions, r is the reflection and t is the transmission coefficient. They are defined as the ratio of the reflected, respectively transmitted, and the incoming wave amplitude.

The reflection and transmission coefficients (r and t) only depend on the impedance ratio K. Figure 2.5 shows this dependence. The transmission coefficient t decreases with the impedance ratio K.

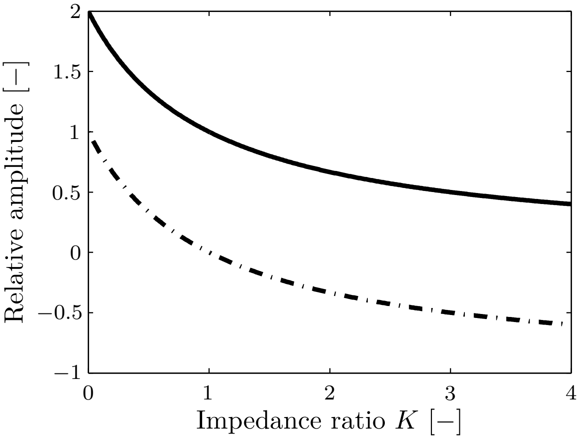

Figure 2.5: The reflection (dashed-dotted line) and transmission (solid line) coefficients (r and t).

The displacement field corresponding to the transmitted waves in the semi-infinite halfspace is given by:

$$\hat{u}_x^2(x,\omega) = Te^{-\mathrm{i}k_{\mathrm{p}2}x} = \frac{2}{1+K} Ie^{-\mathrm{i}k_{\mathrm{p}2}x} \tag{2.33}$$

The absolute value of the displacement is independent of x and is equal to $T = tI$. Figure 2.6 shows the wave field at 50 Hz and 100 Hz for wave velocities $C_{\mathrm{p}1} = 200\,\mathrm{m/s}$ and $C_{\mathrm{p}2} = 400\,\mathrm{m/s}$ and mass densities $\rho_1 = \rho_2 = 2000\,\mathrm{kg/m^3}$. The corresponding impedance ratio K is equal to 2. In the left halfspace, there is constructive and destructive interference between the incoming and reflected waves. In the right halfspace, the wavelength is twice as large and the amplitude is only two third of the modulus of the incoming wave.

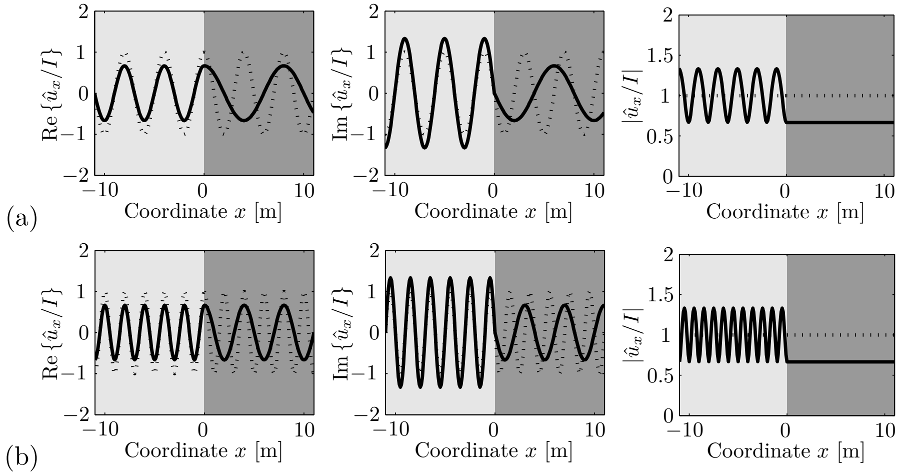

Figure 2.6: Real part, imaginary part and modulus of the wave field for a homogeneous full space (dotted line) and two different semi-infinite halfspaces (solid line) at (a) 50 Hz and (b) 100 Hz.

2.3.2 Wave reflection and transmission through a layer embedded in a homogeneous full space

A layer with finite thickness is embedded in a homogeneous full space, as shown in figure 2.7. An incoming wave (I) is partly reflected by the layer (R) and a part is transmitted through the layer (T). The displacement field in the layer consists of waves that travel in both directions (A and B), and that are reflected and transmitted at the boundaries. The displacement fields in the different parts are given by:

$$\begin{cases} \hat{u}_x^{1-}(x,\omega) = Ie^{-\mathrm{i}k_{\mathrm{p}1}(x+L_2)} + Re^{+\mathrm{i}k_{\mathrm{p}1}(x+L_2)} & x \leq -L_2 \\ \hat{u}_x^{2}(x,\omega) = Ae^{-\mathrm{i}k_{\mathrm{p}2}x} + Be^{+\mathrm{i}k_{\mathrm{p}2}x} & -L_2 \leq x \leq 0 \\ \hat{u}_x^{1+}(x,\omega) = Te^{-\mathrm{i}k_{\mathrm{p}1}x} & 0 \leq x \end{cases} \tag{2.34}$$

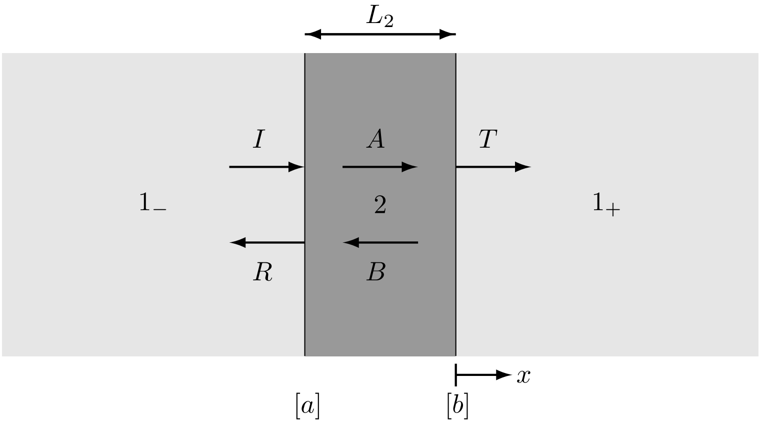

Figure 2.7: A layer with finite thickness embedded in a homogeneous full space.

The direct stiffness method is again applied to find the displacements at the interfaces $[a]$ and $[b]$:

$$\begin{bmatrix} \mathrm{i}\omega\rho_1 C_{\mathrm{p}1} + \omega\rho_2 C_{\mathrm{p}2}\cot k_{\mathrm{p}2}L_2 & -\omega\rho_2 C_{\mathrm{p}2}\csc k_{\mathrm{p}2}L_2 \\ -\omega\rho_2 C_{\mathrm{p}2}\csc k_{\mathrm{p}2}L_2 & \mathrm{i}\omega\rho_1 C_{\mathrm{p}1} + \omega\rho_2 C_{\mathrm{p}2}\cot k_{\mathrm{p}2}L_2 \end{bmatrix} \begin{Bmatrix} \underline{\hat{u}}_{xa} \\ \underline{\hat{u}}_{xb} \end{Bmatrix} = \begin{Bmatrix} 2\mathrm{i}\omega\rho_1 C_{\mathrm{p}1} I \\ 0 \end{Bmatrix} \tag{2.35}$$

Solving this results in the displacement $\underline{\hat{u}}_{xb} = \hat{u}_x^{1+}(0,\omega) = T$, and the transmitted wave field $\hat{u}_x^{1+}(x,\omega)$ [116]:

$$\hat{u}_x^{1+}(x,\omega) = Te^{-\mathrm{i}k_{\mathrm{p}1}x} = \frac{4KIe^{-\mathrm{i}k_{\mathrm{p}1}x}}{(1+K)^2 e^{+\mathrm{i}k_{\mathrm{p}2}L_2} - (1-K)^2 e^{-\mathrm{i}k_{\mathrm{p}2}L_2}} = tI \tag{2.36}$$

The amplitude of the transmitted wave is given by:

$$|\hat{u}_x^{1+}| = \frac{2KI}{\sqrt{4K^2\cos^2(k_{\mathrm{p}2}L_2) + (1+K^2)^2\sin^2(k_{\mathrm{p}2}L_2)}} = |t|I \tag{2.37}$$

For a given thickness L_2, this value is equal to I (or $|t| = 1$) if $k_{\mathrm{p}2}L_2 = n\pi,\ n = 0\ldots\infty$, or:

$$f = \frac{nC_{\mathrm{p}2}}{2L_2} \tag{2.38}$$

For a given frequency, the thicknesses of the layer where $|\hat{u}_x^{1+}| = I$ (for a given wavelength $\lambda_{\mathrm{p}2} = \dfrac{C_{\mathrm{p}2}}{f}$) are:

$$L_2 = \frac{n\lambda_{\mathrm{p}2}}{2} \tag{2.39}$$

For $k_{\mathrm{p}2}L_2 = (m+1/2)\pi,\ m = 0\ldots\infty$, $|\hat{u}_x^{1+}|$ is minimal and equal to $\dfrac{2K}{1+K^2}$, i.e. for frequencies f satisfying:

$$f = \frac{(2m+1)C_{\mathrm{p}2}}{4L_2} \tag{2.40}$$

or for thicknesses L_2:

$$L_2 = \frac{(2m+1)\lambda_{p2}}{4} \tag{2.41}$$

The wave transmission has therefore a minimum when the thickness of the layer is equal to a quarter of the wavelength.

Consider for example $C_{\mathrm{p}1} = 200\,\mathrm{m/s}$, $\rho_1 = 2000\,\mathrm{kg/m^3}$, $L_2 = 2\,\mathrm{m}$, and $\rho_2 = 2000\,\mathrm{kg/m^3}$. Figure 2.8 shows the modulus of the transmission coefficients for three different cases: $C_{\mathrm{p}2} = 200\,\mathrm{m/s}$ ($K = 1$), $C_{\mathrm{p}2} = 100\,\mathrm{m/s}$ ($K = 0.5$), and $C_{\mathrm{p}2} = 400\,\mathrm{m/s}$ ($K = 2$). For $C_{\mathrm{p}2} = C_{\mathrm{p}1} = 200\,\mathrm{m/s}$, the waves propagate through a homogeneous full space and the modulus of the transmission coefficient is $|t| = 1$ for all frequencies. For $C_{\mathrm{p}2} = 100\,\mathrm{m/s}$, the modulus of the transmission coefficient $|t|$ is maximal and equal to 1 for $f = 25, 50, 75, \ldots$ Hz and minimal and equal to 0.8 for $f = 12.5, 37.5, 62.5, \ldots$ Hz. For $C_{\mathrm{p}2} = 400\,\mathrm{m/s}$, the modulus of the transmission coefficient $|t|$ is maximal and equal to 1 for $f = 100, 200, 300, \ldots$ Hz and minimal and equal to 0.8 for $f = 50, 150, 250, \ldots$ Hz.

For the last case ($C_{\mathrm{p}1} = 200\,\mathrm{m/s}$, $\rho_1 = 2000\,\mathrm{kg/m^3}$, $L_2 = 2\,\mathrm{m}$, $C_{\mathrm{p}2} = 400\,\mathrm{m/s}$, and $\rho_2 = 2000\,\mathrm{kg/m^3}$), the wave fields at 50 Hz and 100 Hz are plotted in figure 2.9. At 50 Hz, the incoming wave is partly reflected by the layer, and the transmitted wave amplitude is reduced to four fifth of the incoming wave amplitude. On the contrary, at 100 Hz, nothing is reflected by the layer and the amplitude of the transmitted wave is equal to the amplitude of the incoming wave.

2.4 Periodic stacking of layers

2.4.1 Bloch waves

In this section, a periodic stacking of layers is considered. Every periodic cell consists of a layer of material 1 with thickness L_1 and a layer of material 2

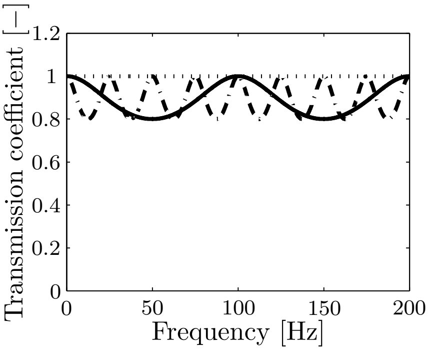

Figure 2.8: Modulus of the transmission coefficient $|t|$ for a layer embedded in a full space with impedance ratio $K = 1$ (dotted line), $K = 0.5$ (dashed-dotted line), and $K = 2$ (solid line).

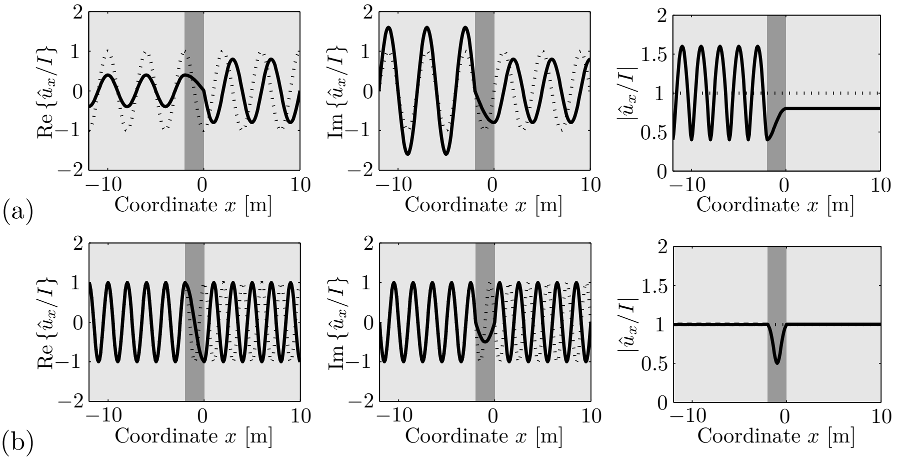

Figure 2.9: Real part, imaginary part and modulus of the wave field for a homogeneous full space (dotted line) and for a layer embedded in this full space with thickness 2 m (solid solid line) at (a) 50 Hz and (b) 100 Hz.

with thickness L_2 and has a total thickness $L = L_1 + L_2$. A part of the infinite periodic structure is shown in figure 2.10. The displacements in the different layers can be expressed as:

$$\begin{cases} \hat{u}_{x1}^{n-1}(x,\omega) = C_{n-1}e^{-\mathrm{i}k_{\mathrm{p}1}x} + D_{n-1}e^{+\mathrm{i}k_{\mathrm{p}1}x} & -L_1 \leq x \leq 0 \\ \hat{u}_{x2}^{n}(x,\omega) = A_n e^{-\mathrm{i}k_{\mathrm{p}2}(x-L_2)} + B_n e^{+\mathrm{i}k_{\mathrm{p}2}(x-L_2)} & 0 \leq x \leq L_2 \\ \hat{u}_{x1}^{n}(x,\omega) = C_n e^{-\mathrm{i}k_{\mathrm{p}1}(x-L)} + D_n e^{+\mathrm{i}k_{\mathrm{p}1}(x-L)} & L_2 \leq x \leq L \end{cases} \tag{2.42}$$

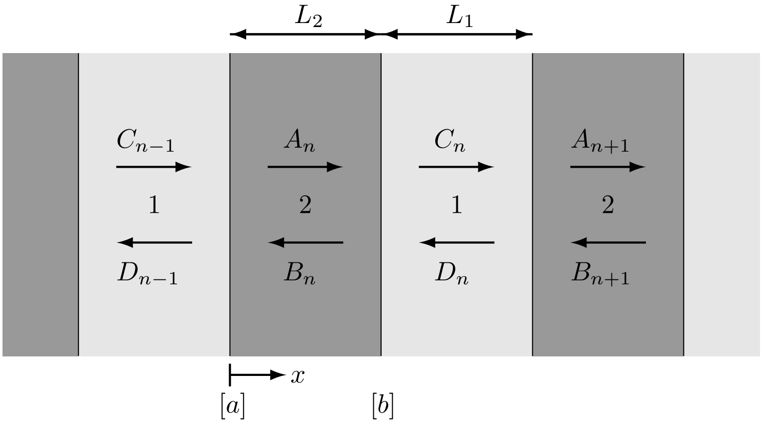

Figure 2.10: Part of the infinite periodic structure.

From the continuity of displacements and the stress equilibrium at interfaces $[a]$ and $[b]$, a relation can be derived between C_{n-1} and D_{n-1} on the left hand side and C_n and D_n on the right hand side of periodic cell n. These can be written in the following matrix form:

$$\begin{Bmatrix} C_{n-1} \\ D_{n-1} \end{Bmatrix} = \mathbf{H} \begin{Bmatrix} C_n \\ D_n \end{Bmatrix} \tag{2.43}$$

Here, the transfer matrix $\mathbf{H}$ is equal to:

$$\mathbf{H} = \begin{bmatrix} H_{11} & H_{12} \\ H_{21} & H_{22} \end{bmatrix} \tag{2.44}$$

with (similar to the expressions in [179]):

$$\begin{aligned}
H_{11} &= e^{+\mathrm{i}k_{\mathrm{p}1}L_1} \left[\cos(k_{\mathrm{p}2}L_2) + \frac{\mathrm{i}}{2} \left(K + \frac{1}{K} \right) \sin(k_{\mathrm{p}2}L_2) \right] \\
H_{12} &= e^{-\mathrm{i}k_{\mathrm{p}1}L_1} \left[\frac{\mathrm{i}}{2} \left(K - \frac{1}{K} \right) \sin(k_{\mathrm{p}2}L_2) \right] \\
H_{21} &= e^{+\mathrm{i}k_{\mathrm{p}1}L_1} \left[-\frac{\mathrm{i}}{2} \left(K - \frac{1}{K} \right) \sin(k_{\mathrm{p}2}L_2) \right] \\
H_{22} &= e^{-\mathrm{i}k_{\mathrm{p}1}L_1} \left[\cos(k_{\mathrm{p}2}L_2) - \frac{\mathrm{i}}{2} \left(K + \frac{1}{K} \right) \sin(k_{\mathrm{p}2}L_2) \right]
\end{aligned} \tag{2.45}$$

The periodicity gives rise to so-called Bloch waves. These waves are characterized by the following eigenvalue problem with $\lambda_j = e^{\pm \mathrm{i}kL}$ as the complex eigenvalues [179]:

$$\begin{bmatrix} H_{11} & H_{12} \\ H_{21} & H_{22} \end{bmatrix} \begin{Bmatrix} C_n \\ D_n \end{Bmatrix} = e^{\pm \mathrm{i}kL} \begin{Bmatrix} C_n \\ D_n \end{Bmatrix} \tag{2.46}$$

where $L = L_1 + L_2$ and k is the wavenumber of the Bloch wave. The eigenvalues of a 2×2 matrix are the roots of the characteristic equation:

$$\det(\mathbf{H} - \lambda \mathbf{I}) = \lambda_j^2 - \mathrm{Tr}(\mathbf{H})\lambda_j + \det(\mathbf{H}) = 0 \tag{2.47}$$

In this expression, $\mathrm{Tr}(\mathbf{H})$ is the trace of the matrix $\mathbf{H}$, equal to $H_{11} + H_{22}$. The determinant $\det(\mathbf{H}) = H_{11}H_{22} - H_{21}H_{12}$ is equal to 1 (see appendix A). The roots of this equation are:

$$\lambda_j = \frac{\mathrm{Tr}(\mathbf{H})}{2} \pm \sqrt{\left(\frac{\mathrm{Tr}(\mathbf{H})}{2}\right)^2 - \det(\mathbf{H})} = \frac{\mathrm{Tr}(\mathbf{H})}{2} \pm \mathrm{i}\sqrt{1 - \left(\frac{\mathrm{Tr}(\mathbf{H})}{2}\right)^2} \tag{2.48}$$

Since $\lambda_j = e^{\pm \mathrm{i}kL} = \cos kL \pm \mathrm{i} \sin kL$, the following applies [37]:

$$\begin{aligned} \cos(kL) &= \frac{\mathrm{Tr}(\mathbf{H})}{2} \\ &= \cos(k_{\mathrm{p}1}L_1)\cos(k_{\mathrm{p}2}L_2) - \frac{1}{2}\left(K + \frac{1}{K}\right)\sin(k_{\mathrm{p}1}L_1)\sin(k_{\mathrm{p}2}L_2) \end{aligned} \tag{2.49}$$

This is a dispersion relation between the wavenumber k and the frequency ω, since the wavenumbers $k_{\mathrm{p}1} = \omega / C_{\mathrm{p}1}$ and $k_{\mathrm{p}2} = \omega / C_{\mathrm{p}2}$ depend on the frequency ω.

Consider the same material properties as before: $C_{\mathrm{p}1} = 200\,\mathrm{m/s}$, $\rho_1 = 2000\,\mathrm{kg/m^3}$, and $\rho_2 = 2000\,\mathrm{kg/m^3}$. The thicknesses of the layers are $L_1 = 1\,\mathrm{m}$ and $L_2 = 2\,\mathrm{m}$ ($L = L_1 + L_2 = 3\,\mathrm{m}$). Furthermore, three values of $C_{\mathrm{p}2}$ are considered: $C_{\mathrm{p}2} = 200\,\mathrm{m/s}$ ($K = 1$), $C_{\mathrm{p}2} = 100\,\mathrm{m/s}$ ($K = 0.5$), and $C_{\mathrm{p}2} = 400\,\mathrm{m/s}$ ($K = 2$). Figure 2.11 shows the function $\cos(kL)$ appearing in equation (2.49) for the different cases. Figure 2.12 shows the real and imaginary part of the wavenumber k. At the frequencies where the right hand side of equation (2.49) gives a value between -1 and 1, a real-valued wavenumber k is obtained. However, in the range of frequencies where the absolute value of the right-hand side of equation (2.49) is larger than 1, the wavenumber k becomes complex. As a consequence, the passing wave is not only subjected to a phase shift, but is also attenuated. In this range, a stopband occurs.

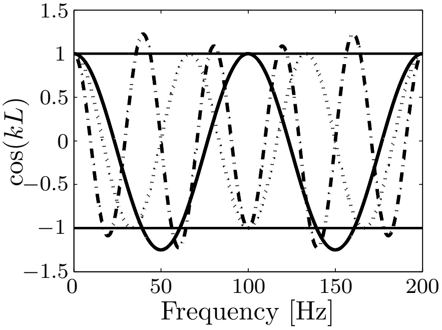

Figure 2.11: The function $\cos(kL)$ (equation (2.49)) as a function of the frequency with impedance ratio $K = 1$ (dotted line), $K = 0.5$ (dashed-dotted line), and $K = 2$ (solid line).

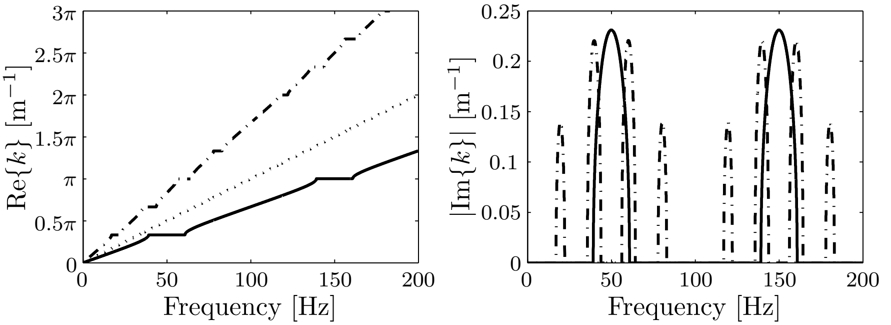

(a) (b)

Figure 2.12: (a) Real and (b) imaginary part of the wavenumber k with impedance ratio $K = 1$ (dotted line), $K = 0.5$ (dashed-dotted line), and $K = 2$ (solid line).

2.4.2 Stopbands

In this subsection, the location and width of the stopbands is determined. Figure 2.13 shows the stopbands in the $(k_{\mathrm{p}1}L_1, k_{\mathrm{p}2}L_2)$ plane by plotting equation (2.49) for $\cos(kL) < -1$ and $\cos(kL) > 1$. The location of the stopbands is primarily dependent on the values of $k_{\mathrm{p}1}L_1$ and $k_{\mathrm{p}2}L_2$, while the width of the stopbands is primarily dependent on the value of K. The location of the stopbands is shown schematically in figure 2.14. Expressions for the location and the width of the stopbands are derived below.

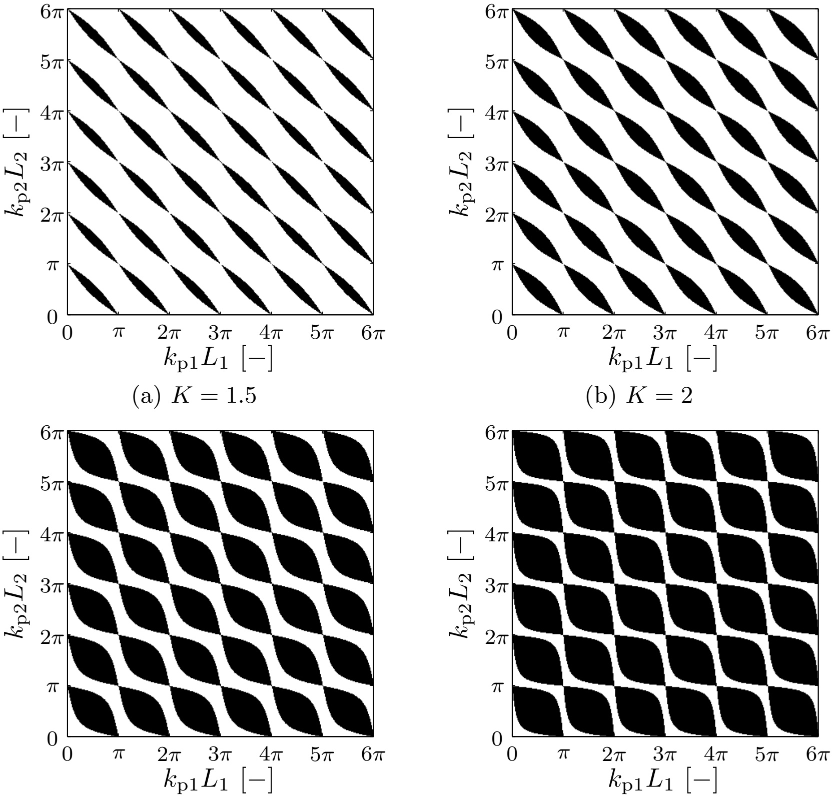

(a) $K = 1.5$

(b) $K = 2$

(c) $K = 5$

(d) $K = 10$

Figure 2.13: Stop bands in the $(k_{\mathrm{p}1}L_1, k_{\mathrm{p}2}L_2)$ plane for an impedance ratio (a) $K = 1.5$, (b) $K = 2$, (c) $K = 5$, and (d) $K = 10$.

It can be shown that for $k_{\mathrm{p}1}L_1 + k_{\mathrm{p}2}L_2 = n\pi,\ n = 1\ldots\infty$, $|\cos(kL)|$ is always larger than or equal to 1 (figure 2.14):

$$\begin{aligned}
\cos(kL) &= \cos(k_{\mathrm{p}1}L_1)\cos(k_{\mathrm{p}2}L_2) - \frac{1}{2}\left(K + \frac{1}{K}\right)\sin(k_{\mathrm{p}1}L_1)\sin(k_{\mathrm{p}2}L_2) \\
&= \cos(k_{\mathrm{p}1}L_1)\cos(n\pi - k_{\mathrm{p}1}L_1) \\
&\quad - \frac{1}{2}\left(K + \frac{1}{K}\right)\sin(k_{\mathrm{p}1}L_1)\sin(n\pi - k_{\mathrm{p}1}L_1) \\
&= \begin{cases} 1 + \dfrac{(1-K)^2}{2K}\sin^2(k_{\mathrm{p}1}L_1) & \text{for } n \text{ even} \\[2ex] -1 - \dfrac{(1-K)^2}{2K}\sin^2(k_{\mathrm{p}1}L_1) & \text{for } n \text{ odd} \end{cases}
\end{aligned} \tag{2.50}$$

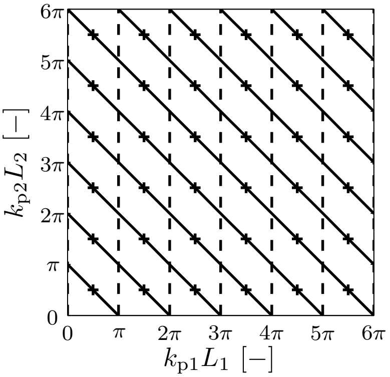

Figure 2.14: $(k_{\mathrm{p}1}L_1, k_{\mathrm{p}2}L_2)$ pairs corresponding to the frequencies f_{cs} close to the center of the stopbands (solid lines), the frequencies f_{ns} where no stopbands are observed (dashed lines), and the frequencies f_{mc} for which the function $\cos kL$ has a maximum (plus marks).

Since the impedance ratio $K \geq 0$, it holds that $\dfrac{(1-K)^2}{2K} \geq 0$ (and $\dfrac{(1-K)^2}{2K} = 0$ for $K = 1$). Also $\sin^2(k_{\mathrm{p}1}L_1) \geq 0$ (and $\sin^2(k_{\mathrm{p}1}L_1) = 0$ for $k_{\mathrm{p}1}L_1 = m\pi,\ m = 0\ldots\infty$), which means that the function $\cos(kL) \geq 1$ for n even and $\cos(kL) \leq -1$ for n odd. As a consequence, the frequencies f_{cs} for which $k_{\mathrm{p}1}L_1 + k_{\mathrm{p}2}L_2 = n\pi,\ n = 1\ldots\infty$ are located in a stopband if the impedance ratio $K \neq 1$ and if $k_{\mathrm{p}1}L_1 \neq m\pi,\ m = 0\ldots\infty$ (figure 2.14). These frequencies f_{cs} are located near to the center of the stopbands:

$$\omega_{\mathrm{cs}} = \frac{n\pi}{\dfrac{L_1}{C_{\mathrm{p1}}} + \dfrac{L_2}{C_{\mathrm{p2}}}} \tag{2.51}$$

or:

$$f_{\mathrm{cs}} = \frac{n}{2\left(\dfrac{L_1}{C_{\mathrm{p1}}} + \dfrac{L_2}{C_{\mathrm{p2}}}\right)} \tag{2.52}$$

There are two exceptions for these frequencies f_{cs} to be located in a stopband: for an impedance ratio $K = 1$ and for $k_{\mathrm{p1}}L_1 = m\pi,\ m = 0\ldots\infty$. The latter expression defines the frequencies f_{ns} where no stopbands are observed:

$$\omega_{ns} = \frac{m\pi C_{\mathrm{p1}}}{L_1} \tag{2.53}$$

or:

$$f_{\mathrm{ns}} = \frac{mC_{\mathrm{p1}}}{2L_1} \tag{2.54}$$

Alternatively, the frequencies where no stopbands are observed can be obtained from $k_{\mathrm{p2}}L_2 = m\pi,\ m = 0\ldots\infty$.

The most pronounced stopbands occur at frequencies for which $|\cos(kL)|$ has a maximum. As the maxima are found at frequencies f_{mc} for which $\cos(k_{\mathrm{p1}}L_1)$ and $\cos(k_{\mathrm{p2}}L_2)$ are equal to zero, these frequencies satisfy the equations $k_{\mathrm{p1}}L_1 = (p + 1/2)\pi,\ p = 0\ldots\infty$ and $k_{\mathrm{p2}}L_2 = (q + 1/2)\pi,\ q = 0\ldots\infty$ (figure 2.14), or:

$$f_{\mathrm{mc}} = \frac{(2p+1)C_{\mathrm{p1}}}{4L_1} = \frac{(2q+1)C_{\mathrm{p2}}}{4L_2} \tag{2.55}$$

The case where $p = q = 0$ is called the quarter wave-stack condition [179], since the thicknesses of the layers are equal to the quarter of the wavelengths λ_1 and λ_2:

$$L_1 = \frac{\lambda_1}{4} = \frac{C_{\mathrm{p1}}}{4f} \quad \text{and} \quad L_2 = \frac{\lambda_2}{4} = \frac{C_{\mathrm{p2}}}{4f} \tag{2.56}$$

This condition, that can also be written as $k_{\mathrm{p1}}L_1 = k_{\mathrm{p2}}L_2 = \dfrac{\pi}{2}$, is of particular importance, as will be shown later on.

The width of the stopbands can be derived for the special case where $k_{\mathrm{p1}}L_1 = k_{\mathrm{p2}}L_2$. Indeed, equation (2.49) becomes:

$$\begin{aligned} \cos(kL) &= \cos^2(k_{\mathrm{p1}}L_1) - \frac{1}{2}\left(K + \frac{1}{K}\right)\sin^2(k_{\mathrm{p1}}L_1) \\ &= 1 - \frac{(1+K)^2}{2K}\sin^2(k_{\mathrm{p1}}L_1) \end{aligned} \tag{2.57}$$

Since $\frac{(1+K)^2}{2K} \geq 0$ (as the impedance ratio $K \geq 0$) and $\sin^2(k_{\mathrm{p}1}L_1) \geq 0$, it holds that $\cos(kL) \leq 1$. As a consequence, the stopbands are located between the frequencies where $\cos(kL) = -1$, or:

$$\begin{aligned} \frac{(1+K)^2}{2K}\sin^2(k_{\mathrm{p}1}L_1) = 2 \Leftrightarrow \sin^2(k_{\mathrm{p}1}L_1) &= \frac{4K}{(1+K)^2} \\ \Leftrightarrow \sin(k_{\mathrm{p}1}L_1) &= \frac{\pm 2\sqrt{K}}{1+K} \end{aligned} \tag{2.58}$$

The points $(k_{\mathrm{p}1}L_1)_1 = \arcsin\left(\frac{2\sqrt{K}}{1+K}\right)$ and $(k_{\mathrm{p}1}L_1)_2 = \pi - \arcsin\left(\frac{2\sqrt{K}}{1+K}\right)$ are solutions of this equation, and hence:

$$\Delta(k_{\mathrm{p}1}L_1) = \pi - 2\arcsin\left(\frac{2\sqrt{K}}{1+K}\right) \tag{2.59}$$

Note that $\Delta(k_{\mathrm{p}1}L_1) = 0$ for an impedance ratio $K = 1$ and that $\Delta(k_{\mathrm{p}1}L_1) = \pi$ for $K = 0$ and $K = \infty$. For the latter cases, the width is equal to the distance between stopband frequencies, implying that the entire frequency range is a stopband. Figure 2.15 shows $\Delta(k_{\mathrm{p}1}L_1)$ as a function of the impedance ratio K. The width increases with the difference in impedance, as was previously shown in figure 2.13. The width Δf of the stopbands in terms of frequency is:

$$\Delta f = \frac{C_{\mathrm{p}1}}{2\pi L_1}\Delta(k_{\mathrm{p}1}L_1) = \frac{C_{\mathrm{p}1}}{L_1}\left[\frac{1}{2} - \frac{1}{\pi}\arcsin\left(\frac{2\sqrt{K}}{1+K}\right)\right] \tag{2.60}$$

2.4.3 Transmission for a stacking of periodic layers

Consider different periodic unit cells consisting of two different layers stacked one after the other, as shown in figure 2.16. The solution of the wave propagation in a row of N periodic cells is easily obtained from the transfer matrix in equation (2.43):

$$\begin{Bmatrix} C_0 \\ D_0 \end{Bmatrix} = \begin{bmatrix} H_{11} & H_{12} \\ H_{21} & H_{22} \end{bmatrix}^N \begin{Bmatrix} C_N \\ D_N \end{Bmatrix} \tag{2.61}$$

The N-th power of an unimodular matrix can be computed based on the following Chebyshev identity [180] (see appendix A):

$$\begin{bmatrix} H_{11} & H_{12} \\ H_{21} & H_{22} \end{bmatrix}^N = \begin{bmatrix} H_{11}\Psi_{N-1} - \Psi_{N-2} & H_{12}\Psi_{N-1} \\ H_{21}\Psi_{N-1} & H_{21}\Psi_{N-1} - \Psi_{N-2} \end{bmatrix} \tag{2.62}$$

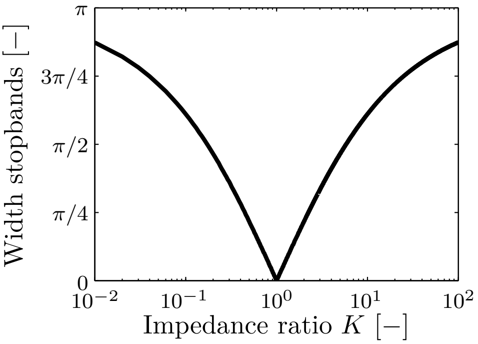

Figure 2.15: The width $\Delta(k_{\mathrm{p}1}L_1) = \Delta(k_{\mathrm{p}2}L_2)$ of the stopbands as a function of the impedance ratio K.

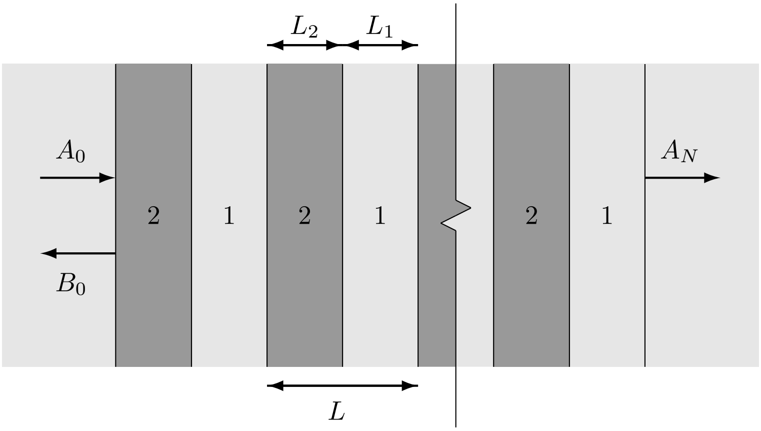

Figure 2.16: Periodic stacking of layers.

with Ψ_N is equal to:

$$\Psi_N = \frac{\sin((N+1)kL)}{\sin(kL)} \tag{2.63}$$

As waves only propagate in the positive direction, the amplitude of the wave propagating in negative direction is equal to $D_N = 0$, and the transmission coefficient t after N periodic cells is equal to:

$$t = \frac{C_N}{C_0} = \frac{1}{H_{11}\Psi_{N-1} - \Psi_{N-2}} \tag{2.64}$$

For example when $N = 1$, $\Psi_{N-1} = 1$ and $\Psi_{N-2} = 0$, resulting in:

$$\begin{aligned} C_N = \frac{C_0}{H_{11}} &= \frac{I}{e^{+\mathrm{i}k_{\mathrm{p}1}L_1}\left[\cos(k_{\mathrm{p}2}L_2) + \frac{\mathrm{i}}{2}\left(K + \frac{1}{K}\right)\sin(k_{\mathrm{p}2}L_2)\right]} \\ &= \frac{4KIe^{-\mathrm{i}k_{\mathrm{p}1}L_1}}{(1+K)^2e^{+\mathrm{i}k_{\mathrm{p}2}L_2} - (1-K)^2e^{-\mathrm{i}k_{\mathrm{p}2}L_2}} \end{aligned} \tag{2.65}$$

which is identical to expression (2.36) previously obtained, if in this equation x is evaluated at L_1.

For these periodic media, the modulus of the transmission coefficient $|t|$ is equal to 1 if $kL = \frac{n\pi}{N}$, $n = 1 \ldots N-1$. For these values, Ψ_{N-1} is equal to:

$$\Psi_{N-1} = \frac{\sin(NkL)}{\sin(kL)} = \frac{\sin(n\pi)}{\sin\left(\frac{n\pi}{N}\right)} = 0 \tag{2.66}$$

Furthermore, Ψ_{N-2} is equal to:

$$\begin{aligned} \Psi_{N-2} &= \frac{\sin((N-1)kL)}{\sin(kL)} \\ &= \frac{\sin\left(\left(1 - \frac{1}{N}\right)n\pi\right)}{\sin\left(\frac{n\pi}{N}\right)} \\ &= \frac{\sin(n\pi)\cos\left(\frac{n\pi}{N}\right) - \cos(n\pi)\sin\left(\frac{n\pi}{N}\right)}{\sin\left(\frac{n\pi}{N}\right)} \\ &= -\cos(n\pi) = \mp 1 \end{aligned} \tag{2.67}$$

Therefore, the following holds for the transmission coefficient t:

$$t = \frac{1}{H_{11}\Psi_{N-1} - \Psi_{N-2}} = \pm 1 \tag{2.68}$$

which proves that the modulus of the transmission coefficient $|t|$ is equal to 1 for $kL = \frac{n\pi}{N}$, $n = 1 \ldots N-1$.

Consider again the following material properties: $C_{\mathrm{p}1} = 200\,\mathrm{m/s}$, $\rho_1 = 2000\,\mathrm{kg/m^3}$, $\rho_2 = 2000\,\mathrm{kg/m^3}$, $L_1 = 1\,\mathrm{m}$, and $L_2 = 2\,\mathrm{m}$ ($L = 3\,\mathrm{m}$).

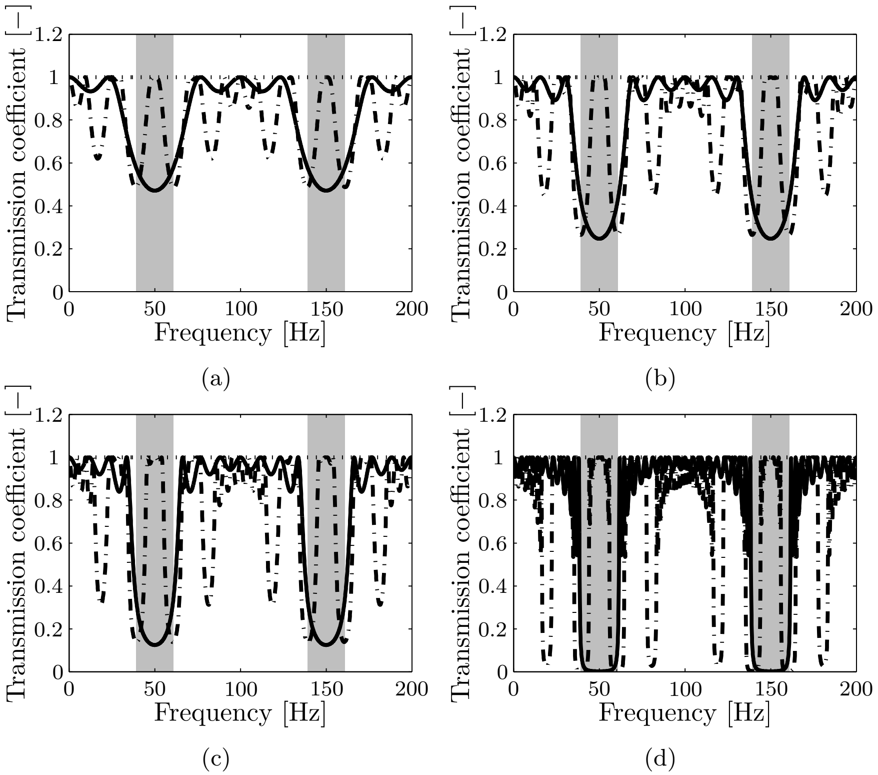

(a)

(b)

(c)

(d)

Figure 2.17: Modulus of the transmission coefficient $|t|$ for (a) two (b) three, (c) four, and (d) ten periodic cells with $K = 1$ (dotted line), $K = 0.5$ (dashed-dotted line), and $K = 2$ (solid line). The gray areas indicate the theoretical stopbands for $K = 2$ as predicted by equations (2.52) and (2.60).

Furthermore, three values of C_{p2} are considered: $C_{\mathrm{p2}} = 200\,\mathrm{m/s}$ ($K = 1$), $C_{\mathrm{p2}} = 100\,\mathrm{m/s}$ ($K = 0.5$), and $C_{\mathrm{p2}} = 400\,\mathrm{m/s}$ ($K = 2$). Figure 2.17 shows the modulus of the transmission coefficient for different numbers of periodic cells. The location of the stopbands corresponds to the predicted frequency ranges shown in figure 2.12, where the stopbands occur for complex values of the wavenumber k. The location of the stopbands in the frequency range is therefore approximated by equation (2.52). For $C_{\mathrm{p2}} = 400\,\mathrm{m/s}$, $k_{\mathrm{p1}}L_1 = k_{\mathrm{p2}}L_2$, and the width of the stopbands is given by equation (2.60). The frequency bands with low transmission are more pronounced for an increasing number of periodic cells. An increasing number of periodic cells leads to a lower minimum transmission coefficient in the stopbands (figure 2.18).

The corresponding wave fields at 50 Hz and 100 Hz are shown for $C_{p2} = 400$ m/s

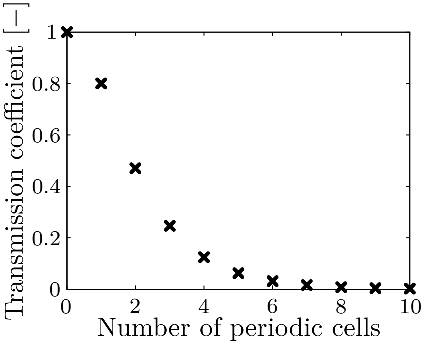

Figure 2.18: Modulus of the transmission coefficient $|t|$ at the center frequency of the first stopband (i.e. at 50 Hz) as a function of the number of periodic cells for $K = 2$.

for two periodic cells in figure 2.19, for three periodic cells in figure 2.20, and for four periodic cells in figure 2.21. Equation (2.52) predicts a stopband at 50 Hz. On the contrary, at 100 Hz, the modulus of the transmission coefficient $|t|$ is equal to 1, as is predicted by equation (2.54).

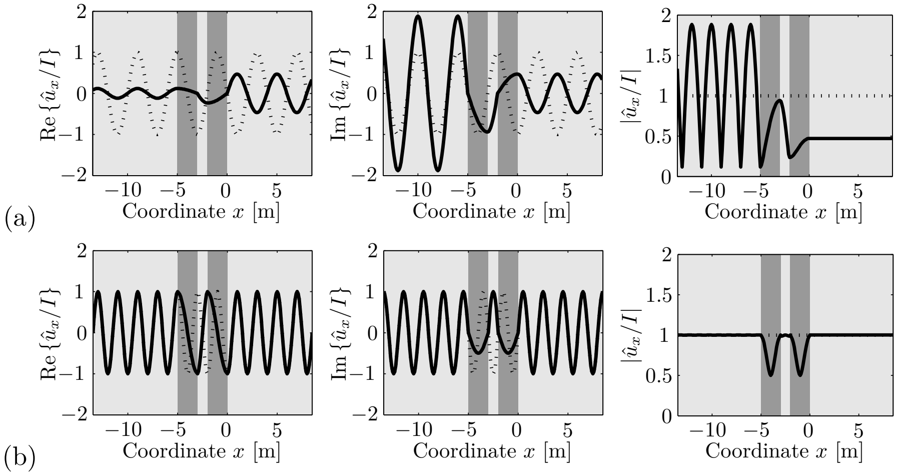

Figure 2.19: Real part, imaginary part and modulus of the wave field for a homogeneous full space (dotted line) and for two periodic cells embedded in this full space with thicknesses $L_1 = 1\,\mathrm{m}$ and $L_2 = 2\,\mathrm{m}$ (solid line) at (a) 50 Hz and (b) 100 Hz..

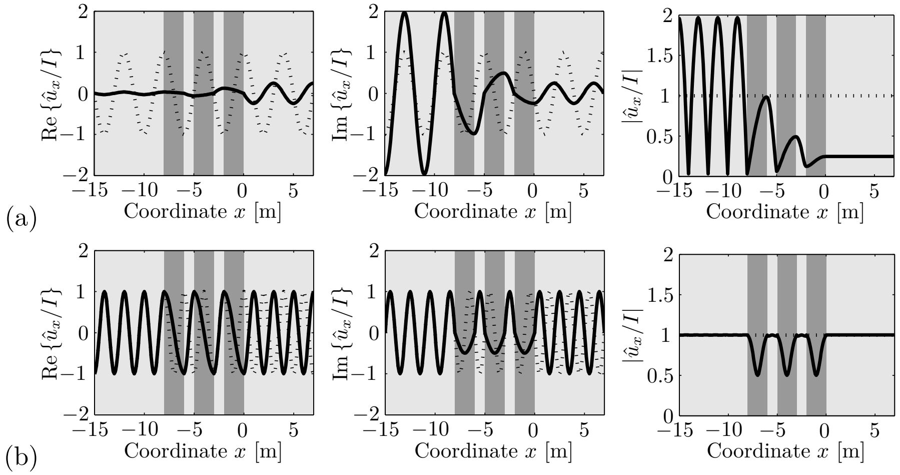

Figure 2.20: Real part, imaginary part and modulus of the wave field for a homogeneous full space (dotted line) and for three periodic cells embedded in this full space with thicknesses $L_1 = 1\,\mathrm{m}$ and $L_2 = 2\,\mathrm{m}$ (solid line) at (a) 50 Hz and (b) 100 Hz.

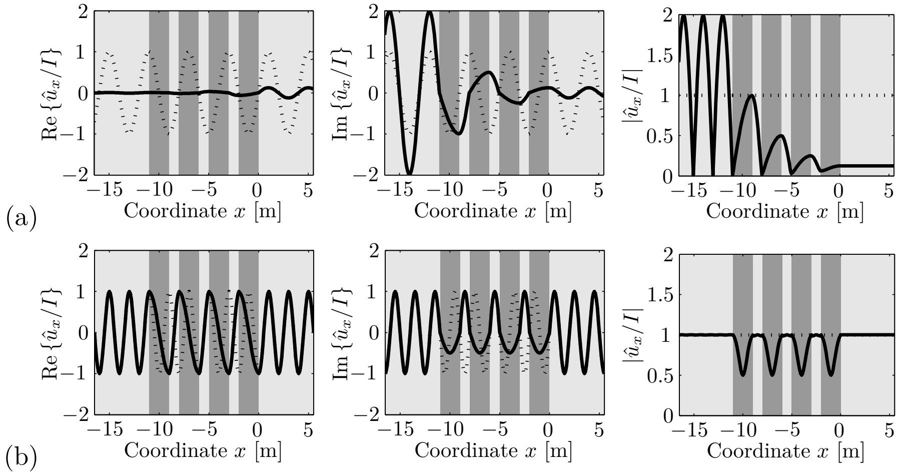

Figure 2.21: Real part, imaginary part and modulus of the wave field for a homogeneous full space (dotted line) and for four periodic cells embedded in this full space with thicknesses $L_1 = 1\,\mathrm{m}$ and $L_2 = 2\,\mathrm{m}$ (solid line) at (a) 50 Hz and (b) 100 Hz.

2.5 Conclusion

In this chapter, wave propagation through one-dimensional elastodynamic media was studied. An incoming wave is partly reflected by and partly transmitted through a periodic stacking of layers. The one-dimensional wave propagation is modeled using the direct stiffness method.

The performance of a layer embedded in a homogeneous full space is studied. Constructive and destructive interference of the incoming and reflected waves result in standing waves, which contain spatial nodes where the amplitude of the wave field has a minimum and anti-nodes where the amplitude has a maximum. A part is transmitted through the layer, and the amplitude of the transmitted wave field has a minimum for layer thicknesses equal to one fourth, three fourth, ... of the wavelength.

Periodic stacking of layers results in stopbands, frequency bands where the transmission is attenuated. Bloch's theory is applied to determine the location and the width of the stopbands. For layer thicknesses equal to one fourth of the wavelength, referred to as the quarter wave stack condition, the most pronounced stopbands occur. Lower amplitudes of the transmitted wave field are found for a higher number of periodic cells.

The theoretical results from this chapter are used in the next chapters for analyzing the performance of double wall barriers in chapter 3 and for interpreting the topology optimization results in chapter 4.

Chapter 3

Double wall barriers for three-dimensional elastic wave propagation

3.1 Introduction

This chapter discusses the performance of single and double stiff wall barriers the reduction of ground vibration transmission. In acoustics, the sound transmission through single and double walls is often predicted using analytical models. For infinite and thin single walls without flexural rigidity, the well-known mass law applies predicting that the sound reduction increases with 6 dB per octave [56]. When the flexural rigidity is taken into account, trace matching between the incident air waves and the bending waves of the plate leads to coincidence which decreases the sound reduction of the plate [55].

Analytical models for double walls show the presence of mass-spring-mass resonance above which the sound reduction increases with 18 dB per octave [70]. Cavity resonances, corresponding to standing waves in the cavity, appear at higher frequencies and decrease the sound reduction [24, 70]. As in building acoustics, double walls can reduce sound levels much better than single walls between the double wall resonance frequency and the first cavity resonance frequency [70], it is analyzed in this chapter whether a double wall barrier has advantages compared to a single wall barrier.

The aim of the barrier is to mitigate ground vibrations caused by passing trains.

The train loading can be modeled in a simplified way as a series of incoherent point sources. To assess the barrier's performance, the response caused by a vertical point load is analyzed. The considered wave propagation problem is shown in figure 3.1. One specific case, with fixed geometry and material properties, representing a jet grouting wall in a sandy soil is analyzed in this chapter. Afterwards, the influence of the geometry and the material properties is evaluated.

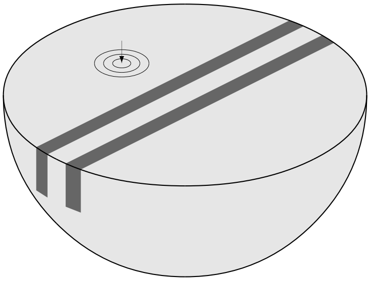

Figure 3.1: A semi-infinite halfspace excited by a point load at the surface. A double wall barrier is introduced to reduce the wave propagation close to the surface of the halfspace.

Previous studies have shown that accounting for three-dimensional effects is crucial when wave impeding barriers for railway induced vibrations are considered [53]. The numerical solution of three-dimensional elastodynamic problems is computationally demanding. The high computational cost limits the practical use of three-dimensional finite element (FE) models. This is especially the case when multiple solutions have to be calculated, for example for stochastic problems and for the iterative optimization procedures investigated in this text. A number of assumptions are often made in an attempt to reduce the computational effort. The resulting models exploit the (assumed) regularity of the problem geometry. If the structure can be assumed to be periodic, a Floquet transform can be used to obtain the solution of the original three–dimensional problem based on the discretization of a single periodic cell [38, 46, 84]. In many cases, the structure can be assumed to have an invariant cross section. In this case, a computationally efficient two-and-a-half-dimensional (2.5D) approach can be applied, where the Fourier transform from the longitudinal coordinate to the wavenumber domain allows for the representation of the three-dimensional radiated wave field on a two-dimensional mesh [73, 75, 144, 153].

The 2.5D concept has been used for many applications. 2.5D finite elements (FE) were used by Gavrić to model thin-walled [76] and solid [77] waveguides. Stamos and Beskos [153] consider 2.5D boundary elements (BE) to model the seismic response of long lined tunnels embedded in a halfspace. By using a dynamic substructuring technique, the complex structure is modeled for example by means of finite elements, while boundary elements are used for the regular soil [73]. These formulations have been used by Sheng et al. [144] and Andersen en Nielsen [9] for the prediction of railway traffic induced vibrations, and by Lombaert et al. [117] for the prediction of road traffic induced vibrations.

Instead of using boundary elements, finite elements can be used where spurious reflections at the boundaries are prevented with, for example, absorbing boundary conditions [124], infinite elements [28, 166], or perfectly matched layers (PMLs) [17, 25]. In a 2.5D framework, a 2.5D finite-infinite element approach proposed by Yang and Hung [177] and a 2.5D perfectly matched layer technique described by François et al. [72] have been proposed. The latter approach is used in this work.

The problem is introduced in section 3.2, after which the 2.5D FE-PML method is presented (section 3.3). In section 3.4, the performance of double and single wall barriers are analyzed and in section 3.5, a physical interpretation is given. Finally, the influence of the geometry and the material properties are discussed (section 3.6).

3.2 Problem description

The problem considered is a (double) wall barrier with invariant cross section in a halfspace which is assumed homogeneous to facilitate physical interpretation (figure 3.2). Table 3.1 lists the material properties of the homogeneous halfspace, which are typical for sandy soils, and of the inserted walls, which are stiffer than the surrounding soil and typical for jet grouting.

The halfspace is excited at the surface by a point source. In order to define the geometry, the right-handed Cartesian frame of reference in figure 3.2 is chosen, where the origin coincides with the position of the source point. The vibration levels at three receivers are analyzed, located at $(x = 15\,\mathrm{m}, y = 0\,\mathrm{m}, z = 0\,\mathrm{m})$, $(x = 15\,\mathrm{m}, y = 5\,\mathrm{m}, z = 0\,\mathrm{m})$, and $(x = 15\,\mathrm{m}, y = 15\,\mathrm{m}, z = 0\,\mathrm{m})$. These positions will be referred to as receiver 1, receiver 2, and receiver 3, respectively.

The performance of a double wall barrier is benchmarked against the one of a single wall barrier with the same depth and volume of material. The wall barriers are located symmetrically with respect to the center of the source and

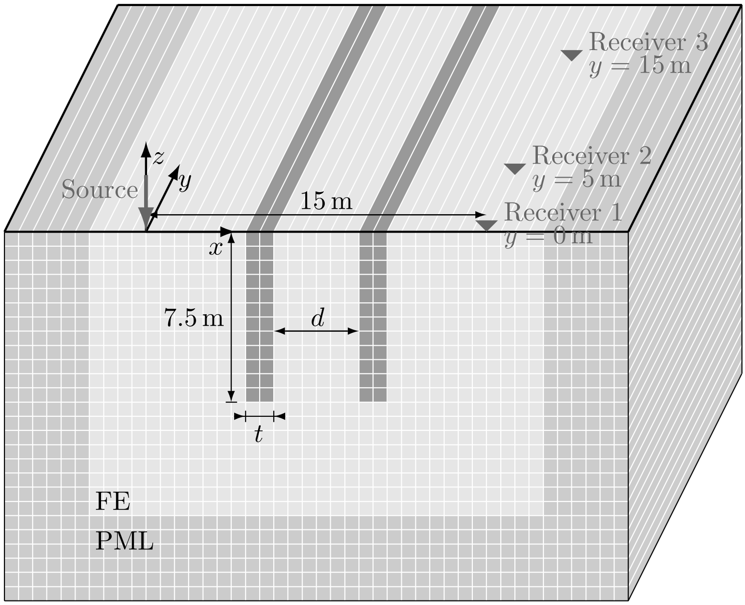

Figure 3.2: The three-dimensional wave propagation problem with a double wall barrier. The mesh is added as illustration only and is not the actual finite element mesh.

Table 3.1: Material properties of the original homogeneous halfspace and the stiff wall barrier.

	Homogeneous halfspace	Stiff wall barrier
Mass density ρ [kg/m^3]	2000	2000
Dilatational wave velocity C_p [m/s]	400	950
Shear wave velocity C_s [m/s]	200	550
Dilatational material damping ratio β_p [%]	2.5	2.5
Shear material damping ratio β_s [%]	2.5	2.5

the first receiver. The single wall barrier has a thickness $2t_w = 2\,\mathrm{m}$ and the center axis is located at a distance of $7.5\,\mathrm{m}$ from the point source. The two walls of the double wall barrier have a thickness of $t_w = 1\,\mathrm{m}$. The center axis of both walls is located at a distance of respectively $5\,\mathrm{m}$ and $10\,\mathrm{m}$ from the point source (the spacing between the walls is $d = 4\,\mathrm{m}$).

The performance of the wall barrier depends on the material properties and the geometry of the wall. Two phenomena play a role. First, for deep walls, incident waves are reflected, reducing wave transmission [4]. Second, the bending stiffness of the wall prevents the propagation of waves when the trace wavelength (the distance between two wave fronts in the direction along the barrier) is smaller than the bending wavelength of the barrier, similar to the coincidence phenomenon in building acoustics [53]. The two phenomena will be referred to as the reflection effect and the stiffness effect.

The depth of the barrier, 7.5 m, is large enough for both effects to play a role in the performance. Waves are reflected by the barrier if the depth is larger than 0.6 times the Rayleigh wavelength [27]. Furthermore, wave propagation is prevented by the bending stiffness of the wall at frequencies larger than the critical frequency ω_{c} [53]:

$$\omega_{\mathrm{c}} \approx \frac{C_{\mathrm{R}}^2}{h}\sqrt{\frac{12\rho}{E}} \tag{3.1}$$

where h is the depth, ρ the mass density, and E the elastic modulus of the barrier and C_{R} is the Rayleigh wave velocity of the soil. The latter is approximately calculated as (e.g. [2]):

$$C_{\mathrm{R}} = \frac{0.862 + 1.14\nu}{1+\nu} C_{\mathrm{s}} \tag{3.2}$$

where ν is the Poisson ratio of the homogeneous halfspace material. For the material properties in table 3.1, the Rayleigh wave velocity of the soil is equal to 186.3 m/s. For frequencies above $f_{\mathrm{c}} = 2.9\,\mathrm{Hz}$, the barrier is therefore deep enough (7.5 m) to mobilize the bending stiffness of the barrier around the x-axis, while for frequencies above 14.9 Hz, it is also deep enough to reflect incoming waves.

3.3 Two-and-a-half dimensional finite element method

When the structure has an invariant cross section, a computationally efficient two-and-a-half-dimensional (2.5D) approach can be applied, where a Fourier transform from the longitudinal coordinate to the wavenumber domain allows for the representation of the three-dimensional wave field on a two-dimensional mesh. The methodology used in this text was developed by François et al. [72, 73].

The derivation for elastic 2.5D volume elements with an invariant cross section is addressed in this section. First the governing equations are discussed. Subsequently, the domain is discretized and the finite element equations are derived. To take into account the radiation of waves to infinity, perfectly matched layers (PMLs) are added at the boundaries of the finite element mesh. Only volume elements are discussed, while appendix B covers the two-and-a-half dimensional finite element method for elastic shell elements, which will be used in chapter 6.

3.3.1 Governing equations

In an elastic three-dimensional domain Ω (figure 3.3), the stresses $\hat{\sigma}_{ij}$ and the displacements $\hat{u}_i$ satisfy the following equilibrium equations [2]:

$$\begin{cases} \dfrac{\partial \hat{\sigma}_{xx}}{\partial x} + \dfrac{\partial \hat{\sigma}_{xy}}{\partial y} + \dfrac{\partial \hat{\sigma}_{zx}}{\partial z} = -\omega^2 \rho \hat{u}_x \\ \dfrac{\partial \hat{\sigma}_{xy}}{\partial x} + \dfrac{\partial \hat{\sigma}_{yy}}{\partial y} + \dfrac{\partial \hat{\sigma}_{yz}}{\partial z} = -\omega^2 \rho \hat{u}_y \\ \dfrac{\partial \hat{\sigma}_{zx}}{\partial x} + \dfrac{\partial \hat{\sigma}_{yz}}{\partial y} + \dfrac{\partial \hat{\sigma}_{zz}}{\partial z} = -\omega^2 \rho \hat{u}_z \end{cases} \tag{3.3}$$

where ω is the circular frequency and ρ is the mass density.

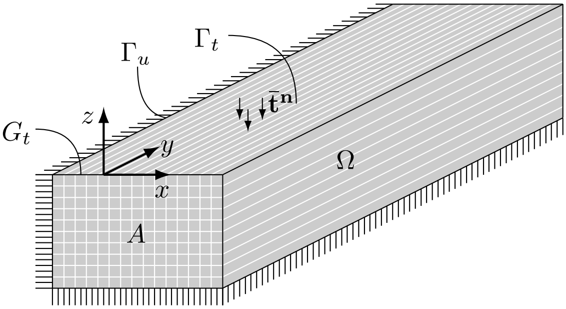

Figure 3.3: Domain Ω with longitudinal invariant cross-section A and Dirichlet (Γ_u) and Neumann boundary (Γ_t) conditions.

By separating the in-plane coordinates x and z and the longitudinal variable y, the equilibrium equations become:

$$\left(\begin{bmatrix} \frac{\partial}{\partial x} & 0 & 0 & 0 & 0 & \frac{\partial}{\partial z} \\ 0 & 0 & 0 & \frac{\partial}{\partial x} & \frac{\partial}{\partial z} & 0 \\ 0 & 0 & \frac{\partial}{\partial z} & 0 & 0 & \frac{\partial}{\partial x} \end{bmatrix} + \begin{bmatrix} 0 & 0 & 0 & 1 & 0 & 0 \\ 0 & 1 & 0 & 0 & 0 & 0 \\ 0 & 0 & 0 & 0 & 1 & 0 \end{bmatrix} \frac{\partial}{\partial y}\right) \begin{Bmatrix} \hat{\sigma}_{xx} \\ \hat{\sigma}_{yy} \\ \hat{\sigma}_{zz} \\ \hat{\sigma}_{xy} \\ \hat{\sigma}_{yz} \\ \hat{\sigma}_{zx} \end{Bmatrix} = -\omega^2 \rho \begin{Bmatrix} \hat{u}_x \\ \hat{u}_y \\ \hat{u}_z \end{Bmatrix} \tag{3.4}$$

which can be written as:

$$\left(\mathbf{L}_1^{\mathrm{T}} + \mathbf{L}_2^{\mathrm{T}} \frac{\partial}{\partial y}\right) \hat{\boldsymbol{\sigma}} = -\omega^2 \rho \hat{\mathbf{u}} \tag{3.5}$$

Linear elastic constitutive behavior is assumed [2], leading to the following relation between stresses and strains:

$$\begin{aligned} \hat{\boldsymbol{\sigma}} = \begin{Bmatrix} \hat{\sigma}_{xx} \\ \hat{\sigma}_{yy} \\ \hat{\sigma}_{zz} \\ \hat{\sigma}_{xy} \\ \hat{\sigma}_{yz} \\ \hat{\sigma}_{zx} \end{Bmatrix} &= \left((\lambda + 2\mu) \begin{bmatrix} 1 & 1 & 1 & 0 & 0 & 0 \\ 1 & 1 & 1 & 0 & 0 & 0 \\ 1 & 1 & 1 & 0 & 0 & 0 \\ 0 & 0 & 0 & 0 & 0 & 0 \\ 0 & 0 & 0 & 0 & 0 & 0 \\ 0 & 0 & 0 & 0 & 0 & 0 \end{bmatrix} \right. \\ &\quad \left. + \mu \begin{bmatrix} 0 & -2 & -2 & 0 & 0 & 0 \\ -2 & 0 & -2 & 0 & 0 & 0 \\ -2 & -2 & 0 & 0 & 0 & 0 \\ 0 & 0 & 0 & 1 & 0 & 0 \\ 0 & 0 & 0 & 0 & 1 & 0 \\ 0 & 0 & 0 & 0 & 0 & 1 \end{bmatrix} \right) \begin{Bmatrix} \hat{\epsilon}_{xx} \\ \hat{\epsilon}_{yy} \\ \hat{\epsilon}_{zz} \\ \hat{\gamma}_{xy} \\ \hat{\gamma}_{yz} \\ \hat{\gamma}_{zx} \end{Bmatrix} \\ &= \left((\lambda + 2\mu)\, \mathbf{c}_{\mathrm{p}} + \mu \mathbf{c}_{\mathrm{s}} \right) \hat{\boldsymbol{\epsilon}} \\ &= \mathbf{C} \hat{\boldsymbol{\epsilon}} \end{aligned} \tag{3.6}$$

where λ and μ are the Lamé coefficients, and $\mathbf{C} = (\lambda + 2\mu)\, \mathbf{c}_{\mathrm{p}} + \mu \mathbf{c}_{\mathrm{s}}$ the constitutive tensor. Note that $\lambda + 2\mu = \rho C_{\mathrm{p}}^2$ is the constrained modulus and $\mu = \rho C_{\mathrm{s}}^2$ is the shear modulus, with C_{p} and C_{s} the dilatational and shear wave velocity, respectively.

Following the correspondence principle [136, 137], hysteretic damping is modeled in the frequency domain by the introduction of complex material properties, denoted by a prime ($'$):

$$\begin{cases} (\lambda + 2\mu)' = (\lambda + 2\mu)\left(1 + 2\mathrm{i}\beta_{\mathrm{p}}\right) \\ \mu' = \mu(1 + 2\mathrm{i}\beta_{\mathrm{s}}) \end{cases} \tag{3.7}$$

where β_{p} and β_{s} represent the hysteretic material damping ratio for the dilatational waves and the shear waves, respectively.

The strains are calculated from the displacements [2]:

$$\begin{cases} \hat{\epsilon}_{xx} = \dfrac{\partial \hat{u}_x}{\partial x} \\ \hat{\epsilon}_{yy} = \dfrac{\partial \hat{u}_y}{\partial y} \\ \hat{\epsilon}_{zz} = \dfrac{\partial \hat{u}_z}{\partial z} \\ \hat{\gamma}_{xy} = \dfrac{\partial \hat{u}_x}{\partial y} + \dfrac{\partial \hat{u}_y}{\partial x} \\ \hat{\gamma}_{yz} = \dfrac{\partial \hat{u}_y}{\partial z} + \dfrac{\partial \hat{u}_z}{\partial y} \\ \hat{\gamma}_{xz} = \dfrac{\partial \hat{u}_x}{\partial z} + \dfrac{\partial \hat{u}_z}{\partial x} \end{cases} \tag{3.8}$$

These equations can be summarized as:

$$\hat{\boldsymbol{\epsilon}} = \begin{Bmatrix} \hat{\epsilon}_{xx} \\ \hat{\epsilon}_{yy} \\ \hat{\epsilon}_{zz} \\ \hat{\gamma}_{xy} \\ \hat{\gamma}_{yz} \\ \hat{\gamma}_{zx} \end{Bmatrix} = \left(\begin{bmatrix} \frac{\partial}{\partial x} & 0 & 0 \\ 0 & 0 & 0 \\ 0 & 0 & \frac{\partial}{\partial z} \\ 0 & \frac{\partial}{\partial x} & 0 \\ 0 & \frac{\partial}{\partial z} & 0 \\ \frac{\partial}{\partial z} & 0 & \frac{\partial}{\partial x} \end{bmatrix} + \begin{bmatrix} 0 & 0 & 0 \\ 0 & 1 & 0 \\ 0 & 0 & 0 \\ 1 & 0 & 0 \\ 0 & 0 & 1 \\ 0 & 0 & 0 \end{bmatrix} \frac{\partial}{\partial y} \right) \begin{Bmatrix} \hat{u}_x \\ \hat{u}_y \\ \hat{u}_z \end{Bmatrix} = \left(\mathbf{L}_1 + \mathbf{L}_2 \frac{\partial}{\partial y} \right) \hat{\mathbf{u}} \tag{3.9}$$

At the boundaries of the elastic domain, Neumann boundary conditions are imposed [2]:

$$\hat{\mathbf{t}}^{\mathbf{n}} = \hat{\boldsymbol{\sigma}} \cdot \mathbf{n} = \bar{\mathbf{t}}^{\mathbf{n}} \tag{3.10}$$

with $\mathbf{n}$ the unit outward normal vector of the boundary Γ_t and $\bar{\mathbf{t}}^{\mathbf{n}}$ the imposed tractions on the boundary. The equilibrium equations in equation (3.5) and the Neumann boundary conditions in equation (3.10) are formulated in a weak form by considering a virtual displacement field $\hat{\mathbf{v}}$ on the domain Ω:

$$\int_{\Omega} \hat{\mathbf{v}}^{\mathrm{T}} \left[\left(\mathbf{L}_1^{\mathrm{T}} + \mathbf{L}_2^{\mathrm{T}} \frac{\partial}{\partial y} \right) \hat{\boldsymbol{\sigma}} \right] \mathrm{d}\Omega + \omega^2 \int_{\Omega} \hat{\mathbf{v}}^{\mathrm{T}} \rho \hat{\mathbf{u}} \mathrm{d}\Omega - \int_{\Gamma_t} \hat{\mathbf{v}}^{\mathrm{T}} \left(\hat{\mathbf{t}}^{\mathbf{n}} - \bar{\mathbf{t}}^{\mathbf{n}} \right) \mathrm{d}\Gamma = 0 \tag{3.11}$$

Integration by parts and application of the divergence theorem leads to:

$$\begin{aligned}\int_{\Gamma} \hat{\mathbf{v}}^{\mathrm{T}} \hat{\mathbf{t}}^{\mathbf{n}} \mathrm{d}\Gamma - \int_{\Omega} \left[\left(\mathbf{L}_1 + \mathbf{L}_2 \frac{\partial}{\partial y} \right) \hat{\mathbf{v}} \right]^{\mathrm{T}} \hat{\boldsymbol{\sigma}} \mathrm{d}\Omega + \omega^2 \int_{\Omega} \hat{\mathbf{v}}^{\mathrm{T}} \rho \hat{\mathbf{u}} \mathrm{d}\Omega \\ - \int_{\Gamma_t} \hat{\mathbf{v}}^{\mathrm{T}} \left(\hat{\mathbf{t}}^{\mathbf{n}} - \bar{\mathbf{t}}^{\mathbf{n}} \right) \mathrm{d}\Gamma = 0\end{aligned} \tag{3.12}$$

Since $\Gamma = \Gamma_t \cup \Gamma_u$ with Γ_u the part of Γ on which homogeneous Dirichlet conditions are applied, this equation becomes:

$$\int_{\Gamma_u} \hat{\mathbf{v}}^{\mathrm{T}} \hat{\mathbf{t}}^{\mathbf{n}} \mathrm{d}\Gamma - \int_{\Omega} \left[\left(\mathbf{L}_1 + \mathbf{L}_2 \frac{\partial}{\partial y} \right) \hat{\mathbf{v}} \right]^{\mathrm{T}} \hat{\boldsymbol{\sigma}} \mathrm{d}\Omega + \omega^2 \int_{\Omega} \hat{\mathbf{v}}^{\mathrm{T}} \rho \hat{\mathbf{u}} \mathrm{d}\Omega + \int_{\Gamma_t} \hat{\mathbf{v}}^{\mathrm{T}} \bar{\mathbf{t}}^{\mathbf{n}} \mathrm{d}\Gamma = 0 \tag{3.13}$$

As the virtual displacement field $\hat{\mathbf{v}}$ is chosen to satisfy the Dirichlet conditions on the boundary Γ_u, the first integral vanishes:

$$\int_{\Omega} \left[\left(\mathbf{L}_1 + \mathbf{L}_2 \frac{\partial}{\partial y} \right) \hat{\mathbf{v}} \right]^{\mathrm{T}} \hat{\boldsymbol{\sigma}} \mathrm{d}\Omega - \omega^2 \int_{\Omega} \hat{\mathbf{v}}^{\mathrm{T}} \rho \hat{\mathbf{u}} \mathrm{d}\Omega = \int_{\Gamma_t} \hat{\mathbf{v}}^{\mathrm{T}} \bar{\mathbf{t}}^{\mathbf{n}} \mathrm{d}\Gamma \tag{3.14}$$

3.3.2 Discretization

As the cross section is longitudinally invariant, the finite element discretization of the displacements $\hat{\mathbf{u}}$ is written as [73]:

$$\hat{\mathbf{u}}(x, y, z, \omega) \approx \mathbf{N}(x, z) \underline{\hat{\mathbf{u}}}(y, \omega) \tag{3.15}$$

where $\mathbf{N}(x, z)$ are shape functions defined over the cross section and $\underline{\hat{\mathbf{u}}}(y, \omega)$ is the discretized displacement vector which is a function of the longitudinal coordinate y and the frequency ω.

The strains therefore become:

$$\hat{\boldsymbol{\epsilon}} = \mathbf{L}_1 \mathbf{N} \underline{\hat{\mathbf{u}}} + \mathbf{L}_2 \mathbf{N} \frac{\partial \underline{\hat{\mathbf{u}}}}{\partial y} = \mathbf{B}_1 \underline{\hat{\mathbf{u}}} + \mathbf{B}_2 \frac{\partial \underline{\hat{\mathbf{u}}}}{\partial y} \tag{3.16}$$

with $\mathbf{B}_1 = \mathbf{L}_1 \mathbf{N}$ and $\mathbf{B}_2 = \mathbf{L}_2 \mathbf{N}$. The stresses are given by:

$$\hat{\boldsymbol{\sigma}} = \mathbf{C} \hat{\boldsymbol{\epsilon}} = \mathbf{C} \mathbf{B}_1 \underline{\hat{\mathbf{u}}} + \mathbf{C} \mathbf{B}_2 \frac{\partial \underline{\hat{\mathbf{u}}}}{\partial y} \tag{3.17}$$

A standard Galerkin procedure [33] is followed, where the same discretization is used for the virtual displacement vector $\hat{\mathbf{v}}$ as for the displacement vector $\hat{\mathbf{u}}$:

$$\hat{\mathbf{v}}(x, y, z, \omega) \approx \mathbf{N}(x, z) \underline{\hat{\mathbf{v}}}(y, \omega) \tag{3.18}$$

The virtual work formulation in equation (3.14) now becomes:

$$\begin{aligned}
&-\omega^2 \int_{\Omega} \underline{\hat{\mathbf{v}}}^{\mathrm{T}} \mathbf{N}^{\mathrm{T}} \rho \mathbf{N} \underline{\hat{\mathbf{u}}} \mathrm{d}\Omega + \int_{\Omega} \left(\underline{\hat{\mathbf{v}}}^{\mathrm{T}} \mathbf{B}_1^{\mathrm{T}} + \left(\frac{\partial \underline{\hat{\mathbf{v}}}}{\partial y} \right)^{\mathrm{T}} \mathbf{B}_2^{\mathrm{T}} \right) \mathbf{C} \left(\mathbf{B}_1 \underline{\hat{\mathbf{u}}} + \mathbf{B}_2 \frac{\partial \underline{\hat{\mathbf{u}}}}{\partial y} \right) \mathrm{d}\Omega \\
&\quad = \int_{\Gamma_t} \underline{\hat{\mathbf{v}}}^{\mathrm{T}} \mathbf{N}^{\mathrm{T}} \bar{\mathbf{t}}^{\mathbf{n}} \mathrm{d}\Gamma
\end{aligned} \tag{3.19}$$

This equation is further elaborated, rewriting the volume integrals as an integral over the longitudinal coordinate y and the cross section A:

$$\begin{aligned}
&-\omega^2 \int_y \underline{\hat{\mathbf{v}}}^{\mathrm{T}} \left(\int_A \mathbf{N}^{\mathrm{T}} \rho \mathbf{N} \mathrm{d}A \right) \underline{\hat{\mathbf{u}}} \mathrm{d}y + \int_y \underline{\hat{\mathbf{v}}}^{\mathrm{T}} \left(\int_A \mathbf{B}_1^{\mathrm{T}} \mathbf{C} \mathbf{B}_1 \mathrm{d}A \right) \underline{\hat{\mathbf{u}}} \mathrm{d}y \\
&\quad + \int_y \underline{\hat{\mathbf{v}}}^{\mathrm{T}} \left(\int_A \mathbf{B}_1^{\mathrm{T}} \mathbf{C} \mathbf{B}_2 \mathrm{d}A \right) \frac{\partial \underline{\hat{\mathbf{u}}}}{\partial y} \mathrm{d}y + \int_y \left(\frac{\partial \underline{\hat{\mathbf{v}}}}{\partial y} \right)^{\mathrm{T}} \left(\int_A \mathbf{B}_2^{\mathrm{T}} \mathbf{C} \mathbf{B}_1 \mathrm{d}A \right) \underline{\hat{\mathbf{u}}} \mathrm{d}y \\
&\quad + \int_y \left(\frac{\partial \underline{\hat{\mathbf{v}}}}{\partial y} \right)^{\mathrm{T}} \left(\int_A \mathbf{B}_2^{\mathrm{T}} \mathbf{C} \mathbf{B}_2 \mathrm{d}A \right) \frac{\partial \underline{\hat{\mathbf{u}}}}{\partial y} \mathrm{d}y = \int_y \underline{\hat{\mathbf{v}}}^{\mathrm{T}} \left(\int_{G_t} \mathbf{N}^{\mathrm{T}} \bar{\mathbf{t}}^{\mathbf{n}} \mathrm{d}s \right) \mathrm{d}y
\end{aligned} \tag{3.20}$$

where G_t is the intersection of the surface Γ_t with the plane $y = 0$.

Integration by parts on the terms containing derivatives $\dfrac{\partial \underline{\hat{\mathbf{v}}}}{\partial y}$ leads to:

$$\begin{aligned}
&-\omega^2 \int_y \underline{\hat{\mathbf{v}}}^{\mathrm{T}} \left(\int_A \mathbf{N}^{\mathrm{T}} \rho \mathbf{N} \mathrm{d}A \right) \underline{\hat{\mathbf{u}}} \mathrm{d}y + \int_y \underline{\hat{\mathbf{v}}}^{\mathrm{T}} \left(\int_A \mathbf{B}_1^{\mathrm{T}} \mathbf{C} \mathbf{B}_1 \mathrm{d}A \right) \underline{\hat{\mathbf{u}}} \mathrm{d}y \\
&\quad + \int_y \underline{\hat{\mathbf{v}}}^{\mathrm{T}} \left(\int_A \mathbf{B}_1^{\mathrm{T}} \mathbf{C} \mathbf{B}_2 \mathrm{d}A \right) \frac{\partial \underline{\hat{\mathbf{u}}}}{\partial y} \mathrm{d}y - \int_y \underline{\hat{\mathbf{v}}}^{\mathrm{T}} \left(\int_A \mathbf{B}_2^{\mathrm{T}} \mathbf{C} \mathbf{B}_1 \mathrm{d}A \right) \frac{\partial \underline{\hat{\mathbf{u}}}}{\partial y} \mathrm{d}y \\
&\quad - \int_y \underline{\hat{\mathbf{v}}}^{\mathrm{T}} \left(\int_A \mathbf{B}_2^{\mathrm{T}} \mathbf{C} \mathbf{B}_2 \mathrm{d}A \right) \frac{\partial^2 \underline{\hat{\mathbf{u}}}}{\partial y^2} \mathrm{d}y = \int_y \underline{\hat{\mathbf{v}}}^{\mathrm{T}} \left(\int_{G_t} \mathbf{N}^{\mathrm{T}} \bar{\mathbf{t}}^{\mathbf{n}} \mathrm{d}s \right) \mathrm{d}y
\end{aligned} \tag{3.21}$$

where one of the terms resulting from the integration by parts is omitted as it is equal to zero due to Sommerfeld's radiation condition [151].

Since this equation holds for any virtual displacement $\underline{\hat{\mathbf{v}}}$, it is equivalent to [73]:

$$-\omega^2 \mathbf{M} \underline{\hat{\mathbf{u}}}(y, \omega) + \mathbf{K}^0 \underline{\hat{\mathbf{u}}}(y, \omega) + \mathbf{K}^1 \frac{\partial \underline{\hat{\mathbf{u}}}(y, \omega)}{\partial y} + \mathbf{K}^2 \frac{\partial^2 \underline{\hat{\mathbf{u}}}(y, \omega)}{\partial y^2} = \underline{\hat{\mathbf{p}}}(y, \omega) \tag{3.22}$$

with:

$$\mathbf{M} = \int_A \mathbf{N}^{\mathrm{T}} \rho \mathbf{N} \mathrm{d}A \tag{3.23}$$

$$\mathbf{K}^0 = \int_A \mathbf{B}_1^{\mathrm{T}}\mathbf{C}\mathbf{B}_1 \mathrm{d}A \tag{3.24}$$

$$\mathbf{K}^1 = \int_A \mathbf{B}_1^{\mathrm{T}}\mathbf{C}\mathbf{B}_2 \mathrm{d}A - \int_A \mathbf{B}_2^{\mathrm{T}}\mathbf{C}\mathbf{B}_1 \mathrm{d}A \tag{3.25}$$

$$\mathbf{K}^2 = -\int_A \mathbf{B}_2^{\mathrm{T}}\mathbf{C}\mathbf{B}_2 \mathrm{d}A \tag{3.26}$$

$$\underline{\hat{\mathbf{p}}}(y,\omega) = \int_{G_t} \mathbf{N}^{\mathrm{T}}\bar{\mathbf{t}}^{\mathbf{n}}\left(x,y,z,\omega\right)\mathrm{d}s \tag{3.27}$$

The differential equation (3.22) is solved by a Fourier transform of the longitudinal coordinate y to the longitudinal wavenumber k_y [71]:

$$\tilde{f}(k_y) = \mathcal{F}\left[\hat{f}\left(y\right); k_y\right] = \int\limits_{-\infty}^{\infty} e^{+\mathrm{i}k_y y}\hat{f}\left(y\right)\mathrm{d}y \tag{3.28}$$

$$\hat{f}(y) = \mathcal{F}^{-1}\left[\tilde{f}(k_y); y\right] = \frac{1}{2\pi}\int_{-\infty}^{\infty} e^{-\mathrm{i}k_y y}\tilde{f}(k_y)\mathrm{d}k_y \tag{3.29}$$

This results in the following equation [73]:

$$\left(-\omega^2\mathbf{M} + \mathbf{K}^0 - ik_y\mathbf{K}^1 - k_y^2\mathbf{K}^2\right)\underline{\tilde{\mathbf{u}}}\left(k_y,\omega\right) = \underline{\tilde{\mathbf{p}}}\left(k_y,\omega\right) \tag{3.30}$$

where a tilde above a variable denotes its representation in the frequency-wavenumber domain. For reasons of brevity, these equilibrium equations are written as follows:

$$\tilde{\mathbf{K}}_k\underline{\tilde{\mathbf{u}}}_k = \underline{\tilde{\mathbf{p}}}_k \tag{3.31}$$

where $\tilde{\mathbf{K}}_k = -\omega^2\mathbf{M} + \mathbf{K}^0 - \mathrm{i}k_{yk}\mathbf{K}^1 - k_{yk}^2\mathbf{K}^2$, $\underline{\tilde{\mathbf{u}}}_k = \underline{\tilde{\mathbf{u}}}\left(k_{yk},\omega\right)$, and $\underline{\tilde{\mathbf{p}}}_k = \underline{\tilde{\mathbf{p}}}\left(k_{yk},\omega\right)$. The dependence on the frequency ω is implicitly considered.

The response $\underline{\hat{\mathbf{u}}}(y)$ in the spatial domain is obtained by the inverse Fourier transform from the wavenumber k_y to the coordinate y in equation (3.29). To compute this Fourier transform, it is often discretized as [48, 66]:

$$\underline{\hat{\mathbf{u}}}_l = \frac{1}{2\pi}\sum_{k=1}^{N_k}\underline{\tilde{\mathbf{u}}}_k e^{-\mathrm{i}2\pi(l-1)(k-1)/N}\Delta k_y \tag{3.32}$$

which can be computed with a Fast Fourier Transform (FFT) algorithm.

3.3.3 Perfectly matched layers

Perfectly matched layers (PMLs) are added at the boundaries of the finite element domain to prevent spurious reflections [72]. The coordinates in the PML layer in the direction normal to the interface between the elastodynamic domain and the PML domain are denoted by s. The complex stretched coordinates $\bar{s}$ are then defined by [41, 40]:

$$\bar{s} = \int_{0}^{s} \lambda_s \left(s\right) \mathrm{d}s \tag{3.33}$$

where $\lambda_s \left(s\right)$ is a stretching function. In the elastodynamic domain, the stretching functions are $\lambda_s = 1$, making the stretched coordinates $\bar{s}$ equal to the coordinates s. In order to attenuate both propagating and evanescent waves, the following stretching functions are classically used in the PML domain [17, 18, 25, 41]:

$$\lambda_s \left(s\right) = 1 + f_s^{\mathrm{e}} \left(s\right) - \mathrm{i}\frac{f_s^{\mathrm{p}} \left(s\right)}{a_0} \tag{3.34}$$

with $f_s^{\mathrm{p}} \left(s\right)$ and $f_s^{\mathrm{e}} \left(s\right)$ the attenuation functions for propagating and evanescent waves, respectively, and the dimensionless frequency a_0 taken as $a_0 = \omega L / C_{\mathrm{s}}$ with L a characteristic length, chosen as the thickness of the PML layer. The following linear attenuation functions are applied [16, 26]:

$$f_s^{\mathrm{e}} \left(s\right) = f_{s0}^{\mathrm{e}} \frac{s}{L} \tag{3.35}$$

$$f_s^{\mathrm{p}} \left(s\right) = f_{s0}^{\mathrm{p}} \frac{s}{L} \tag{3.36}$$

In this text, the values $f_{s0}^{\mathrm{e}} = 0$ and $f_{s0}^{\mathrm{p}} = 20$ are used for the attenuation coefficients, as suggested by Basu and Chopra [17] and François et al. [72].

The mass and stiffness matrices are derived considering the stretched coordinates. The partial derivative with respect to $\bar{s}$ is equal to [72]:

$$\frac{\partial}{\partial \bar{s}} = \frac{1}{\lambda_s \left(s\right)} \frac{\partial}{\partial s} \tag{3.37}$$

For the 2.5D geometry under consideration, stretching is applied to the x- and z-coordinates only. This results in the following modified equilibrium equations:

$$\left(\begin{bmatrix} \frac{1}{\lambda_x}\frac{\partial}{\partial x} & 0 & 0 & 0 & 0 & \frac{1}{\lambda_z}\frac{\partial}{\partial z} \\ 0 & 0 & 0 & \frac{1}{\lambda_x}\frac{\partial}{\partial x} & \frac{1}{\lambda_z}\frac{\partial}{\partial z} & 0 \\ 0 & 0 & \frac{1}{\lambda_z}\frac{\partial}{\partial z} & 0 & 0 & \frac{1}{\lambda_x}\frac{\partial}{\partial x} \end{bmatrix} + \begin{bmatrix} 0 & 0 & 0 & 1 & 0 & 0 \\ 0 & 1 & 0 & 0 & 0 & 0 \\ 0 & 0 & 0 & 0 & 1 & 0 \end{bmatrix} \frac{\partial}{\partial y}\right) \begin{Bmatrix} \hat{\sigma}_{xx} \\ \hat{\sigma}_{yy} \\ \hat{\sigma}_{zz} \\ \hat{\sigma}_{xy} \\ \hat{\sigma}_{yz} \\ \hat{\sigma}_{zx} \end{Bmatrix} = -\omega^2 \rho \begin{Bmatrix} \hat{u}_x \\ \hat{u}_y \\ \hat{u}_z \end{Bmatrix} \tag{3.38}$$

which can be written as:

$$\left(\bar{\mathbf{L}}_1^{\mathrm{T}} + \mathbf{L}_2^{\mathrm{T}} \frac{\partial}{\partial y}\right) \hat{\boldsymbol{\sigma}} = -\omega^2 \rho \hat{\mathbf{u}} \tag{3.39}$$

Similarly, the strain tensor becomes:

$$\hat{\boldsymbol{\epsilon}} = \left(\bar{\mathbf{L}}_1 + \mathbf{L}_2 \frac{\partial}{\partial y}\right) \hat{\mathbf{u}} \tag{3.40}$$

To avoid integration by parts of the stretching functions λ_x and λ_z in the weak form of the virtual work equation, the equilibrium equation (3.39) is multiplied with a factor $\lambda_x \lambda_z$ [72]:

$$\lambda_x \lambda_z \left(\bar{\mathbf{L}}_1^{\mathrm{T}} + \mathbf{L}_2^{\mathrm{T}} \frac{\partial}{\partial y}\right) \hat{\boldsymbol{\sigma}} + \omega^2 \lambda_x \lambda_z \rho \hat{\mathbf{u}} = 0 \tag{3.41}$$

The following equation is found in the wavenumber domain by applying the same procedure as before [72]:

$$\left(-\omega^2 \bar{\mathbf{M}} + \bar{\mathbf{K}}^0 - ik_y \bar{\mathbf{K}}^1 - k_y^2 \bar{\mathbf{K}}^2\right) \underline{\tilde{\mathbf{u}}}\left(k_y, \omega\right) = \underline{\tilde{\bar{\mathbf{p}}}}\left(k_y, \omega\right) \tag{3.42}$$

where:

$$\bar{\mathbf{M}} = \int_A \lambda_x \lambda_z \mathbf{N}^{\mathrm{T}} \rho \mathbf{N} \mathrm{d}A \tag{3.43}$$

$$\bar{\mathbf{K}}^0 = \int_A \lambda_x \lambda_z \bar{\mathbf{B}}_1^{\mathrm{T}} \mathbf{C} \bar{\mathbf{B}}_1 \mathrm{d}A \tag{3.44}$$

$$\bar{\mathbf{K}}^1 = \int_A \lambda_x \lambda_z \bar{\mathbf{B}}_1^{\mathrm{T}} \mathbf{C} \mathbf{B}_2 \mathrm{d}A - \int_A \lambda_x \lambda_z \mathbf{B}_2^{\mathrm{T}} \mathbf{C} \bar{\mathbf{B}}_1 \mathrm{d}A \tag{3.45}$$

$$\bar{\mathbf{K}}^2 = -\int_A \lambda_x \lambda_z \mathbf{B}_2^{\mathrm{T}} \mathbf{C} \mathbf{B}_2 \mathrm{d}A \tag{3.46}$$

$$\underline{\hat{\bar{\mathbf{p}}}}(y,\omega) = \int_{G_t} \lambda_x \lambda_z \mathbf{N}^{\mathrm{T}} \bar{\mathbf{t}}^{\mathbf{n}} \left(x,y,z,\omega\right) \mathrm{d}s \tag{3.47}$$

with $\bar{\mathbf{B}}_1 = \bar{\mathbf{L}}_1 \mathbf{N}$.

3.4 Analysis of a double wall barrier

The aim is to analyze the performance of the double wall barrier in reducing ground vibration caused by passing trains. The displacement field resulting from a passing train can be modeled in a simplified way, applying axle loads as a series of incoherent point loads [119, 169]. First, the displacement field resulting from a point load is evaluated. Second, the simplified model with incoherent point loads is applied to assess the response for train loading.

3.4.1 Point load

In a homogeneous halfspace excited by a vertical unit point load, cylindrical wave fronts propagate through the soil. The amplitude decreases with the distance to the point source as a result of geometric attenuation and material damping in the soil. Figures 3.4a and 3.5a show the real part of the vertical displacement field respectively at 25 Hz and 50 Hz for the homogeneous halfspace.

The wave propagation is altered when the single or double wall, introduced in section 3.2, is inserted in the halfspace. Figures 3.4 and 3.5 show the real part of the vertical displacement and the corresponding insertion loss for both cases at 25 Hz and 50 Hz respectively, with the insertion loss $\hat{\mathrm{IL}}$ defined as:

$$\hat{\mathrm{IL}}(x,y,z,\omega) = 20 \log_{10} \frac{\left|\hat{u}_z^{\mathrm{ref}}(x,y,z,\omega)\right|}{\left|\hat{u}_z(x,y,z,\omega)\right|} \tag{3.48}$$

where $\hat{u}_z^{\mathrm{ref}}(x,y,z,\omega)$ is the vertical displacement before and $\hat{u}_z(x,y,z,\omega)$ the vertical displacement after introducing the considered mitigation measure in the soil.

The waves are partly reflected by the barriers. The reflected waves interfere constructively and destructively with the incoming waves, causing the alternating regions of low and high insertion loss at the surface. For the double

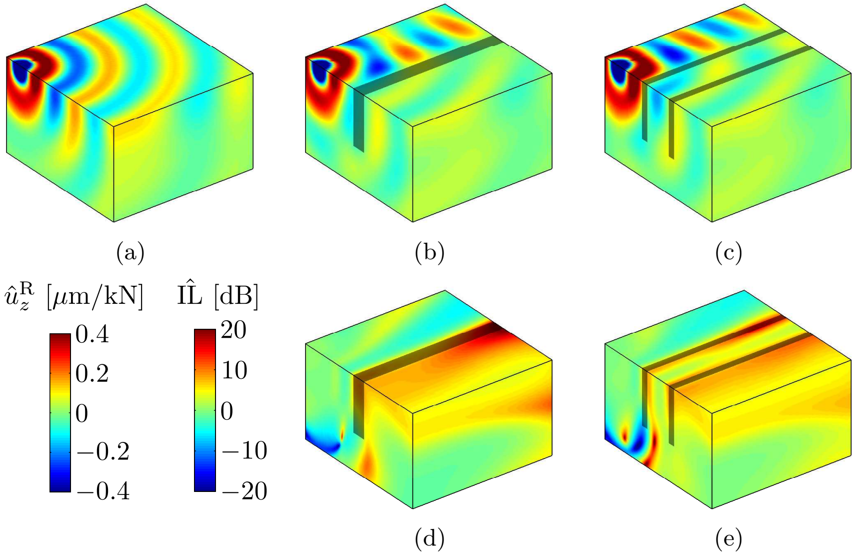

(a) (b) (c)

(d) (e)

Figure 3.4: Real part of the vertical displacement $\hat{u}_z$ at 25 Hz resulting from a unit point load for (a) the original homogeneous halfspace, (b) the single stiff wall barrier (wall thickness $2t_w = 2\,\mathrm{m}$), and (c) the double stiff wall barrier (wall thickness $t_w = 1\,\mathrm{m}$ and spacing $d = 4\,\mathrm{m}$) in sandy soil. Corresponding insertion loss $\hat{\mathrm{IL}}$ for (d) the single stiff wall barrier and (e) the double stiff wall barrier in sandy soil.

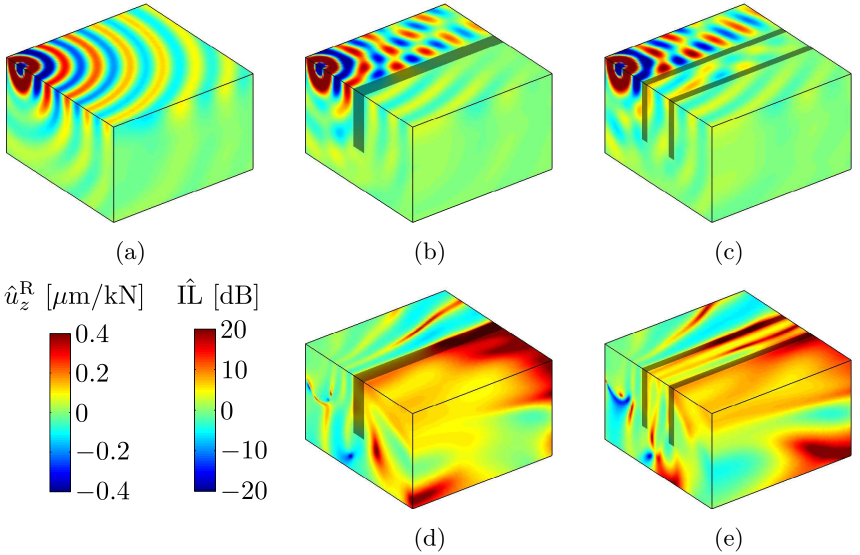

(a) (b) (c)

(d) (e)

Figure 3.5: Real part of the vertical displacement $\hat{u}_z$ at 50 Hz resulting from a unit point load for (a) the original homogeneous halfspace, (b) the single stiff wall barrier (wall thickness $2t_w = 2\,\mathrm{m}$), and (c) the double stiff wall barrier (wall thickness $t_w = 1\,\mathrm{m}$ and spacing $d = 4\,\mathrm{m}$) in sandy soil. Corresponding insertion loss $\hat{\mathrm{IL}}$ for (d) the single stiff wall barrier and (e) the double stiff wall barrier in sandy soil.

wall barrier, interference is also found between waves traveling in between both walls.

The insertion loss behind the wall barrier is positive at the surface, meaning that the transmission of Rayleigh waves is reduced. The insertion loss is higher at larger distances in the y-direction. This is due to the stiffness effect, as will be discussed in subsection 3.5.1.

Figure 3.6 shows the amplitude of the vertical displacement and the insertion loss as a function of the frequency for the three receiver points (defined in figure 3.2). At low frequencies, the depth of the wall barrier is small compared to the penetration depth of the incoming surface waves, resulting in low insertion losses. From about 25 Hz, corresponding to a shear wavelength equal to 7.5 m, an insertion loss between 5 dB and 13 dB is obtained.

For receivers 1 and 2, the insertion loss for the double wall barrier is only slightly higher than for the single wall barrier for most of the frequency range. At larger distances, for example for receiver 3, the single wall barrier has a slightly better performance than the double wall barrier for the frequency range considered. For this receiver, however, the amplitude is considerably lower than for receivers 1 and 2 resulting from the longer distance to the source, and therefore the better performance is less significant.

3.4.2 Train loading

In the previous section, the performance of the double wall barrier has been studied for a point source at the surface. However, the goal is to mitigate ground vibration caused by passing trains. The time history of the vibration velocity due to a moving train can be subdivided into three parts: an increasing level when the train approaches the receiver where the response is measured, an approximately stationary level when the train passes the receiver and a decreasing level when the train moves away from the receiver. Previous studies have indicated that the stationary part of the response can be well approximated using a simplified model for train loading, applying the dynamic axle loads at fixed positions as a series of incoherent point loads of the same magnitude [169].

The axle positions are taken from a typical four-car EMU train, with a car length of 26.4 m, and a total length of 105.6 m. The bogie center distance is 19 m and the distance between two axles of a bogie is 2.7 m. The train, represented by a series of point loads parallel to the y-axis, has its center at the origin in figure 3.2. The y-coordinates of the axle loads are shown in figure 3.7.

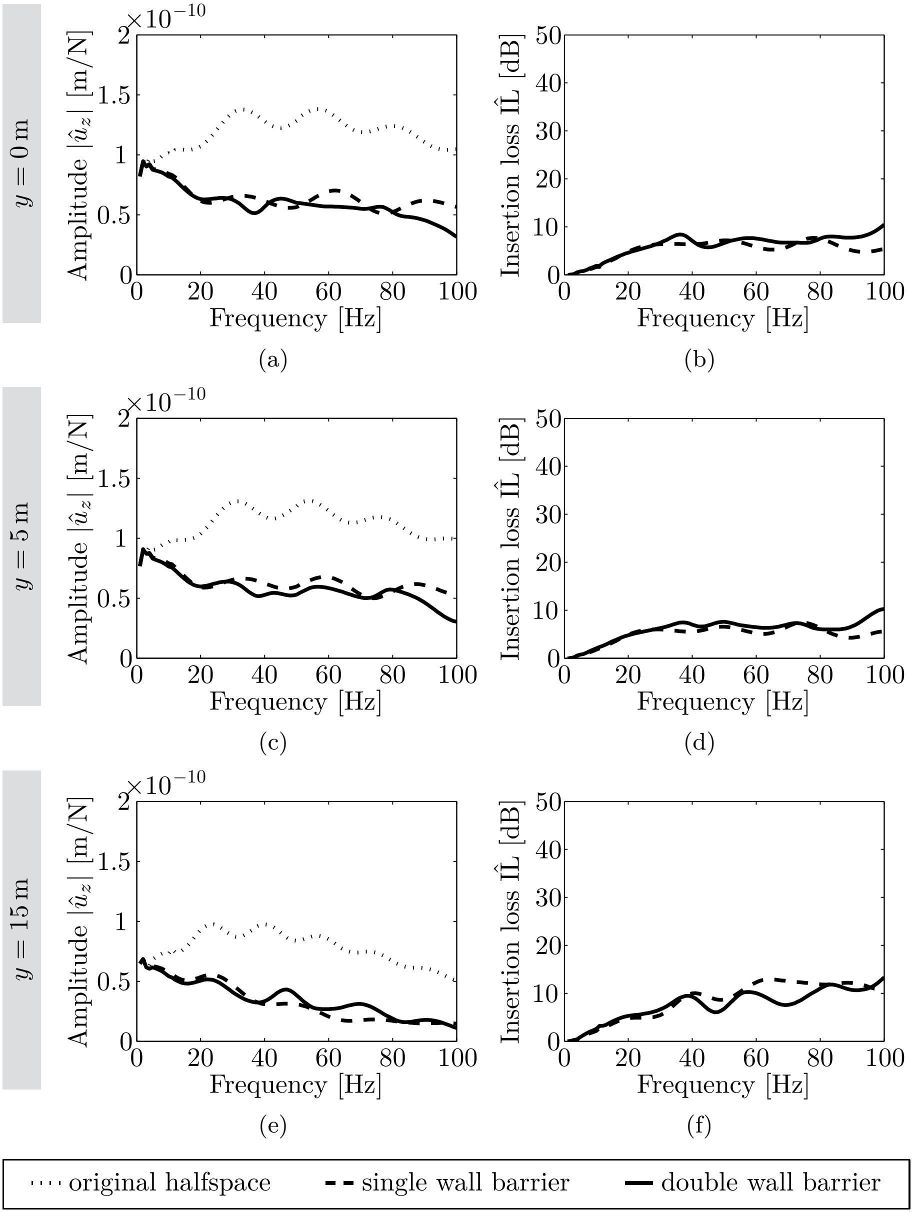

Figure 3.6: Amplitude of the vertical displacement $|\hat{u}_z|$ resulting from a point load for the original halfspace (dotted line), the single stiff wall barrier (dashed line; wall thickness $2t_w = 2\,\mathrm{m}$), and the double stiff wall barrier (solid line; wall thickness $t_w = 1\,\mathrm{m}$ and spacing $d = 4\,\mathrm{m}$) in sandy soil at the different receiver points: (a) receiver 1, (c) receiver 2, and (e) receiver 3 (figure 3.2). Corresponding insertion loss $\hat{\mathrm{IL}}$ for the single stiff wall barrier (dashed line) and the double stiff wall barrier (solid line) in sandy soil at the different receiver points: (b) receiver 1, (d) receiver 2, and (f) receiver 3.

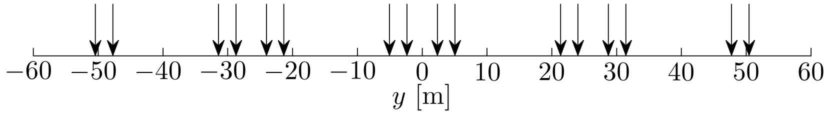

Figure 3.7: The axle positions of a typical four-car EMU train.

The amplitude of the vertical displacement and insertion loss at receiver 1 are shown in figure 3.8 for the considered single and double stiff wall barriers (with a wall thickness $t_w = 1\,\mathrm{m}$ and a spacing $d = 4\,\mathrm{m}$ between the two walls). As a result of geometric attenuation and material damping in the soil, the excitation points closest to the receiver point contribute most to the response at the receiver point. Therefore, the insertion loss is similar to the insertion loss found for a point source at the closest axle position. The double wall barrier performs slightly better than the single wall barrier over the entire frequency range considered, but again this improvement is limited.

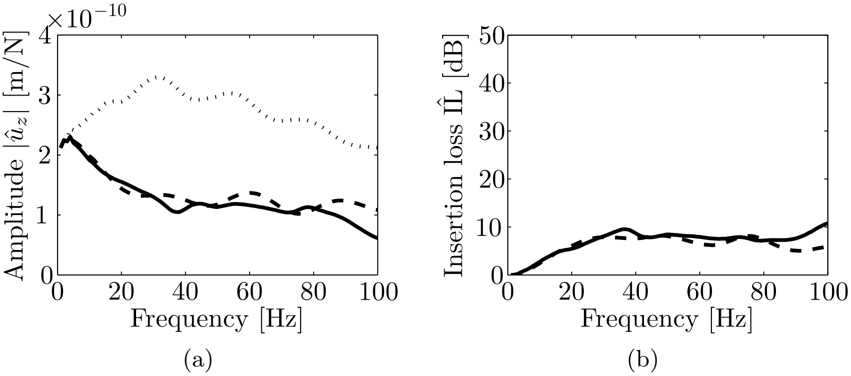

(a)

(b)

Figure 3.8: (a) Amplitude of the vertical displacement $\hat{u}_z$ at receiver 1 (figure 3.2) resulting from a train load for the original halfspace (dotted line), the single stiff wall barrier (dashed line; wall thickness $2t_w = 2\,\mathrm{m}$), and the double stiff wall barrier (solid line; wall thickness $t_w = 1\,\mathrm{m}$ and spacing $d = 4\,\mathrm{m}$) in sandy soil. (b) Corresponding insertion loss $\hat{\mathrm{IL}}$ for the single stiff wall barrier (dashed line) and the double stiff wall barrier (solid line) in sandy soil.

To conclude, the single and double wall barrier similarly perform over the frequency range considered. The double wall barrier has a slightly better performance in the area closest to the source, which is also the area with the highest vibration levels. As a similar performance is found for a point load and a train load, the physical interpretation is limited to the simplest case of a point load.

3.5 Physical interpretation

As stated in section 3.4, it is known from literature that two phenomena play an important role for the performance of single wall barriers: the stiffness effect [53] and reflection [74]. The role of these phenomena for double wall barriers is investigated in this section.

3.5.1 The stiffness effect

Free vibration of a single wall The stiffness effect of a single wall barrier can be explained by considering the dispersion relations for free vibration. Without any excitation, equation (3.30) becomes:

$$\left(-\omega^2\mathbf{M} + \mathbf{K}_0 - ik_y\mathbf{K}_1 - k_y^2\mathbf{K}_2\right)\tilde{\mathbf{u}}(k_y, \omega) = 0 \tag{3.49}$$

The dispersion curves for the beam are calculated by computing the longitudinal wavenumber k_y as a function of the circular frequency ω. Since equation (3.49) is a quadratic equation in k_y, this equation is reformulated to a linear equation as follows [164]:

$$\begin{bmatrix} -\omega^2\mathbf{M} + \mathbf{K}_0 & \mathbf{0} \\ \mathbf{0} & \mathbf{I} \end{bmatrix} \begin{Bmatrix} \tilde{\mathbf{u}}_1 \\ \tilde{\mathbf{u}}_2 \end{Bmatrix} = k_y \begin{bmatrix} i\mathbf{K}_1 & \mathbf{K}_2 \\ \mathbf{I} & \mathbf{0} \end{bmatrix} \begin{Bmatrix} \tilde{\mathbf{u}}_1 \\ \tilde{\mathbf{u}}_2 \end{Bmatrix} \tag{3.50}$$

where $\tilde{\mathbf{u}}_1 = \tilde{\mathbf{u}}$ and $\tilde{\mathbf{u}}_2 = k_y\tilde{\mathbf{u}}$. This corresponds to a generalized eigenvalue problem of the form $\mathbf{Ax} = \lambda\mathbf{Bx}$ where the eigenvalues λ represent the wavenumbers k_y and the first half of the eigenvectors $\mathbf{x}$ represent the corresponding mode shapes.

In this way, the dispersion relations and the corresponding mode shapes are calculated for the single wall barrier. The dispersion curves are computed for frequencies f from 0 Hz to 100 Hz in steps of 2 Hz. For $f = 0$ Hz, the system in equation (3.50) becomes ill-conditioned. Therefore, a small value is considered instead. Figure 3.9 shows the dispersion curves as a function of the frequency f and the slowness p_y, which is defined as $p_y = k_y/\omega = 1/C_y$ with C_y the longitudinal wave velocity. At low frequencies, four eigenvalues are found. Two shear-bending modes, a torsion mode and a longitudinal mode are distinguished. The other modes propagate only from a certain cut-on frequency.

The dispersion relations for the modes propagating at 0 Hz have also been computed by means of analytical expressions presented in the literature and derived in appendix C. For the longitudinal waves, the following expression holds [135]:

$$-\rho A\omega^2 + EAk_y^2 = 0 \tag{3.51}$$

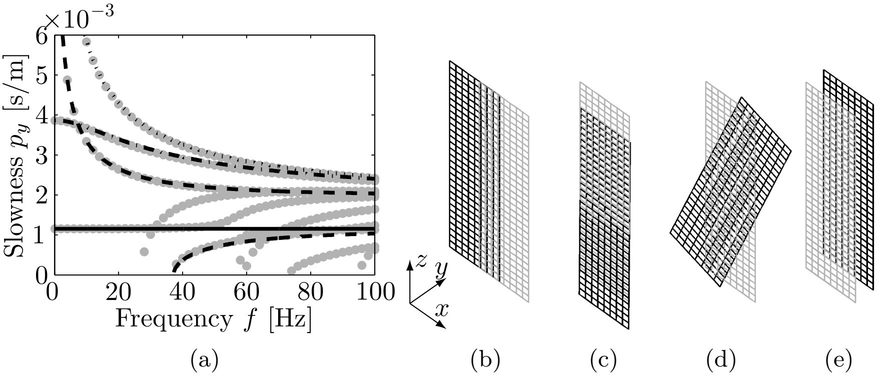

Figure 3.9: (a) Dispersion curves for the single stiff wall (with a width of 2 m and a height of 7.5 m). Dispersion curves computed from equation (3.50) are indicated with gray dots. The analytically calculated dispersion curves are superimposed: the longitudinal mode (solid line), Timoshenko's bending mode around the x-axis (dashed line), Timoshenko's bending mode around the z-axis (dotted line), and Barr's torsion mode (dashed-dotted line). The associated modes at $f \approx 0$ Hz (from high to low value of p_y) are displayed for (b) the shear-bending mode around the z-axis, (c) the shear-bending mode around the x-axis, (d) the torsion mode, and (e) the longitudinal mode.

where A is the area of the cross section, ρ is the mass density, and E is Young's modulus of the beam. For the bending waves, Timoshenko's theory leads to the following dispersion relation [163]:

$$-\rho A\omega^2 + EIk_y^4 - \rho I\left(1+\frac{E}{\kappa G}\right)\omega^2 k_y^2 + \frac{\rho^2 I}{\kappa G}\omega^4 = 0 \tag{3.52}$$

with I the moment of inertia, G the shear modulus of the beam, and κ the shear coefficient. For rectangular solid beams, $\kappa = 10(1+\nu)/(12+11\nu)$ [54]. The dispersion relation for the torsional waves can be described by Barr's theory [15]:

$$\begin{aligned} &-\rho I_\mathrm{p}\omega^2 + GI_\mathrm{t}k_y^2 - \rho I_\phi \frac{I_\mathrm{p}}{I_\mathrm{p}-I_\mathrm{t}}\left(\kappa' + \frac{E}{G}\right)\omega^2 k_y^2 + EI_\phi\kappa'\frac{I_\mathrm{p}}{I_\mathrm{p}-I_\mathrm{t}}k_y^4 \\ &+\rho^2\frac{I_\phi}{G}\frac{I_\mathrm{p}}{I_\mathrm{p}-I_\mathrm{t}}\omega^4 = 0 \end{aligned} \tag{3.53}$$

In this equation, I_p is the polar second moment of inertia, I_t is the torsion constant and I_ϕ is the warping constant. The non-dimensional parameter κ' adjusts the wave velocity to the Rayleigh wave velocity at zero wavelength [154] and is equal to 0.84 for $\nu = 0.25$. These dispersion curves are plotted in figure 3.9 as well, and clearly correspond with the dispersion curves found by solving equation (3.50).

Since the loading is vertical, it is mainly the bending mode around the x-axis which is activated and therefore determines the mitigation mechanism of the wall barrier. When the wavenumber k_y exceeds the free bending dispersion curve k_{b} of the barrier, which corresponds to a trace wavelength λ_y smaller than the bending wavelength λ_{b}, the bending stiffness of the barrier will hinder the wave transmission [53].

Insertion loss in the frequency-wavenumber domain Since the calculations are performed in the frequency-wavenumber domain, the insertion loss in a point can easily be plotted as a function of the frequency f and the longitudinal slowness $p_y = k_y/\omega$. This is done in figure 3.10 for both the single and double wall barrier.

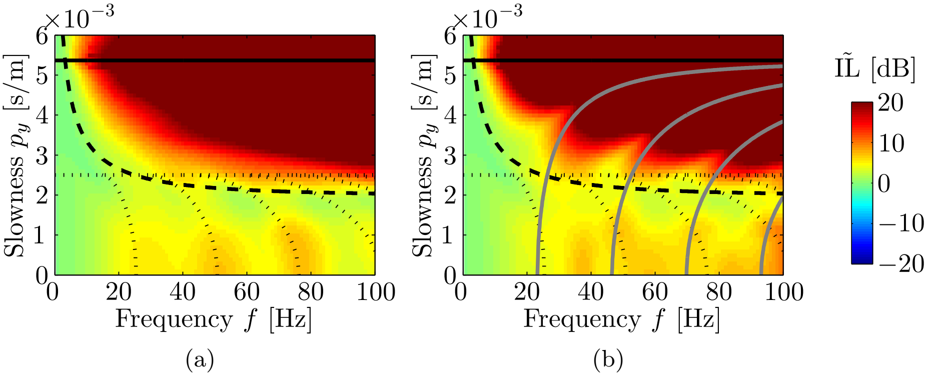

Figure 3.10: Insertion loss $\tilde{\mathrm{IL}}(x = 15\,\mathrm{m}, k_y, z = 0\,\mathrm{m}, \omega)$ for (a) the single stiff wall barrier (wall thickness $2t_w = 2\,\mathrm{m}$) and (b) the double stiff wall barrier (wall thickness $t_w = 1\,\mathrm{m}$ and spacing $d = 4\,\mathrm{m}$) in sandy soil. Superimposed are the analytical dispersion curve for Timoshenko's bending mode around the x-axis (black dashed line), the Rayleigh wave slowness (black solid line), and the frequency-slowness curves which show the phase shift between wave fronts in the reference case and in the case of stiffening (black dotted lines). For the double wall barrier, the dispersion curves caused by the standing waves between the walls are added (gray solid lines).

When the longitudinal wavenumber k_y exceeds the Rayleigh wavenumber k_{R}, corresponding to a slowness $p_{\mathrm{R}} = 1/C_{\mathrm{R}} = 5.37 \times 10^{-3}\,\mathrm{s/m}$, the lateral wavenumber $k_x = \sqrt{k_\mathrm{R}^2 - k_y^2}$ is imaginary and the wave in the x-direction becomes evanescent. Consequently, the free field response is very small for these wavenumbers. Therefore, an upper limit of 6×10^{-3} s/m is considered for the slowness p_y shown in figure 3.10.

Since the P-wave travels faster in the stiffer wall barrier than in the surrounding soil, there is a phase shift between wave fronts in the reference case and in the case with the wall barrier for slownesses up to the P-wave slowness, $p_\mathrm{p} = 1/C_\mathrm{p} = 2.5 \times 10^{-3}\,\mathrm{s/m}$. This phase shift can be expressed for $n = 0 \cdots \infty$ by [53]:

$$\left(\sqrt{k_{\mathrm{R}1}^2 - k_y^2} - \sqrt{k_{\mathrm{p}1}^2 - k_y^2}\right)\Delta x - \omega \frac{w}{C_{\mathrm{p}2} - C_{\mathrm{p}1}} = 2\pi n \tag{3.54}$$

where w is the thickness of the wall barrier (equal to $2t_w$) and Δx the distance between source and receiver (equal to 15 m).

In figure 3.10, the dispersion curve for the bending mode around the x-axis is superimposed. As the bending stiffness around the x-axis is proportional to the width of the barrier, the single and the double wall barrier both have the same bending stiffness. Therefore, the free bending dispersion curves of both barriers coincide. The insertion losses become very high when the slowness p_y exceeds the value p_b corresponding to free bending waves around the x-axis of the barrier, or, reciprocally, for wavelengths λ_y smaller than the bending wavelength λ_b. The wave transmission is then dominated by the stiffness of the wall, resulting in a reduction of the displacements. The single and double wall barrier have therefore the best performance at receiver points located at larger distances y along the barrier, as was indicated before.

3.5.2 Reflection

Standing waves The insertion loss in the frequency-slowness domain (figure 3.10) is similar for the single and the double wall barrier. However, there are frequency-slowness pairs for which the insertion loss for the double wall barrier is smaller. For these frequency-wavenumber pairs, standing waves occur in the space between the two walls as a result of constructive and destructive interference of surface waves. This leads to an increase of the transmitted wave field, as in the case of cavity resonance in building acoustics [70].

Standing waves appear when the distance between the two walls is equal to an integer (m) multiple of half the wavelength in the x-direction:

$$d = \frac{m\lambda_x}{2} = \frac{m\pi}{k_x} = \frac{mC_\mathrm{R}}{2f\cos\theta} \tag{3.55}$$

Here, use is made of the relation $k_x = k_\mathrm{R}\cos\theta$ (figure 3.11). After reformulation, where use is made of the relation $\sin\theta = k_y/k_\mathrm{R}$, the (positive) dispersion relation for the standing waves becomes:

$$k_y = k_\mathrm{R}\sqrt{1 - \left(\frac{mC_\mathrm{R}}{2df}\right)^2} \tag{3.56}$$

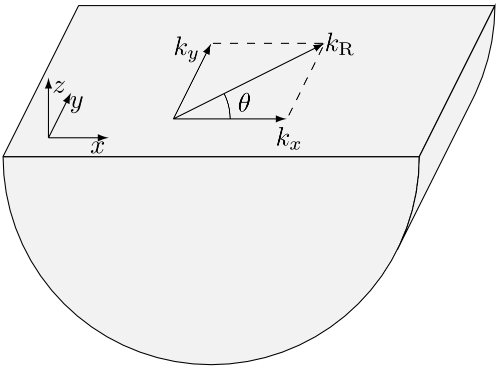

Figure 3.11: Definition of the wavenumber components for Rayleigh waves.

These dispersion relations are superimposed in figure 3.10b. The cut-on frequencies f_co, i.e. the frequencies for which $k_y = 0$, are given by:

$$f_\mathrm{co} = \frac{mC_\mathrm{R}}{2d} \tag{3.57}$$

Values of the first cut-on frequency f_co lower than 100 Hz are only found for distances d larger than $C_\mathrm{R}/(2 \times 100\,\mathrm{Hz}) = 0.93\,\mathrm{m}$. For smaller distances, there are no standing waves in the frequency range considered. For increasing frequency, or decreasing wavelength, the wavenumber k_y approaches the Rayleigh wavenumber $k_\mathrm{R} = \omega/C_\mathrm{R}$.

The frequency-wavenumber pairs in figure 3.10b where the insertion loss is small, indeed correspond to the dispersion relation for standing waves. This explains the weaker performance of the double wall barrier for $y = 15\,\mathrm{m}$ (figure 3.6f), as the stiffness effect is affected by the standing waves.

Influence of the geometry Although in building acoustics, the double walls perform much better between the mass-spring-mass resonance and the first cavity resonance, this does not seem to be the case for double wall barriers in soil. However, the one-dimensional analysis in chapter 2 showed a clear improvement for multiple wave barriers as a result of stopbands. The location of these stopbands depends on the wave velocities of the considered materials and the thickness of the different layers (equation (2.52)). The analysis of section 3.4 has therefore been repeated for multiple values of the wall thickness t_w and the spacing d between the walls.

Figure 3.12 shows the amplitude of the vertical displacement and the insertion loss (equation (3.48)) at receiver 1 (defined in figure 3.2) for multiple values of the wall thickness t_w and the spacing d between the walls. For a small wall thickness ($t_w = 0.5\,\mathrm{m}$), the insertion loss for a double wall is similar to the insertion loss for the single wall and the results are relatively insensitive to the spacing d between the walls. Since the wall thickness t_w of each wall is small compared to the wavelength of the transmitted wave, the performance of the wall barrier is mainly determined by its bending stiffness around the x-axis, which is the same for the single and double wall. For a wall thickness $t_w = 1\,\mathrm{m}$, the performance of the single and double wall barriers improves as a larger thickness implies a larger stiffness of the barriers. The difference in performance between the single and double wall barrier is, however, still hardly significant. For a wall thickness $t_w = 2\,\mathrm{m}$, a larger difference between the performance of the single wall barrier and double wall barrier is observed. At some frequencies, the performance is considerably better than for a single wall barrier. The distance between the walls clearly influences the performance.

The insertion loss for the single and double wall barrier is plotted in the frequency-slowness domain in figure 3.13 for a wall thickness $t_w = 2\,\mathrm{m}$ and a spacing $d = 4\,\mathrm{m}$ between the walls. The insertion loss for slownesses p_y above the slowness p_b corresponding to free bending waves around the x-axis of the barrier is similar for the single and double wall barrier, except for the decreased insertion losses due to the standing wave phenomenon. For small values of the slowness p_y, however, higher insertion losses are observed for the double wall barrier. The barrier's performance for a line load, corresponding to $p_y = 0\,\mathrm{s/m}$, is therefore analyzed.

In figure 3.14, the insertion loss computed for a line load is compared with the insertion loss computed for a point load. The displacements for the line load are obtained using equation (3.30) where the longitudinal wavenumber k_y is set to 0. The insertion losses obtained in both cases are similar. At low frequencies, the difference between the performance of single and double barriers is rather small. At higher frequencies, where the difference in performance becomes significant, the depth of the wall is large compared to the penetration depth of the incoming Rayleigh wave and the wave propagation is determined by reflection. Reflection plays a role for depths larger than 0.6 times the Rayleigh wavelength [27], i.e. for frequencies above 14.9 Hz. For higher frequencies, it can

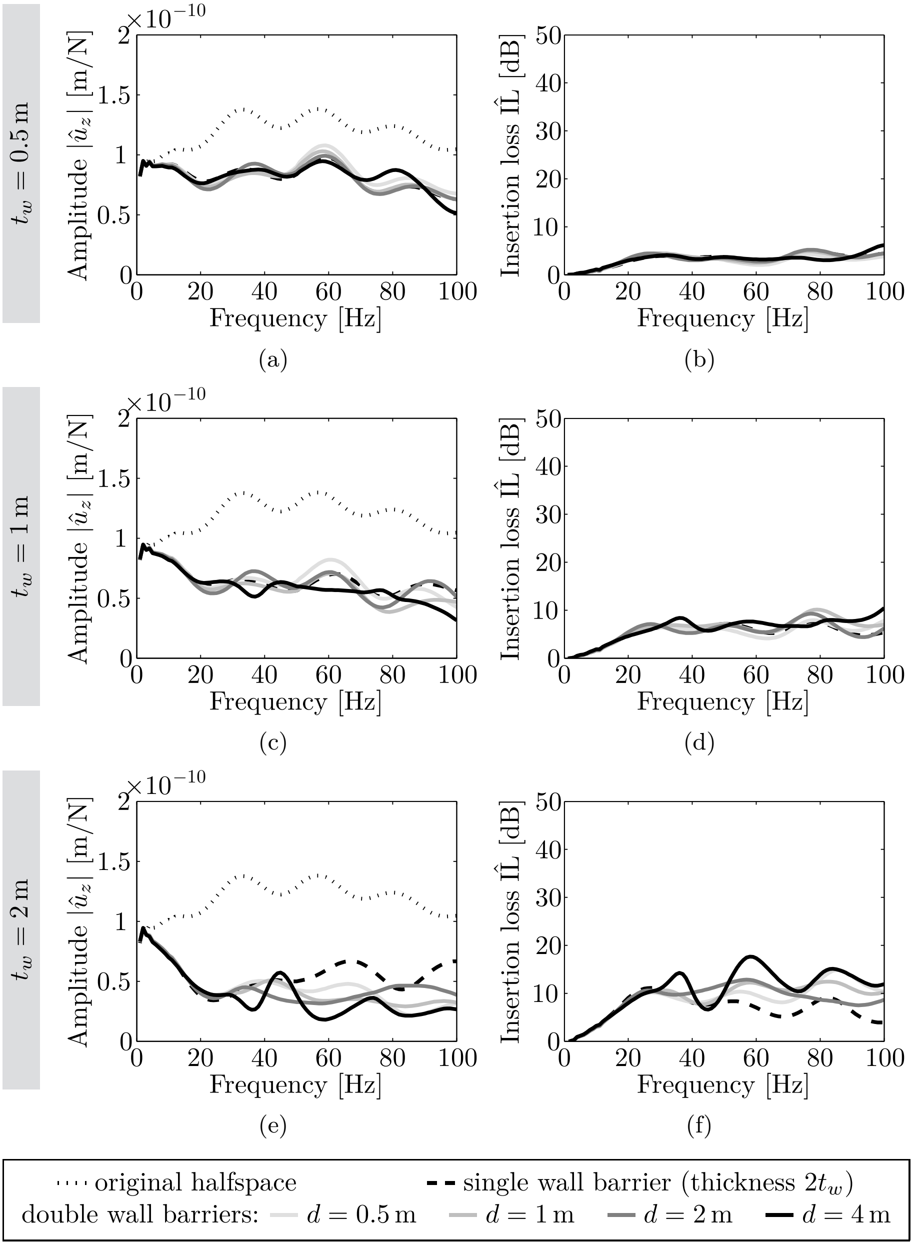

Figure 3.12: Amplitude of the vertical displacement $\hat{u}_z$ and insertion loss $\hat{\mathrm{IL}}$ at receiver 1 (figure 3.2) resulting from a point load for a wall thickness t_w of (a)-(b) 0.5 m, (c)-(d) 1 m, and (e)-(f) 2 m in sandy soil. For the original halfspace, the amplitude is shown with a dotted line, for the single stiff wall barrier (wall thickness $2t_w$) with a dashed line. The results are plotted for different distances d between the walls: 0.5 m, 1 m , 2 m, and 4 m (from light gray to black solid lines).

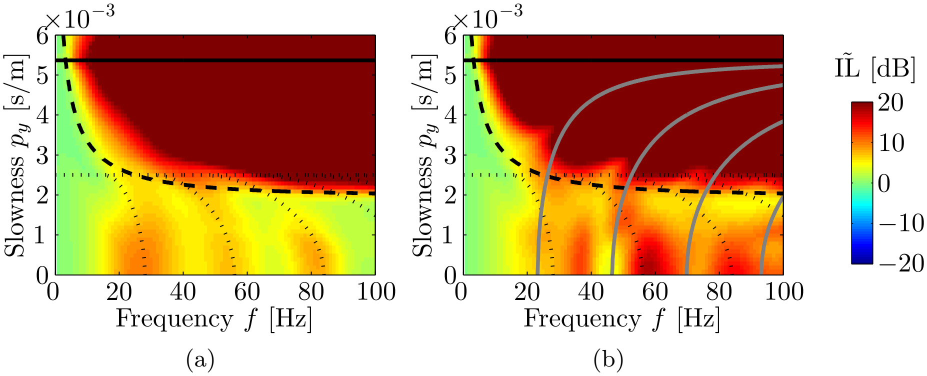

(a) (b)

Figure 3.13: Insertion loss $\tilde{\mathrm{IL}}(x = 15\,\mathrm{m}, k_y, z = 0\,\mathrm{m}, \omega)$ for (a) the single stiff wall barrier (wall thickness $2t_w = 2\,\mathrm{m}$) and (b) the double stiff wall barrier (wall thickness $t_w = 2\,\mathrm{m}$ and spacing $d = 4\,\mathrm{m}$) in sandy soil. Superimposed are the analytical dispersion curve for Timoshenko's bending mode around the x-axis (black dashed line), the Rayleigh wave slowness (black solid line), and the frequency-slowness curves which show the phase shift between wave fronts in the reference case and in the case of stiffening (black dotted lines). For the double wall barrier, the dispersion curves caused by the standing waves between the walls are added (gray solid lines).

therefore be expected that an equivalent one-dimensional model of the wave transmission can give insight in the interpretation of the response due to a line and point load. A one-dimensional equivalent model furthermore allows to verify the similarity with double wall behavior in acoustics.

The equivalent one-dimensional model shown in figure 3.15 is used. The model consists of a homogeneous full space which is intersected by a (double) wall barrier. An incoming wave with amplitude I arrives at the wall barrier and is partly reflected (R) and partly transmitted (T). The insertion loss $\hat{\mathrm{IL}}_{1\mathrm{D}}$ is calculated as:

$$\hat{\mathrm{IL}}_{1\mathrm{D}} = 20 \log_{10} \left| \frac{I}{T} \right| \tag{3.58}$$

where the amplitude T of the transmitted wave field is calculated with the direct stiffness method.

The acoustic and elastodynamic performance of the double wall is investigated by considering two different background media: air and sandy soil. In the first case, the double wall barrier is situated into air, with a wave velocity C_1 of $340\,\mathrm{m/s}$ and a mass density ρ_1 of $1.2\,\mathrm{kg/m^3}$. A damping ratio of 2.5% is assumed. The material properties of the double wall barrier are given in

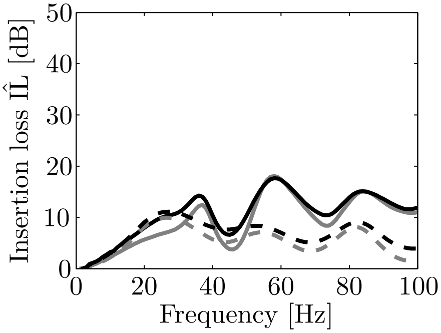

Figure 3.14: Insertion loss $\hat{\mathrm{IL}}$ at receiver 1 (figure 3.2) for the single stiff wall barrier (dashed line; wall thickness $2t_w = 2\,\mathrm{m}$) and the double stiff wall barrier (solid line; wall thickness $t_w = 2\,\mathrm{m}$ and spacing $d = 4\,\mathrm{m}$) in sandy soil, for both a point load (2.5D model, black line) and line load (2D model, gray line).

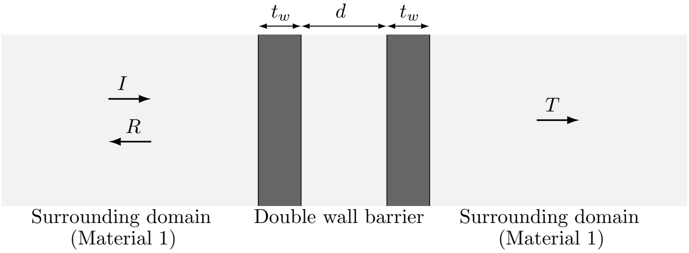

Figure 3.15: The one-dimensional wave propagation problem with a double wall barrier.

table 3.1. In the one-dimensional model, only the wave velocity in the direction of the wave transmission plays a role. In order to enable a comparison with the results of the second case, the Rayleigh wave velocity of the barrier is used in the model. The results are shown in figure 3.16 for both the single and double wall barrier.

For the single wall with a thickness $2t_w$, the well-known mass-law applies [56], which can be written as:

$$\hat{\mathrm{IL}}_{\mathrm{1D}} = 10\log_{10}\left[1 + \left(\frac{\omega\rho_2 t}{\rho_1 C_1}\right)^2\right] \approx 20\log_{10}\left(\frac{\omega\rho_2 t}{\rho_1 C_1}\right) \tag{3.59}$$

where a subscript 1 stands for the air and the subscript 2 stands for the wall. This relation gives an increase of the insertion loss $\hat{\mathrm{IL}}_{\mathrm{1D}}$ by 6 dB per octave band.

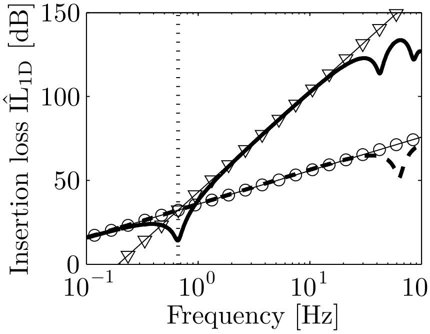

Figure 3.16: Insertion loss $\hat{\mathrm{IL}}_{\mathrm{1D}}$ for the one-dimensional problem as a function of the frequency in the case of the single stiff wall barrier (dashed line; wall thickness $2t_w = 2\,\mathrm{m}$) and the double stiff wall barrier (solid line; wall thickness $t_w = 2\,\mathrm{m}$ and spacing $d = 4\,\mathrm{m}$) in air. Superimposed are the mass law (thin line with circles), the value of the resonance frequency (dotted vertical line), and the theoretical values for frequencies above this frequency (thin line with triangles).

At low frequencies, the performance of the double wall (with spacing $d = 4\,\mathrm{m}$) is similar. However, from a certain frequency onwards, the two performances diverge. This frequency is the double wall resonance frequency f_0, which can be calculated by considering two masses connected by a spring [70]:

$$f_0 = \frac{1}{2\pi}\sqrt{\frac{\rho_1 C_1^2}{d}\frac{2}{\rho_2 t}} \tag{3.60}$$

For frequencies above the double wall resonance frequency, the performance is theoretically approximated by [70]:

$$\hat{\mathrm{IL}}_{\mathrm{1D}} \approx 20\log_{10}\left[\frac{\omega^3 d\rho_2^2 t_w^2}{2\rho_1^2 C_1^3}\right] \tag{3.61}$$

which corresponds to an increase of 18 dB per octave band. The double wall therefore performs better as compared to a single wall with the same total thickness ($2t_w$). This is the so-called double wall phenomenon [70]. At higher frequencies, cavity resonance appears, adversely affecting the performance, which is still better, however, than for the single wall.

In soil, the physics are different however. This is illustrated by considering again the problem in figure 3.15, with the properties in table 3.1 for both the wall barrier and the surrounding soil. The wave velocities corresponding to the Rayleigh waves in the three-dimensional case are used in this equivalent one-dimensional model. The resulting performance is shown in figure 3.17 for both the single and double wall barrier.

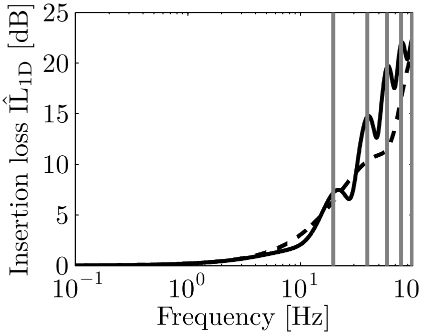

Figure 3.17: Insertion loss $\hat{\mathrm{IL}}_{\mathrm{1D}}$ for the one-dimensional problem as a function of the frequency in the case of the single stiff wall barrier (dashed line; wall thickness $2t_w = 2\,\mathrm{m}$) and the double stiff wall barrier (solid line; wall thickness $t_w = 2\,\mathrm{m}$ and spacing $d = 4\,\mathrm{m}$) in sandy soil. Superimposed are the stopband frequencies in equation (2.52) (gray lines).

For the single wall barrier, the insertion loss is very low at low frequencies. For higher frequencies, the insertion loss goes up to 21 dB at 100 Hz. Therefore, the insertion loss is much lower than for the wall barrier located in air. Furthermore, the performance of the single wall does not follow the mass law as it depends on the impedance ratio for the original soil and the wall barrier and on the wave velocity in and the thickness of the wall barrier.

Similarly, also the double wall barrier behaves differently in soil. The insertion loss goes up to 22.5 dB at 100 Hz and therefore exceeds the insertion loss for single wall barriers at higher frequencies. Moreover, larger values are observed at particular frequencies, where less energy is transmitted, caused by the stopband phenomenon for multiple wave barriers described in chapter 2. The location of the stopbands can be predicted using equation (2.52). These frequencies are superimposed in figure 3.17 and correspond well with the maxima found in the insertion loss for the one-dimensional problem. Note that the insertion loss does not go to zero in between the stopbands, due to the effect of material damping (not considered in chapter 2).

Table 3.2 compares these stopband frequencies with the local maxima observed in the insertion loss for the different models (1D, 2D, and 2.5D). A good agreement is found between the different models for the local maxima in the insertion loss. Although no local maximum is found beneath 37 Hz for the 2.5D model, the insertion loss in figure 3.14 shows a change in curvature around 21 Hz, indicating an increase resulting from this stopband effect.

Table 3.2: Theoretical frequencies calculated with equation (2.52) compared with local maxima in the insertion loss for respectively the 1D, 2D, and 2.5D model.

Stopband frequencies f_{stop}	Local maxima 1D	Local maxima 2D	Local maxima 2.5D
20 Hz	21 Hz		
39 Hz	40 Hz	36 Hz	37 Hz
59 Hz	60 Hz	58 Hz	58 Hz
79 Hz	80 Hz	84 Hz	84 Hz

The influence of the geometry can thus be explained using the one-dimensional model. Figure 3.18 shows the insertion loss for the one-dimensional problem for wall thicknesses $t_w \in [0,3]$ and spacings $d \in [0,4]$ at three different frequencies: 20 Hz, 40 Hz, 60 Hz, and 80 Hz. The lines corresponding to $k_1 d + k_2 t_w = n\pi$ for $n = 1, 2, \ldots$, which indicate for which geometries the center location of a stopband is situated at this frequency, are superimposed. For the considered frequencies, these lines more or less intersect the point with $t_w = 2\,\mathrm{m}$ and $d = 4\,\mathrm{m}$.

For each frequency, there are local optima at certain thickness-distance pairs. At these optima, the thickness of the walls (t_w) and the intermediate soil (d) are equal to a quarter of the Rayleigh wavelength ($p = 1 \cdots \infty$, $q = 1 \cdots \infty$):

$$\begin{cases} t_w^{\mathrm{opt}} = \dfrac{(2p-1)\lambda_{\mathrm{R2}}}{4} = \dfrac{(2p-1)C_{\mathrm{R2}}}{4f} \\ d^{\mathrm{opt}} = \dfrac{(2q-1)\lambda_{\mathrm{R1}}}{4} = \dfrac{(2q-1)C_{\mathrm{R1}}}{4f} \end{cases} \tag{3.62}$$

At 20 Hz, the optimal geometry consists of $t_w^{\mathrm{opt}} = (2p-1) \times 6.3\,\mathrm{m}$ and $d^{\mathrm{opt}} = (2q-1) \times 2.3\,\mathrm{m}$. Since the optimal thickness t_w^{opt} is much larger than the maximum value of 2 m considered in the 2.5D computation, the quarter wave-stack condition cannot be satisfied for low frequencies, and the geometry has only a small effect on the insertion loss. At 40 Hz, the optimal geometry consists of $t_w^{\mathrm{opt}} = (2p-1) \times 3.1\,\mathrm{m}$ and $d^{\mathrm{opt}} = (2q-1) \times 1.2\,\mathrm{m}$. A large thickness is again needed for the optimal geometry, but the 2.5D layout with $t_w = 2\,\mathrm{m}$ and $d = 4\,\mathrm{m}$ in figure 3.12 is located closer to a quarter wave-stack geometry, resulting in a higher improvement in the performance than at 20 Hz. At 60 Hz, the optimal geometry consists of $t_w^{\mathrm{opt}} = (2p-1) \times 2.1\,\mathrm{m}$ and $d^{\mathrm{opt}} = (2q-1) \times 0.8\,\mathrm{m}$. For

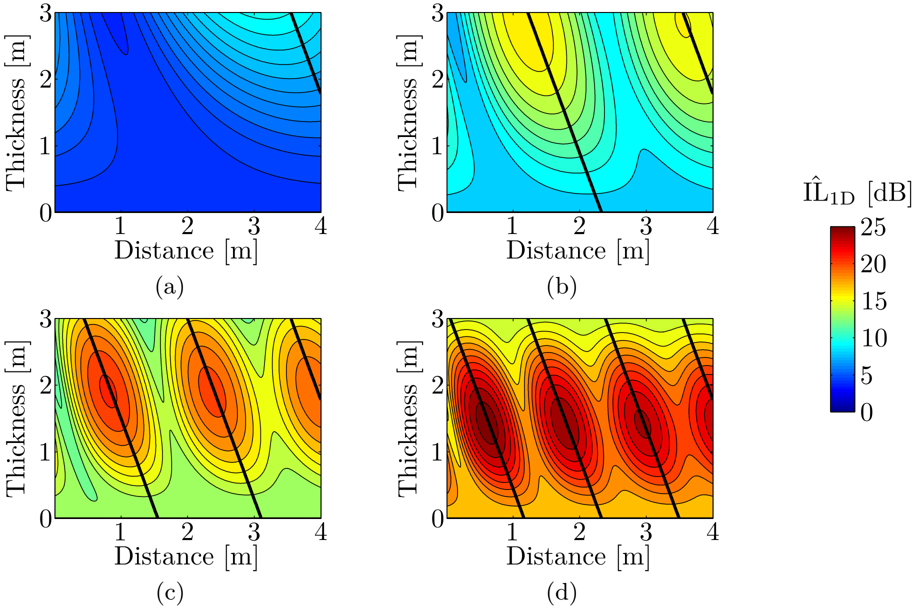

(a) (b) (c) (d)

Figure 3.18: Insertion loss for the one-dimensional problem $\hat{\mathrm{IL}}_{\mathrm{1D}}$ as a function of the wall thickness t_w and the distance d between the walls in the case of the double stiff wall barrier in sandy soil at (a) 20 Hz, (b) 40 Hz, (c) 60 Hz, and (d) 80 Hz. The lines corresponding to $k_1 d + k_2 t_w = n\pi$ for $n = 1, 2, \ldots$ are superimposed.

$p = 1$ and $q = 3$, we have an optimal wall thickness $t_w^{\mathrm{opt}} = 2.1\,\mathrm{m}$ and an optimal spacing $d^{\mathrm{opt}} = 3.9\,\mathrm{m}$. This geometry is close to the 2.5D layout with $t_w = 2\,\mathrm{m}$ and $d = 4\,\mathrm{m}$, where a high value was found at 60 Hz. At 80 Hz, the optimal parameters become $t_w^{\mathrm{opt}} = (2p - 1) \times 1.6\,\mathrm{m}$ and $d^{\mathrm{opt}} = (2q - 1) \times 0.6\,\mathrm{m}$. For $p = 1$ and $q = 4$, we have an optimal wall thickness $t_w^{\mathrm{opt}} = 1.6\,\mathrm{m}$ and an optimal spacing $d^{\mathrm{opt}} = 4.1\,\mathrm{m}$, again rather close to the 2.5D layout with $t_w = 2\,\mathrm{m}$ and $d = 4\,\mathrm{m}$.

It is clear that the thickness and the spacing between the walls influence the reflection of incoming waves. For small thicknesses, the quarter wave-stack geometry is only obtained at high frequencies, and the distance between the walls has no large influence. However, for large thicknesses, the quarter wave-stack condition plays an important role and increases the performance of the double wall barrier in the range of interest.

3.6 Influence of the material parameters

Influence of the barrier properties It is now investigated how the performance changes when the jet grouting walls are replaced by concrete slurry walls. The wall has a mass density $\rho = 2500\,\mathrm{kg/m^3}$, a dilatational wave velocity $C_\mathrm{p} = 3795\,\mathrm{m/s}$, a shear wave velocity $C_\mathrm{s} = 2191\,\mathrm{m/s}$, and material damping ratios $\beta_\mathrm{p} = \beta_\mathrm{s} = 2.5\,\%$. A concrete wall thickness t_w of 0.5 m is considered here. The distance between the walls is again $d = 4\,\mathrm{m}$.

Figure 3.19 shows the amplitude of the vertical displacement and the corresponding insertion loss at receiver 1 (defined in figure 3.2). Although the insertion loss has rather large values in both the case of the single and double wall barrier, the double wall barrier does not perform better than the single wall barrier over the frequency range considered. Because of the high stiffness of the wall, a large wall thickness would be needed to satisfy the quarter wave-stack condition in the frequency range.

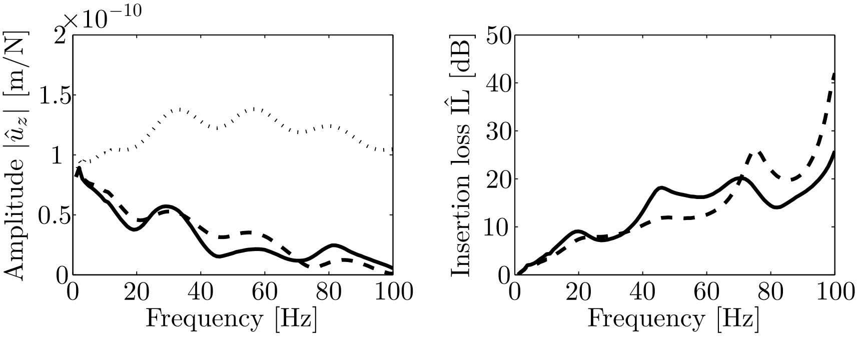

(a) (b)

Figure 3.19: (a) Amplitude of the vertical displacement $\hat{u}_z$ at receiver 1 (figure 3.2) resulting from a point load for the original halfspace (dotted line), the single concrete wall barrier (dashed line; wall thickness $2t_w = 2\,\mathrm{m}$) and the double concrete wall barrier (solid line; wall thickness $t_w = 0.5\,\mathrm{m}$ and spacing $d = 4\,\mathrm{m}$) in sandy soil. (b) Corresponding insertion loss $\hat{\mathrm{IL}}$ at receiver 1 for the single concrete wall barrier (dashed line) and the double concrete wall barrier (solid line) in sandy soil.

In figure 3.20, the insertion loss is shown as a function of the frequency f and the slowness p_y. The insertion loss again has high values above the bending wave dispersion curve, and is for the double wall barrier reduced by the standing waves in between the two walls. Because of the large stiffness of the wall, the bending wave dispersion curve is situated in the lower part of the slowness range, resulting in a high insertion loss caused by the stiffness effect for a large slowness range and therefore in a high insertion loss as observed in figure 3.19.

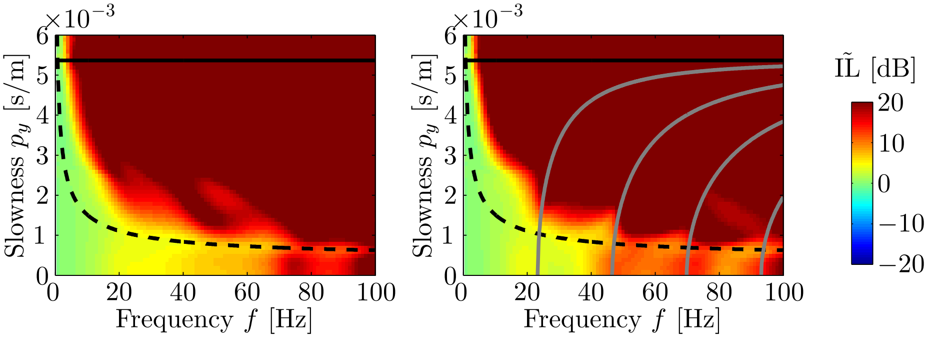

(a) (b)

Figure 3.20: Insertion loss $\tilde{\mathrm{IL}}(x = 15\,\mathrm{m}, k_y, z = 0\,\mathrm{m}, \omega)$ for (a) the single concrete wall barrier (wall thickness $2t_w = 2\,\mathrm{m}$) and (b) the double concrete wall barrier (wall thickness $t_w = 0.5\,\mathrm{m}$ and spacing $d = 4\,\mathrm{m}$) in sandy soil. Superimposed are the analytical dispersion curve for Timoshenko's bending mode around the x-axis (black dashed line) and the Rayleigh wave slowness (black solid line). For the double wall barrier, the dispersion curves caused by the standing waves between the walls are added (gray solid lines).

Influence of the soil properties The effectiveness of the barrier also depends, for given barrier properties, on the material properties of the soil. Consider soft clay, with a mass density $\rho = 2500\,\mathrm{kg/m^3}$, a dilatational wave velocity $C_\mathrm{p} = 120\,\mathrm{m/s}$, a shear wave velocity $C_\mathrm{s} = 60\,\mathrm{m/s}$, and material damping ratios $\beta_\mathrm{p} = \beta_\mathrm{s,conc} = 2.5\,\%$. Figure 3.21 shows the amplitude of the vertical displacement and the insertion loss as a function of the frequency at receiver 1 (defined in figure 3.2). The insertion loss is rather large for the entire frequency range considered.

In figure 3.22, the insertion loss is shown as a function of the frequency f and the slowness p_y. As the soil has a lower Rayleigh wave velocity, there are more standing waves in the frequency range considered. Moreover, the Rayleigh wavenumber k_R increases for a softer soil. As a consequence, the response at the receiver positions is increasingly dominated by the effect of the bending stiffness. This results in an increased performance of the barrier.

To conclude, for a large difference in stiffness between the soil and the barrier, the stiffness effect dominates and the single and double wall barrier have a similar performance. For a smaller difference in stiffness, reflection of incoming

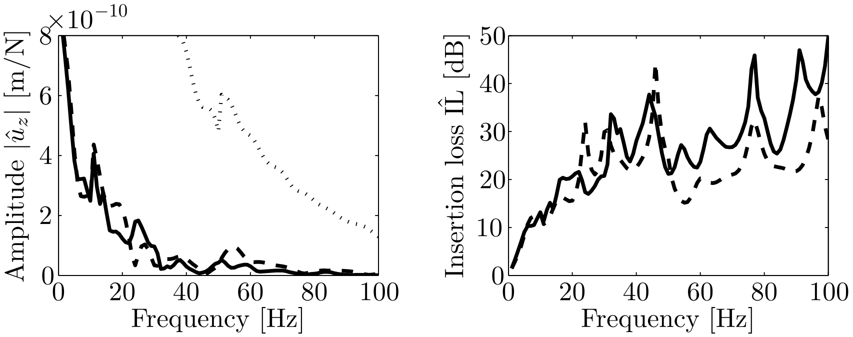

(a) (b)

Figure 3.21: (a) Amplitude of the vertical displacement $\hat{u}_z$ at receiver 1 (figure 3.2) resulting from a point load for the original halfspace (dotted line), the single stiff wall barrier (dashed line; wall thickness $2t_w = 2\,\mathrm{m}$) and the double stiff wall barrier (solid line; wall thickness $t_w = 1\,\mathrm{m}$ and spacing $d = 4\,\mathrm{m}$) in soft clay soil. (b) Corresponding insertion loss $\hat{\mathrm{IL}}$ at receiver 1 for the single stiff wall barrier (dashed line) and the double stiff wall barrier (solid line) in soft clay soil.

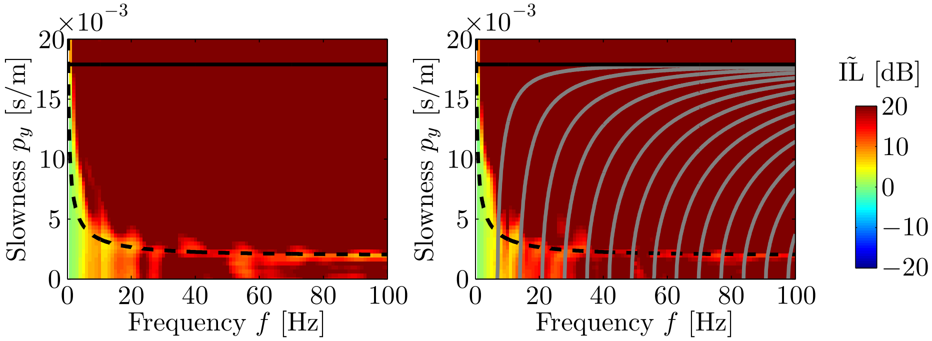

(a) (b)

Figure 3.22: Insertion loss $\tilde{\mathrm{IL}}(x = 15\,\mathrm{m}, k_y, z = 0\,\mathrm{m}, \omega)$ for (a) the single stiff wall barrier (wall thickness $2t_w = 2\,\mathrm{m}$) and (b) the double stiff wall barrier (wall thickness $t_w = 1\,\mathrm{m}$ and spacing $d = 4\,\mathrm{m}$) in soft clay soil. Superimposed are the analytical dispersion curve for Timoshenko's bending mode around the x-axis (black dashed line) and the Rayleigh wave slowness (black solid line). For the double wall barrier, the dispersion curves caused by the standing waves between the walls are added (gray solid lines).

waves becomes more important, and a good choice of the thickness and the distance between the walls improves the performance of the double wall barrier.

3.7 Conclusion

This chapter discussed the performance of double wall barriers. These barriers are located between the source and the receivers to reduce the transmission of environmental ground vibration. A computationally efficient two-and-a-half dimensional finite element method is used, where the three-dimensional wave field is represented on a two-dimensional mesh by using the Fourier transform from the longitudinal coordinate to the wavenumber domain.

A double wall barrier into a homogeneous soil is discussed. This double wall barrier is compared with a single wall barrier with the same volume and depth (7.5 m). A similar insertion loss is found for a simplified train load and a point load located at the closest axle position have a similar insertion loss.

The performance of the single and double wall barriers depends on two phenomena. The first is the stiffness effect, where the bending stiffness of the barrier will hinder wave transmission for trace wavelengths λ_y smaller than the bending wavelength λ_b. For trace wavelengths smaller than the Rayleigh wavelength λ_R, the wave in the x-direction becomes evanescent. The stiffness effect therefore applies for trace wavelengths λ_y between the Rayleigh wavelength λ_R and the bending wavelength λ_b. As the first relates to the stiffness of the soil and the second to the stiffness of the barrier, the response will be dominated by the stiffness effect for large differences between the two stiffnesses.

For low differences between the two stiffnesses, the performance for high trace wavelengths λ_y becomes more important. The performance is then dominated by the second discussed phenomenon: reflection. It was shown that an equivalent one-dimensional model, which was introduced in chapter 2, can be used to assess the reflection effect of the barrier. The stopband phenomenon is again observed, and an optimal performance is found for thicknesses equal to a quarter of the wavelength.

However, large wall thicknesses and distances between the walls are needed to satisfy the quarter wave-stack condition. In the next chapters, topology optimization is used to find novel, improved design geometries.

Chapter 4

Topology optimization for one-dimensional elastic wave propagation

4.1 Introduction

The propagation of plane harmonic waves through a one-dimensional periodic domain was analyzed in chapter 2. Depending on the material properties and the thicknesses of the layers, stop- and passbands may arise. In this chapter, the optimal layer configuration in a finite design domain is investigated. Topology optimization [23] is used to obtain the optimized designs.

The general problem considered in this chapter is shown in figure 4.1. A plane wave is propagating through a full space. It encounters a domain located in the full space that reflects waves. In this design domain, a wave barrier is constructed by inserting layers with material different from the background material. This layered structure is optimized such that the transmittance through the design domain is minimized.

In Hussein et al. [91], one-dimensional periodic cells are designed using genetic algorithms. The use of non-gradient approaches, however, is in this case inefficient since a lot of function evaluations are needed [148]. Lee et al. [114] considered a topology optimization problem optimizing the layout of an acoustical foam consisting of air and poroelastic layers. The transfer matrix method was used to model the wave propagation and the inefficient

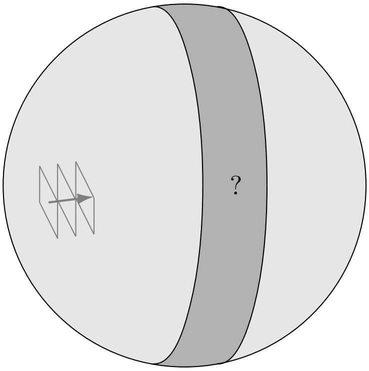

Figure 4.1: General problem: a harmonic wave propagating in a full space encounters the design domain.

finite difference method was used to calculate the sensitivities. The adjoint method was used by Bellido and Donoso [19] for topology optimization of two layers in an elastic rod in the case of harmonic excitation.

The chapter is organized as follows. First, density based topology optimization is introduced in its general form, including regularization techniques, continuation schemes, the derivation of the sensitivities, and the optimization algorithm used. Next, the one-dimensional optimization problem is formulated for three types of excitation and the corresponding results are discussed.

4.2 Topology optimization method

4.2.1 Density based approach

In topology optimization problems, a design domain Ω_{des} is considered where material $\Omega_{\text{ins}} \subset \Omega_{\text{des}}$ is inserted (figure 4.2). Topology optimization simultaneously optimizes the size, shape and topology of the inserted material [23]. The material can be distributed over the entire domain, there can be holes in the inserted design, and the different features of the design are not necessarily connected.

In density based topology optimization, the most widely used approach is

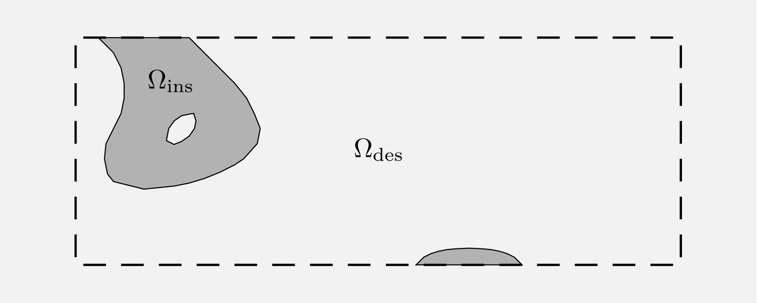

Figure 4.2: Material distribution in a design domain.

the so-called *first discretize, then optimize* strategy [89]. In contrast to the approach where the discretization is performed last, such an approach allows using existing software for solving the partial differential equations (such as finite element or direct stiffness software). Furthermore, mathematical difficulties encountered with the optimization in function spaces are avoided. This approach is therefore also adopted in this work. The discretization of the design variables is most easily done with the same mesh as the one used to solve the partial differential equations.

For each element e in the design domain Ω_{des}, the material distribution is parametrized using element densities ρ_e. The value $\rho_e = 0$ indicates that element e has the properties of the background material, while $\rho_e = 1$ corresponds to the properties of the inserted material:

$$\rho_e = \begin{cases} 0 & \text{if } e \in \Omega_{\text{des}} \setminus \Omega_{\text{ins}} \\ 1 & \text{if } e \in \Omega_{\text{ins}} \end{cases} \tag{4.1}$$

where Ω_{ins} is the domain where material is inserted.

The goal is to distribute the material in the design domain such that the performance of the resulting structure is optimized for particular load cases given some constraints. Solving the optimization problem allows finding the best compromise between the performance and the cost, for example by optimizing the stiffness of a structure for a given amount of material. The topology optimization problem is generally formulated as:

$$\begin{aligned} \min_{\boldsymbol{\rho}} \quad & f\left(\boldsymbol{\rho}, \mathbf{u}\left(\boldsymbol{\rho}\right)\right) \\ \text{s.t.} \quad & \mathbf{h}\left(\boldsymbol{\rho}, \mathbf{u}\left(\boldsymbol{\rho}\right)\right) \leq 0 \\ & \rho_e \in \{0, 1\} \qquad \forall e \in \Omega_{\text{des}} \end{aligned} \tag{4.2}$$

where f is the objective function, $\mathbf{h}$ is the vector of inequality constraints, $\boldsymbol{\rho}$ is the vector containing the design variables ρ_e for $e = 1 \ldots N_e$, and $\mathbf{u}$ are the state variables.

The state variables $\mathbf{u} \in \mathbb{C}^{n^{\mathrm{DOF}}}$ correspond to the displacement vector found with the direct stiffness method or the finite element method (see previous chapters). In general, these state equations have the following form:

$$\mathbf{g}\left(\boldsymbol{\rho}, \mathbf{u}\right) = \mathbf{K}\left(\boldsymbol{\rho}\right)\mathbf{u} - \mathbf{p} = \mathbf{0} \tag{4.3}$$

where $\mathbf{K} \in \mathbb{C}^{n^{\mathrm{DOF}} \times n^{\mathrm{DOF}}}$ is the (dynamic) stiffness matrix, and $\mathbf{p} \in \mathbb{C}^{n^{\mathrm{DOF}}}$ is the load vector. In this work, the load vector is assumed to be independent of the design variables, although this can easily be generalized. Through this equation, the state variables $\mathbf{u}$ are a function of the design variables $\boldsymbol{\rho}$. Alternatively, the state variables $\mathbf{u}$ can be added as optimization variables, with the state equation (4.3) added as constraint to the optimization problem. This is referred to as the simultaneous analysis and design (SAND) approach, whereas the optimization problem presented in equation (4.2) is referred to as the nested approach (sometimes called NAND: nested analysis and design).

The optimization variables in the optimization problem (equation (4.2)) can take only integer values (0 or 1). This integer formulation can for example be solved using so-called hard kill methods where material in an element is added ($\rho_e = 1$) or removed ($\rho_e = 0$). Examples are the Evolutionary Structural Optimization (ESO) [90, 175] and the Bi-directional ESO (BESO) [176] method. This approach has, however, been criticized. Critics include the absence of a relation between the criteria imposed on the different elements and the aimed objective function, doubts about the efficiency, and the difficulties in extending the procedure to other constraints or multi-load problems [138]. In the common density based approach, the discrete optimization problem is transformed into a continuous problem by allowing the design variables ρ_e to vary continuously in the interval $[0, 1]$. The following relaxed problem is solved:

$$\begin{aligned} \min_{\boldsymbol{\rho}} \quad & f\left(\boldsymbol{\rho}, \mathbf{u}\left(\boldsymbol{\rho}\right)\right) \\ \text{s. t.} \quad & \mathbf{h}\left(\boldsymbol{\rho}, \mathbf{u}\left(\boldsymbol{\rho}\right)\right) \leq 0 \\ & 0 \leq \rho_e \leq 1 \qquad \forall e \in \Omega_{\mathrm{des}} \end{aligned} \tag{4.4}$$

This problem is much more easily solved with available optimization methods, as gradient-based methods can be applied.

The displacement vector $\mathbf{u}$ is solved from equation (4.3), in which the stiffness matrix $\mathbf{K}$ depends on the material parameters α of the problem (mass density, Young's modulus, constrained modulus, shear modulus, wave velocity, impedance, etc.). The considered parameter α should be equal to the property

α_{ref} of the background material if $\rho_e = 0$ and equal to the property α_{ins} of the inserted material if $\rho_e = 1$. Since the relaxed problem in equation (4.4) is solved, the design variable ρ_e can take all real values between 0 and 1. A material interpolation scheme is therefore needed to relate the material parameters to the intermediate design variables.

The simplest material interpolation is a linear interpolation between the properties of the two materials:

$$\alpha = (1 - \rho_e)\,\alpha_{\text{ref}} + \rho_e \alpha_{\text{ins}} = \alpha_{\text{ref}} + \rho_e\,(\alpha_{\text{ins}} - \alpha_{\text{ref}}) \tag{4.5}$$

This often leads to gray designs, however, where there are regions with intermediate design variables, i.e. design variables with values not close to 0 or 1. The corresponding intermediate material parameters have no physical interpretation (except for some advanced composite materials) and are therefore unwanted. In topology optimization, the so-called Solid Isotropic Material with Penalization (SIMP) approach [22, 139] is often used, where intermediate densities are made less favorable by reducing their relative cost-efficiency. For structural optimization, the material interpolation is often done between a void phase ($\alpha_{\text{ref}} = 0$) and a material phase ($\alpha_{\text{ins}} \neq 0$), and the SIMP interpolation has the form $\alpha = \rho_e^p \alpha_{\text{ins}}$ with $p > 1$ the penalization parameter. This is generalized here for a two-material optimization:

$$\alpha = \alpha_{\text{ref}} + \rho_e^p\,(\alpha_{\text{ins}} - \alpha_{\text{ref}}) \tag{4.6}$$

This interpolation function is shown in figure 4.3 for $p = 3$. Over the entire interval $(0, 1)$, the curve lies below the linear interpolation curve. For intermediate densities ρ_e, the material parameters α are close to those of the background material α_{ref}. The performance is therefore hardly changed, while the cost, which is often related to the volume and therefore proportional to the sum of the design variables ρ_e, increases. It is therefore not efficient to add material with intermediate design variables, leading to more 0/1 designs. Note however, that this interpolation only works when a volume constraint is active.

For two-material problems, the following interpolation function is often used [23]:

$$\alpha = (1 - \rho_e)^p\,\alpha_{\text{ref}} + \rho_e^p \alpha_{\text{ins}} \tag{4.7}$$

This interpolation function is shown in figure 4.3 as well for $p = 3$. It is clear that for static optimization problems, for which often a higher stiffness leads to a better performance, the design variables will be pushed to the extremes, i.e. $\rho_e = 0$ and $\rho_e = 1$.

However, for the problems considered in this work, not only stiffness, but also impedance plays a role. In chapter 2, it was shown that the impedance

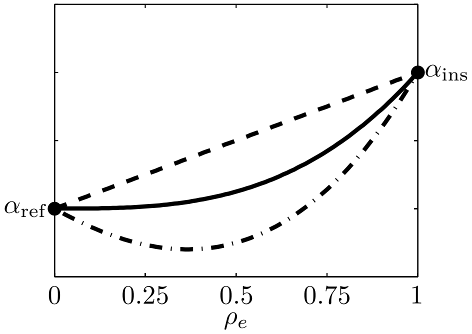

Figure 4.3: Different material interpolations: linear interpolation (dashed line), SIMP interpolation (solid line) and classical two-material interpolation (dashed-dotted line) for a value $p = 3$ of the penalization parameter.

ratio determines the transmission and reflection at an interface. A higher impedance ratio reduces the transmission through a layer. When equation (4.7) is used as interpolation for material properties that are proportional to the mass density or the wave velocity, the optimization will result in a gray layer ($0 < \rho_e < 1$) between the white ($\rho_e = 0$) and black ($\rho_e = 1$) regions, as the impedance ratio between the materials in the black and gray region are larger than the impedance ratio between the materials in the black and white region (figure 4.3).

The classical two-material interpolation scheme in equation (4.7) is therefore not used in this work. In general, linear interpolation (equation (4.5)) is used for material parameters that determine the mass (such as the mass density ρ), and the SIMP interpolation in equation (4.6) is used for parameters that determine the stiffness (such as the constrained modulus ρC_{p}^2 and the shear modulus ρC_{s}^2). Unless stated otherwise, the penalization parameter p is set to 3. However, when the performance is only determined by the difference in impedance, more particularly for the one-dimensional wave propagation problem considered in this chapter, the linear interpolation in equation (4.5) is used, as the difference in impedances pushes the design variables to a 0/1 design. The phenomenon where 0/1 designs are obtained without penalization is in the literature referred to as self-penalization. This is for example observed in the case of piezoelectric composites [173], and is found for the optimization problems considered in this chapter.

4.2.2 Regularization techniques and continuation schemes

Topology optimization has some classical numerical issues, such as mesh dependency, meaning that the solution depends on the level of discretization, and checkerboarding, which concerns the formation of adjacent black and white elements arranged in checkerboard patterns due to the artificial stiffness given to these patterns e.g. by the finite element model [150]. To prevent these numerical issues in topology optimization and to restrain the complexity of the final design, the densities or sensitivities are controlled with regularization techniques [59].

Two classes of regularization techniques can be distinguished: constraint and filtering techniques. The latter is the most popular largely due to its ease of implementation. Filtering techniques are also used in this text as they allow formulating the robust topology optimization problem considered in section 5.3. Most common are the density [30, 36] and sensitivity [150] filter, which modify the density or sensitivity of an element based on the densities or sensitivities of the neighbouring elements. Filters based on the solution of Helmholtz-type differential equations were also developed [105, 112]. These filters reduce computational requirements as no neighbourhood information has to be computed and stored.

In density filtering, the physical material distribution is represented by a new field of variables $\tilde{\rho}_e$ which are obtained by smoothing the design variables ρ_e:

$$\tilde{\rho}_e = \frac{\sum_{i=1}^{N_e} w_{ei} v_i \rho_i}{\sum_{j=1}^{N_e} w_{ej} v_j} \tag{4.8}$$

where v_i is the volume of element i and the filter kernel w_{ei} is typically determined by the following linear conic function:

$$w_{ei} = \max\left(R - r_{ei}, 0\right) \tag{4.9}$$

with R the chosen filter radius, determining the minimum length scale of the optimized design, and r_{ei} the center-to-center distance between elements e and i. The filter kernel w_{ei} is maximal for $i = e$ $(r_{ei} = 0)$ and equal to the filter radius R. For larger distances r_{ei}, the filter kernel decreases linearly with the distance from element e. For elements i at a distance r_{ei} larger than the filter radius R, the filter kernel is zero. For a filter radius smaller than 1 element, the filtered densities $\tilde{\rho}_e$ are equal to the design variables ρ_e.

Although density (and sensitivity) filters efficiently solve the mesh-dependency and checkerboarding, an unwanted consequence of this kind of filtering is the formation of gray transition zones between black and white regions. Several

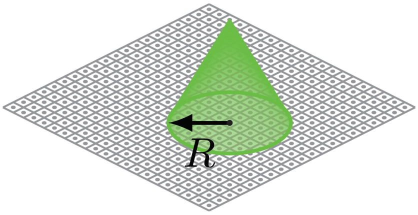

Figure 4.4: Linear conic function used for density filtering [94].

schemes have been developed to resolve this issue by projecting the filtered densities to 0 or 1. These are called projection filters and include morphology-based filters [146] and density filters followed by a Heaviside projection [82]. In this work, the latter are used as the mechanisms causing the 0/1 designs can be interpreted more easily and as they allow defining the robust optimization problem in section 5.3. The physical distribution is again represented by a new field of variables $\bar{\rho}_e$ which are obtained by applying the following Heaviside projection function to the filtered variables $\tilde{\rho}_e$:

$$\bar{\rho}_e = H(\tilde{\rho}_e - \eta) = \begin{cases} 0 & \text{if } \tilde{\rho}_e < \eta \\ 1 & \text{if } \tilde{\rho}_e \geq \eta \end{cases} \tag{4.10}$$

where $H(x)$ is the Heaviside step function and η is the projection threshold.

For gradient based optimization, this function is approximated by a differentiable function. Various approximations of the Heaviside function have been proposed in the literature. In this work, the following relaxed Heaviside projection is used [172]:

$$\bar{\rho}_e = \frac{\tanh(\beta\eta) + \tanh(\beta(\tilde{\rho}_e - \eta))}{\tanh(\beta\eta) + \tanh(\beta(1-\eta))} \tag{4.11}$$

where β is a sharpness parameter, controlling the smoothness of the projection, and the densities $\tilde{\rho}_e$ are obtained from equation (4.8). This expression for the relaxed Heaviside projection is shorter, simpler, and faster to compute compared to alternative expressions proposed in the literature [172]. Figure 4.5 shows this relaxed Heaviside projection for $\eta = 0.5$ and for different values of the sharpness parameter β. Increasing the sharpness parameter β results in a better approximation of the Heaviside step function, but also significantly increases the nonlinearity of the function. As a rule of thumb for determining a value for the sharpness parameter β, the projected design should contain one layer of gray elements between the white and black regions.

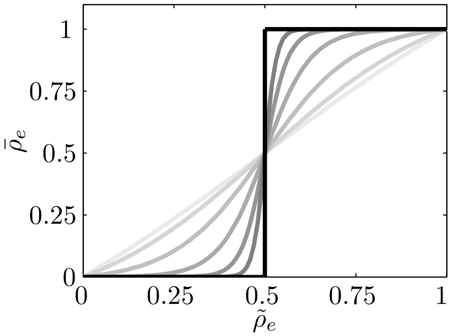

Figure 4.5: Approximate Heaviside projection function based on equation (4.11) for $\eta = 0.5$ and for different values of β: 1, 2, 4, 8, 16, and 32 (light gray to dark gray lines). These are compared with the Heaviside step function from equation (4.10) (black line).

The projected variables represent the physical material distribution. As the objective function and the constraints are defined in terms of the physical material distribution, equation (4.4) becomes:

$$\begin{aligned} \min_{\boldsymbol{\rho}} \quad & f\left(\bar{\boldsymbol{\rho}}, \mathbf{u}\left(\bar{\boldsymbol{\rho}}\right)\right) \\ \text{s.t.} \quad & \mathbf{h}\left(\bar{\boldsymbol{\rho}}, \mathbf{u}\left(\bar{\boldsymbol{\rho}}\right)\right) \leq 0 \\ & 0 \leq \rho_e \leq 1 \qquad\qquad \forall e \in \Omega_{\text{des}} \end{aligned} \tag{4.12}$$

with

$$\mathbf{g}\left(\bar{\boldsymbol{\rho}}, \mathbf{u}\right) = \mathbf{K}\left(\bar{\boldsymbol{\rho}}\right)\mathbf{u} - \mathbf{p} = \mathbf{0} \tag{4.13}$$

where the stiffness matrix $\mathbf{K}$ depends on the element densities through the material parameters α_j, $j = 1 \ldots N_\alpha$. These are given by a linear ($p_j = 1$) or SIMP interpolation of the material properties of the background and inserted material:

$$\alpha_j = \alpha_{j,\text{ref}} + \bar{\rho}_e^{p_j}\left(\alpha_{j,\text{ins}} - \alpha_{j,\text{ref}}\right) \tag{4.14}$$

An optimization problem is convex if the objective function f is convex, the equality constraints $g_i = 0$ are affine and the inequality constraints $h_i \leq 0$ are convex [31]. In topology optimization, the objective function is typically non-convex and the optimization problem in equation (4.12) is a non-convex large-scale problem with a large number of design variables. Therefore many local optima may exist. To avoid getting stuck in a local optimum in an early stage of the optimization, continuation schemes can be used. In these schemes, some regularization parameters are gradually changed such that the optimization problem starts from a smooth problem [150]. This problem is regularly changed (for example every iteration) until the background problem is reached.

When using projection filters, two parameters can be used for the continuation schemes: the sharpness parameter β of the Heaviside projection and the filter radius R of the density filtering. As the sharpness parameter β controls the smoothness of the Heaviside projection, a low value can be used at the beginning of the optimization, which is slowly increased until the Heaviside step function is well approximated. The filter radius can be altered as well, starting from a large value which is gradually decreased until the intended value is reached.

Although these continuation schemes avoid getting stuck in a local optimum in an early stage of the optimization, they do not guarantee that a global optimum is obtained. Non-gradient based algorithms, such as genetic algorithms, simulated annealing, and differential evolution schemes, are based on global search techniques. However, in contrast to what is sometimes claimed, this does not imply convergence to global optima. Furthermore, their efficiency can be questioned [148].

4.2.3 Sensitivities

In this work, the optimization problem in equation (4.12) is solved with gradient based algorithms. Efficiently computing the derivatives of the objective and the constraint functions is essential as these have to be determined in each iteration step. The computation of the sensitivities of an objective or constraint function is discussed below. The objective function and the constraints are generally formulated as $\phi\left(\bar{\boldsymbol{\rho}}\left(\tilde{\boldsymbol{\rho}}\left(\boldsymbol{\rho}\right)\right), \mathbf{u}\left(\bar{\boldsymbol{\rho}}\left(\tilde{\boldsymbol{\rho}}\left(\boldsymbol{\rho}\right)\right)\right)\right)$.

The objective and constraint functions are usually written in terms of the physical element densities $\bar{\boldsymbol{\rho}}$. The derivatives of these functions to the design variables $\boldsymbol{\rho}$ are obtained using the chain rule:

$$\frac{\mathrm{d}\phi}{\mathrm{d}\rho_i} = \sum_{e=1}^{N_e} \frac{\mathrm{d}\phi}{\mathrm{d}\bar{\rho}_e} \frac{\partial \bar{\rho}_e}{\partial \tilde{\rho}_e} \frac{\partial \tilde{\rho}_e}{\partial \rho_i} \tag{4.15}$$

The latter two factors result from the projection filter, and can be found by taking the derivative of equation (4.11):

$$\frac{\partial \bar{\rho}_e}{\partial \tilde{\rho}_e} = \frac{\beta \mathrm{sech}^2\left(\beta\left(\tilde{\rho}_e - \eta\right)\right)}{\tanh\left(\beta\eta\right) + \tanh\left(\beta(1-\eta)\right)} \tag{4.16}$$

and of equation (4.8):

$$\frac{\partial \tilde{\rho}_e}{\partial \rho_i} = \frac{w_{ie} v_i}{\sum_{j=1}^{N_e} w_{ej} v_j} \tag{4.17}$$

Several techniques are available for the computation of the first term in equations (4.15), $\frac{\mathrm{d}\phi}{\mathrm{d}\bar{\rho}_e}$. These include finite differences, the imaginary trick method, the direct approach, and the adjoint approach. These are briefly described below.

Finite differences Finite differences is a generally applicable numerical differentiation method [132]. This method allows computing the derivative of ϕ in the direction $\Delta\bar{\boldsymbol{\rho}}$:

$$\frac{\mathrm{d}\phi}{\mathrm{d}\bar{\boldsymbol{\rho}}}\Delta\bar{\boldsymbol{\rho}} \approx \frac{\phi\left(\bar{\boldsymbol{\rho}} + \epsilon\Delta\bar{\boldsymbol{\rho}}, \mathbf{u}\left(\bar{\boldsymbol{\rho}} + \epsilon\Delta\bar{\boldsymbol{\rho}}\right)\right) - \phi\left(\bar{\boldsymbol{\rho}}, \mathbf{u}\left(\bar{\boldsymbol{\rho}}\right)\right)}{\epsilon} \tag{4.18}$$

where ϵ is a small fixed number. Selecting a too large value of ϵ results in linearization errors, while for too small values of ϵ numerical cancellation errors might arise. An often used rule of thumb is $\epsilon = \sqrt{\epsilon_{\text{mach}}}$ with ϵ_{mach} the machine precision [132].

Imaginary trick method For real-valued analytic functions ϕ, the imaginary trick method can be applied [61]:

$$\frac{\mathrm{d}\phi}{\mathrm{d}\bar{\boldsymbol{\rho}}}\Delta\bar{\boldsymbol{\rho}} \approx \frac{\operatorname{Im}\left\{\phi\left(\bar{\boldsymbol{\rho}} + \mathrm{i}\epsilon\Delta\bar{\boldsymbol{\rho}}, \mathbf{u}\left(\bar{\boldsymbol{\rho}} + \mathrm{i}\epsilon\Delta\bar{\boldsymbol{\rho}}\right)\right)\right\}}{\epsilon} \tag{4.19}$$

As there is no danger of numerical cancellation errors, the number ϵ can be chosen very small and the derivative can be computed up to machine precision. This method is most easily used in programming languages which do not declare the type of variables beforehand. In this way, functions for real variables can also be executed with complex variables.

The advantage of the finite difference method is that it can always be applied even if the function is only available in compiled form. For both the finite difference and the imaginary trich method, no analytic expression of the gradient need to be derived. However, to determine the entire gradient, N_e directional derivatives corresponding to every component of $\boldsymbol{\rho}$ have to be computed. In topology optimization, the size N_e of this vector is considerable as there is a large number of design variables. As this function often relates to the state variables $\mathbf{u}$, the system of state equations (4.13) also has to be computed $N_e + 1$ times in the nested approach. This is of course very costly from a computational point of view.

Direct approach In the direct differentiation approach [42], the derivatives of $\phi\left(\bar{\boldsymbol{\rho}}, \mathbf{u}\left(\bar{\boldsymbol{\rho}}\right)\right)$ are computed as follows:

$$\frac{\mathrm{d}\phi}{\mathrm{d}\bar{\rho}_e} = \frac{\partial \phi}{\partial \bar{\rho}_e} + \frac{\partial \phi}{\partial \mathbf{u}}\frac{\partial \mathbf{u}}{\partial \bar{\rho}_e} + \frac{\partial \phi}{\partial \mathbf{u}^*}\frac{\partial \mathbf{u}^*}{\partial \bar{\rho}_e} \tag{4.20}$$

where $(\cdot)^*$ denotes the complex conjugate. The derivatives of the function ϕ with respect to the complex state variables $\mathbf{u}$ are calculated analytically and are given by:

$$\frac{\partial \phi}{\partial \mathbf{u}} = \frac{1}{2}\left(\frac{\partial \phi}{\partial \mathbf{u}^{\mathrm{R}}} - \mathrm{i}\frac{\partial \phi}{\partial \mathbf{u}^{\mathrm{I}}}\right) \tag{4.21}$$

$$\frac{\partial \phi}{\partial \mathbf{u}^*} = \frac{1}{2}\left(\frac{\partial \phi}{\partial \mathbf{u}^{\mathrm{R}}} + \mathrm{i}\frac{\partial \phi}{\partial \mathbf{u}^{\mathrm{I}}}\right) \tag{4.22}$$

where $\mathbf{u}^{\mathrm{R}} = \mathrm{Re}\{\mathbf{u}\}$ and $\mathbf{u}^{\mathrm{I}} = \mathrm{Im}\{\mathbf{u}\}$ are the real and imaginary part of the state vectors $\mathbf{u}$. Note that for analytic functions, for which the Cauchy-Riemann equations $\dfrac{\partial \phi}{\partial \mathbf{u}^{\mathrm{I}}} = \mathrm{i}\dfrac{\partial \phi}{\partial \mathbf{u}^{\mathrm{R}}}$ apply, the conjugate complex derivative in equation (4.22) becomes equal to zero and the last term in equation (4.20) disappears. Most functions, such as the simple example $\phi\left(\mathbf{u}\right) = \mathbf{u}$, are analytical. However, functions involving complex conjugate variables such as $\phi\left(\mathbf{u}\right) = \mathbf{u}^*$ are mostly not analytic.

In the direct approach, the derivatives of the state variables $\mathbf{u}$ with respect to the element densities $\bar{\rho}_e$ are computed by applying the implicit function theorem to the governing state equations (4.13):

$$\frac{\partial \mathbf{g}}{\partial \bar{\rho}_e} = \frac{\partial \mathbf{K}}{\partial \bar{\rho}_e}\mathbf{u} + \mathbf{K}\frac{\partial \mathbf{u}}{\partial \bar{\rho}_e} = \mathbf{0} \Rightarrow \mathbf{K}\frac{\partial \mathbf{u}}{\partial \bar{\rho}_e} = -\frac{\partial \mathbf{K}}{\partial \bar{\rho}_e}\mathbf{u} \tag{4.23}$$

This system resembles the system of state equations (4.13), but with a different right hand side or loading. From this, the derivatives $\dfrac{\partial \mathbf{u}^*}{\partial \bar{\rho}_e} = \left(\dfrac{\partial \mathbf{u}}{\partial \bar{\rho}_e}\right)^*$ are calculated and introduced into equation (4.20).

Adjoint approach The adjoint approach is more efficient for topology optimization problems, which have typically a large number of design variables. By inserting equation (4.23) into equation (4.20), the following expression is obtained:

$$\begin{aligned}
\frac{\mathrm{d}\phi}{\mathrm{d}\bar{\rho}_e} &= \frac{\partial\phi}{\partial\bar{\rho}_e} - \frac{\partial\phi}{\partial\mathbf{u}}\mathbf{K}^{-1}\frac{\partial\mathbf{K}}{\partial\bar{\rho}_e}\mathbf{u} - \frac{\partial\phi}{\partial\mathbf{u}^*}\left(\mathbf{K}^{-1}\frac{\partial\mathbf{K}}{\partial\bar{\rho}_e}\mathbf{u}\right)^* \\
&= \frac{\partial\phi}{\partial\bar{\rho}_e} - \frac{\partial\phi}{\partial\mathbf{u}}\mathbf{K}^{-1}\frac{\partial\mathbf{K}}{\partial\bar{\rho}_e}\mathbf{u} - \left(\frac{\partial\phi}{\partial\mathbf{u}}\mathbf{K}^{-1}\frac{\partial\mathbf{K}}{\partial\bar{\rho}_e}\mathbf{u}\right)^* \\
&= \frac{\partial\phi}{\partial\bar{\rho}_e} + 2\,\mathrm{Re}\left\{-\frac{\partial\phi}{\partial\mathbf{u}}\mathbf{K}^{-1}\frac{\partial\mathbf{K}}{\partial\bar{\rho}_e}\mathbf{u}\right\} \\
&= \frac{\partial\phi}{\partial\bar{\rho}_e} + 2\,\mathrm{Re}\left\{\boldsymbol{\lambda}^{\mathrm{T}}\frac{\partial\mathbf{K}}{\partial\bar{\rho}_e}\mathbf{u}\right\}
\end{aligned} \tag{4.24}$$

where use is made of the identity $\dfrac{\partial\phi}{\partial\mathbf{u}^*} = \left(\dfrac{\partial\phi}{\partial\mathbf{u}}\right)^*$ for real-valued functions ϕ. The adjoint vector $\boldsymbol{\lambda} \in \mathbb{C}^{n^{\mathrm{DOF}}}$ is calculated from the adjoint equation:

$$\mathbf{K}^{\mathrm{T}}\boldsymbol{\lambda} = -\left(\frac{\partial\phi}{\partial\mathbf{u}}\right)^{\mathrm{T}} \tag{4.25}$$

This equation again resembles the system of the state equations (4.13). There is, however, a different right-hand side, referred to as the adjoint load, and the adjoint vector is pre-multiplied by the transpose of the stiffness matrix instead of the stiffness matrix itself. In most cases, $\mathbf{K}^{\mathrm{T}} = \mathbf{K}$, but this is for example not the case for the two-and-a-half-dimensional finite element model: in expression (3.22), the transpose of the element stiffness matrix $\mathbf{K}^1$ is equal to $\left(\mathbf{K}^1\right)^{\mathrm{T}} = -\mathbf{K}^1$ (see equation (3.25)).

Note that both the direct and adjoint approach require the derivatives $\dfrac{\partial\mathbf{K}}{\partial\bar{\rho}_e}$ of the stiffness matrix with respect to the element densities. The stiffness matrix is related to the element densities through the material parameters α_j, $j = 1\ldots N_\alpha$. From equation (4.14), it follows that:

$$\frac{\partial\mathbf{K}}{\partial\bar{\rho}_e} = \sum_{j=1}^{N_\alpha}\frac{\partial\mathbf{K}}{\partial\alpha_j}\frac{\partial\alpha_j}{\partial\bar{\rho}_e} = \sum_{j=1}^{N_\alpha} p_j\bar{\rho}_e^{p_j-1}\left(\alpha_{j,\mathrm{ins}} - \alpha_{j,\mathrm{ref}}\right)\frac{\partial\mathbf{K}}{\partial\alpha_j} \tag{4.26}$$

The adjoint approach has the advantage that only one (instead of N_e) additional equation similar to the state equation (4.13) needs to be computed for every function ϕ, but the disadvantage is that an extra equation has to be solved for each constraint. The direct approach is therefore advantageous when a large number of constraints is present, while the adjoint approach is advantageous for a large number of element densities. In topology optimization, the number of element densities is typically much larger than the number of constraints, which makes the adjoint method much more efficient for topology optimization problems. The adjoint method is also adopted in this work. As the sensitivities have to be derived analytically, they are checked using finite differences or the imaginary trick technique.

4.2.4 Optimization algorithm

As pointed out before, gradient based optimization algorithms are used to solve the topology optimization problems in this work. In the nested approach, the computational cost of the optimization algorithm is typically small compared to the cost of computing the state variables and sensitivities. The method of moving asymptotes (MMA) [155] is often used as gradient based optimization algorithm. The Matlab implementation of Svanberg is used in this work [156]. MMA solves the following generalized optimization problem:

$$\begin{aligned} \min_{\mathbf{x}} \quad & f_0(\mathbf{x}) & \\ \text{s.t.} \quad & f_i(\mathbf{x}) \leq 0 & i = 1 \dots m \\ & \mathbf{x}^{\min} \leq \mathbf{x} \leq \mathbf{x}^{\max} & \end{aligned} \tag{4.27}$$

where $\mathbf{x} \in \mathbb{R}^n$, are the design variables, $f_0(\mathbf{x})$ is the objective function and $f_i(\mathbf{x})$ are the constraints.

MMA is a sequential approximate optimization (SAO) method, in which a separable convex first order approximating subproblem is constructed in every iteration. The solution of the subproblem for the current iteration point $\mathbf{x}^{(k)}$ yields the next iteration point $\mathbf{x}^{(k+1)}$. The MMA subproblems are given by:

$$\begin{aligned} \min_{\mathbf{x}} \quad & \tilde{f}_0^{(k)}(\mathbf{x}) & \\ \text{s.t.} \quad & \tilde{f}_i^{(k)}(\mathbf{x}) & i = 1 \dots m \\ & \boldsymbol{\alpha}^{(k)} \leq \mathbf{x} \leq \boldsymbol{\beta}^{(k)} & j = 1 \dots n \end{aligned} \tag{4.28}$$

where $\boldsymbol{\alpha}^{(k)}$ and $\boldsymbol{\beta}^{(k)}$ are the lower and upper bound of the current iteration point $\mathbf{x}^{(k)}$ which differ from the original bounds $\mathbf{x}^{\min}$ and $\mathbf{x}^{\max}$ as they also limit the maximum step-length. MMA uses rational functions as approximating functions $\tilde{f}_0^{(k)}(\mathbf{x})$ and $\tilde{f}_i^{(k)}(\mathbf{x})$. The choice of these functions is based on gradient information at the current iteration point and on lower and upper asymptotes $l_j^{(k)}$ and $u_j^{(k)}$ which are updated in each iteration. The approximating functions are given by [156]:

$$\tilde{f}_i^{(k)}(\mathbf{x}) = \sum_{j=1}^{n} \left(\frac{p_{ij}^{(k)}}{u_j^{(k)} - x_j} + \frac{q_{ij}^{(k)}}{x_j - l_j^{(k)}} \right) + r_i^{(k)} \tag{4.29}$$

with [156]:

$$p_{ij}^{(k)} = \left(u_j^{(k)} - x_j^{(k)} \right)^2 \left(\max\left\{ \frac{\partial f_i}{\partial x_j}\left(\mathbf{x}^{(k)}\right), 0 \right\} + \frac{\rho_i}{x_j^{\max} - x_j^{\min}} \right) \tag{4.30}$$

$$q_{ij}^{(k)} = \left(x_j^{(k)} - l_j^{(k)} \right)^2 \left(\max\left\{ -\frac{\partial f_i}{\partial x_j}\left(\mathbf{x}^{(k)}\right), 0 \right\} + \frac{\rho_i}{x_j^{\max} - x_j^{\min}} \right) \tag{4.31}$$

$$r_i^{(k)} = f_i\left(\mathbf{x}^{(k)}\right) - \sum_{j=1}^{n} \left(\frac{p_{ij}^{(k)}}{u_j^{(k)} - x_j^{(k)}} + \frac{q_{ij}^{(k)}}{x_j^{(k)} - l_j^{(k)}} \right) \tag{4.32}$$

where the parameter ρ_i is a fixed small, positive number such as 10^{-5}. Default rules for updating the lower asymptotes $l_j^{(k)}$ and the upper asymptotes $u_j^{(k)}$ can be found in [156].

The approximating functions $\tilde{f}_i^{(k)}$ are always first order approximation functions of the original function f_i at the current iteration point $\mathbf{x}^{(k)}$. Furthermore, they are strictly convex, making the subproblem in equation (4.28) strictly convex. These subproblems can therefore be solved to global optimality using efficient convex optimization algorithms, such as interior-point algorithms.

4.3 Optimization of one-dimensional wave barriers

In this section, topology optimization is applied to a simple one-dimensional problem. The problem is sketched, the sensitivities are derived and the optimized designs are discussed.

4.3.1 Problem description

Figure 4.6 shows the optimization problem. Dilatational waves with amplitude I propagate through a homogeneous full space of a certain material. To reduce the wave transmission, stiffer material is inserted in the design domain, a region with a width of 10 m that is situated between two halfspaces. The inserted material partly reflects the incoming waves, decreasing the amplitude T of the

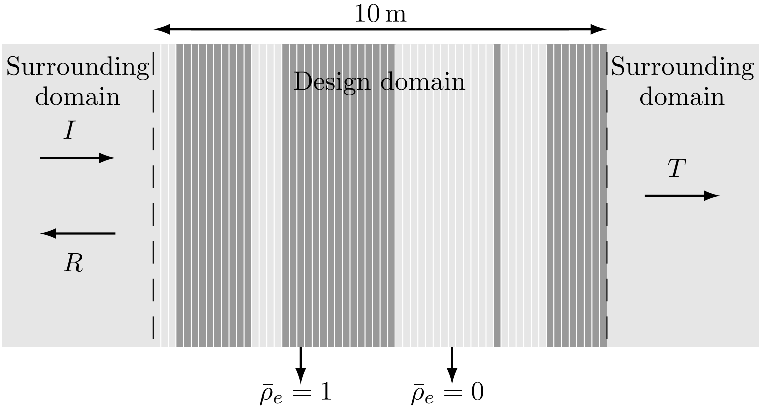

Figure 4.6: One-dimensional topology optimization problem. The mesh is added as illustration only and is not the actual one.

Table 4.1: Material properties used in the optimization of the one-dimensional design.

	Background material	Inserted material
Mass density ρ [kg/m^3]	2000	2000
Dilatational wave velocity C_p [m/s]	200	400
Dilatational damping ratio β_p [%]	0.0	0.0

transmitted waves. The material properties of the background and inserted material are given in table 4.1.

The direct stiffness method (chapter 2) is used to calculate the displacement field. The design domain is discretized using N_e layer elements. Each of these elements is given an element density $\bar{\rho}_e$. Recall that elements with $\bar{\rho}_e = 0$ have the material properties of the background material, while elements with $\bar{\rho}_e = 1$ have the material properties of the inserted material. The problem is modeled by means of the direct stiffness method, using N_e layer elements and two halfspaces at both sides of the design domain, resulting in a total of $N_e + 2$ elements. The elements are numbered as follows: 0 (left halfspace), 1 (first element design domain), $\ldots N_e$ (last element design domain), $N_e + 1$ (right halfspace). By solving the state equation $\hat{\mathbf{K}}\underline{\hat{\mathbf{u}}} = \underline{\hat{\mathbf{p}}}$, the displacements vector $\underline{\hat{\mathbf{u}}} = [\underline{\hat{u}}_0 \cdots \underline{\hat{u}}_{N_e+1}]^\mathrm{T}$ is obtained.

The transmission coefficient is defined as the ratio of the amplitudes of the transmitted and incoming wave. For a harmonic wave with amplitude $I = 1$ of the incoming wave, the transmission coefficient is equal to the amplitude $T = \left|\underline{\hat{u}}_{N_e+1}\right|$ of the transmitted wave. The transmittance is defined as the square of the modulus of the transmission coefficient, i.e. $|t|^2 = \left|\underline{\hat{u}}_{N_e+1}\right|^2$.

Depending on the type of excitation, different optimization problems have been studied for one-dimensional problems: (1) harmonic sources at a known frequency, (2) broadband sources, and (3) harmonic sources at a frequency situated in a given range. An example of a broadband source is the axle loading of trains and road traffic, while pumps rotate at a certain (constant or variable) frequency and are therefore harmonic sources. The different optimization problems and the resulting designs are discussed in the following subsections.

4.3.2 Harmonic sources

Optimal distribution of the inserted material minimizes the transmittance. As 0/1 designs are obtained without penalization (self-penalization), linear material interpolation is used and no volume constraint is imposed. The only constraint defines the limits of the element densities. For harmonic incident waves, the optimization problem is given by:

$$\begin{aligned} \min_{\boldsymbol{\rho}} \quad & f\left(\underline{\hat{\mathbf{u}}}\left(\bar{\boldsymbol{\rho}}\right)\right) = \sum_{j=0}^{N_e+1} l_j \left|\hat{u}_j\right|^2 = \underline{\hat{\mathbf{u}}}^{\mathrm{H}}\mathbf{L}\underline{\hat{\mathbf{u}}} & \\ \text{s. t.} \quad & 0 \leq \rho_e \leq 1 & e = 1 \ldots N_e \end{aligned} \tag{4.33}$$

where $(\cdot)^{\mathrm{H}}$ is the Hermitian (or conjugate) transpose, $\underline{\hat{\mathbf{u}}}$ the displacement vector, and l_j is a weighting factor. $\mathbf{L}$ is a zero matrix with ones at the diagonal elements corresponding to the degrees of freedom where the displacement is to be minimized. As the amplitude of the transmitted wavefield is minimized, $l_{N_e+1} = 1$ (and $l_k = 0 \; \forall k \neq N_e + 1$) or $\mathbf{L}\left(N_e + 1, N_e + 1\right) = 1$. Note that since $I = 1$, the objective function is equal to the transmittance.

The sensitivities are calculated using the adjoint method (equation (4.24)):

$$\frac{\mathrm{d}f}{\mathrm{d}\bar{\rho}_e} = 2\,\mathrm{Re}\left\{\boldsymbol{\lambda}^{\mathrm{T}}\frac{\partial\hat{\mathbf{K}}}{\partial\bar{\rho}_e}\underline{\hat{\mathbf{u}}}\right\} \tag{4.34}$$

where the adjoint variable $\boldsymbol{\lambda}$ is obtained by solving the system of adjoint equations (equation (4.25)):

$$\hat{\mathbf{K}}^{\mathrm{T}}\boldsymbol{\lambda} = -\left(\frac{\partial\phi}{\partial\underline{\hat{\mathbf{u}}}}\right)^{\mathrm{T}} = -\mathbf{L}\underline{\hat{\mathbf{u}}}^{*} \tag{4.35}$$

Note that the optimization problem in equation (4.33) is non-convex as the objective function $f\left(\underline{\hat{\mathbf{u}}}\left(\bar{\boldsymbol{\rho}}\right)\right)$ is non-convex.

Optimization algorithms that can deal with non-convex problems, such as MMA, should therefore be used. Continuation schemes are furthermore used to avoid getting stuck in a local optimum in an early stage of the optimization. The following continuation schemes are used. The sharpness parameter β starts from a low value (1) and is doubled every 50 iterations until the value 32 is obtained. The filter radius R on the contrary starts from a high value (16) and is halved every 50 iterations until it is equal to 0.5. The MMA algorithm is stopped after 300 iterations.

The results of the optimization problem are shown for $N_e = 200$ elements. The material interpolation is performed on the mass density ρ and the dilatational wave velocity C_p. Four distinct frequencies are considered, namely 20 Hz, 40 Hz, 60 Hz, and 80 Hz. A design domain which is fully filled with the inserted material, as shown in figure 4.7, is taken as reference case. This design is also taken as the initial design. The aim is to find a design that minimizes the transmittance, as defined in the optimization problem (4.33). The evolution of the objective function for the optimization at $f = 40\,\mathrm{Hz}$ is shown in figure 4.8. Every 50 iterations, a jump occurs when the regularization parameters are adjusted, resulting in a different optimization problem and therefore a different optimum. In the last iteration step, the change in objective function is equal to 4×10^{-8}.

Figure 4.7: Fully filled design used as initial design for the one-dimensional optimization. The boundaries of the design domain are indicated with a gray dashed line.

The optimized designs and the corresponding transmission coefficient as a function of the frequency are shown in figure 4.9. The transmission coefficient for the reference case of a fully filled design is also shown. This figure clearly demonstrates that the resulting designs perform much better at the optimization frequency (they have lower transmission coefficients) than the fully filled design. Note that for stiffness based problems, such as the minimization of the response for a beam subjected to a static load, the fully filled design would be the optimized design as it provides the most stiffness and no volume constraint is present in the optimization problem. However, due to the self-

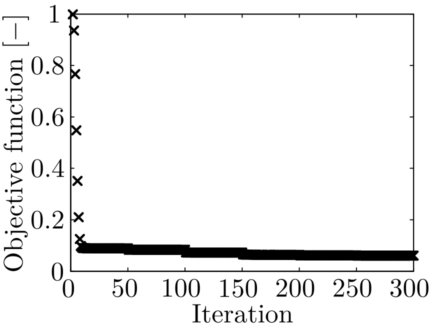

Figure 4.8: Convergence of the optimization problem for the design optimized at a frequency of 40 Hz (figure 4.9c).

penalization for the problems considered here, the optimal designs differ from the fully filled design.

The optimized designs are periodic and result in stopbands and passbands. For higher frequencies, the alternating layers of background and inserted material become thinner. As a result, the design domain can accommodate for a larger number of layers, which leads to lower values of the transmission coefficient and wider stopbands.

These considerations allow interpreting the optimized designs using the analysis in chapter 2. With the material properties in table 4.1, the thicknesses L_{ref} (background material) and L_{ins} (inserted material) in table 4.2 satisfy the quarter-wave stack condition. At the frequencies 40 Hz, 60 Hz, and 80 Hz, the optimized designs fulfill the quarter-wave stack conditions, since the thicknesses of the layers agree with the thicknesses in table 4.2. The designs optimized at 60 Hz and 80 Hz show a white layer at the left and right sides of the design domain. Shifting the inserted layers to the left or the right does not change the performance of the barrier (as long as the inserted layers are located entirely in the design domain). Starting from another initial design therefore can lead to a slightly different design, where the inserted layers are shifted.

At 20 Hz, however, the thicknesses given by the quarter-wave stack condition are 2.5 m and 5 m for the inserted and background material, respectively. In this case, the design domain is not sufficiently large to accommodate two layers of the inserted material. The thickness of the inserted layers is therefore smaller than the one obtained with the quarter-wave stack condition, as can be seen in figure 4.9. If the design domain would have a length of 12.5 m, the corresponding optimized design at 20 Hz would again fulfill the quarter-wave stack condition, resulting in a more pronounced dip of the transmission

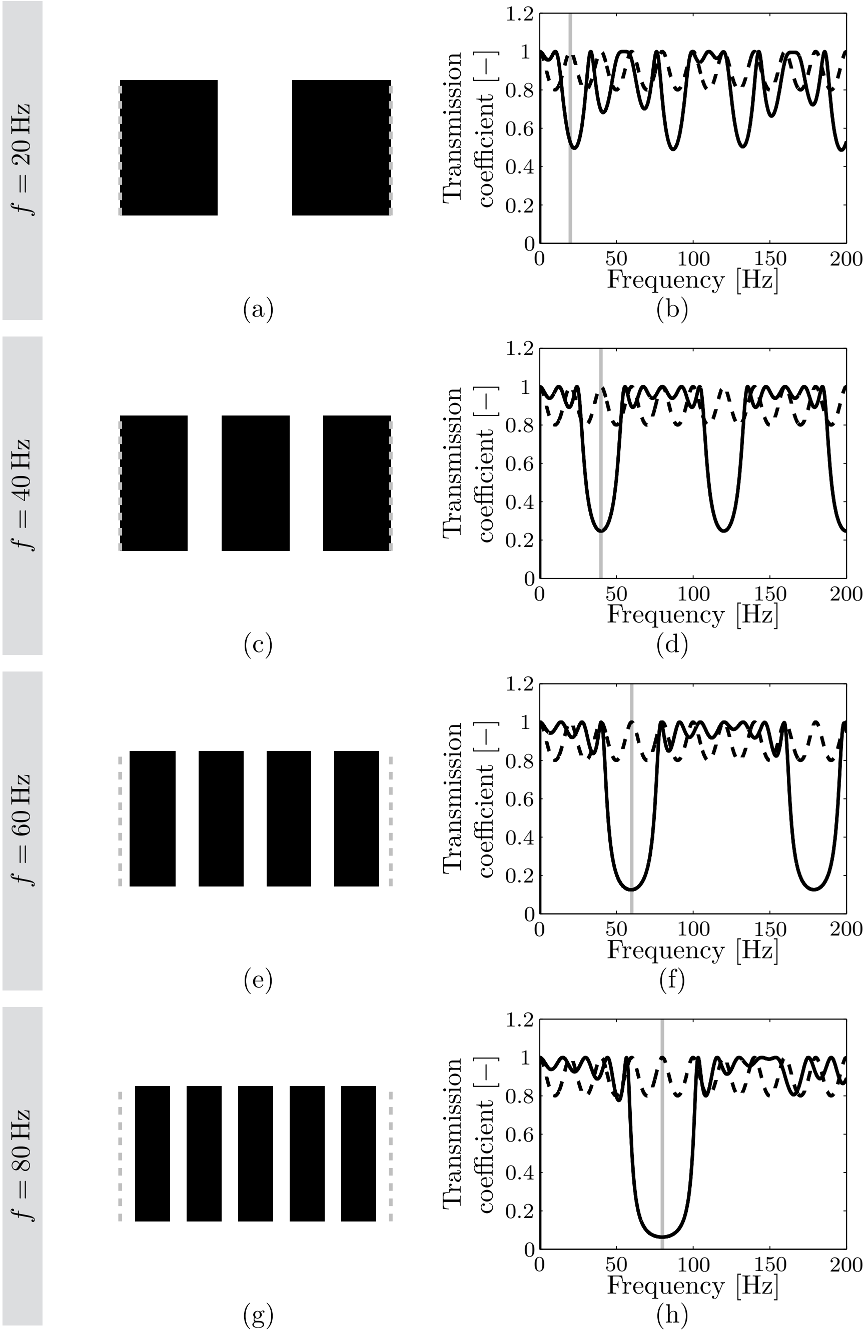

Figure 4.9: One-dimensional designs optimized at a frequency of (a) 20 Hz, (c) 40 Hz, (e) 60 Hz, and (g) 80 Hz. The boundaries of the design domain are indicated with a gray dashed line. Transmission coefficient as a function of the frequency for the reference case of a fully filled design (dashed line) and for the designs optimized at (b) 20 Hz, (d) 40 Hz, (f) 60 Hz, and (h) 80 Hz (solid line).

coefficient at 20 Hz.

Frequency [Hz]	L_ref [m]	L_ins [m]
20	2.500	5.000
40	1.250	2.500
60	0.833	1.667
80	0.625	1.250

Table 4.2: Thicknesses of the layers fulfilling the quarter-wave stack conditions for $C_\mathrm{p1} = 200$ m/s and $C_\mathrm{p2} = 400$ m/s.

Note that a better transmittance is obtained at higher frequencies. Because of the smaller thicknesses satisfying the quarter wave stack condition, multiple sequences of alternating layers are present. This leads to an increased reduction of the transmission (see section 2.4). Moreover, smaller thicknesses lead to wider stopbands, as can be derived from equation (2.60).

4.3.3 Broadband sources

For broadband sources, the frequency averaged transmittance is minimized. The optimization problem therefore is given by:

$$\begin{aligned} \min_{\boldsymbol{\rho}} \quad & \frac{1}{f_\mathrm{u} - f_\mathrm{l}} \int_{f_\mathrm{l}}^{f_\mathrm{u}} \underline{\hat{\mathbf{u}}}^\mathrm{H} \mathbf{L} \underline{\hat{\mathbf{u}}} \mathrm{d}f \\ \mathrm{s.\,t.} \quad & 0 \leq \rho_e \leq 1 \qquad\qquad e = 1 \dots N_e \end{aligned} \tag{4.36}$$

The frequency range $f \in [f_\mathrm{l}, f_\mathrm{u}]$ is discretized using N_f frequencies, which results in the following optimization problem:

$$\begin{aligned} \min_{\boldsymbol{\rho}} \quad & \frac{1}{N_f} \sum_{j=1}^{N_f} \underline{\hat{\mathbf{u}}}_j^\mathrm{H} \mathbf{L} \underline{\hat{\mathbf{u}}}_j \\ \mathrm{s.\,t.} \quad & 0 \leq \rho_e \leq 1 \qquad\qquad e = 1 \dots N_e \end{aligned} \tag{4.37}$$

where $\underline{\hat{\mathbf{u}}}_j = \underline{\hat{\mathbf{u}}}\,(f_j)$ is the displacement vector corresponding to the jth frequency. The number of frequencies N_f (which is equal to $(f_\mathrm{u} - f_\mathrm{l})/\Delta f - 1$) should be sufficiently large to ensure that the result is representative for the entire frequency range, but preferably as small as possible to keep the computation time limited. As for the direct approach the system of equation needs to be solved $N_f \times (N_e + 1)$ (N_f forward computations and $N_f \times N_e$ computations for the sensitivities), the adjoint approach is much more efficient, as the system of equations needs to be solved only $2N_f$ times (N_f forward and N_f adjoint computations). The total gradient of the objective function is then equal to the sum of these sensitivities divided by the number of frequencies N_f:

$$\frac{\mathrm{d}f}{\mathrm{d}\bar{\rho}_e} = \frac{2}{N_f} \sum_{j=1}^{N_f} \mathrm{Re}\left\{ \boldsymbol{\lambda}_j^{\mathrm{T}} \frac{\partial \hat{\mathbf{K}}_j}{\partial \bar{\rho}_e} \underline{\hat{\mathbf{u}}}_j \right\} \tag{4.38}$$

Note that, depending on the actual loading, more weight can be given to certain frequencies by introducing a weighting function.

The optimization is performed first for a frequency interval of 20 Hz, more specifically for the intervals $10 - 30$ Hz, $30 - 50$ Hz, $50 - 70$ Hz, and $70 - 90$ Hz. The frequency range is discretized with $N_f = 21$ equidistant frequencies. The resulting designs are shown in figure 4.10. The designs are equal to those optimized for the harmonic waves at 20 Hz, 40 Hz, 60 Hz, and 80 Hz. The stopbands resulting from the periodic designs are sufficiently large for the frequency interval considered here.

For a larger frequency interval of 60 Hz, for example the frequency range $20 - 80$ Hz, however, this no longer applies. For a discretization with $N_f = 61$ frequencies, the optimized design is shown in figure 4.11. The optimized design consists of alternating layers with different thicknesses. The resulting transmission coefficient as a function of the frequency does not show the characteristic periodic sequence of stop- and passbands. Instead, multiple stopbands overlap each other, resulting in a frequency averaged transmittance of 0.36 which is much lower than the frequency averaged transmittance of 0.81 for the reference case of the fully filled design. Note that especially the transmittance at higher frequencies is reduced, as for these frequencies, smaller thicknesses are needed to fulfill the quarter wave-stack condition.

The calculated frequency averaged transmittance depends on the selected discretization of the frequency interval, which should be dense enough as the curve in figure 4.11 is not smooth. To assess the influence of the discretization, the optimization is done for multiple discretizations of the frequency interval. Figure 4.12 shows the influence of the number of frequencies N_f in the discretization. Both the value of the objective function (i.e. the discretized mean transmittance) and the mean transmittance of the optimized design calculated with $N_{\mathrm{f}} = 2001$ ($\Delta f = 0.01$ Hz), giving an indication of the actual performance, are shown.

For the narrower frequency intervals ($10 - 30$ Hz, $30 - 50$ Hz, $50 - 70$ Hz, and $70 - 90$ Hz), there is a rather fast convergence. For all considered frequency intervals, discretizing with only $N_f = 5$ frequencies leads to the optimized

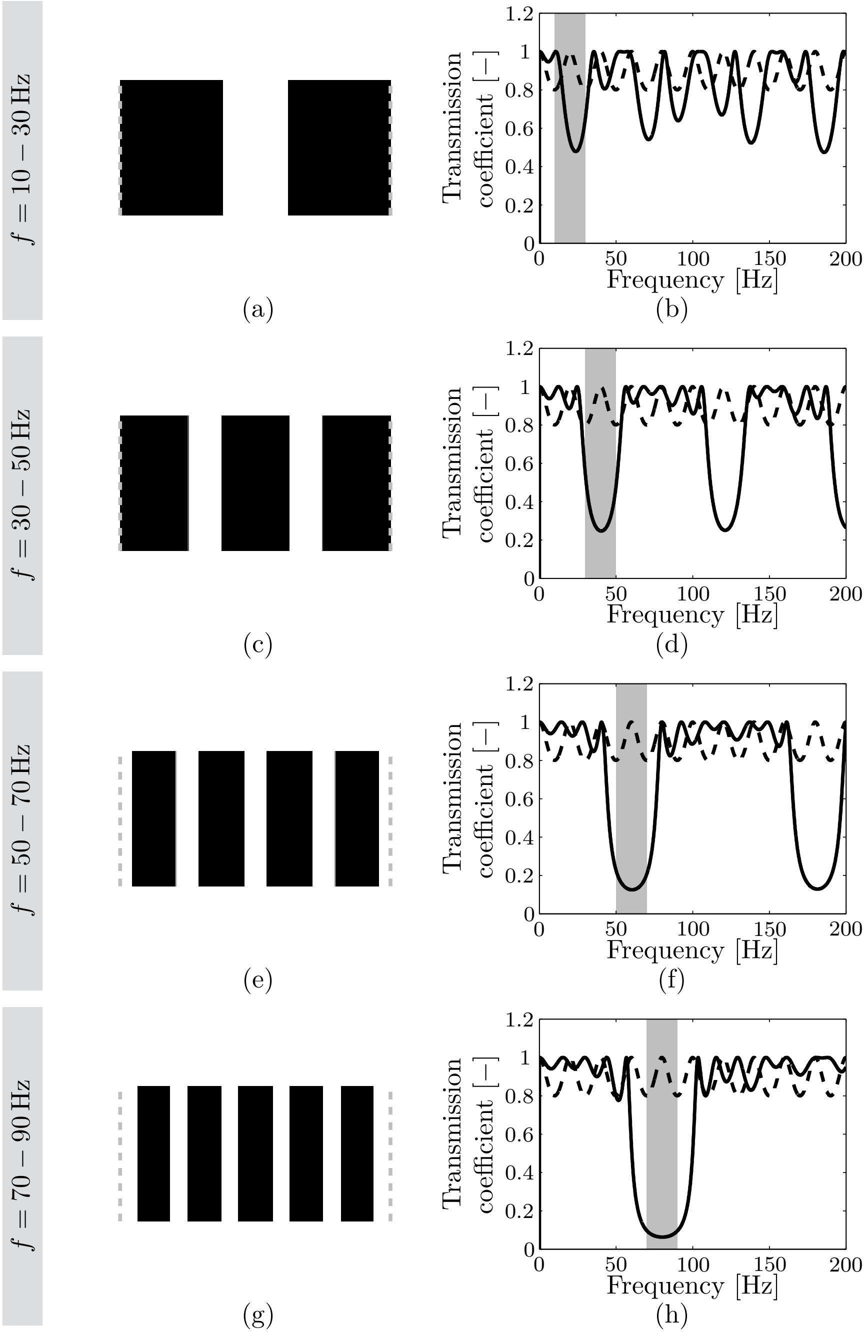

(a) (b)

(c) (d)

(e) (f)

(g) (h)

Figure 4.10: One-dimensional designs optimized at a frequency of (a) $10-30\,\mathrm{Hz}$, (c) $30-50\,\mathrm{Hz}$, (e) $50-70\,\mathrm{Hz}$, and (g) $70-90\,\mathrm{Hz}$. The boundaries of the design domain are indicated with a gray dashed line. Transmission coefficient as a function of the frequency for the reference case of a fully filled design (dashed line) and for the designs optimized at (b) $10-30\,\mathrm{Hz}$, (d) $30-50\,\mathrm{Hz}$, (f) $50-70\,\mathrm{Hz}$, and (h) $70-90\,\mathrm{Hz}$ (solid line).

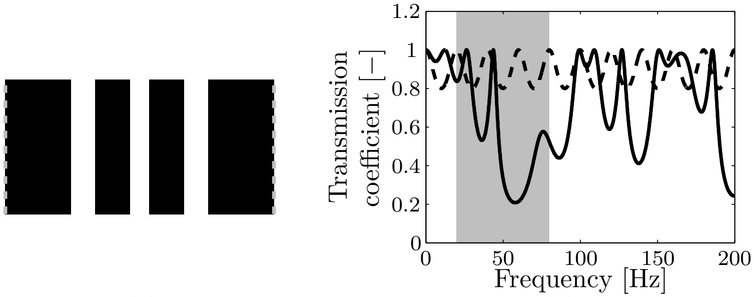

(a) (b)

Figure 4.11: (a) One-dimensional design optimized for the average transmittance over the frequency range $20-80\,\mathrm{Hz}$ with $N_f = 61$ (local optimum). The boundaries of the design domain are indicated with a gray dashed line. (b) Transmission coefficient as a function of the frequency for the reference case of a fully filled design (dashed line) and for the optimized design (solid line).

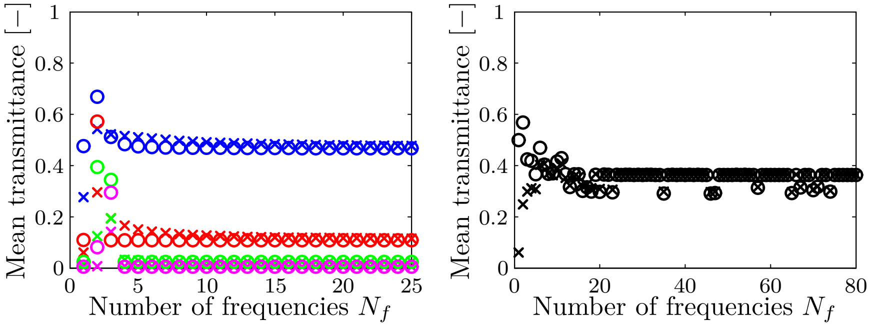

(a) (b)

Figure 4.12: Influence of the number of frequencies N_f considered in the optimization on the value of the objective function (x-marks) and the mean transmittance, computed with $\Delta f = 0.01\,\mathrm{Hz}$ (circles). In (a), four frequency ranges are considered with $f_\mathrm{u} - f_\mathrm{l} = 20\,\mathrm{Hz}$ (from top to bottom): $10-30\,\mathrm{Hz}$ (blue), $30-50\,\mathrm{Hz}$ (red), $50-70\,\mathrm{Hz}$ (green), and $70-90\,\mathrm{Hz}$ (magenta). In (b), the frequency range $20-80\,\mathrm{Hz}$ (black) is considered.

design obtained with $N_f = 21$ frequencies, although the mean transmittance is slightly overrated.

For the wider frequency interval ($20-80\,\mathrm{Hz}$), the objective function converges to two different solutions. In most cases, for $N_f \geq 12$ frequencies, the optimization leads to the design given in figure 4.11 and the optimized mean transmittance is equal to 0.36. However, for some discretizations, e.g. for $N_f = 35$ a different optimized design is obtained, shown in figure 4.13, which corresponds to a mean transmittance of 0.29. As the mean transmittance for $N_f = 61$ is higher, this is only a local optimum, while the design for $N_f = 35$ is presumably the global optimum.

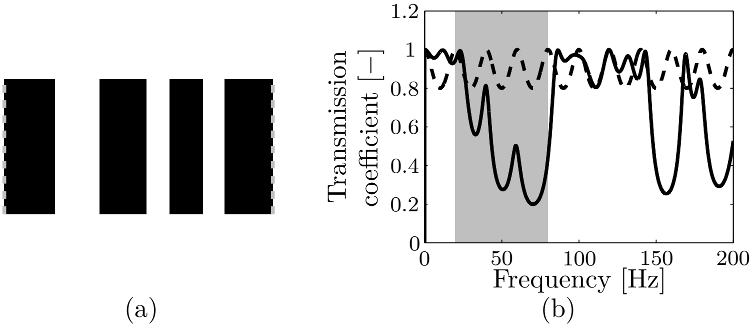

(a) (b)

Figure 4.13: (a) Design optimized for the average transmittance over the frequency range 20 − 80 Hz with $N_f = 35$ (presumed global optimum). The boundaries of the design domain are indicated with a gray dashed line. (b) Transmission coefficient as a function of the frequency for the reference case of a fully filled design (dashed line) and for the optimized design (solid line).

Despite the continuation schemes for the sharpness parameter β and the filter radius R, it is therefore not possible to avoid the local optima. The local optimum corresponds to a symmetric design, while the presumed global optimum corresponds to an asymmetric design. This suggests that the initial design directs the optimization to the symmetric local optimum. Considering an asymmetric initial design could therefore be applied to prevent the optimization from getting stuck in the symmetric local optimum. The calculations have therefore been repeated for an initial design where the volume densities increase linearly from 0 to 1, as shown in figure 4.14. The influence of the number of frequencies N_f on the performance of the obtained designs is shown in figure 4.15. The presumed global optimum is found for all frequency discretizations from $N_f = 11$ frequencies and the problem of the local optima seems to be solved.

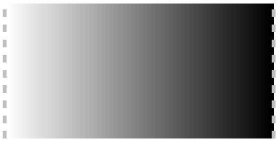

Figure 4.14: Alternative initial design for the one-dimensional optimization. The boundaries of the design domain are indicated with a gray dashed line.

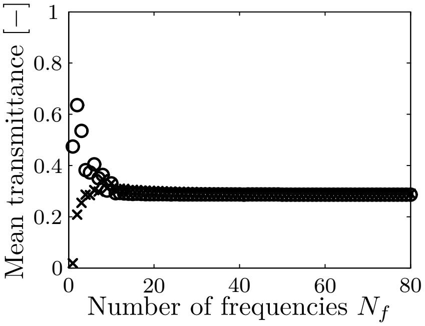

Figure 4.15: Influence of the number of frequencies N_f considered in the optimization on the value of the objective function (x-marks) and the mean transmittance, computed with $\Delta f = 0.01\,\mathrm{Hz}$ (circles). The frequency range $20 - 80\,\mathrm{Hz}$ is considered and the initial design of the optimization is taken to be the one in figure 4.14.

4.3.4 Harmonic sources at a frequency in a given range

The transmission coefficients in figures 4.11 and 4.13 have peaks at particular frequencies between the stopbands. These peaks are so narrow that they do not significantly contribute to the overall mean transmittance, but they could be important in the case of narrowband sources. Moreover, the lowest frequencies in the frequency range have a transmission coefficient close to 1. To avoid the occurrence of the peaks and to obtain a better performance for the lowest frequencies, the optimization problem can be reformulated as a minimax problem: instead of minimizing the frequency averaged transmittance, the maximal value of the transmittance in a given frequency range is considered. This allows obtaining the best solution in the case of sources operating at unknown frequencies in a frequency range. The optimization problem is therefore given by:

$$\begin{aligned} \min_{\boldsymbol{\rho}} \quad & \max_{f} \left\{ \underline{\hat{\mathbf{u}}}^{\mathrm{H}} \mathbf{L} \underline{\hat{\mathbf{u}}} \right\} \\ \mathrm{s.\,t.} \quad & 0 \leq \rho_e \leq 1 \qquad e = 1 \dots N_e \end{aligned} \tag{4.39}$$

where the state variables $\underline{\hat{\mathbf{u}}}$ depend both on the element densities $\bar{\rho}_e$ and the frequency $f \in [f_{\mathrm{l}}, f_{\mathrm{u}}]$.

This problem is, however, not differentiable. To resolve this, the problem is reformulated using a bound formulation:

$$\begin{aligned} \min_{\boldsymbol{\rho}, s} \quad & s \\ \mathrm{s.\,t.} \quad & \underline{\hat{\mathbf{u}}}_j^{\mathrm{H}} \mathbf{L} \underline{\hat{\mathbf{u}}}_j \leq s \quad j = 1 \dots N_f \\ & 0 \leq \rho_e \leq 1 \quad e = 1 \dots N_e \end{aligned} \tag{4.40}$$

The frequency interval $[f_{\mathrm{l}}, f_{\mathrm{u}}]$ is discretized using N_f equidistant frequencies.

The optimization problem in equation (4.40) contains, besides the boundaries for the element densities $\bar{\rho}_e$, N_f additional constraints, for which the sensitivities need to be calculated. The sensitivities are again most efficiently calculated using the adjoint equation for every discretized frequency.

Figure 4.16 shows the optimized design and the corresponding value of the transmission coefficient for a target frequency range 20-80 Hz, using $N_{\mathrm{f}} = 61$ frequencies. The maximum transmittance is equal to 0.57 for the optimized design, while it is equal to 1 for the fully filled design. The optimization still gives better results for higher frequencies, but local peaks are avoided. The value of the mean transmittance is however equal to 0.43, which is much higher than the value 0.29 obtained with the minimization of the mean transmittance. Clearly, there is a trade-off between the mean and the maximum transmittance in the frequency range considered. This observation underlines the importance of selecting the most suitable formulation of the optimization problem, which will depend on the characteristics of the vibration source (narrowband or broadband).

The influence of the selected frequency discretization is shown in figure 4.17 for initial designs consisting of both the fully filled (figure 4.7) and the asymmetric (figure 4.14) design. For the fully filled initial design, again two local optima are found for $N_f > 20$. For the asymmetric initial design, the discretization does not play a role for $N_f > 20$. However, the optimized design is the worst of the two local designs obtained with the fully filled initial design. Continuation schemes or asymmetric initial designs can therefore not always avoid local optima.

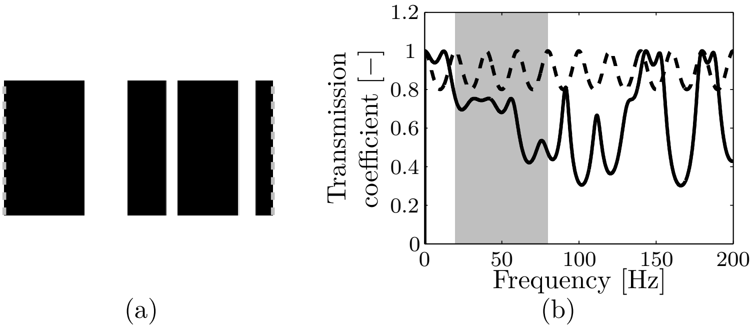

Figure 4.16: (a) One-dimensional design optimized for the maximum transmittance over the frequency range $20 - 80\,\mathrm{Hz}$ with $N_f = 61$. The boundaries of the design domain are indicated with a gray dashed line. (b) Transmission coefficient as a function of the frequency for the reference case of a fully filled design (dashed line) and for the optimized design (solid line).

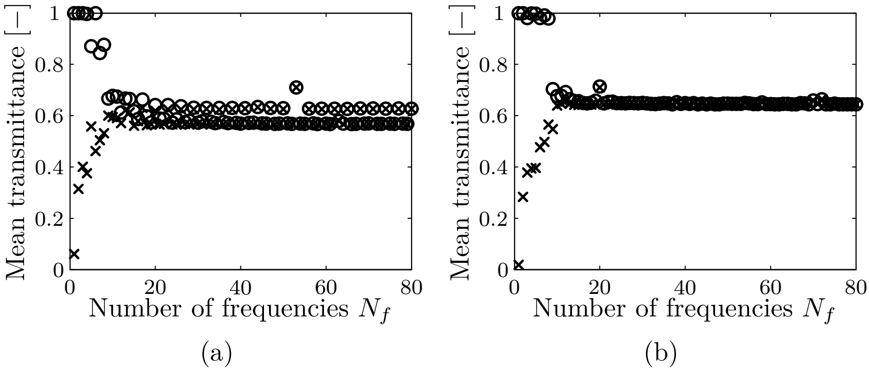

Figure 4.17: Influence of the number of frequencies N_f considered in the optimization on the value of the objective function (x-marks) and the maximum transmittance, computed with $\Delta f = 0.01\,\mathrm{Hz}$ (circles). The frequency range $20 - 80\,\mathrm{Hz}$ is considered. The initial design is in (a) the fully filled design in figure 4.7 and in (b) the asymmetric design in figure 4.14.

4.4 Conclusion

In this chapter, density based topology optimization is introduced. Regularization techniques allow controlling the complexity of the final design and preventing numerical issues. The optimization problem is often non-convex. By using continuation schemes, where the regularization parameters are gradually changed, the iterative optimization does not get stuck in a local optimum in an early stage of the optimization. A gradient based algorithm, namely the Method of Moving Asymptotes (MMA), is used to solve the topology optimization problem. In most cases, the adjoint method is the most efficient in calculating the sensitivities.

Topology optimization is applied to a simple one-dimensional problem. A plane wave propagating in a full space encounters a one-dimensional design domain, in which a stiffer material is optimally distributed. Three types of excitation are considered: harmonic incoming waves at a known frequency, broadband sources, and harmonic sources at a frequency situated in a given range. 0/1 designs are obtained for linear interpolation schemes.

If the design domain allows this, the optimized design for harmonic sources consists of a periodic configuration of layers with thicknesses equal to a quarter of a wavelength as found in chapter 2. For broadband sources and harmonic sources at an unknown frequency situated in a given range, the designs are more complex, as multiple frequencies are considered in the optimization. Continuation schemes and asymmetric initial designs do not always lead to the global optimum.

The next chapters consider transmission for a halfspace excited at the surface. Topology optimization is used to search for designs with a better performance than the double wall barriers considered in chapter 3.

Chapter 5

Topology optimization for two-dimensional elastic wave propagation

5.1 Introduction

The aim is to reduce the transmission of vibrations caused by passing trains on the surface of a semi-infinite halfspace, representing the soil. As a first approximation, the train loading is approximated by a line load. The problem addressed in this chapter is shown in figure 5.1. A wave barrier is introduced to reduce the resulting vibrations in the halfspace close to the surface. The wave barrier is designed such that the vibration transmission is minimized.

As the loading, the soil and the wave barrier are assumed to be longitudinally invariant, this problem can be modeled using a two-dimensional model. Comparative studies between two- and three-dimensional models have been performed by a number of researchers. Andersen and Jones [8] compared the ground responses to underground trains using two- and three-dimensional coupled finite element - boundary element models, showing that for the cases they consider, the results obtained with the two-dimensional model correspond well with those from the three-dimensional model at most frequencies. Yang et al. [178] compared responses of underground tunnels to moving train loads using two-dimensional and two-and-a-half-dimensional finite - infinite element approaches. They suggested to use the two-dimensional model as a conservative

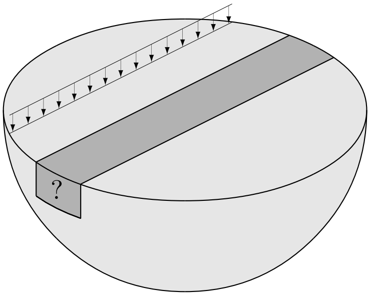

Figure 5.1: General problem: a semi-infinite halfspace excited at the surface by a line load. A wave barrier reduces the wave propagation close to the surface of the halfspace.

model, as the soil response obtained with this model appears to be the upper limit for the responses obtained with the two-and-a-half-dimensional model for different train speeds. Previous studies have, however, also pointed out the importance of accounting for the three-dimensional effects of wave impeding barriers for railway induced vibrations [53]. This is therefore addressed in the next chapter.

This chapter is divided in two main parts. In the first part (section 5.2), topology optimization is applied to optimize the design of the wave barrier. The three cases considered in the previous chapter are addressed: harmonic sources, broadband sources and harmonic sources at an unknown frequency. The second part (section 5.3) deals with robustness against geometric imperfections and feasibility of the design obtained for broadband sources.

5.2 Topology optimization

5.2.1 Problem description

Figure 5.2 shows the considered optimization problem. A homogeneous elastic halfspace is excited at the surface by a vertical line load. The aim is to minimize the response at a receiver point, located at the surface of the halfspace. Therefore, a design domain is considered between the source and the receiver where a stiffer material is introduced. The design domain has a cross-sectional area of $7.5 \times 5\,\mathrm{m}^2$ and is located at a distance of $5\,\mathrm{m}$ from the excitation point. The performance is optimized at a receiver point located at another 5 m from the design domain, and, therefore, 15 m from the excitation point. The properties of the original material and the inserted material are summarized in table 5.1.

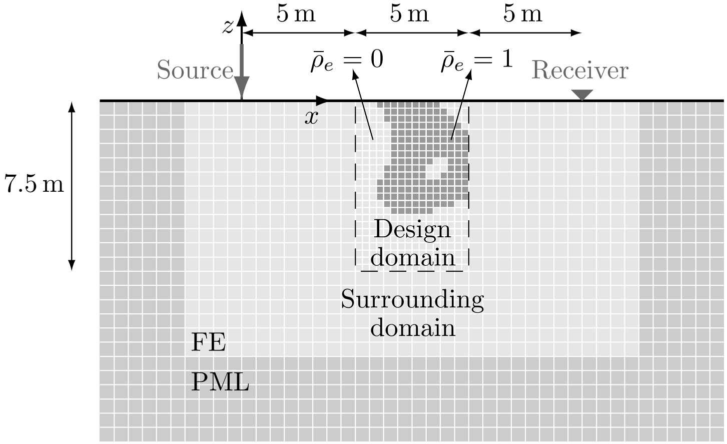

Figure 5.2: The optimization problem for the two-dimensional halfspace. The mesh is added as illustration only and is not the actual finite element mesh.

Table 5.1: Material properties of the original homogeneous halfspace and the inserted material.

	Original material	Inserted material
Mass density ρ [kg/m^3]	2000	2000
Dilatational wave velocity C_p [m/s]	400	950
Shear wave velocity C_s [m/s]	200	550
Dilatational material damping ratio β_p [%]	2.5	2.5
Shear material damping ratio β_s [%]	2.5	2.5

Note that there is only one receiver point and that a homogeneous soil is considered. This simple problem is used to illustrate the methodology and to more easily interpret the obtained results. However, the response and therefore the optimized design will change if different receiver points are considered. Also the material properties and the heterogeneity of the soil can considerably influence the optimized design. It is therefore important, when designing a wave barrier, to not disregard these aspects.

The elastodynamic problem is solved using the finite element method introduced in chapter 3. As a two-dimensional problem is considered, the longitudinal wavenumber k_y is set to zero and only the displacements in the x- and z-direction are considered. The resulting elements are two-dimensional eight-node elements in plane strain. For the mesh, an element size of 0.25 m is used, corresponding to ten elements per shear wavelength λ_{s} at a frequency of 80 Hz, which is the upper limit considered in this work.

To efficiently compute the system of equations $\hat{\mathbf{K}}\underline{\hat{\mathbf{u}}} = \hat{\mathbf{p}}$, the finite element model can be divided in two parts: one part containing the elements whose properties do not change during the optimization process, that is the the surrounding domain Ω_{s} including the PML domain, and another part containing the design domain Ω_{d} which is altered every iteration. The forward system of equations can therefore be written as:

$$\begin{bmatrix} \hat{\mathbf{K}}_{\mathrm{ss}} & \hat{\mathbf{K}}_{\mathrm{sd}} \\ \hat{\mathbf{K}}_{\mathrm{ds}} & \hat{\mathbf{K}}_{\mathrm{dd}} \end{bmatrix} \begin{Bmatrix} \underline{\hat{\mathbf{u}}}_{\mathrm{s}} \\ \underline{\hat{\mathbf{u}}}_{\mathrm{d}} \end{Bmatrix} = \begin{Bmatrix} \underline{\hat{\mathbf{p}}}_{\mathrm{s}} \\ \underline{\hat{\mathbf{p}}}_{\mathrm{d}} \end{Bmatrix} \tag{5.1}$$

where subscript s refers to the surrounding domain including the PML layers (with $n_{\mathrm{s}}^{\mathrm{DOF}}$ degrees of freedom) and subscript d refers to the design domain (with $n_{\mathrm{d}}^{\mathrm{DOF}}$ degrees of freedom). From this equation, the displacements $\underline{\hat{\mathbf{u}}}_{\mathrm{s}}$ can be computed in terms of the load vector $\underline{\hat{\mathbf{p}}}_{\mathrm{s}}$ and the displacement vector $\underline{\hat{\mathbf{u}}}_{\mathrm{d}}$:

$$\underline{\hat{\mathbf{u}}}_{\mathrm{s}} = \hat{\mathbf{K}}_{\mathrm{ss}}^{-1}\underline{\hat{\mathbf{p}}}_{\mathrm{s}} - \hat{\mathbf{K}}_{\mathrm{ss}}^{-1}\hat{\mathbf{K}}_{\mathrm{sd}}\underline{\hat{\mathbf{u}}}_{\mathrm{d}} \tag{5.2}$$

which can be inserted in the second system of equations:

$$\left(\hat{\mathbf{K}}_{\mathrm{dd}} - \hat{\mathbf{K}}_{\mathrm{ds}}\hat{\mathbf{K}}_{\mathrm{ss}}^{-1}\hat{\mathbf{K}}_{\mathrm{sd}}\right)\underline{\hat{\mathbf{u}}}_{\mathrm{d}} = \underline{\hat{\mathbf{p}}}_{\mathrm{d}} - \hat{\mathbf{K}}_{\mathrm{ds}}\hat{\mathbf{K}}_{\mathrm{ss}}^{-1}\underline{\hat{\mathbf{p}}}_{\mathrm{s}} \tag{5.3}$$

The inverse of $\hat{\mathbf{K}}_{\mathrm{ss}}$ stays unchanged during the optimization, and can be calculated in a preprocessing step. This means that only the system in equation (5.3) with $n_{\mathrm{d}}^{\mathrm{DOF}}$ degrees of freedom needs to be solved every iteration instead of the forward system $\hat{\mathbf{K}}\underline{\hat{\mathbf{u}}} = \underline{\hat{\mathbf{p}}}$ with $n^{\mathrm{DOF}} = n_{\mathrm{s}}^{\mathrm{DOF}} + n_{\mathrm{d}}^{\mathrm{DOF}}$ degrees of freedom. Equation (5.2), used to compute the displacements $\underline{\hat{\mathbf{u}}}_{\mathrm{s}}$, then consists only of some matrix multiplications, which is computationally very cheap. The computation and storage of the inverse $\hat{\mathbf{K}}_{\mathrm{ss}}^{-1}$ can, however, be expensive.

Alternatively, domain d can be extended such that the matrices $\hat{\mathbf{K}}_{\mathrm{sd}}$ and $\hat{\mathbf{K}}_{\mathrm{ds}}$, which contain the degrees of freedom that couple the two domains, remain unchanged during the optimization. Then, the terms $\hat{\mathbf{K}}_{\mathrm{ss}}^{-1}\hat{\mathbf{p}}_{\mathrm{s}}$ and $\hat{\mathbf{K}}_{\mathrm{ss}}^{-1}\hat{\mathbf{K}}_{\mathrm{sd}}$ can be efficiently computed in a preprocessing step using an LU-factorization of

$\hat{\mathbf{K}}_{\mathrm{ss}}$. When $n_{\mathrm{s}}^{\mathrm{DOF}} > n_{\mathrm{d}}^{\mathrm{DOF}}$, the computation of $\hat{\mathbf{K}}_{\mathrm{ss}}^{-1}\hat{\mathbf{K}}_{\mathrm{sd}}$ (and $\hat{\mathbf{K}}_{\mathrm{ss}}^{-1}\hat{\mathbf{p}}_{\mathrm{s}}$) can be more efficient than the computation of $\hat{\mathbf{K}}_{\mathrm{ss}}^{-1}$.

As the element densities of the optimization problem define the material properties of the finite elements in the design domain, the finite element mesh determines the number of element densities. If a distribution of the element densities over a finer mesh is intended, projection methods can be applied [83]. If a distribution of the element densities over a coarser mesh is intended, the mesh of the finite element model can be refined. However, solving the system of equations $\hat{\mathbf{K}}\underline{\hat{\mathbf{u}}} = \underline{\hat{\mathbf{p}}}$ is computationally the most expensive in the iterative topology optimization procedure and this computational cost strongly increases with the number of elements in the model. By only refining the finite element mesh of the design domain, the computational cost is kept to a minimum for the desired detail of design. If only rectangular elements are considered, this, however, results in a mismatch between the two meshes at the boundaries of the design domain (figure 5.2).

Kristensen [109] suggested to add constraints on the displacements of the non-connecting nodes such that these nodes are connected to the surrounding domain. This method is adopted in this work, mainly due to its ease of implementation as only rectangular elements are used. Two examples are shown in figure 5.3. The constraints impose that the displacements at intermediate nodes of the finer mesh coincide with the displacements at the corresponding position on the coarser mesh. The displacements along the edge of the coarser mesh can be computed from the three nodes on this edge since the shape functions are parabolic. The resulting constraint equations can be written in matrix form:

$$\mathbf{Q}\underline{\hat{\mathbf{u}}} = \mathbf{0} \tag{5.4}$$

where the matrix $\mathbf{Q}$ collects the coefficients of the constraint equations.

The constraints in equation (5.4) can be enforced using different methods e.g. using a transformation matrix, adding penalty functions, using Lagrange multipliers, etc. [47, chapter 13]. The efficiency of the different methods is similar. Here, Lagrange multipliers are used,leading to the following system of equations:

$$\begin{bmatrix} \hat{\mathbf{K}} & \mathbf{Q}^T \\ \mathbf{Q} & \mathbf{0} \end{bmatrix} \begin{Bmatrix} \underline{\hat{\mathbf{u}}} \\ \boldsymbol{\chi} \end{Bmatrix} = \begin{Bmatrix} \underline{\hat{\mathbf{p}}} \\ \mathbf{0} \end{Bmatrix} \tag{5.5}$$

where the vector $\boldsymbol{\chi}$ collects the Lagrange multipliers.

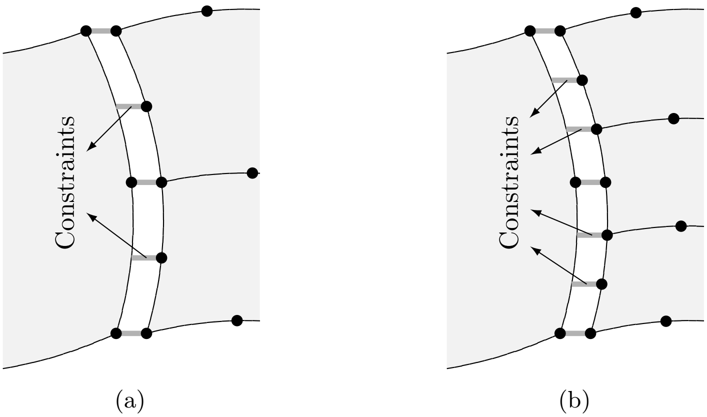

Figure 5.3: Constraints added to the intermediate nodes of the finer mesh in the design domain for a ratio of the element size of the surrounding domain to the element size of the design domain equal to (a) 2 and (b) 3.

5.2.2 Optimization problem

Consider again the topology optimization problem shown in figure 5.2. The aim is to maximize the insertion loss (IL) which is defined as:

$$\hat{\mathrm{IL}}\left(\omega\right) = 10\log_{10}\left(\frac{(\underline{\hat{\mathbf{u}}}^{\mathrm{ref}})^{\mathrm{H}}\mathbf{L}\underline{\hat{\mathbf{u}}}^{\mathrm{ref}}}{\underline{\hat{\mathbf{u}}}^{\mathrm{H}}\mathbf{L}\underline{\hat{\mathbf{u}}}}\right) \tag{5.6}$$

with $(\cdot)^{\mathrm{H}}$ the Hermitian (or conjugate) transpose, $\underline{\hat{\mathbf{u}}}^{\mathrm{ref}}$ the displacement vector of the original field (the homogeneous halfspace) and $\underline{\hat{\mathbf{u}}}$ the displacement vector of the actual field. $\mathbf{L}$ is a sparse selection matrix, containing ones at the diagonal elements corresponding to the degrees of freedom selected for assessing the effectiveness of the wave barrier. For a single degree of freedom, this expression is equivalent to equation (3.48). The problem is reformulated as a minimization problem, with $\phi = -\mathrm{IL}$ as objective function, and is subjected to a volume constraint:

$$\begin{aligned} \min_{\boldsymbol{\rho}} \quad & 10\log_{10}\left(\frac{\underline{\hat{\mathbf{u}}}^{\mathrm{H}}\mathbf{L}\underline{\hat{\mathbf{u}}}}{(\underline{\hat{\mathbf{u}}}^{\mathrm{ref}})^{\mathrm{H}}\mathbf{L}\underline{\hat{\mathbf{u}}}^{\mathrm{ref}}}\right) \\ \text{s. t.} \quad & \sum_{e=1}^{N_e} v_e\bar{\rho}_e \leq V^{\max} \\ & 0 \leq \rho_e \leq 1 \qquad\qquad \forall e = 1\ldots N_e \end{aligned} \tag{5.7}$$

where N_e is the number of elements in the design domain. The upper limit for the volume $V^{\max}$ is set to 20% of the total volume.

As a gradient-based approach is used, the derivatives of the objective function are required. The adjoint method is again applied to compute the gradient as there is a large number of design variables. The sensitivities for an objective function $f\left(\underline{\mathbf{u}}\left(\bar{\boldsymbol{\rho}}\right)\right)$ are given by:

$$\frac{\mathrm{d}f}{\mathrm{d}\bar{\rho}_e} = 2\,\mathrm{Re}\left\{\boldsymbol{\lambda}^{\mathrm{T}}\frac{\partial\hat{\mathbf{K}}}{\partial\bar{\rho}_e}\underline{\mathbf{u}}\right\} \tag{5.8}$$

where the adjoint vector $\boldsymbol{\lambda}$ is obtained from the system of adjoint equations [167]:

$$\begin{bmatrix}\hat{\mathbf{K}} & \mathbf{Q}^{T}\\ \mathbf{Q} & \mathbf{0}\end{bmatrix}\begin{Bmatrix}\boldsymbol{\lambda}\\ \boldsymbol{\mu}\end{Bmatrix} = \begin{Bmatrix}-\left(\dfrac{\partial f}{\partial\hat{\mathbf{u}}}\right)^{\mathrm{T}}\\ \mathbf{0}\end{Bmatrix} \tag{5.9}$$

with $\boldsymbol{\mu}$ the Lagrange multipliers for the adjoint system of equations. For the objective function of the optimization problem in equation (5.7), the top part of the vector on the right-hand side is equal to:

$$-\left(\frac{\partial f}{\partial\underline{\hat{\mathbf{u}}}}\right)^{\mathrm{T}} = \frac{-10}{\ln(10)}\frac{\mathbf{L}\underline{\hat{\mathbf{u}}}^{*}}{\underline{\hat{\mathbf{u}}}^{\mathrm{H}}\mathbf{L}\underline{\hat{\mathbf{u}}}} \tag{5.10}$$

A continuation scheme is used to avoid getting stuck in a local optimum in an early stage of the optimization. The initial value for the smoothness parameter β is 2; this value is doubled every 30 iterations up to a maximum value of 16. A constant filter radius R is used throughout the optimization, equal to 2.5 elements. The MMA algorithm is stopped after 120 iterations.

As in the previous chapter, different excitations are considered in the optimization: harmonic sources, broadband sources and harmonic sources at an unknown frequency in a given range. The different objective functions and the resulting designs are discussed in the following three subsections.

5.2.3 Harmonic sources

In this subsection, harmonic vibration sources are considered. As initial design, all element densities are assigned a value $\rho_e = 0.2$. Two cases are considered. First, only the vertical component of the displacement at the output point is considered in the calculation of the insertion loss (and therefore the objective function). Second, the norm of the displacement vector is considered.

When only the vertical displacement in the output point is considered, the insertion loss becomes:

$$\hat{\mathrm{IL}}_z(\omega) = 10\log_{10}\left(\frac{(\hat{\underline{\mathbf{u}}}^{\mathrm{ref}})^{\mathrm{H}}\mathbf{L}\hat{\underline{\mathbf{u}}}^{\mathrm{ref}}}{\hat{\underline{\mathbf{u}}}^{\mathrm{H}}\mathbf{L}\hat{\underline{\mathbf{u}}}}\right) = 20\log_{10}\left(\left|\frac{\hat{\underline{u}}^{\mathrm{ref}}_{\mathrm{rec}z}}{\hat{\underline{u}}_{\mathrm{rec}z}}\right|\right) \tag{5.11}$$

where $\hat{\underline{u}}^{\mathrm{ref}}_{\mathrm{rec}z}$ and $\hat{\underline{u}}_{\mathrm{rec}z}$ are the displacements at the receiver point in the z-direction for the homogeneous halfspace and after the introduction of the barrier. The insertion losses of the optimized design and a reference rectangular design with dimensions 7.5 m × 1 m are compared in the following. The reference design is shown in figure 5.4. Note that this design is not optimized and, depending on the considered excitation, a better performing rectangular design is possible.

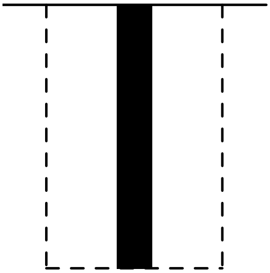

Figure 5.4: The reference design: a rectangular single wall barrier.

The optimization has been performed on Intel® Core™ 2 Duo (2.54 GHz) CPUs. The computing time of the optimization is 18 minutes. Figure 5.5 shows the evolution of the objective function during the optimization for harmonic excitation at 25 Hz. Every 30 iterations, a jump occurs when the sharpness parameter β is adjusted. In the last iteration step, the change in objective function is equal to 6×10^{-5}. The design optimized for harmonic excitation at 25 Hz and the corresponding insertion loss $\hat{\mathrm{IL}}_z$ are shown in figure 5.6.

In the neighborhood of the targeted frequency of 25 Hz, the insertion loss obtained for the optimized design is significantly larger than for the reference design. At higher frequencies, from around 35 Hz, the optimized design performs worse than the reference design and at frequencies above 50 Hz, the insertion loss of the optimized design is close to zero. In this frequency range, the penetration depth of the Rayleigh waves is too small, implying that these waves are not affected by the stiffened material introduced at depth.

The optimized design is symmetric due to the symmetric nature of the problem. The initial design is symmetric and both the load $\hat{\mathbf{p}}$ and the adjoint load

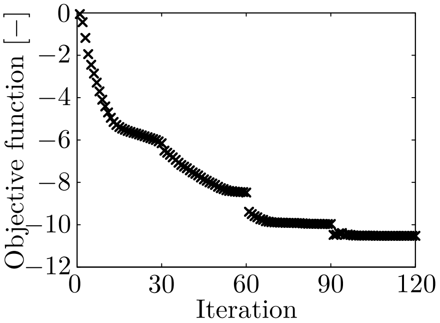

Figure 5.5: Convergence of the optimization problem for the design maximizing $\hat{\mathrm{IL}}_z$ (equation (5.11)) at 25 Hz (figure 5.6a).

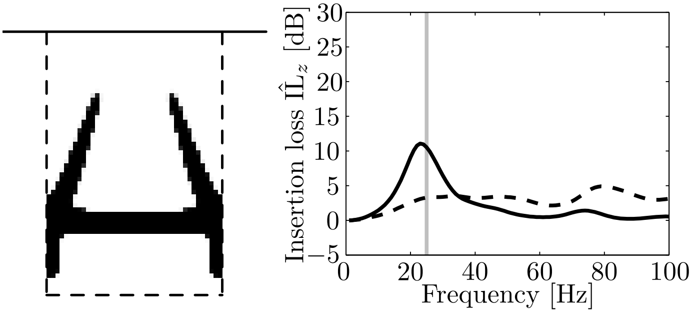

(a) (b)

Figure 5.6: (a) Optimized design maximizing $\hat{\mathrm{IL}}_z$ at 25 Hz, and (b) resulting insertion loss $\hat{\mathrm{IL}}_z$ (Eq. (5.11)) as a function of the frequency for the reference design in figure 5.4 (dashed line) and the optimized design (solid line).

$\dfrac{-10}{\ln(10)} \dfrac{\mathbf{L}\hat{\underline{\mathbf{u}}}^*}{\hat{\underline{\mathbf{u}}}^{\mathrm{H}}\mathbf{L}\hat{\underline{\mathbf{u}}}}$ have only a single entry, at degrees of freedom that are positioned symmetrically with respect to the design domain. This makes the sensitivities in equation (5.8) symmetrical, resulting in a symmetric design. Different asymmetric initial designs have also been tested, resulting in asymmetric optimized designs, but none performed better than the design obtained in figure 5.6.

In order to verify the change in the horizontal response in the output point, the insertion losses $\hat{\mathrm{IL}}_x$ and $\hat{\mathrm{IL}}$, corresponding to the insertion loss of the horizontal response and of the vector sum, are defined as:

$$\hat{\mathrm{IL}}_x(\omega) = 20\log_{10}\left(\left|\frac{\underline{\hat{u}}_{\mathrm{rec}x}^{\mathrm{ref}}}{\underline{\hat{u}}_{\mathrm{rec}x}}\right|\right) \tag{5.12}$$

$$\hat{\mathrm{IL}}(\omega) = 20\log_{10}\left(\frac{\sqrt{\left|\underline{\hat{u}}_{\mathrm{rec}x}^{\mathrm{ref}}\right|^2 + \left|\underline{\hat{u}}_{\mathrm{rec}z}^{\mathrm{ref}}\right|^2}}{\sqrt{\left|\underline{\hat{u}}_{\mathrm{rec}x}\right|^2 + \left|\underline{\hat{u}}_{\mathrm{rec}z}\right|^2}}\right) \tag{5.13}$$

The insertion losses $\hat{\mathrm{IL}}_x$ and $\hat{\mathrm{IL}}$ for the optimized design in figure 5.6a are shown in figure 5.7. The design optimized for the vertical response at 25 Hz leads to a much higher horizontal response at 25 Hz than the reference design and the response is even higher than for the original homogeneous halfspace. As a consequence, the insertion loss of the vector sum $\hat{\mathrm{IL}}$ of the optimized design is hardly higher than for the reference design.

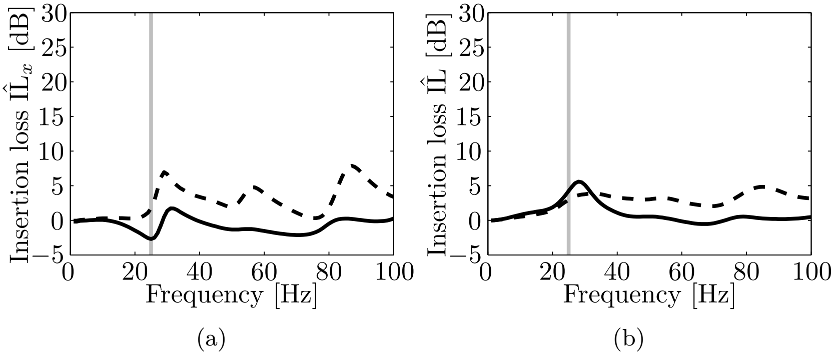

Figure 5.7: The insertion loss (a) $\hat{\mathrm{IL}}_x$ (equation (5.12)) and (b) $\hat{\mathrm{IL}}$ (equation (5.13)) as a function of the frequency for the reference design in figure 5.4 (dashed line) and the optimized design in figure 5.6a (solid line).

Maximizing the insertion loss of the vector sum in equation (5.13) for a harmonic line source at 25 Hz results in the design and insertion loss $\hat{\mathrm{IL}}$ in figure 5.8. By including of the horizontal displacement in the objective function the optimized design is no longer symmetric. Comparing figures 5.7b and 5.8b shows that the resulting insertion loss $\hat{\mathrm{IL}}$ is considerably higher. At 25 Hz, the optimized design leads to a reduction of 6.4 dB compared to the original situation which is 3.4 dB higher than the insertion loss of the reference design in figure 5.4.

The optimized design in figure 5.8a consists of four main features: (1) the vertical part at the left hand side of the design domain, (2) the curved part from

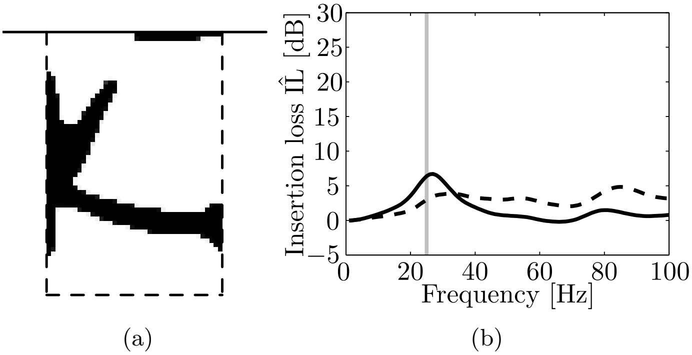

(a) (b)

Figure 5.8: (a) Optimized design maximizing $\hat{\mathrm{IL}}$ at 25 Hz, and (b) resulting insertion loss $\hat{\mathrm{IL}}$ (equation (5.13)) as a function of the frequency for the reference design in figure 5.4 (dashed line) and the optimized design (solid line).

the center of the vertical part to the right hand side of the design domain, (3) the inclined part going upward from the center of the vertical part, and (4) the small horizontal part at the surface. In order to verify the role of these features, figure 5.9 shows the real part of the displacement field and the insertion loss at 25 Hz in the surrounding domain for the homogeneous halfspace, for the reference design, for part (1) of the optimized design, for parts (1) and (2) of the optimized design and for the entire design. The vertical part (1) works mainly as a traditional wall barrier that reflects the incoming waves. Since the design domain comprising the optimal wave barriers is located at the surface of the halfspace, the incoming waves are mainly Rayleigh waves. The Rayleigh waves in a halfspace consisting of solely the original material (with the properties given in table 5.1) have a wave speed C_{R} equal to 186 m/s, or a wavelength λ_{R} equal to 7.5 m at 25 Hz. The depth of the vertical part extends more or less from $0.15\lambda_{\mathrm{R}}$ to $0.85\lambda_{\mathrm{R}}$. Part (2) directs the waves downwards in the domain, reducing the response at the surface. The two other parts strengthen the reflection of the incoming waves and assist in guiding them away from the surface. It should be noted, however, that due to the complex nature of the wave propagation, the performance of the entire design is not the sum of the performances of the different features.

The optimized design and its performance change significantly when the wavelength becomes smaller. Consider for example excitation at 50 Hz. The optimized design and the resulting insertion loss $\hat{\mathrm{IL}}$ are shown in figure 5.10. The peak in the insertion loss at 50 Hz reaches a very high value of 62.3 dB, and is much higher than for the reference design in figure 5.4, where the insertion loss reaches a value of 3.0 dB at 50 Hz.

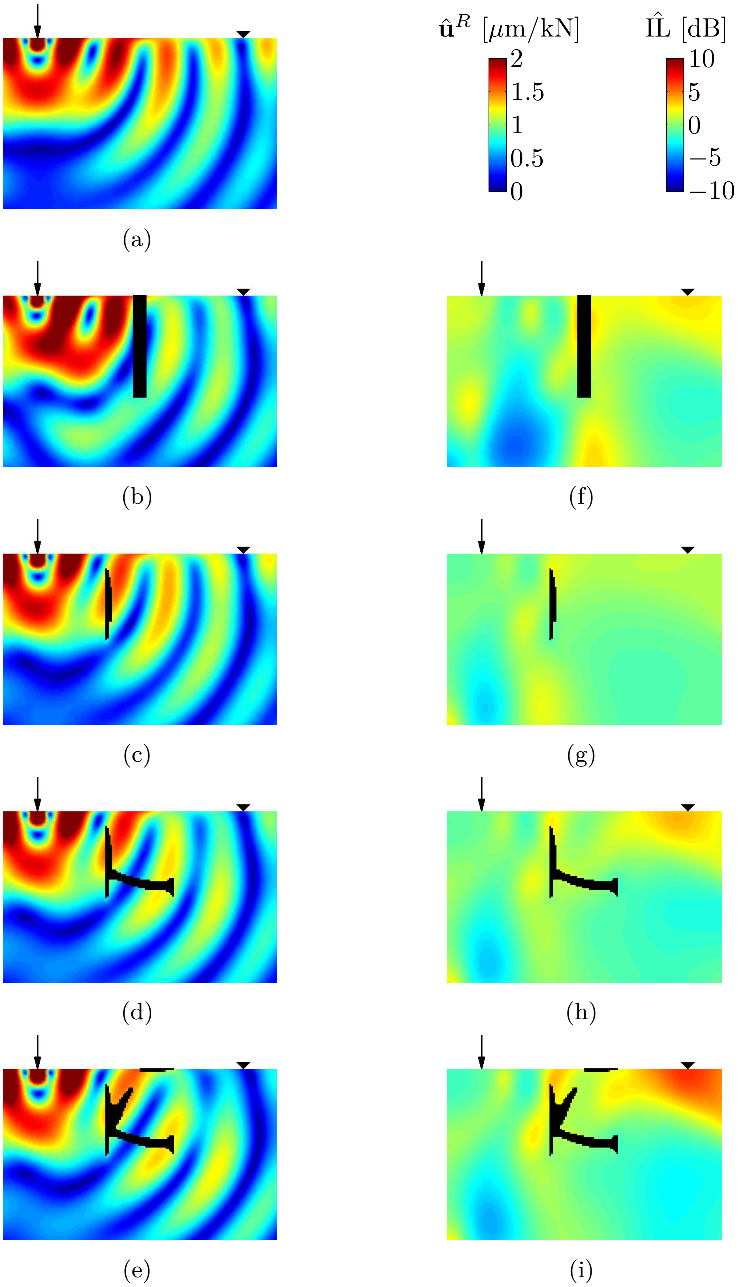

Figure 5.9: Real part of the displacement field $\hat{\mathbf{u}}^R$ at 25 Hz (a) for the original domain and after the introduction of (b) the reference design in figure 5.4, (c) part (1) of the optimized design, (d) parts (1) and (2) of the optimized design, and (e) the entire optimized design maximizing IL at 25 Hz (figure 5.8a). Insertion loss IL at 25 Hz after the introduction of (f) the reference design in figure 5.4, (g) part (1) of the optimized design, (h) parts (1) and (2) of the optimized design, and (i) the entire optimized design maximizing IL at 25 Hz (figure 5.8a).

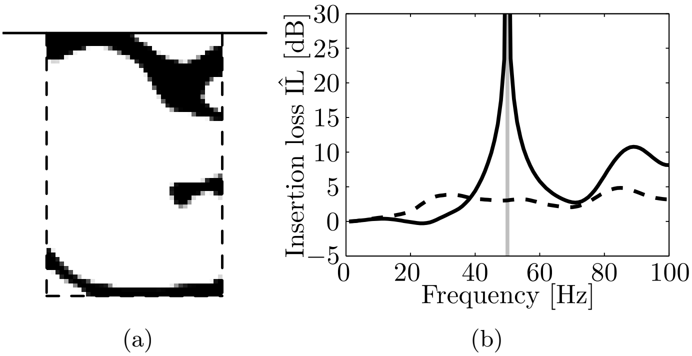

Figure 5.10: (a) Optimized design maximizing $\hat{\mathrm{IL}}$ at 50 Hz, and (b) resulting insertion loss $\hat{\mathrm{IL}}$ (equation (5.13)) as a function of the frequency for the reference design in figure 5.4 (dashed line) and the optimized design (solid line).

In the optimized design of figure 5.10a, material is introduced in three main areas: (1) the top part, partially horizontal and partially inclined, (2) a small middle part, and (3) the curved bottom part at a depth of $2\lambda_{\mathrm{R}}$. Figure 5.11 shows the real part of the displacement field and the insertion loss at 50 Hz in the surrounding domain for the homogeneous halfspace, for the reference design, for the left half of part (1) of the optimized design, for part (1) of the optimized design, and for the entire design. The left half of the top part (1) splits the incoming Rayleigh waves with a wavelength equal to 3.7 m at 50 Hz in two waves, one propagating through the stiffened material and one redirected downwards. The depth of this part is equal to $0.2\lambda_{\mathrm{R}}$. The right half of part (1) directs the waves downwards, away from the surface, outperforming the reference design already by 7.6 dB (compare figures 5.11f and 5.11h). The waves that are redirected downwards by the top part, are guided and reflected by the middle part (2) and the bottom part (3) and finally interfere with the waves transmitted by the top part, minimizing the displacement at the surface. This destructive interference is very sensitive to geometric imperfections, as will be shown in section 5.3.

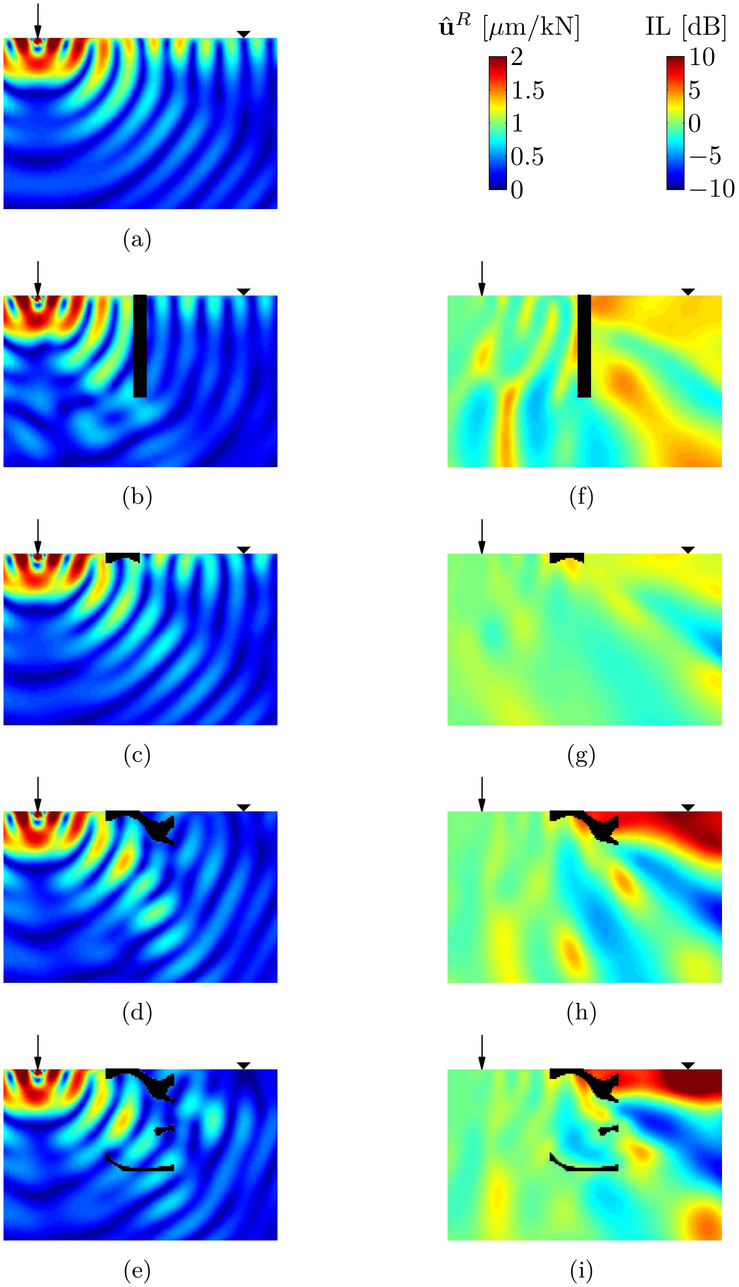

Figure 5.11: Real part of the displacement field $\hat{\mathbf{u}}^R$ at 50 Hz (a) for the original domain and after the introduction of (b) the reference design in figure 5.4, (c) the left half of part (1) of the optimized design, (d) part (1) of the optimized design, and (e) the entire optimized design maximizing $\hat{\mathrm{IL}}$ at 50 Hz (figure 5.10a). Insertion loss $\hat{\mathrm{IL}}$ at 50 Hz after the introduction of (f) the reference design in figure 5.4, (g) the left half of part (1) of the optimized design, (h) part (1) of the optimized design, and (i) the entire optimized design maximizing $\hat{\mathrm{IL}}$ at 50 Hz (figure 5.10a).

5.2.4 Broadband sources

In this section, a broadband source operating over a frequency range $[f_{\mathrm{l}}, f_{\mathrm{u}}]$ is considered. In this case, the frequency averaged insertion loss $\overline{\mathrm{IL}}$ is maximized:

$$\overline{\mathrm{IL}} = \frac{1}{f_{\mathrm{u}} - f_{\mathrm{l}}} \int\limits_{f_{\mathrm{l}}}^{f_{\mathrm{u}}} \hat{\mathrm{IL}}(f)\mathrm{d}f = \frac{10}{f_{\mathrm{u}} - f_{\mathrm{l}}} \int\limits_{f_{\mathrm{l}}}^{f_{\mathrm{u}}} \log_{10}\left(\frac{\left|\hat{\underline{u}}^{\mathrm{ref}}_{\mathrm{rec}x}(f)\right|^2 + \left|\hat{\underline{u}}^{\mathrm{ref}}_{\mathrm{rec}z}(f)\right|^2}{\left|\hat{\underline{u}}_{\mathrm{rec}x}(f)\right|^2 + \left|\hat{\underline{u}}_{\mathrm{rec}z}(f)\right|^2} \right) \mathrm{d}f \tag{5.14}$$

The optimization problem minimizes the objective function $f = -\overline{\mathrm{IL}}$, where the integral in equation (5.14) is approximated by a discretization of the frequency range by N_f equidistant frequencies.

$$\begin{aligned} \min_{\boldsymbol{\rho}} \quad & \frac{10}{N_{\mathrm{f}}} \sum_{j=1}^{N_f} \log_{10}\left(\frac{\left|\hat{\underline{u}}_{\mathrm{rec}x}(f_j)\right|^2 + \left|\hat{\underline{u}}_{\mathrm{rec}z}(f_j)\right|^2}{\left|\hat{\underline{u}}^{\mathrm{ref}}_{\mathrm{rec}x}(f_j)\right|^2 + \left|\hat{\underline{u}}^{\mathrm{ref}}_{\mathrm{rec}z}(f_j)\right|^2} \right) \\ \mathrm{s.\,t.} \quad & \sum_{e=1}^{N_e} v_e \bar{\rho}_e \leq V^{\max} \\ & 0 \leq \rho_e \leq 1 \qquad\qquad\qquad\qquad \forall e = 1 \ldots N_e \end{aligned} \tag{5.15}$$

Figure 5.12 shows the design optimized over the frequency range from 20−80 Hz, using $N_f = 10$ frequencies in equation (5.15), and the resulting insertion loss $\hat{\mathrm{IL}}$. The frequency averaged insertion loss is equal to 3.0 dB for the reference design and 12.6 dB for the optimized design. Increasing the number of frequencies N_f hardly changes the optimal design geometry, indicating that taking only 10 frequencies into account is sufficient.

The optimization leads to designs which mainly reduce transmission at higher frequencies, as it is easier to obtain high insertion loss values in this frequency range, as observed in the previous subsection. Figure 5.13 shows the real part of the displacement field for frequencies of 30 Hz ($\lambda_{\mathrm{R}} = 6.2$m), 50 Hz ($\lambda_{\mathrm{R}} = 3.7$m), and 70 Hz ($\lambda_{\mathrm{R}} = 2.7$m) in the surrounding domain for the homogeneous halfspace, the reference design and the design optimized for the average insertion loss in the frequency range $20 - 80$ Hz. For the highest frequencies of the target range, almost all the energy is reflected by the structure, resulting in a negative insertion loss value in front of the design domain and a high insertion loss value behind the design domain. However, the insertion loss for the lowest frequencies is rather small, and below 40 Hz ($\lambda_{\mathrm{R}} = 4.7$m), the insertion loss for the optimized design is lower than for the reference design. If needed, more weight can be given to certain frequencies by introducing a weighting function in equation (5.14).

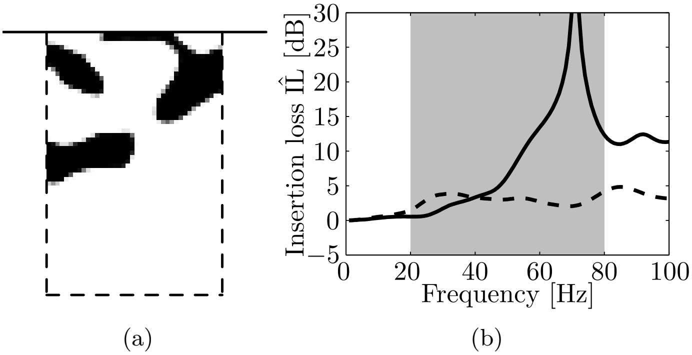

(a) (b)

Figure 5.12: (a) Optimized design maximizing $\overline{\mathrm{IL}}$ over the frequency range $20 - 80\,\mathrm{Hz}$ (discretized with 10 frequencies), and (b) resulting insertion loss $\hat{\mathrm{IL}}$ (equation (5.13)) as a function of the frequency for the reference design in figure 5.4 (dashed line) and the optimized design (solid line).

5.2.5 Harmonic sources at a frequency in a given range

In this section, harmonic sources at an unknown frequency in a given frequency range are considered. In this case, the minimal insertion loss is maximized, and the optimization problem becomes:

$$\begin{aligned}
\min_{\boldsymbol{\rho}} \quad & \max_{\substack{f_j \\ j=1\ldots N_f}} \; 10\log_{10}\left(\frac{\left|\underline{\hat{u}}_{\mathrm{rec}x}(f_j)\right|^2 + \left|\underline{\hat{u}}_{\mathrm{rec}z}(f_j)\right|^2}{\left|\underline{\hat{u}}^{\mathrm{ref}}_{\mathrm{rec}x}(f_j)\right|^2 + \left|\underline{\hat{u}}^{\mathrm{ref}}_{\mathrm{rec}z}(f_j)\right|^2}\right) \\
\mathrm{s.\,t.} \quad & \sum_{e=1}^{N} v_e \bar{\rho}_e \leq V^{\max} \\
& 0 \leq \rho_e \leq 1 \qquad\qquad \forall e = 1\ldots N_e
\end{aligned} \tag{5.16}$$

The frequency range is discretized using $N_f = 10$ equidistant frequencies. This problem is not differentiable and is therefore reformulated using a bound formulation as in section 4.3.4. Figure 5.14 shows the design optimized over the frequency range $20 - 80\,\mathrm{Hz}$, corresponding to Rayleigh wavelengths between $2.3\,\mathrm{m}$ and $9.3\,\mathrm{m}$, and the resulting insertion loss. The minimal insertion loss is equal to $1.5\,\mathrm{dB}$ for the reference design and $3.2\,\mathrm{dB}$ for the optimized design. The insertion loss is higher than for the reference design in the entire frequency range considered. This improvement, however, is rather small for most of the frequency range and is accompanied with a considerable loss in feasibility. The optimized design contains a part (1) that maximizes the insertion loss in the lower frequency range (bottom left, compare with figure 5.8a) and a part (2) for the higher frequency range (top right, compare with figure 5.10a).

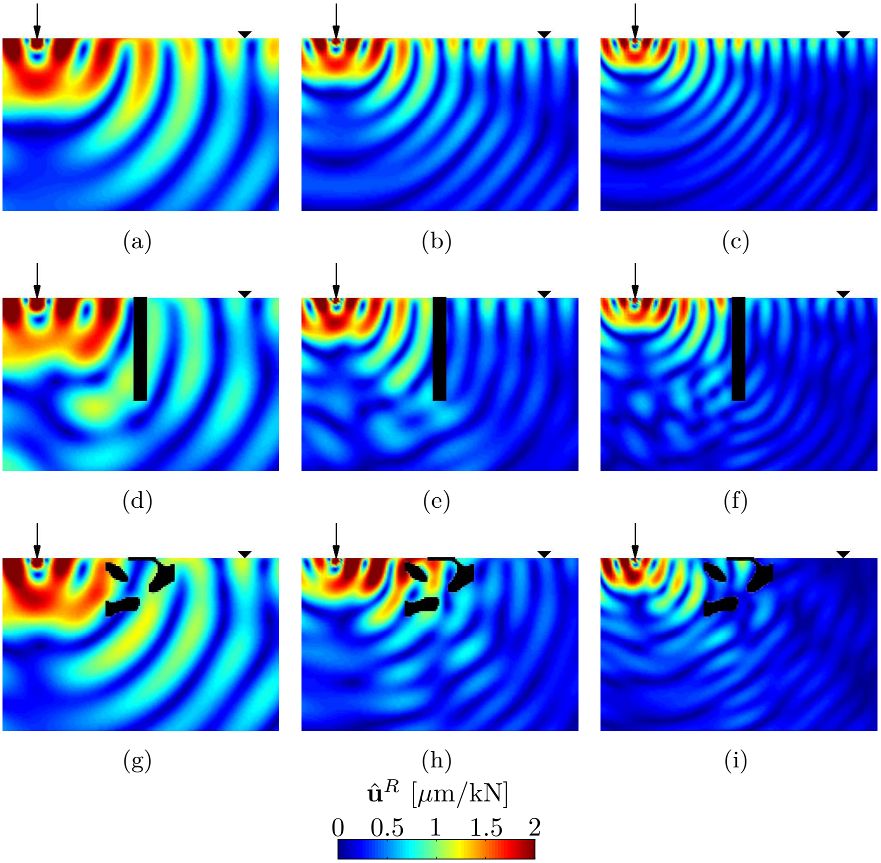

Figure 5.13: Real part of the displacement field $\hat{\mathbf{u}}^R$ in the homogeneous halfspace for excitation at (a) 30 Hz, (b) 50 Hz, and (c) 70 Hz, with the reference design for excitation at (d) 30 Hz, (e) 50 Hz, and (f) 70 Hz, and with the design maximizing the frequency averaged insertion loss $\overline{\mathrm{IL}}$ for excitation at (g) 30 Hz, (h) 50 Hz, and (i) 70 Hz.

5.3 Robust optimization and practical designs

5.3.1 Geometric imperfections

Topology optimization leads to designs which are optimal for the specific problem considered. In many cases, the performance is very sensitive to geometric imperfections. Consider for example the design in figure 5.10a. This

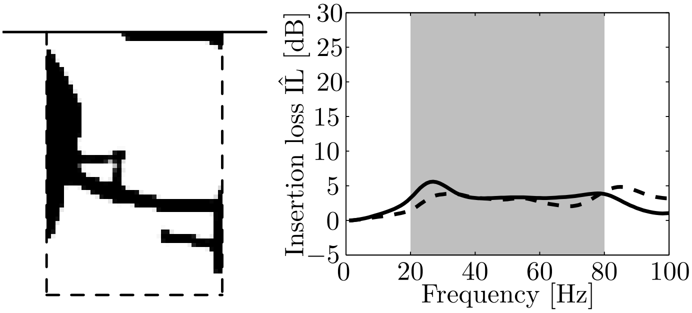

(a) (b)

Figure 5.14: (a) Optimized design maximizing $\min_{f_n} \hat{\mathrm{IL}}(f_n)$ over the frequency range $20 - 80$ Hz (discretized with 10 frequencies), and (b) resulting insertion loss $\hat{\mathrm{IL}}$ (equation (5.13)) as a function of the frequency for the reference design in figure 5.4 (dashed line) and the optimized design (solid line).

design contains small features, making it very sensitive to deviations in the geometry of these features. As a consequence, the performance of the actual wave barrier with construction errors present may be far from optimal.

The influence of errors in the (in-plane) dimensions of the stiffened material can be verified by varying the Heaviside projection threshold η in equation (4.11) [143]. For low values of the Heaviside projection threshold (e.g. $\eta = 0.25$), lower values of the filtered densities are projected to the stiffened material as well, and the dimensions of the stiffened material increase, leading to so-called dilated designs. For high values of the Heaviside projection threshold (e.g. $\eta = 0.75$), only the higher values of the filtered densities are projected to the stiffened material, and the dimensions of the stiffened material decrease, leading to so-called eroded designs.

Figures 5.15a-c show the dilated, intermediate, and eroded version of the design optimized at a frequency of 25 Hz (figure 5.8). The corresponding insertion loss values are indicated in figure 5.15d, which shows the insertion loss as a function of the projection threshold. Increasing the Heaviside projection threshold η results in a reduction of the dimensions of the stiffened material. This is accompanied by a decrease in the insertion loss. The upper value $\eta = 1$ removes almost all stiffened material from the design ($\underline{\hat{\mathbf{u}}} \approx \underline{\hat{\mathbf{u}}}^{\mathrm{ref}}$), and the insertion loss (equation (5.6)) becomes close to zero.

Figure 5.16 shows the influence of the Heaviside projection threshold η for the design optimized for reducing transmission at a frequency of 50 Hz (figure 5.10). In contrast to the design optimized at a frequency of 25 Hz, a high value occurs

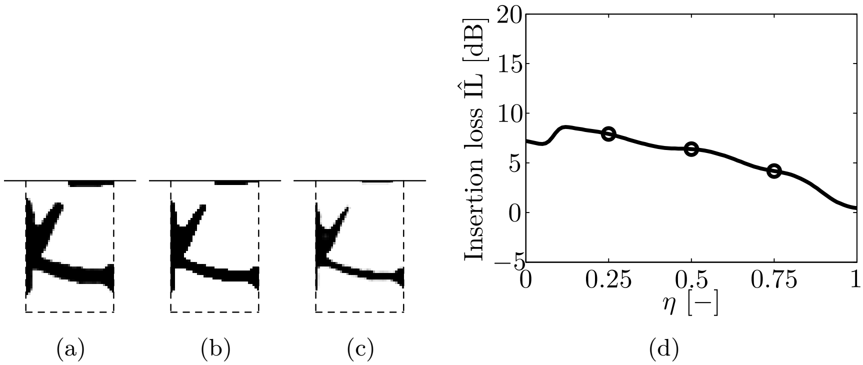

Figure 5.15: The (a) dilated ($\eta = 0.25$), (b) intermediate ($\eta = 0.5$), and (c) eroded ($\eta = 0.75$) version of the optimized design maximizing the insertion loss $\hat{IL}$ at a frequency of 25 Hz (figure 5.8a) and (d) the influence of the projection threshold η on the insertion loss $\hat{IL}$ at 25 Hz.

at $\eta = 0.5$ (intermediate design). The performance is therefore very sensitive to thickness variations as these disturb the previously discussed interference. For the dilated design ($\eta = 0.25$), a high performance is still obtained thanks to the top part of the design, which is largely affected for the eroded design ($\eta = 0.75$).

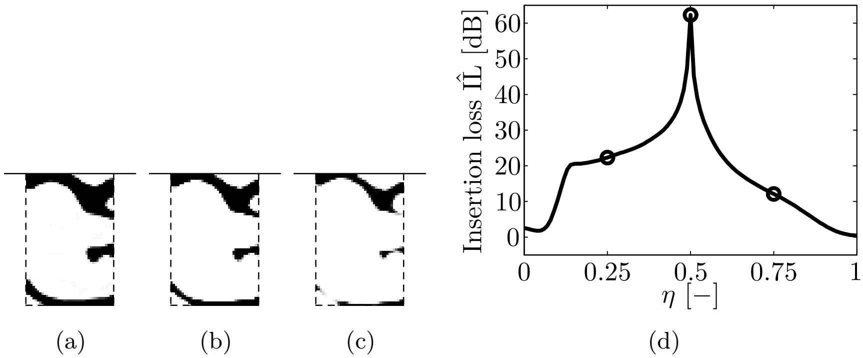

Figure 5.16: The (a) dilated ($\eta = 0.25$), (b) intermediate ($\eta = 0.5$), and (c) eroded ($\eta = 0.75$) version of the optimized design maximizing the insertion loss $\hat{IL}$ at a frequency of 50 Hz (figure 5.10a) and (d) the influence of the projection threshold η on the insertion loss $\hat{IL}$ at 50 Hz.

The effect of the projection threshold on the designs maximizing the frequency averaged and minimal insertion loss in the frequency range 20 – 80 Hz is shown in figures 5.17 and 5.18. These results show that the design maximizing the minimal insertion loss (equation (5.16)) is less sensitive to thickness variations than the design maximizing the frequency averaged insertion loss (equation (5.15)). The former is significantly affected only for higher values of the projection threshold η, leading to modifications in the top part of the design which result in a lower performance at higher frequencies. The design maximizing the frequency averaged insertion loss is much more sensitive, and especially for projection thresholds larger than 0.5 the performance strongly decreases.

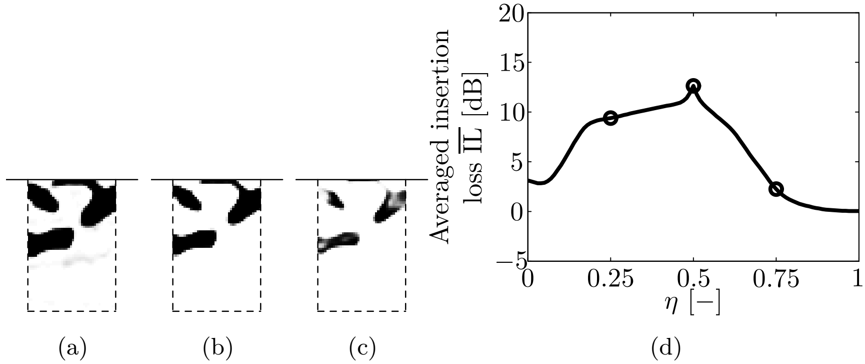

Figure 5.17: The (a) dilated ($\eta = 0.25$), (b) intermediate ($\eta = 0.5$), and (c) eroded ($\eta = 0.75$) version of the optimized design maximizing the frequency averaged insertion loss $\overline{\mathrm{IL}}$ over the frequency range 20 – 80 Hz (figure 5.12a) and (d) the influence of the projection threshold η on the frequency averaged insertion loss $\overline{\mathrm{IL}}$ in the frequency range 20 – 80 Hz.

5.3.2 Robust topology optimization

In order to obtain designs which are less sensitive to this type of geometric imperfections, a robust topology optimization approach is adopted. Here, robust topology optimization is applied to account for deviations from the design geometry maximizing the frequency averaged insertion loss. The interval of the projection threshold is set to $[0.25, 0.75]$.

Since the insertion loss in figure 5.17 is rather smooth, a worst case formulation [147, 172] considering only three cases is expected to give good

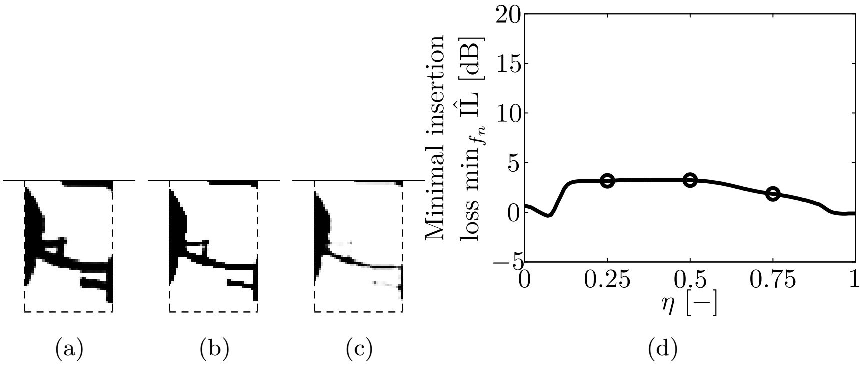

Figure 5.18: The (a) dilated ($\eta = 0.25$), (b) intermediate ($\eta = 0.5$), and (c) eroded ($\eta = 0.75$) version of the optimized design maximizing the minimal insertion loss $\min_{f_n} \hat{\mathrm{IL}}(f_n)$ over the frequency range 20 − 80 Hz (figure 5.14a) and (d) the influence of the projection threshold η on the minimal insertion loss $\min_{f_n} \hat{\mathrm{IL}}$ in the frequency range 20 − 80 Hz.

results. The robust optimization problem is formulated as follows:

$$\begin{aligned} \min_{\boldsymbol{\rho}} \quad & \max\left\{f\left(\bar{\boldsymbol{\rho}}^{\mathrm{d}}\right), f\left(\bar{\boldsymbol{\rho}}^{\mathrm{i}}\right), f\left(\bar{\boldsymbol{\rho}}^{\mathrm{e}}\right)\right\} \\ \text{s. t.} \quad & \sum_{e=1}^{N_e} v_e \bar{\rho}_e^{\mathrm{d}} \leq V_{\mathrm{d}}^{\max} \\ & 0 \leq \rho_e \leq 1 \qquad\qquad \forall e = 1 \ldots N_e \end{aligned} \tag{5.17}$$

where $\bar{\boldsymbol{\rho}}^{\mathrm{d}}$, $\bar{\boldsymbol{\rho}}^{\mathrm{i}}$, and $\bar{\boldsymbol{\rho}}^{\mathrm{e}}$ are the dilated ($\eta^{\mathrm{d}} = \eta^{\mathrm{i}} - \Delta\eta$), intermediate ($\eta^{\mathrm{i}}$) and eroded ($\eta^{\mathrm{e}} = \eta^{\mathrm{i}} + \Delta\eta$) volume densities, respectively. Every 20 iterations, the volume constraint on the dilated design $V_{\mathrm{d}}^{\max}$ is updated such that $V_{\mathrm{d}}^{\max} = \frac{\sum_{e=1}^{N_e} v_e \bar{\rho}_e^{\mathrm{d}}}{\sum_{e=1}^{N_e} v_e \bar{\rho}_e^{\mathrm{i}}} V^{\max}$ where $V^{\max}$ is the volume constraint on the intermediate design, equal to 20 % of the design domain.

As before, the dilated design corresponds to a value of the Heaviside projection threshold equal to $\eta = 0.25$, the intermediate design to a value $\eta = 0.5$, and the eroded design to a value $\eta = 0.75$. Figure 5.19 shows the resulting robust design and insertion loss. The design is rather similar to the deterministic design in figure 5.12a and also results in a higher values for the insertion loss at the higher frequencies of the range considered. The thin part of the deterministic design close to the surface (figure 5.12a) has thickened, however. The material is redistributed and some of the other parts have lost material. The changes in geometry lead to a lower (deterministic) performance for the intermediate design, resulting in a frequency averaged insertion loss of 6.6 dB instead of 12.6 dB.

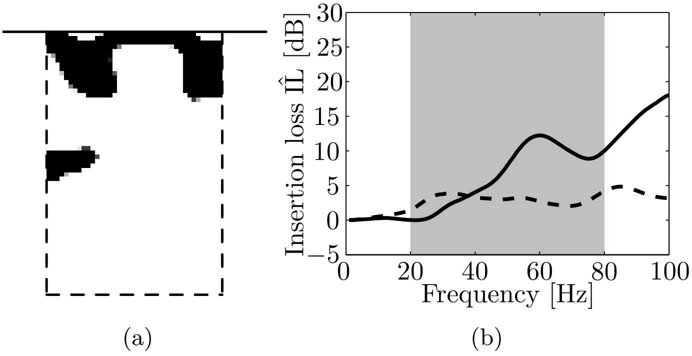

(a) (b)

Figure 5.19: (a) Optimized design maximizing $\overline{\mathrm{IL}}$ over the frequency range 20−80 Hz (discretized with 10 frequencies) using a worst case robust approach, and (b) resulting insertion loss $\hat{\mathrm{IL}}$ (equation (5.13)) as a function of the frequency for the reference design in figure 5.4 (dashed line) and the optimized (intermediate) design (solid line).

The robust design is less sensitive to thickness variations, as can be seen in figure 5.20, where the frequency averaged insertion loss $\overline{\mathrm{IL}}$ is plotted as a function of the projection threshold η. The averaged insertion loss is practically insensitive to the projection threshold η in the range considered. The frequency averaged insertion loss is therefore larger than 5.3 dB over the entire range $\eta = [0.25, 0.75]$.

Because of construction constraints, it may be difficult to reproduce the design in figure 5.19a. Since the design is robust to thickness variations, a simplification of the geometry is not expected to significantly affect the performance of the design. Figure 5.21 shows a manually simplified design and the corresponding insertion loss $\hat{\mathrm{IL}}$ which has been obtained by intuitively positioning two rectangles where the stiffened material is concentrated in the topology optimized design. Comparing figures 5.19b and 5.21b shows that the performance of the latter design is similar to the performance of the design obtained with robust topology optimization. The peak value of the insertion loss at higher frequencies is lower, and the frequency averaged insertion loss is equal to 5.5 dB instead of 6.6 dB, but the simplified design still outperforms the reference design which has a frequency averaged insertion loss of 3.0 dB.

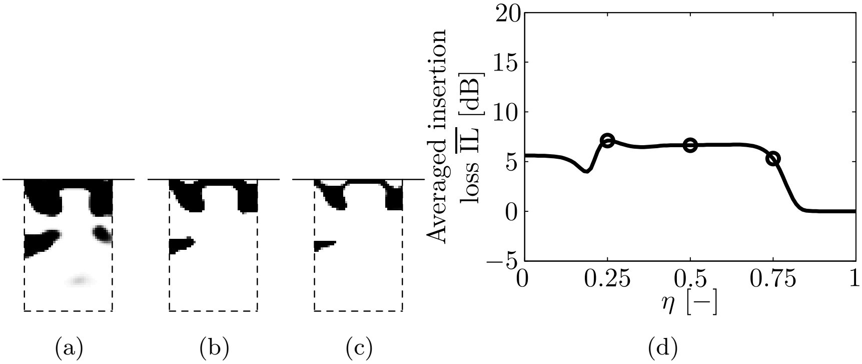

Figure 5.20: The (a) dilated ($\eta = 0.25$), (b) intermediate ($\eta = 0.5$), and (c) eroded ($\eta = 0.75$) version of the robust optimized design maximizing the frequency averaged insertion loss $\overline{\text{IL}}$ over the frequency range $20-80\,\text{Hz}$ (figure 5.19a) and (d) the influence of the projection threshold η on the frequency averaged insertion loss $\overline{\text{IL}}$ in the frequency range $20-80\,\text{Hz}$.

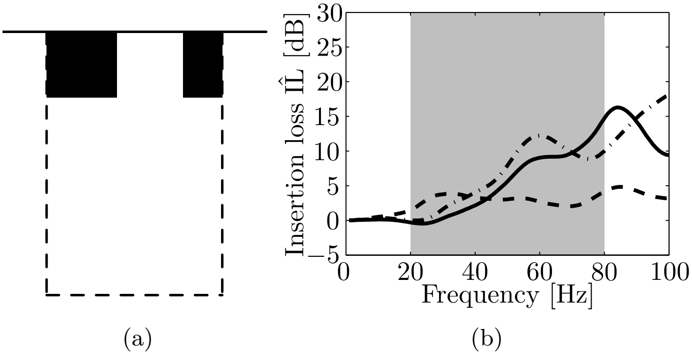

Figure 5.21: (a) Simplified design after manual post-processing of the optimized design maximizing $\overline{\text{IL}}$ over the frequency range $20-80\,\text{Hz}$ (discretized with 10 frequencies) using a worst case robust approach (figure 5.19a), and (b) resulting insertion loss $\hat{\text{IL}}$ (Eq. (5.13)) as a function of the frequency for the reference design in figure 5.4 (dashed line), the robust optimized design in figure 5.19a (dashed-dotted line), and the post-processed design (solid line).

5.3.3 Shape optimization

As topology optimization often leads to designs with a complex layout containing small features, it is not always practical to build the designs. In the previous section, the robust solution is used as a basis for a simplified design solution. However, this design is not an actual optimum for the considered optimization problem. The topology optimization procedure is therefore often followed by a shape and/or size optimization step.

In most shape optimization approaches, the boundaries of the design are parametrized. This is mostly done by dividing the design boundary in a number of segments. These segments can for example be straight lines. The boundaries are then determined by the coordinates of the nodes between the different segments. The shape optimization consists of optimizing the objective function with the coordinates of the nodes as design variables.

In this section, an alternative shape optimization is proposed, which allows reusing the sensitivities derived for the topology optimization problem. Every object o is described by different $(j = 1 \dots N_j^o)$ parameters p_j^o. The sensitivities with respect to the parameter p_j^o in the shape optimization problem are then calculated as:

$$\frac{\mathrm{d}f}{\mathrm{d}p_j^o} = \sum_{e=1}^{N_e} \frac{\mathrm{d}f}{\mathrm{d}\bar{\rho}_e} \frac{\partial \bar{\rho}_e}{\partial p_j^o} \tag{5.18}$$

where only the derivatives $\frac{\partial \bar{\rho}_e}{\partial p_j^o}$ still need to be derived. This can be done analytically.

The parameters p_j^o can be the coordinates of the different nodes, or any other parameter describing the shapes of the different objects. For general polygons, the node coordinates are a good choice. However, for specific objects, such as rectangles, taking the coordinates of all nodes will not necessarily lead to rectangles, as any quadrilateral is possible. Possible strategies to resolve this include the formulation of constraints or the consideration of a limited number of coordinates (for example three x- and two z-coordinates). Alternatively, the rectangle can be parametrized in a different way, for example by the x- and z-coordinate $(X_\mathrm{c}^o, Z_\mathrm{c}^o)$ of the center point, the width W^o, the height H^o and the angle Θ^o (figure 5.22).

To construct the element density field from these parameters, a strategy similar to the projection filter is applied. A pyramid is first constructed after which a (relaxed) Heaviside projection is applied. Consider the following auxiliary

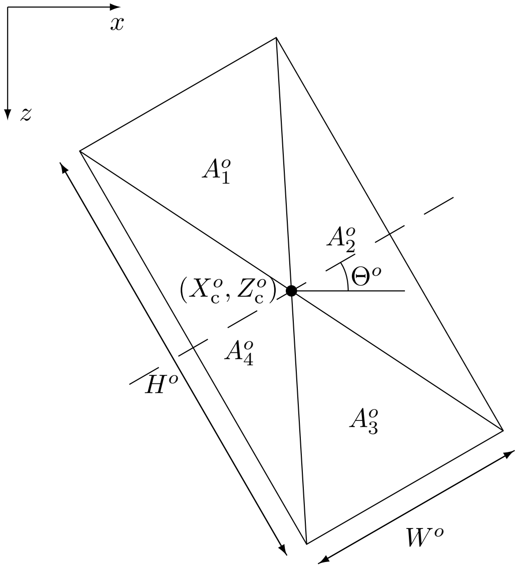

Figure 5.22: Pyramid for the construction of rectangular objects. The function μ_e^o describing this pyramid is built from the auxiliary functions A_1^o, A_2^o, A_3^o, and A_4^o.

functions (figure 5.22):

$$\begin{cases} A_1^o(x_e, z_e) = 1 + \dfrac{2}{H^o}\left[(x_e - X_\mathrm{c}^o)\sin\Theta^o + (z_e - Z_\mathrm{c}^o)\cos\Theta^o\right] \\ A_2^o(x_e, z_e) = 1 - \dfrac{2}{W^o}\left[(x_e - X_\mathrm{c}^o)\cos\Theta^o - (z_e - Z_\mathrm{c}^o)\sin\Theta^o\right] \\ A_3^o(x_e, z_e) = 1 - \dfrac{2}{H^o}\left[(x_e - X_\mathrm{c}^o)\sin\Theta^o + (z_e - Z_\mathrm{c}^o)\cos\Theta^o\right] \\ A_4^o(x_e, z_e) = 1 + \dfrac{2}{W^o}\left[(x_e - X_\mathrm{c}^o)\cos\Theta^o - (z_e - Z_\mathrm{c}^o)\sin\Theta^o\right] \end{cases} \tag{5.19}$$

with (x_e, z_e) the position of element e in the design domain. These auxiliary functions represent planes defined by a point and a line: they are equal to 1 at $(X_\mathrm{c}^o, Z_\mathrm{c}^o)$ and equal to 0 at one edge of the rectangle. Then the pyramid is constructed as:

$$\mu_e^o = \begin{cases} \min\left\{A_1^o(x_e, z_e), A_2^o(x_e, z_e), A_3^o(x_e, z_e), A_4^o(x_e, z_e)\right\} & \text{if } (x_e, z_e) \in \Omega^o \\ 0 & \text{if } (x_e, z_e) \notin \Omega^o \end{cases} \tag{5.20}$$

where Ω^o defines the area of the object. The pyramid is positive for $(x_e, z_e) \in \Omega^o$, equal to 1 at (X_c^o, Z_c^o), and equal to 0 at the four edges of the rectangle. This can reformulated as:

$$\mu_e^o = \max\left\{0, \min\left\{A_1^o(x_e, z_e), A_2^o(x_e, z_e), A_3^o(x_e, z_e), A_4^o(x_e, z_e)\right\}\right\} \tag{5.21}$$

The densities $\tilde{\rho}_e$ are then obtained by summing over the different objects:

$$\tilde{\rho}_e = \sum_{o=1}^{N^o} \mu_e^o \tag{5.22}$$

which are projected to obtain the element densities $\bar{\rho}_e$. All densities equal to zero should remain zero while higher densities should be projected to one (and should be equal to one for $\tilde{\rho}_e = \infty$ as it is possible that $\tilde{\rho}_e > 1$). The relaxed Heaviside projection can therefore have the following form:

$$\bar{\rho}_e = \tanh\left(\beta \tilde{\rho}_e\right) \tag{5.23}$$

where β is again a sharpness parameter.

Figure 5.23 shows the different steps followed to obtain the simplified robust design in figure 5.21a. First the two pyramid density fields $\boldsymbol{\mu}^1$ and $\boldsymbol{\mu}^2$ are constructed using the auxiliary functions in equation (5.19). The addition of both fields leads to the density field $\tilde{\boldsymbol{\rho}}$. By projecting this field using equation (5.23), the actual element density field is obtained. The projection can be regularized by changing the sharpness parameter β.

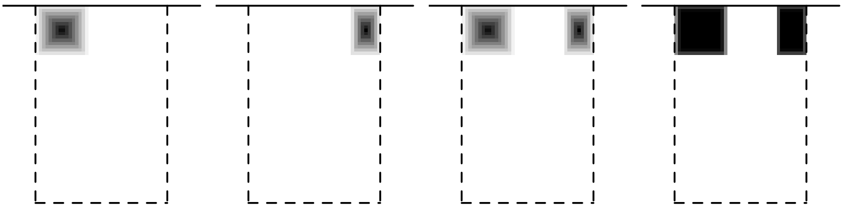
(a) (b) (c) (d)

Figure 5.23: Construction of the element density field for the shape optimization problem: (a) pyramid densities $\boldsymbol{\mu}^1$, (a) pyramid densities $\boldsymbol{\mu}^2$, (c) total densities $\tilde{\boldsymbol{\rho}}$, and (d) element densities $\bar{\boldsymbol{\rho}}$ for a sharpness parameter $\beta = 8$.

The sensitivities of the element densities $\bar{\rho}_e$ with respect to the parameters p_j^o are then calculated using the chain rule:

$$\frac{\partial \bar{\rho}_e}{\partial p_j^o} = \frac{\partial \bar{\rho}_e}{\partial \tilde{\rho}_e} \frac{\partial \tilde{\rho}_e}{\partial \mu_e^o} \frac{\partial \mu_e^o}{\partial p_j^o} \tag{5.24}$$

The second factor is equal to 1 and the first factor is simply computed as:

$$\frac{\partial \bar{\rho}_e}{\partial \tilde{\rho}_e} = \beta \mathrm{sech}^2\left(\beta \tilde{\rho}_e\right) \tag{5.25}$$

The third factor depends on the position of the element in the design domain:

$$\frac{\partial \mu_e^o}{\partial p_j^o} = \begin{cases} \dfrac{\partial A_1^o}{\partial p_j^o}(x_e, z_e) & \text{if } (x_e, z_e) \in \Omega_1^o \\ \dfrac{\partial A_2^o}{\partial p_j^o}(x_e, z_e) & \text{if } (x_e, z_e) \in \Omega_2^o \\ \dfrac{\partial A_3^o}{\partial p_j^o}(x_e, z_e) & \text{if } (x_e, z_e) \in \Omega_3^o \\ \dfrac{\partial A_4^o}{\partial p_j^o}(x_e, z_e) & \text{if } (x_e, z_e) \in \Omega_4^o \\ 0 & \text{if } (x_e, z_e) \notin \Omega^o \end{cases} \tag{5.26}$$

where $\Omega^o = \Omega_1^o \cup \Omega_2^o \cup \Omega_3^o \cup \Omega_4^o$ and $\Omega_n^o \subset \Omega^o$ is the area where $A_n^o \leq A_m^o$, $\forall m \neq n$. Alternatively, these areas are defined as $\Omega_n^o = \{(x_e, z_e) \subset \Omega^o | \mu_e^o = A_n^o\}$. The derivatives of the auxiliary functions A_n^o to the parameters X_c^o, Z_c^o, W^o, H^o, and Θ^o can be derived from equation (5.19). As these derivations are relatively simple, they are not elaborated here. Note that the function μ_e^o is not differentiable at the boundaries of the different domains Ω_n^o. The derivative for one of the adjacent domains is therefore used at the boundaries. This resulted in a smooth convergence, presumably because these boundaries rarely coincide exactly with the element centers.

The parameter optimization is applied for minimizing the frequency averaged insertion loss $\overline{\mathrm{IL}}$ over the frequency range $20 - 80\,\mathrm{Hz}$. A volume constraint is added allowing a maximum volume equal to 20 % of the design domain. The following limits are applied for the design variables: $0 \leq X_c^o \leq L_{x\mathrm{d}}$, $0 \leq Z_c^o \leq L_{z\mathrm{d}}$, $0 \leq W^o \leq \sqrt{L_{x\mathrm{d}}^2 + L_{z\mathrm{d}}^2}$, $0 \leq H^o \leq \sqrt{L_{x\mathrm{d}}^2 + L_{z\mathrm{d}}^2}$, and $-\pi \leq \Theta^o \leq \pi$. In this, $L_{x\mathrm{d}} = 5\,\mathrm{m}$ and $L_{z\mathrm{d}} = 7.5\,\mathrm{m}$ are the width and the height of the design domain. The smoothness parameter β is set equal to 16.

Many local minima exist for this optimization problem, and a continuation scheme for the smoothness parameter β was not found to help. A good initial design is therefore important to obtain a good result. Here the simplified robust design in figure 5.21a is used as initial design. The MMA algorithm is stopped after 200 iterations, corresponding to a computing time of 30 minutes. The evolution of the objective function is shown in figure 5.24. As pointed out before, the convergence proceeds smoothly. At 30 iterations, the change in objective function is equal to 1.6×10^{-4}.

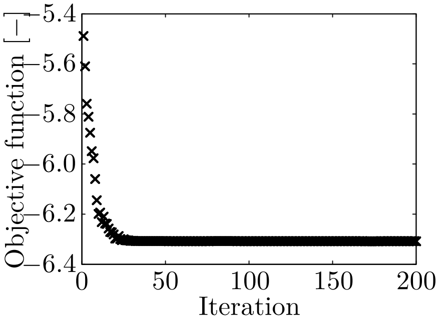

Figure 5.24: Convergence of the optimization problem for the shape optimization problem (figure 5.25).

Figure 5.25 shows the resulting design and the corresponding insertion loss $\hat{\mathrm{IL}}$. The frequency averaged insertion loss increases from 5.5 dB to 6.3 dB due to the better performance at higher frequencies. In the optimized design, the right rectangle has become thicker and shorter, the two rectangles are rotated over a small angle and they are positioned lower in the design domain. As a result of the latter, there is no material inserted at the surface, similarly to the robust optimized design in figure 5.19a.

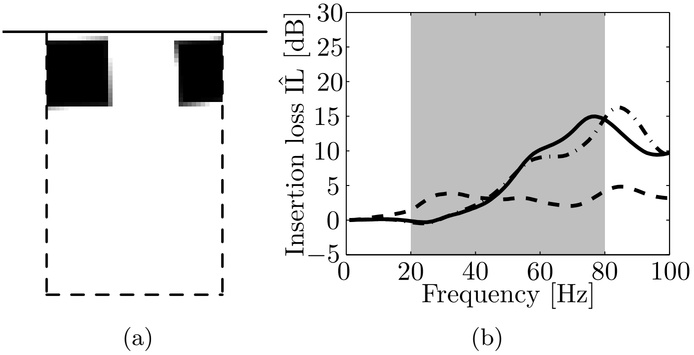

(a) (b)

Figure 5.25: (a) Shape optimized design maximizing $\overline{\mathrm{IL}}$ over the frequency range 20 – 80 Hz (discretized with 10 frequencies), and (b) resulting insertion loss $\hat{\mathrm{IL}}$ (Eq. (5.13)) as a function of the frequency for the reference design in figure 5.4 (dashed line), the simplified robust design in figure 5.21a (dashed-dotted line) and the parameter optimized design (solid line).

5.3.4 Discrete object layout optimization

In the previous section, the number of objects was kept constant while the shape was optimized. In this section, the layout of discrete objects in a design domain is optimized, where (an undefined number of) objects with a fixed shape are distributed over the design domain. The original idea comes from Guest [80, 81], who considered circular objects to be distributed over the design domain. This is extended here to other object shapes.

In the discrete object layout optimization, the design variable field ρ_i is again filtered first, after which these are projected to obtain the physical element densities $\bar{\rho}_e$. For every element e, two neighborhood areas are defined: the local (Ω_e^{L}) and enclosure (Ω_e^{E}) zones. The local neighborhood contains the elements for which the densities are projected to 1, while the enclosure neighborhood defines the zone in which no other object should be projected. For circular objects, the two neighborhoods are defined as:

$$\begin{aligned} \mathbf{x}_i \in \Omega_e^{\mathrm{L}} \quad & \text{if } 0 \leq r_{ei} \leq R^{\mathrm{L}} \\ \mathbf{x}_i \in \Omega_e^{\mathrm{E}} \quad & \text{if } R^{\mathrm{L}} \leq r_{ei} \leq R^{\mathrm{L}} + T^{\mathrm{E}} \end{aligned} \tag{5.27}$$

where r_{ei} is the center-to-center distance between elements e and i, and R^{L} and T^{E} determine the local and enclosure neighborhood.

The design variable field ρ_i is filtered as follows:

$$\begin{aligned} \tilde{\rho}_e^{\mathrm{L}} &= \frac{\sum\limits_{\mathbf{x}_i \in \Omega_e^{\mathrm{L}}} w_{ei}^{\mathrm{L}} \rho_i}{\sum\limits_{\mathbf{x}_i \in \Omega_e^{\mathrm{L}}} w_{ei}^{\mathrm{L}}} \\ \tilde{\rho}_e^{\mathrm{E}} &= \frac{\sum\limits_{\mathbf{x}_i \in \Omega_e^{\mathrm{E}}} w_{ei}^{\mathrm{E}} \rho_i}{\sum\limits_{\mathbf{x}_i \in \Omega_e^{\mathrm{E}}} w_{ei}^{\mathrm{E}}} \end{aligned} \tag{5.28}$$

where the filter kernels are defined by:

$$\begin{aligned} w_{ei}^{\mathrm{L}} &= \begin{cases} \dfrac{R^{\mathrm{L}} - r_{ei}}{R^{\mathrm{L}}} & \text{if } \mathbf{x}_i \in \Omega_e^{\mathrm{L}} \\ 0 & \text{if } \mathbf{x}_i \notin \Omega_e^{\mathrm{L}} \end{cases} \\ w_{ei}^{\mathrm{E}} &= \begin{cases} \dfrac{R^{\mathrm{L}} + T^{\mathrm{E}} - r_{ei}}{T^{\mathrm{E}}} & \text{if } \mathbf{x}_i \in \Omega_e^{\mathrm{E}} \\ 0 & \text{if } \mathbf{x}_i \notin \Omega_e^{\mathrm{E}} \end{cases} \end{aligned} \tag{5.29}$$

The filter kernel for the local neighborhood is equal to 1 for $r_{ei} = 0$ and decreases linearly to 0 for $r_{ei} \geq R^{\mathrm{L}}$. The one for the enclosure neighborhood is equal to 0 for $r_{ei} < R^{\mathrm{L}}$, equal to 1 for $r_{ei} = R^{\mathrm{L}}$, and then decreases linearly to 0 for $r_{ei} \geq R^{\mathrm{L}} + T^{\mathrm{E}}$.

The projection intensities $\tilde{\rho}_e^{\mathrm{L}}$ and $\tilde{\rho}_e^{\mathrm{E}}$ are projected using a relaxed Heaviside function with a threshold at $\tilde{\rho}_e^{\mathrm{L}/\mathrm{E}} = 0$. The following relaxed Heaviside function is used to obtain the pseudo element densities $\bar{\rho}_e^{\mathrm{L}}$ and $\bar{\rho}_e^{\mathrm{E}}$:

$$\begin{aligned}\bar{\rho}_e^{\mathrm{L}} &= 1 - \mathrm{e}^{-\beta\tilde{\rho}_e^{\mathrm{L}}} + \tilde{\rho}_e^{\mathrm{L}}\mathrm{e}^{-\beta}\\ \bar{\rho}_e^{\mathrm{E}} &= 1 - \mathrm{e}^{-\beta\tilde{\rho}_e^{\mathrm{E}}} + \tilde{\rho}_e^{\mathrm{E}}\mathrm{e}^{-\beta}\end{aligned} \tag{5.30}$$

The element densities $\bar{\rho}_e$ are then composed from these pseudo element densities as follows:

$$\bar{\rho}_e = \frac{\bar{\rho}_e^{\mathrm{L}}(2 - \bar{\rho}_e^{\mathrm{E}})}{2} \tag{5.31}$$

For $\bar{\rho}_e^{\mathrm{L}} = 0$, no material is inserted, and therefore the element densities are $\bar{\rho}_e = 0$. For $\bar{\rho}_e^{\mathrm{L}} = 1$ and $\bar{\rho}_e^{\mathrm{E}} = 0$, the element material is inserted, and the element densities are $\bar{\rho}_e = 1$. The case $\bar{\rho}_e^{\mathrm{L}} = \bar{\rho}_e^{\mathrm{E}} = 1$ is undesired, as this means that two objects are mixing. By setting the element densities equal to $\bar{\rho}_e = 0.5$, they are penalized by the material interpolation.

The sensitivities are calculated as follows:

$$\frac{\mathrm{d}\phi}{\mathrm{d}\rho_i} = \sum_{e\in\Omega} \frac{\mathrm{d}\phi}{\mathrm{d}\bar{\rho}_e}\frac{\partial\bar{\rho}_e}{\partial\rho_i} \tag{5.32}$$

The first factor represents the sensitivities with respect to the element density field, which is explained in chapter 4. The second factor is equal to:

$$\frac{\partial\bar{\rho}_e}{\partial\rho_i} = \frac{1}{2}\left((2 - \bar{\rho}_e^{\mathrm{E}})\frac{\partial\bar{\rho}_e^{\mathrm{L}}}{\partial\rho_i} - \rho_L^e\frac{\partial\bar{\rho}_e^{\mathrm{E}}}{\partial\rho_i}\right) \tag{5.33}$$

In this equation, the sensitivities of the pseudo element densities are equal to:

$$\begin{aligned}\frac{\partial\bar{\rho}_e^{\mathrm{L}}}{\partial\rho_i} &= \begin{cases}\left(\beta\mathrm{e}^{-\beta\tilde{\rho}_e^{\mathrm{L}}} + \mathrm{e}^{-\beta}\right)\dfrac{\partial\tilde{\rho}_e^{\mathrm{L}}}{\partial\rho_i} & \text{if } \mathbf{x}_i \in \Omega_e^{\mathrm{L}}\\ 0 & \text{if } \mathbf{x}_i \notin \Omega_e^{\mathrm{L}}\end{cases}\\ \frac{\partial\bar{\rho}_e^{\mathrm{E}}}{\partial\rho_i} &= \begin{cases}\left(\beta\mathrm{e}^{-\beta\tilde{\rho}_e^{\mathrm{E}}} + \mathrm{e}^{-\beta}\right)\dfrac{\partial\tilde{\rho}_e^{\mathrm{E}}}{\partial\rho_i} & \text{if } \mathbf{x}_i \in \Omega_e^{\mathrm{E}}\\ 0 & \text{if } \mathbf{x}_i \notin \Omega_e^{\mathrm{E}}\end{cases}\end{aligned} \tag{5.34}$$

with:

$$\begin{aligned} \frac{\partial \tilde{\rho}_e^{\mathrm{L}}}{\partial \rho_i} &= \frac{w_{ei}^{\mathrm{L}}}{\sum\limits_{j \in \Omega_e^{\mathrm{L}}} w_{ej}^{\mathrm{L}}} \\ \frac{\partial \tilde{\rho}_e^{\mathrm{E}}}{\partial \rho_i} &= \frac{w_{ei}^{\mathrm{E}}}{\sum\limits_{j \in \Omega_e^{\mathrm{E}}} w_{ej}^{\mathrm{E}}} \end{aligned} \tag{5.35}$$

From the author's experience, the SIMP interpolation does not work properly for the problem considered in this work (it leads to a lot of gray, i.e. intermediate design variables), and instead, the Rational Approximation of Material Properties (RAMP) is used. A desirable feature of the RAMP interpolation is that, unlike the SIMP interpolation, it has nonzero sensitivity at zero density $\tilde{\rho}_e$, which resolves numerical difficulties for low densities [59]. The RAMP interpolation is defined as follows:

$$\alpha_j = \alpha_{j,\mathrm{ori}} + \frac{\bar{\rho}_e \left(\alpha_{j,\mathrm{ins}} - \alpha_{j,\mathrm{ori}}\right)}{1 + q_j \left(1 - \bar{\rho}_e\right)} \tag{5.36}$$

with $q_j \geq 0$ the penalty term. This interpolation function with $q_j = 10$ is applied for the stiffness properties (the constrained modulus ρC_{p}^2 and the shear modulus ρC_{s}^2), while for the mass properties (the mass density ρ), a linear interpolation function is applied (equivalent to the RAMP interpolation with $q_j = 0$). These values for the penalty term have been determined by qualitatively comparing the optimized designs. The sensitivities of the stiffness matrix with respect to the element densities then become:

$$\frac{\partial \mathbf{K}}{\partial \bar{\rho}_e} = \sum_{j=1}^{N_\alpha} \frac{\partial \mathbf{K}}{\partial \alpha_j} \frac{\partial \alpha_j}{\partial \bar{\rho}_e} = \sum_{j=1}^{N_\alpha} \frac{\left(1 + q_j\right)\left(\alpha_{j,\mathrm{ins}} - \alpha_{j,\mathrm{ori}}\right)}{\left[1 + q_j \left(1 - \bar{\rho}_e\right)\right]^2} \frac{\partial \mathbf{K}}{\partial \alpha_j} \tag{5.37}$$

Consider again the problem of maximizing the frequency averaged insertion loss over the frequency range $20 - 80\,\mathrm{Hz}$ while the volume of the design should be lower than or equal to $20\,\%$ of the volume of the design domain. The initial value for the smoothness parameter β is 10; this value is doubled every 40 iterations up to a maximum value of 160. Figure 5.26 shows the optimized design and the resulting insertion loss $\hat{\mathrm{IL}}$ for $R^{\mathrm{L}} = 0.5\,\mathrm{m}$ and $T^{\mathrm{E}} = 0.25\,\mathrm{m}$. The distribution of the circles is similar to the material distribution for the topology optimized designs in figure 5.12. As only discrete objects can be distributed in the design domain, the performance is considerably reduced (the averaged insertion loss $\overline{\mathrm{IL}}$ is equal to $3.4\,\mathrm{dB}$). It is still better, however, than for a single wall barrier of $7.5\,\mathrm{m} \times 1\,\mathrm{m}$.

The method can be extended to other objects by changing the filter kernel in equation (5.29). Consider for example a rectangle with width W^{L} and height

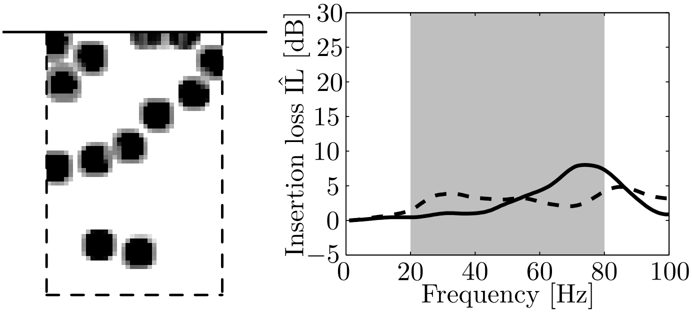

(a) (b)

Figure 5.26: (a) Discrete circle layout optimized design maximizing $\overline{\mathrm{IL}}$ over the frequency range $20-80\,\mathrm{Hz}$ (discretized with 10 frequencies), and (b) resulting insertion loss $\hat{\mathrm{IL}}$ (Eq. (5.13)) as a function of the frequency for the reference design in figure 5.4 (dashed line) and the optimized design (solid line).

H^{L}. Then the filter kernels become:

$$w_{ei}^{\mathrm{L}} = \begin{cases} \min\left[\dfrac{W^{\mathrm{L}} - 2\,|x_i - x_e|}{W^{\mathrm{L}}}, \dfrac{H^{\mathrm{L}} - 2\,|z_i - z_e|}{H^{\mathrm{L}}}\right] & \text{if } \mathbf{x}_i \in \Omega_e^{\mathrm{L}} \\ 0 & \text{if } \mathbf{x}_i \notin \Omega_e^{\mathrm{L}} \end{cases}$$
$$w_{ei}^{\mathrm{E}} = \begin{cases} \min\left[\dfrac{W^{\mathrm{L}} + 2T^{\mathrm{E}} - 2\,|x_i - x_e|}{2T^{\mathrm{E}}}, \dfrac{H^{\mathrm{L}} + 2T^{\mathrm{E}} - 2\,|z_i - z_e|}{2T^{\mathrm{E}}}\right] & \text{if } \mathbf{x}_i \in \Omega_e^{\mathrm{E}} \\ 0 & \text{if } \mathbf{x}_i \notin \Omega_e^{\mathrm{E}} \end{cases} \tag{5.38}$$

The functions can be adjusted for rotated rectangles, for example by using the expression in equation (5.20) as filter kernel for the local neighborhood and an adjusted filter kernel for the enclosed neighborhood. More generally, for a convex polygon, that is a polygon whose interior is a convex set, the following filter kernel can be applied:

$$\begin{aligned} w_{ei}^{\mathrm{L}} &= \begin{cases} \min\limits_{n}\left[\dfrac{\mathrm{d}\left(\mathbf{x}_e, l_{\Gamma i}^{n}\right)}{\mathrm{d}\left(\mathbf{x}_i, l_{\Gamma i}^{n}\right)}\right] & \text{if } \mathbf{x}_i \in \Omega_e^{\mathrm{L}} \\ 0 & \text{if } \mathbf{x}_i \notin \Omega_e^{\mathrm{L}} \end{cases} \\ w_{ei}^{\mathrm{E}} &= \begin{cases} \min\limits_{n}\left[\dfrac{T^{\mathrm{E}} - \mathrm{d}\left(\mathbf{x}_e, l_{\Gamma i}^{n}\right)}{T^{\mathrm{E}}}\right] & \text{if } \mathbf{x}_i \in \Omega_e^{\mathrm{E}} \\ 0 & \text{if } \mathbf{x}_i \notin \Omega_e^{\mathrm{E}} \end{cases} \end{aligned} \tag{5.39}$$

where $\mathrm{d}\left(\mathbf{x}, l\right)$ represents the distance between point $\mathbf{x}$ and line l and $l_{\Gamma i}^{n}$ represents the nth line segment of the border Γ of the polygon around $\mathbf{x}_i$.

Consider rectangular objects with a width $W^{\mathrm{L}} = 1\,\mathrm{m}$, height $H^{\mathrm{L}} = 4\,\mathrm{m}$, and distance $T^{\mathrm{E}} = 0.25\,\mathrm{m}$. Figure 5.27 shows the optimized design and the corresponding insertion loss. The large dimensions of the objects give little design freedom and make it difficult to obtain a good 0/1 design. As a result, the insertion loss is barely better than the rectangular single wall of $7.5\,\mathrm{m} \times 1\,\mathrm{m}$.

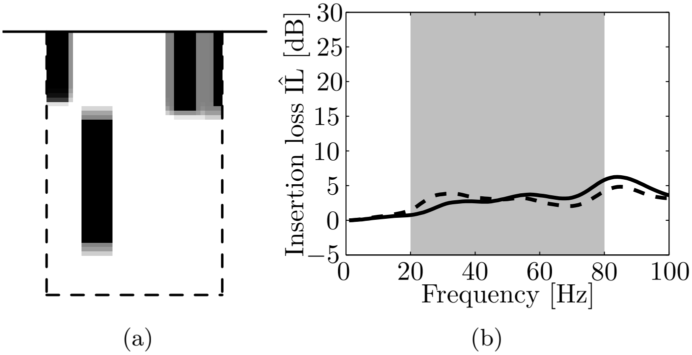

(a) (b)

Figure 5.27: (a) Discrete rectangle layout optimized design maximizing $\overline{\mathrm{IL}}$ over the frequency range $20 - 80\,\mathrm{Hz}$ (discretized with 10 frequencies), and (b) resulting insertion loss $\hat{\mathrm{IL}}$ (Eq. (5.13)) as a function of the frequency for the reference design in figure 5.4 (dashed line) and the optimized design (solid line).

The discrete object layout optimization can also be applied disregarding the enclosure neighborhood. This means that no spacing between the objects is imposed and overlap is possible. The element densities are then found as $\bar{\rho}_e = \bar{\rho}_e^{\mathrm{L}}$. Figure 5.28 shows the optimized design and the corresponding insertion loss. The frequency averaged insertion loss is equal to 5.4 dB which is close to the one found for the simplified robust design. This method is therefore a viable alternative in finding a simple and practical design.

5.4 Conclusion

In this chapter, topology optimization is applied to a two-dimensional problem consisting of a semi-infinite homogeneous halfspace excited by a line load. The vibrations are reduced by inserting a wave barrier which is optimized for maximizing the insertion loss at a receiver position behind the barrier.

Three cases are considered. First, harmonic sources at a fixed frequency are considered, resulting in a distribution of the inserted material that optimally reflects and guides waves away from the surface. At higher frequencies, high

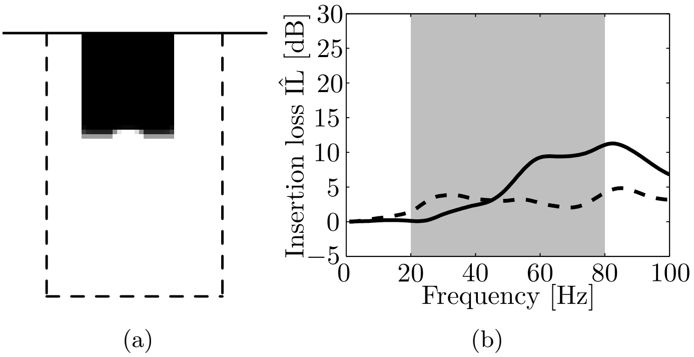

(a) (b)

Figure 5.28: (a) Discrete rectangle layout optimized design considering only the local neighborhood and maximizing $\overline{\mathrm{IL}}$ over the frequency range $20-80\,\mathrm{Hz}$ (discretized with 10 frequencies), and (b) resulting insertion loss $\hat{\mathrm{IL}}$ (Eq. (5.13)) as a function of the frequency for the reference design in figure 5.4 (dashed line) and the optimized design (solid line).

values of the insertion loss are obtained due to interference patterns. Second, broadband sources are considered, resulting in a design that mainly reduces the insertion loss at the highest frequencies, where it is easier to achieve a high insertion loss. Third, harmonic sources at an unknown frequency in a given range are considered, resulting in a design that uniformly increases the insertion loss over the frequency range of interest.

The designs obtained by topology optimization often contain small features. Geometric imperfections can therefore have an important influence on the design performances. Furthermore, the small features are difficult to build in practice. Two methods are therefore presented in this chapter to deal with both issues. As the design optimized for the frequency averaged insertion loss is found to be more sensitive to deviations in design geometry than the one optimized for the minimal insertion loss, the discussed methods are applied to the former case.

To deal with the geometric imperfections, a worst case robust approach is applied. The use of the robust approach makes it furthermore possible to manually simplify the topology with little deterioration of performance. This can be followed by a shape optimization step. An alternative is optimizing the layout of discrete objects in the design domain. The obtained design is characterized by the predefined object, however, and less freedom is therefore given to the shape of the design.

Although the two-dimensional problem considered in this chapter is computationally relatively cheap, the stiffness effect introduced in chapter 3 can influence the behaviour of the barrier at larger longitudinal distances from the source. In the next chapter, topology optimization is therefore applied to three-dimensional problems.

Chapter 6

Topology optimization for three-dimensional elastic wave propagation

6.1 Introduction

Chapter 5 considered a line load on a halfspace as a first approximation of a train load. However, as demonstrated in chapter 3, the three-dimensional nature of the problem needs to be accounted for. Previous studies have indicated that the stationary part of the response can be well approximated by applying the axle loads of the train at fixed positions on the track as a series of incoherent point sources [169].

Before considering a series of point loads, first the response for spatially harmonic line loads and for point loads is studied. This problem is shown in figure 6.1. A semi-infinite halfspace is excited by a point load (or a series of point loads). A nearby wave barrier is introduced to reduce the resulting vibrations behind the barrier. The design of this wave barrier is optimized such that the vibration transmission is minimized.

The length of the structure is in reality finite. The finite size of a structure can be taken into account using a spatial windowing technique. This was first developed in the field of acoustics to calculate the sound transmission through and radiation from finite plates [170]. Coulier et al. [52] have extended this technique to 2.5D FE-BE soil-structure interaction problems. It was

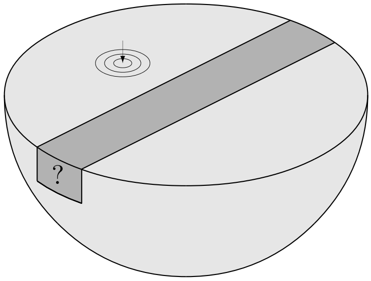

Figure 6.1: General problem: a semi-infinite halfspace excited by a point load at the surface. A wave barrier is introduced to reduce the wave propagation close to the surface of the halfspace.

demonstrated that the spatial windowing technique can even be applied for very short structures. It can, however, only be used as long as the modal behaviour of the structure does not dominate the response [52, 115].

This chapter also discusses a case study. A building is added to the model in which the vibration levels are reduced. The vibrations result from a passing train on a railway track located close to the building. The soil model is therefore coupled to a train-track system. The design of a wave barrier, located between the railway track and the building, is optimized.

The outline of this chapter is as follows. First, wave barriers of infinite length are considered. The sensitivities are derived, and the performance is optimized both for spatially harmonic line loads and point loads. Next, the influence of the barrier's finite length is assessed using a spatial windowing approach. The last part discusses a case study, taking train-track-soil interaction and soil-structure interaction into account.

6.2 Wave barriers of infinite length

Using a Fourier transformation from the longitudinal coordinate y to the longitudinal wavenumber k_y, the problem is decomposed into a series of problems of plane wave propagation. This means that the equilibrium equations of the form (3.31) need to be solved for different wavenumbers. First, the sensitivities are derived, after which results are shown both for spatially harmonic line loads and for point loads.

6.2.1 Sensitivities

The sensitivities are again calculated using the adjoint approach. Consider the general function $\phi\left(\bar{\boldsymbol{\rho}}, \underline{\hat{\mathbf{u}}}\left(\bar{\boldsymbol{\rho}}\right)\right)$, where the displacements $\underline{\hat{\mathbf{u}}}$ in the spatial domain follow from the displacements $\underline{\tilde{\mathbf{u}}}_k$ in the wavenumber domain. Then the derivatives to the element densities $\bar{\rho}_e$ are computed as:

$$\frac{\mathrm{d}\phi}{\mathrm{d}\bar{\rho}_e} = \frac{\partial\phi}{\partial\bar{\rho}_e} + \sum_{k=1}^{N_k}\left[\frac{\partial\phi}{\partial\underline{\tilde{\mathbf{u}}}_k}\frac{\partial\underline{\tilde{\mathbf{u}}}_k}{\partial\bar{\rho}_e} + \frac{\partial\phi}{\partial\underline{\tilde{\mathbf{u}}}_k^*}\frac{\partial\underline{\tilde{\mathbf{u}}}_k^*}{\partial\bar{\rho}_e}\right] \tag{6.1}$$

where the summation is done over the N_k wavenumbers k considered to calculate the response (equation 3.32). The derivatives of the displacement in the wavenumber domain with respect to the element densities are obtained from the equilibrium equations in equation (3.31):

$$\frac{\partial\tilde{\mathbf{K}}_k}{\partial\bar{\rho}_e}\underline{\tilde{\mathbf{u}}}_k + \tilde{\mathbf{K}}_k\frac{\partial\underline{\tilde{\mathbf{u}}}_k}{\partial\bar{\rho}_e} = \mathbf{0} \Leftrightarrow \frac{\partial\underline{\tilde{\mathbf{u}}}_k}{\partial\bar{\rho}_e} = -\tilde{\mathbf{K}}_k^{-1}\frac{\partial\tilde{\mathbf{K}}_k}{\partial\bar{\rho}_e}\underline{\tilde{\mathbf{u}}}_k \tag{6.2}$$

Introducing this expression into equation (6.1), the sensitivities become:

$$\begin{aligned}\frac{\mathrm{d}\phi}{\mathrm{d}\bar{\rho}_e} &= \frac{\partial\phi}{\partial\bar{\rho}_e} - \sum_{k=1}^{N_k}\left[\frac{\partial\phi}{\partial\underline{\tilde{\mathbf{u}}}_k}\tilde{\mathbf{K}}_k^{-1}\frac{\partial\tilde{\mathbf{K}}_k}{\partial\bar{\rho}_e}\underline{\tilde{\mathbf{u}}}_k + \frac{\partial\phi}{\partial\underline{\tilde{\mathbf{u}}}_k^*}\left(\tilde{\mathbf{K}}_k^{-1}\frac{\partial\tilde{\mathbf{K}}_k}{\partial\bar{\rho}_e}\underline{\tilde{\mathbf{u}}}_k\right)^*\right] \\ &= \frac{\partial\phi}{\partial\bar{\rho}_e} + 2\sum_{k=1}^{N_k}\mathrm{Re}\left\{\boldsymbol{\lambda}_k^{\mathrm{T}}\frac{\partial\tilde{\mathbf{K}}}{\partial\bar{\rho}_e}\underline{\tilde{\mathbf{u}}}_k\right\}\end{aligned} \tag{6.3}$$

where the vectors $\boldsymbol{\lambda}_k$ are obtained from the adjoint equations:

$$\tilde{\mathbf{K}}_k^{\mathrm{T}}\boldsymbol{\lambda}_k = -\left(\frac{\partial\phi}{\partial\underline{\tilde{\mathbf{u}}}_k}\right)^{\mathrm{T}} \tag{6.4}$$

As the objective function and the constraints are usually described in terms of the displacements $\hat{\mathbf{u}}$ in the spatial domain, the right-hand side of the adjoint equation is calculated as:

$$\frac{\partial\phi}{\partial\underline{\tilde{\mathbf{u}}}_k} = \frac{\partial\phi}{\partial\underline{\hat{\mathbf{u}}}}\frac{\partial\underline{\hat{\mathbf{u}}}}{\partial\underline{\tilde{\mathbf{u}}}_k} \tag{6.5}$$

where the second factor denotes the sensitivities of the displacement in the spatial domain with respect to the displacements in the wavenumber domain. These depend on the relation between the displacements in the two domains. Two cases are considered: spatially harmonic line loads and point loads.

6.2.2 Spatially harmonic line loads

In section 5.2, two-dimensional wave propagation was considered by setting the longitudinal wavenumber $k_y = 0$ in the 2.5D formulation. For three-dimensional problems, non-zero longitudinal wavenumbers are considered. For spatially harmonic line loads, characterized by a single wavenumber k_y, the displacements in the spatial domain are simply obtained as:

$$\underline{\hat{\mathbf{u}}}\,(y) = \underline{\tilde{\mathbf{u}}}\,(k_y)\, e^{-\mathrm{i}k_y y} \tag{6.6}$$

As a result, the sensitivities of the displacements in the spatial domain to the displacements in the wavenumber domain are equal to:

$$\frac{\partial \underline{\hat{\mathbf{u}}}\,(y)}{\partial \underline{\tilde{\mathbf{u}}}\,(k_y)} = e^{-\mathrm{i}k_y y} \tag{6.7}$$

These sensitivities are used to compute the adjoint load in equation (6.5). As in chapter 5, the insertion loss at a receiver is maximized and therefore taken as objective function. This receiver is located at $(x = 15\,\mathrm{m}, y = 0\,\mathrm{m}, z = 0\,\mathrm{m})$. A volume constraint restricting the volume of the design to $20\,\%$ of the design domain is considered. The wave barrier design is optimized for two harmonic frequencies (25 Hz and 50 Hz) and for three slownesses ($p_y = 0\,\mathrm{s/m}$, $p_y = 1/C_\mathrm{p} = 0.0025\,\mathrm{s/m}$, and $p_y = 1/C_\mathrm{s} = 0.0050\,\mathrm{s/m}$). These three slownesses correspond to Rayleigh waves propagating under an angle θ of respectively 0°, 27.8°, and 68.7° (see also figure 3.11 for the definition of θ).

For the optimized designs presented in this chapter, the number of iterations is limited to 120. A continuation scheme is applied to the sharpness parameter β of the projection filter. The initial value $\beta = 2$ is doubled every 30 iterations until a value of $\beta = 16$ is reached. The results are shown in figures 6.2 to 6.5. The designs optimized at a frequency of 25 Hz and 50 Hz for a slowness $p_y = 0\,\mathrm{s/m}$ were discussed in the previous chapter. The three-dimensional wave fields are shown in figures 6.3c and 6.5c.

The design optimized at 25 Hz for a slowness $p_y = 0.0025\,\mathrm{s/m}$ and the corresponding insertion loss as a function of the frequency are shown in figures 6.2c and d. The insertion loss for the optimized design is equal to 3.9 dB which is rather small but still higher than 2.4 dB obtained for the reference design. In contrast to the design which was obtained for a slowness $p_y = 0\,\mathrm{s/m}$, the design for a slowness $p_y = 0.0025\,\mathrm{s/m}$ is characterized by an important feature close to the surface. This feature is similar to the one previously obtained for the design optimized at 50 Hz for $p_y = 0\,\mathrm{s/m}$ (section 5.2.5) and has the same function of reflecting the incoming waves and guiding them away from the surface, as is shown in figure 6.3f. This is, however, only possible when the width of the horizontal part is large enough. For this higher value of the slowness, the projection of the width of the design domain to the propagation direction of the waves enlarges as the waves propagate at a different angle. This means that the ratio of the projected width and the Rayleigh wavelength enlarges, making it large enough to be effective. However, the ratio between the domain depth and the Rayleigh wavelength is smaller than for the design optimized at 50 Hz for $p_y = 0\,\mathrm{s/m}$, and the very high insertion loss for the latter design is not obtained here.

Figures 6.2e and f show the design optimized at 25 Hz for a slowness $p_y = 0.0050\,\mathrm{s/m}$ and the corresponding insertion loss as a function of the frequency. This design can be interpreted as a double or triple wall barrier. The optimal distance between the walls follows the quarter wave-stack condition, taking into account that the wave now propagates under an angle θ which is defined as $\sin\theta = k_y/k_\mathrm{R} = p_y/p_\mathrm{R}$:

$$d^\mathrm{opt} = \frac{\lambda_x}{4} = \frac{\pi}{2k_x} = \frac{C_\mathrm{R}}{4f\cos\theta} = 5.1\,\mathrm{m} \tag{6.8}$$

The distance between the outer walls, ranging from 3.6 m to 4.3 m, is close to this optimal distance d^opt. As the actual distance is lower than the optimal distance for 25 Hz, this leads to a better performance at higher frequencies. Also the central feature of the double wall contributes to the good performance for higher frequencies, as the spacing d is furthermore decreased. The insertion loss at 25 Hz is already rather high, namely 25.9 dB. The high insertion loss is also observed from the displacement field (figure 6.3f).

The design optimized at 50 Hz for a slowness $p_y = 0.0025\,\mathrm{s/m}$ and the corresponding insertion loss as a function of the frequency are shown in figures 6.4c and d. The design contains a lot of small features. The displacement field in figure 6.5f indicates that the incoming waves are reflected and guided away from the surface. As the main feature is located at the top part of the design domain, the insertion loss is smaller for lower frequencies.

Figures 6.4e and f show the design optimized at 50 Hz for a slowness $p_y = 0.0050\,\mathrm{s/m}$ and the corresponding insertion loss as a function of the frequency. This looks again as a double or triple wall barrier and is very similar to the design optimized at 25 Hz for this slowness. The central feature, however, is located closer to the surface. This results in a better performance for higher frequencies.

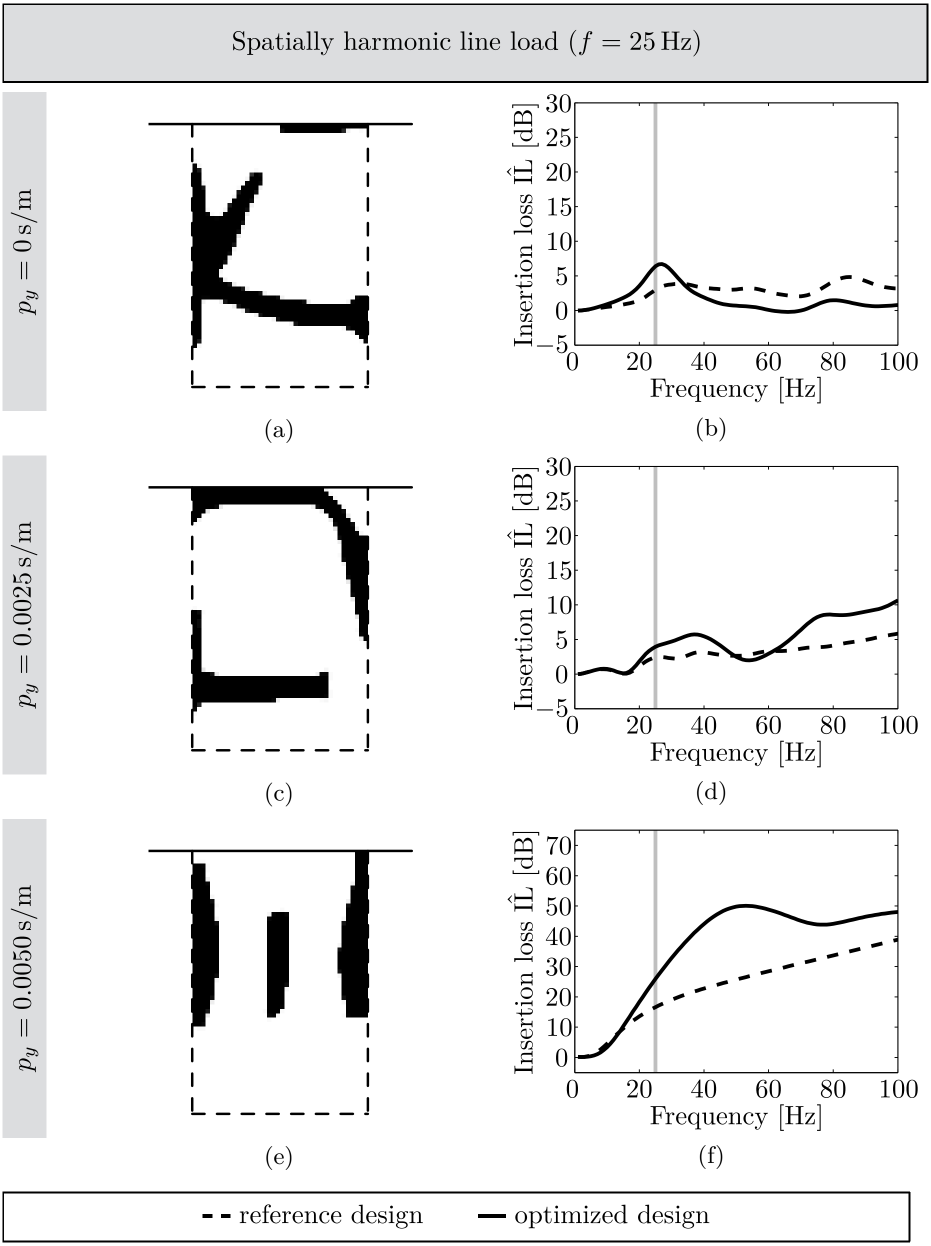

Figure 6.2: Designs optimized at a frequency of 25 Hz for a slowness p_y equal to (a) 0 s/m, (c) 0.0025 s/m, and (e) 0.0050 s/m. Resulting insertion loss as a function of the frequency for the reference design in figure 5.4 (dashed line) and the optimized design (solid line) at a frequency of 25 Hz for a slowness p_y equal to (b) 0 s/m, (d) 0.0025 s/m, and (f) 0.0050 s/m.

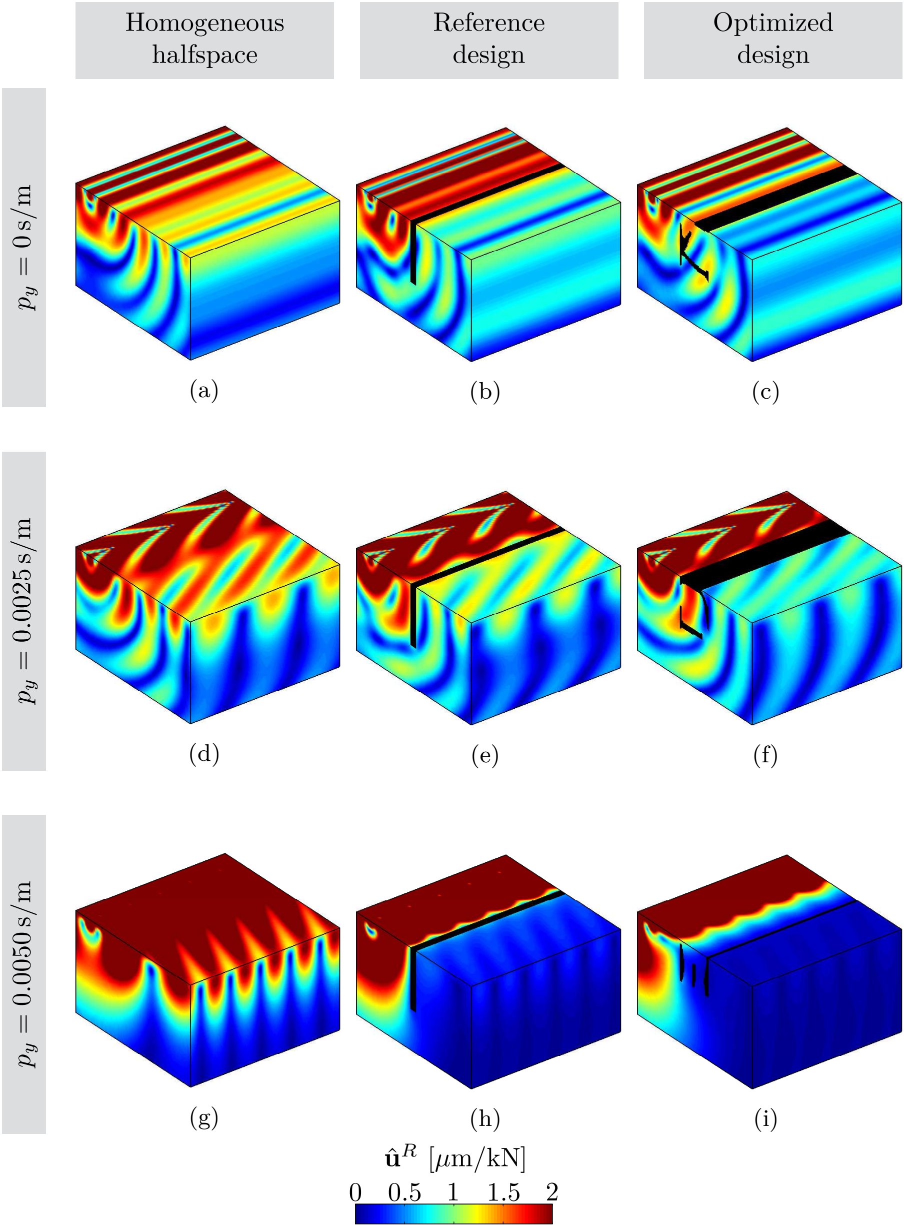

Figure 6.3: Real part of the displacement field $\hat{\mathbf{u}}^R$ for excitation at 25 Hz in the homogeneous halfspace for a slowness p_y equal to (a) 0 s/m, (d) 0.0025 s/m, and (g) 0.0050 s/m, with the reference design for a slowness p_y equal to (b) 0 s/m, (e) 0.0025 s/m, and (h) 0.0050 s/m, and with the designs optimized for a slowness p_y equal to (c) 0 s/m, (f) 0.0025 s/m, and (i) 0.0050 s/m.

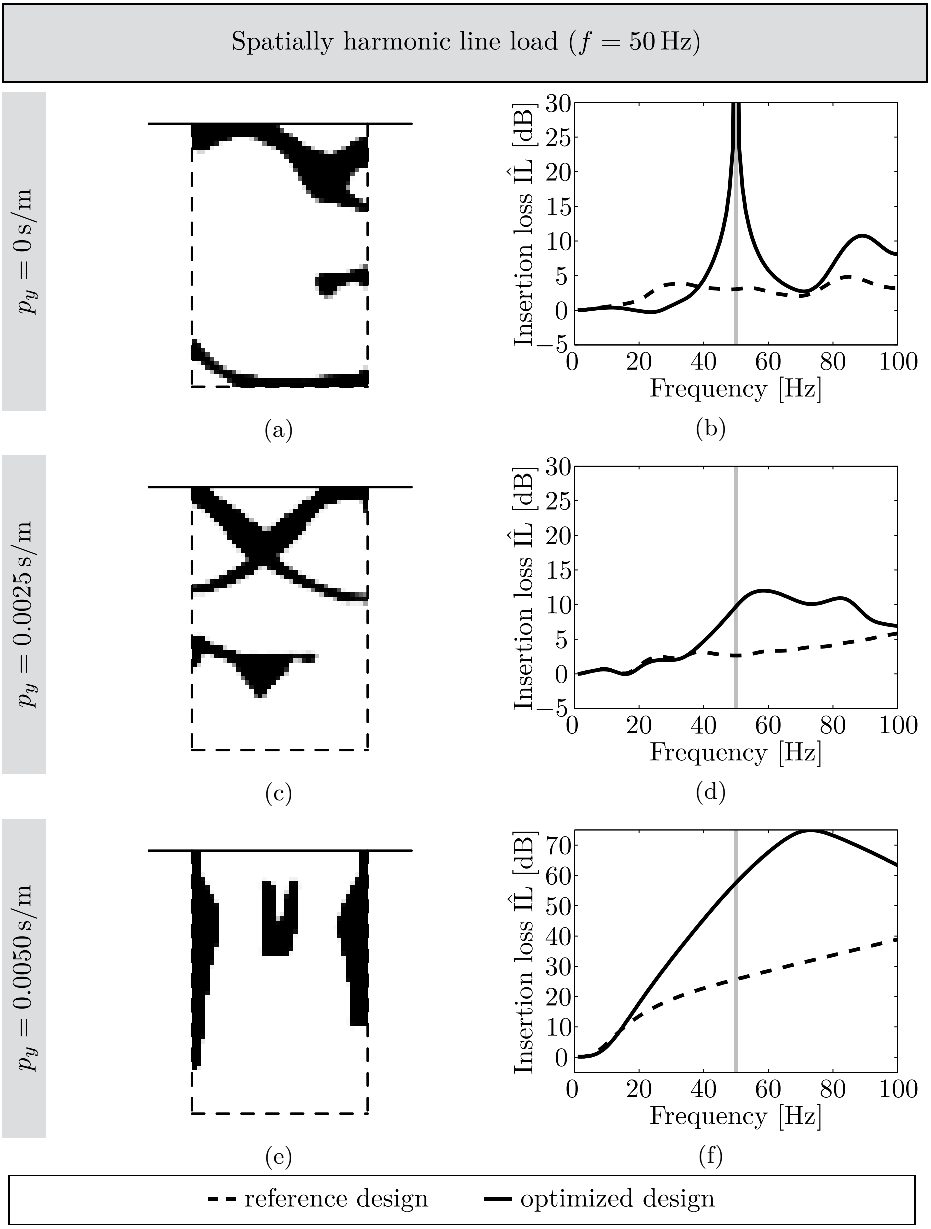

Figure 6.4: Designs optimized at a frequency of 50 Hz for a slowness p_y equal to (a) 0 s/m, (c) 0.0025 s/m, and (e) 0.0050 s/m. Resulting insertion loss as a function of the frequency for the reference design in figure 5.4 (dashed line) and the optimized design (solid line) at a frequency of 50 Hz for a slowness p_y equal to (b) 0 s/m, (d) 0.0025 s/m, and (f) 0.0050 s/m.

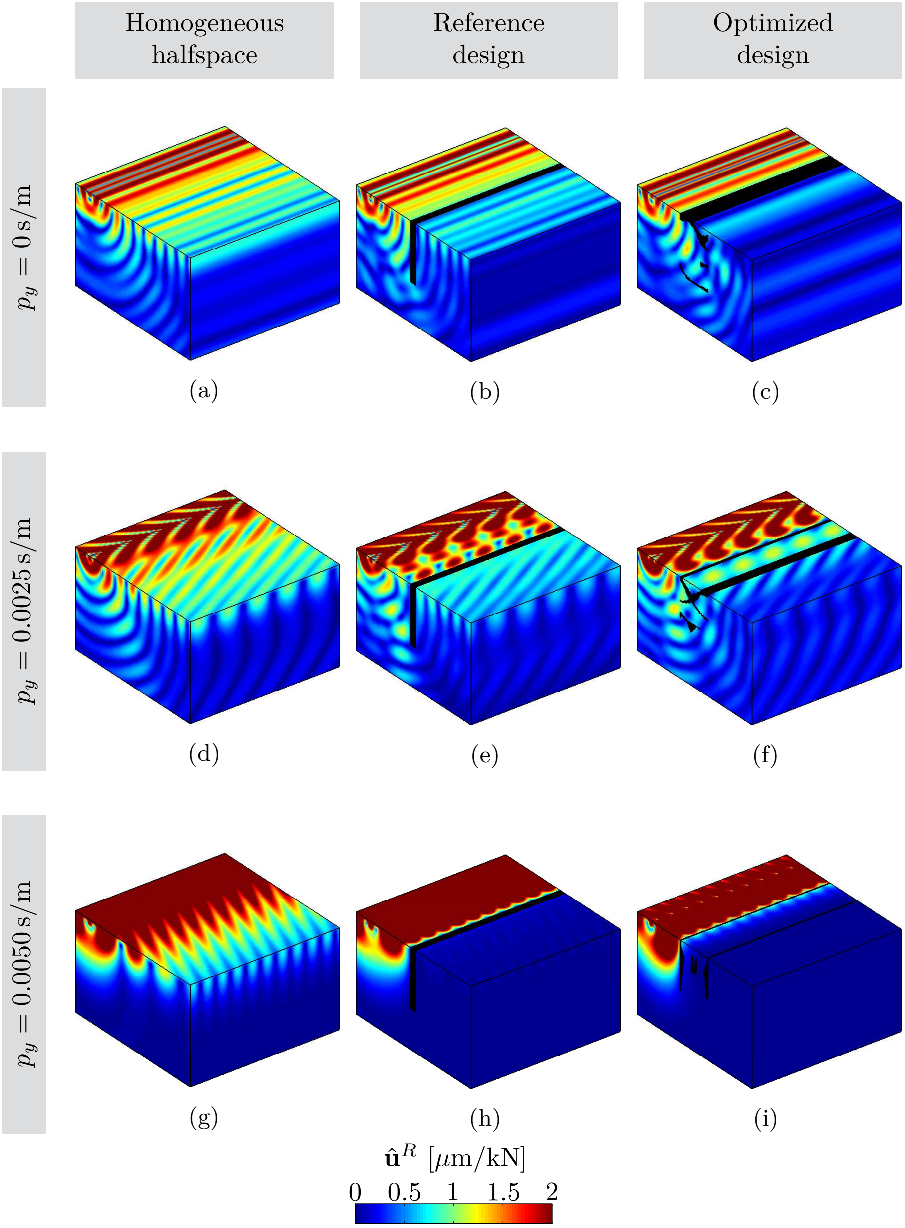
Homogeneous halfspace
Reference design
Optimized design
$p_y = 0\,\mathrm{s/m}$
$p_y = 0.0025\,\mathrm{s/m}$
$p_y = 0.0050\,\mathrm{s/m}$
(a)
(b)
(c)
(d)
(e)
(f)
(g)
(h)
(i)
$\hat{\mathbf{u}}^R$ [μm/kN]
0
0.5
1
1.5
2

Figure 6.5: Real part of the displacement field $\hat{\mathbf{u}}^R$ for excitation at 50 Hz in the homogeneous halfspace for a slowness p_y equal to (a) 0 s/m, (d) 0.0025 s/m, and (g) 0.0050 s/m, with the reference design for a slowness p_y equal to (b) 0 s/m, (e) 0.0025 s/m, and (h) 0.0050 s/m, and with the designs optimized for a slowness p_y equal to (c) 0 s/m, (f) 0.0025 s/m, and (i) 0.0050 s/m.

6.2.3 Point loads

Consider now the case of a point load exciting the halfspace. The problem considered in this subsection is shown in figure 6.6. A homogeneous halfspace is excited at the surface by a point load at ($x = 0\,\mathrm{m}, y = 0\,\mathrm{m}, z = 0\,\mathrm{m}$). The insertion loss at ($x = 15\,\mathrm{m}, y = 0\,\mathrm{m}, z = 0\,\mathrm{m}$) is minimized by inserting a wave barrier in between the source and the receiver in a design domain of $7.5\,\mathrm{m} \times 5\,\mathrm{m}$.

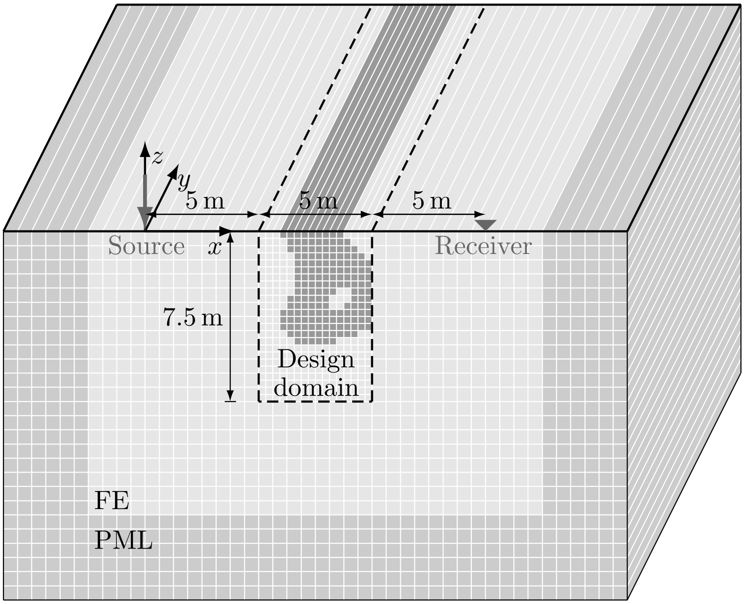

Figure 6.6: The optimization problem for the two-and-a-half-dimensional halfspace excited by a point load. The mesh is added as illustration only and is not the actual finite element mesh.

The response for a point load is obtained from the response in the wavenumber domain by means of the discrete Fourier transform in equation (3.32). The sensitivities of the displacements in the spatial domain with respect to the displacements in the wavenumber are given by:

$$\frac{\partial \underline{\hat{\mathbf{u}}}_l}{\partial \underline{\tilde{\mathbf{u}}}_k} = \frac{1}{2\pi} e^{-\mathrm{i}2\pi(l-1)(k-1)/N} \Delta k_y \tag{6.9}$$

The response in the wavenumber domain is computed for N_k wavenumbers from $k_y = 0\,\mathrm{m}^{-1}$ to $k_y = 3k_\mathrm{s}$ with k_s the shear wavenumber. Note that it is sufficient to only calculate the positive values of k_y. Indeed, for a vertical load (i.e. a load in the z-direction) at $y = 0$, the displacements in the x- and z-direction are even functions with respect to the y-coordinate, while the displacements in the y-direction are odd functions with respect to the y-coordinate. As it can be straightforwardly proven that the Fourier transform of an even and odd function is itself an even and odd function, respectively, the displacements in the x- and z-direction are also even functions with respect to k_y, and the displacements in the y-direction are also odd functions with respect to k_y. Therefore, the displacements related to a negative wavenumber can be simply calculated from the displacements related to the corresponding positive wavenumber, applying an opposite sign for the displacements in the y-direction.

The response for a point load is well approximated taking $N_k = 151$ wavenumbers into account (which means that $\Delta k_y = 0.02 k_\mathrm{s}$). A lower number of wavenumbers results in an undesirable error in the response. The results shown in this chapter are therefore computed with $N_k = 151$ wavenumber. Practically the same sensitivities and designs, however, have been found by taking only $N_k = 49$ wavenumbers into account (which means that $\Delta k_y = 0.0625 k_\mathrm{s}$).

Three cases are considered: optimization of the insertion loss at 25 Hz, of the insertion loss at 50 Hz, and of the frequency averaged insertion loss in the range $20 - 80\,\mathrm{Hz}$. The optimized designs and the corresponding insertion losses $\hat{\mathrm{IL}}$ are shown in figure 6.7. The designs and their performance are very similar to those obtained for a line load. At $y = 0$, the wave fronts resulting from the point load propagate in the x-direction, as is visible in figure 6.8, and hence in the same direction as for the line load. Although the geometric dissipation in the two-dimensional case is smaller than in the three-dimensional case, the wave fields at $y = 0$ for the point load (figure 6.8) therefore strongly resemble the wave fields for a line load (figures 5.9, 5.11, and 5.13). This apparently also results in similar barrier designs.

In chapter 3, it was discussed that stiffness plays a role only at larger longitudinal coordinates y along the barrier. To take the displacements for larger y-coordinates into account, an averaged insertion loss over the

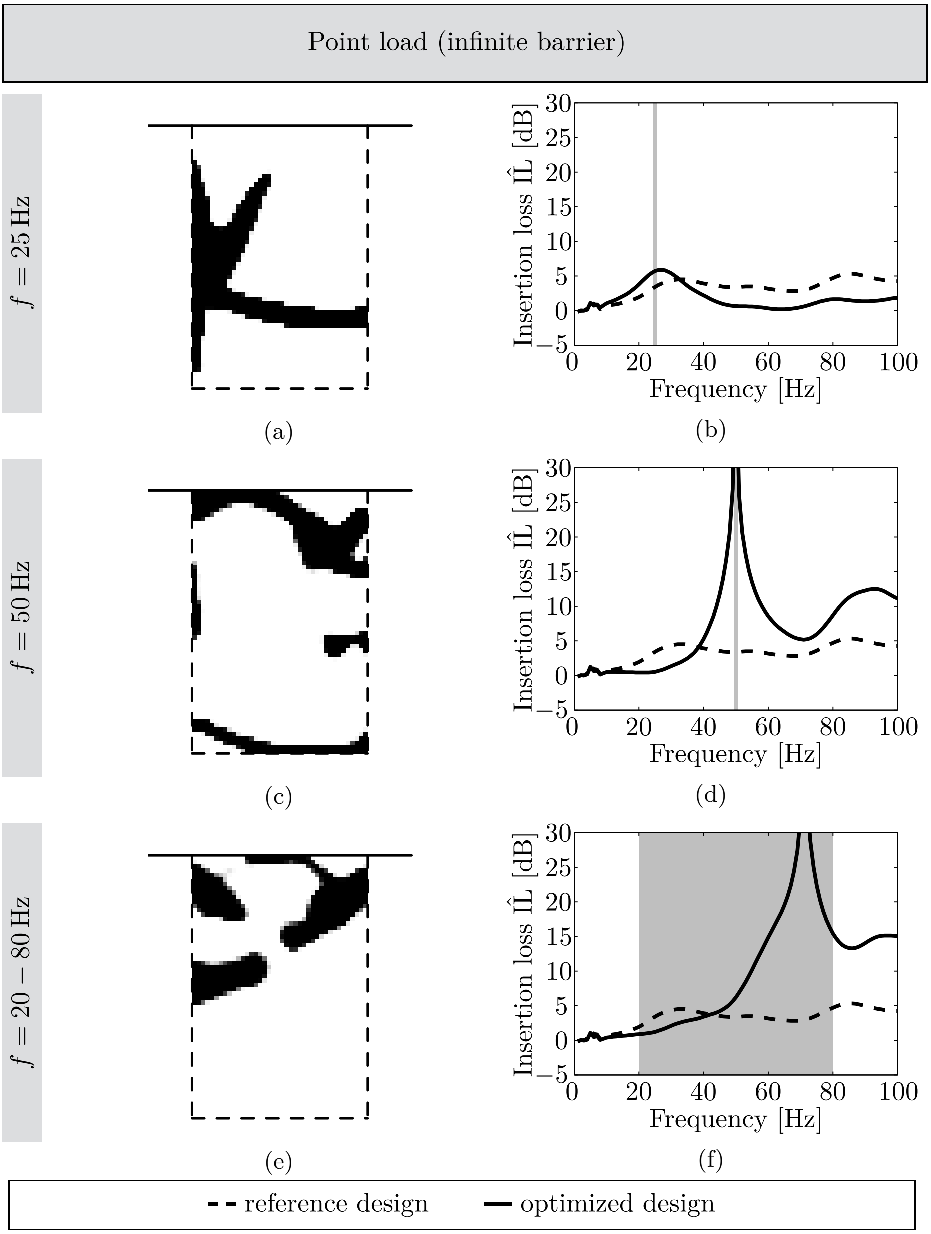

Figure 6.7: Designs optimized for a point load (a) at a frequency of 25 Hz, (c) at a frequency of 50 Hz, and (e) for the frequency range 20 – 80 Hz. Resulting insertion loss as a function of the frequency for the reference design in figure 5.4 (dashed line) and the optimized design (solid line) (b) at a frequency of 25 Hz, (d) at a frequency of 50 Hz, and (f) for the frequency range 20 – 80 Hz.

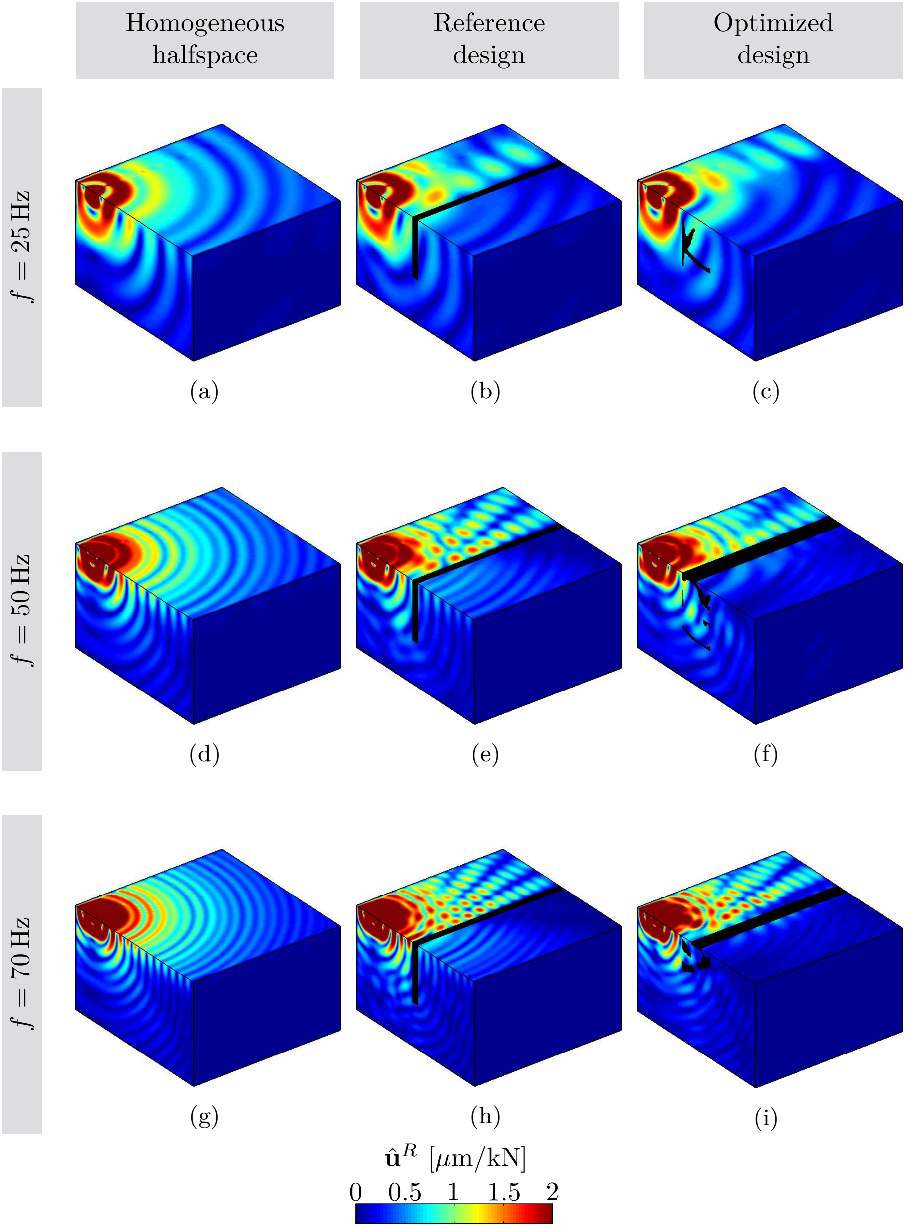

Figure 6.8: Real part of the displacement field $\hat{\mathbf{u}}^R$ in the homogeneous halfspace at a frequency f of (a) 25 Hz, (d) 50 Hz, and (g) 70 Hz, with the reference design at a frequency f of (b) 25 Hz, (e) 50 Hz, and (h) 70 Hz, and with the designs optimized for a receiver at ($x = 15\,\text{m}, y = 0\,\text{m}, z = 0\,\text{m}$) at a frequency of (c) 25 Hz, (f) 50 Hz, and (i) 70 Hz (design optimized for $20 - 80\,\text{Hz}$).

longitudinal direction is considered which is defined as follows:

$$
\begin{aligned}
\hat{\mathrm{IL}}_{L_{\mathrm{rec}}} &= 10\log_{10}\left\{\frac{\int_{-L_{\mathrm{rec}}/2}^{L_{\mathrm{rec}}/2}\left[\left|\hat{\underline{u}}^{\mathrm{ref}}_{\mathrm{rec}x}(y)\right|^2+\left|\hat{\underline{u}}^{\mathrm{ref}}_{\mathrm{rec}y}(y)\right|^2+\left|\hat{\underline{u}}^{\mathrm{ref}}_{\mathrm{rec}z}(y)\right|^2\right]\mathrm{d}y}{\int_{-L_{\mathrm{rec}}/2}^{L_{\mathrm{rec}}/2}\left[\left|\hat{\underline{u}}_{\mathrm{rec}x}(y)\right|^2+\left|\hat{\underline{u}}_{\mathrm{rec}y}(y)\right|^2+\left|\hat{\underline{u}}_{\mathrm{rec}z}(y)\right|^2\right]\mathrm{d}y}\right\} \\
&\approx 10\log_{10}\left\{\frac{\sum_{l=1}^{N_y}\left[\left|\hat{\underline{u}}^{\mathrm{ref}}_{\mathrm{rec}x}(y_l)\right|^2+\left|\hat{\underline{u}}^{\mathrm{ref}}_{\mathrm{rec}y}(y_l)\right|^2+\left|\hat{\underline{u}}^{\mathrm{ref}}_{\mathrm{rec}z}(y_l)\right|^2\right]}{\sum_{l=1}^{N_y}\left[\left|\hat{\underline{u}}_{\mathrm{rec}x}(y_l)\right|^2+\left|\hat{\underline{u}}_{\mathrm{rec}y}(y_l)\right|^2+\left|\hat{\underline{u}}_{\mathrm{rec}z}(y_l)\right|^2\right]}\right\}
\end{aligned}
\tag{6.10}
$$

where $\hat{\underline{u}}^{\mathrm{ref}}_{\mathrm{rec}j}(y)$ and $\hat{\underline{u}}_{\mathrm{rec}j}(y)$ are the displacements at the receiver point at $(x = 15\,\mathrm{m}, y, z = 0\,\mathrm{m})$ in direction j for the homogeneous halfspace and after the introduction of the barrier, respectively. The length L_{rec} is discretized by dividing it in N_y parts with a length of $0.25\,\mathrm{m}$, equal to the mesh of the surrounding domain.

Figure 6.9 shows the designs optimizing the averaged insertion loss for three lengths L_{rec}: $0\,\mathrm{m}$, which corresponds to the previously discussed case, $10\,\mathrm{m}$, and $40\,\mathrm{m}$. For $L_{\mathrm{rec}} = 10\,\mathrm{m}$, the designs strongly resemble the designs obtained for $L_{\mathrm{rec}} = 0\,\mathrm{m}$. The largest displacements are located close to the source, at $y = 0\,\mathrm{m}$, and decrease for increasing y. Therefore, the performance around $y = 0$ determines the averaged insertion loss over the distance considered.

For $L_{\mathrm{rec}} = 40\,\mathrm{m}$, the optimized designs show some differences with respect to the previous designs. Two phenomena seem to play a role. First, if the wave front in the xy plane arrives at a certain angle θ (figure 3.11) with respect to the x-axis, the projected angle with respect to the z-axis in the propagation direction of the wave front is smaller than the angle in the xz-plane. To compensate this, the inclined features are made steeper such that the optimal inclination is obtained for wave fronts propagating at larger angles θ. This is especially seen for the design optimized at $f = 25\,\mathrm{Hz}$. Second, for larger angles θ, the wave transmission is strongly influenced by the stiffness of the wall. Especially the designs optimized at $50\,\mathrm{Hz}$ and for the frequency range $20 - 80\,\mathrm{Hz}$ have a higher bending stiffness. This results in considerably better performances. For example, the displacement-averaged insertion loss $\overline{\hat{\mathrm{IL}}_{40\,\mathrm{m}}}$, frequency averaged in the range $20 - 80\,\mathrm{Hz}$, is equal to $4.0\,\mathrm{dB}$ for the rectangular reference barrier, $7.0\,\mathrm{dB}$ for the barrier optimized for $L_{\mathrm{rec}} = 0\,\mathrm{m}$ (figure 6.9g), and $10.3\,\mathrm{dB}$ for the one optimized for $L_{\mathrm{rec}} = 40\,\mathrm{m}$ (figure 6.9i).

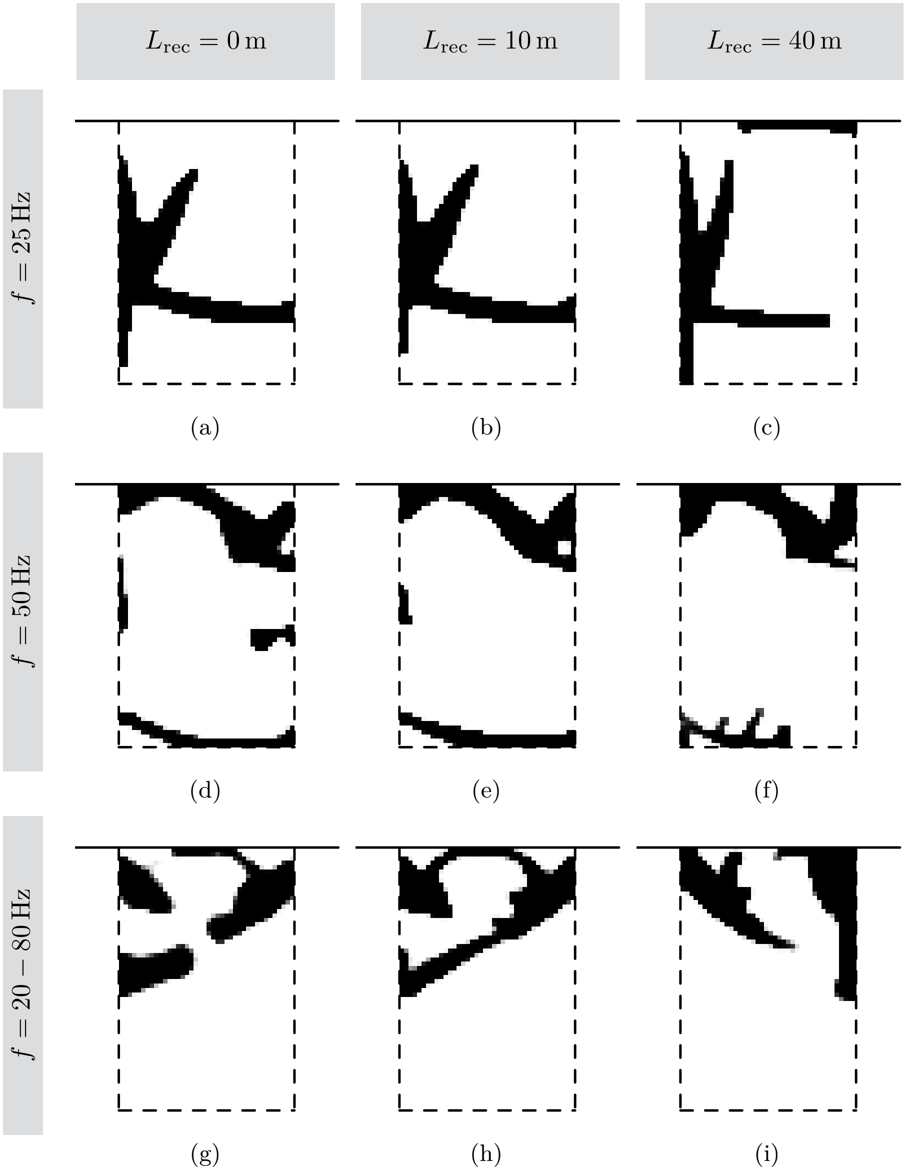
$L_{\mathrm{rec}} = 0\,\mathrm{m}$
$L_{\mathrm{rec}} = 10\,\mathrm{m}$
$L_{\mathrm{rec}} = 40\,\mathrm{m}$
$f = 25\,\mathrm{Hz}$
$f = 50\,\mathrm{Hz}$
$f = 20 - 80\,\mathrm{Hz}$

(a) (b) (c)

(d) (e) (f)

(g) (h) (i)

Figure 6.9: Designs optimizing the insertion loss $\hat{\mathrm{IL}}_{0\,\mathrm{m}}$ at a frequency of (a) 25 Hz, (d) 50 Hz, and (g) $20-80$ Hz. Designs optimizing the averaged insertion loss $\hat{\mathrm{IL}}_{10\,\mathrm{m}}$ for a point load at a frequency of (b) 25 Hz, (e) 50 Hz, and (h) $20-80$ Hz. Designs optimizing the averaged insertion loss $\hat{\mathrm{IL}}_{40\,\mathrm{m}}$ for a point load at a frequency of (c) 25 Hz, (f) 50 Hz, and (i) $20-80$ Hz.

6.3 Wave barriers of finite length

This section discusses the influence of the length of the barrier on the optimized design. The finite length of the barrier is taken into account by applying a spatial window to the radiated wave field [52, 170]. For this purpose, the domain is divided in a subdomain where spatial windowing is applied, i.e. the design domain, and the surrounding domain by means of a subdomain formulation [12]. This formulation is first introduced, after which the spatial windowing technique is explained and applied to the subdomain formulation. Then, topology optimization is applied: the sensitivities are derived and optimized results are presented.

6.3.1 Subdomain formulation

Consider a domain Ω_{s} that is divided into two subdomains: an interior domain $\Omega_{\mathrm{s}}^{\mathrm{i}}$ and an exterior domain $\Omega_{\mathrm{s}}^{\mathrm{e}}$. In this application, the interior subdomain represents the design domain, while the exterior subdomain represents the surrounding FE-PML domain. According to the subdomain formulation, the displacement field $\tilde{\mathbf{u}}_{\mathrm{s}}$ in the soil is decomposed as (figure 6.10) [12]:

$$\tilde{\mathbf{u}}_{\mathrm{s}} = \tilde{\mathbf{u}}_{\mathrm{inc}} + \tilde{\mathbf{u}}_{\mathrm{d0}} + \tilde{\mathbf{u}}_{\mathrm{d}} \tag{6.11}$$

where $\tilde{\mathbf{u}}_{\mathrm{inc}}$ is the incident wave field, which is the displacement field for the homogeneous halfspace (and therefore equal to the previously defined $\tilde{\mathbf{u}}^{\mathrm{ref}}$), $\tilde{\mathbf{u}}_{\mathrm{d0}}$ is the locally diffracted wave field, and $\tilde{\mathbf{u}}_{\mathrm{d}}$ is the diffracted wave field, i.e. the wave field radiated from the interior subdomain. The locally diffracted wave field $\tilde{\mathbf{u}}_{\mathrm{d0}}$ is the displacement field that is radiated in the soil in the exterior domain for an excavated interior domain with $\tilde{\mathbf{u}}_{\mathrm{d0}} = -\tilde{\mathbf{u}}_{\mathrm{inc}}$ at the interface Σ between the exterior and interior subdomain. At this interface, the combined wave field $\tilde{\mathbf{u}}_0 = \tilde{\mathbf{u}}_{\mathrm{d0}} + \tilde{\mathbf{u}}_{\mathrm{inc}}$ is therefore equal to zero.

By imposing continuity of displacements and stress equilibrium at the interface Σ, the discretized force vector $\underline{\tilde{\mathbf{p}}}_{\Sigma}$ due to the incident wave field on the structure can be calculated [133]:

$$\underline{\tilde{\mathbf{p}}}_{\Sigma} = -\int_{\Sigma} \mathbf{N}^{\mathrm{T}} \tilde{\mathbf{t}}^{\mathbf{n}} \left(\tilde{\mathbf{u}}_{\mathrm{inc}}\right) \mathrm{d}\Sigma - \int_{\Sigma} \mathbf{N}^{\mathrm{T}} \tilde{\mathbf{t}}^{\mathbf{n}} \left(\tilde{\mathbf{u}}_{\mathrm{d0}}\right) \mathrm{d}\Sigma \tag{6.12}$$

with $\mathbf{N}$ the shape functions for the FE-PML discretization, and $\tilde{\mathbf{t}}^{\mathbf{n}}\left(\tilde{\mathbf{u}}_{\mathrm{inc}}\right)$ and $\tilde{\mathbf{t}}^{\mathbf{n}}\left(\tilde{\mathbf{u}}_{\mathrm{d0}}\right)$ the traction fields due to the incoming wave field and locally diffracted wave field, respectively, on a plane with unit outward normal vector $\mathbf{n}$. The diffracted wave field is then calculated as:

$$\tilde{\mathbf{K}}\underline{\tilde{\mathbf{u}}}_{\mathrm{d}} = \underline{\tilde{\mathbf{p}}}_{\Sigma} \tag{6.13}$$

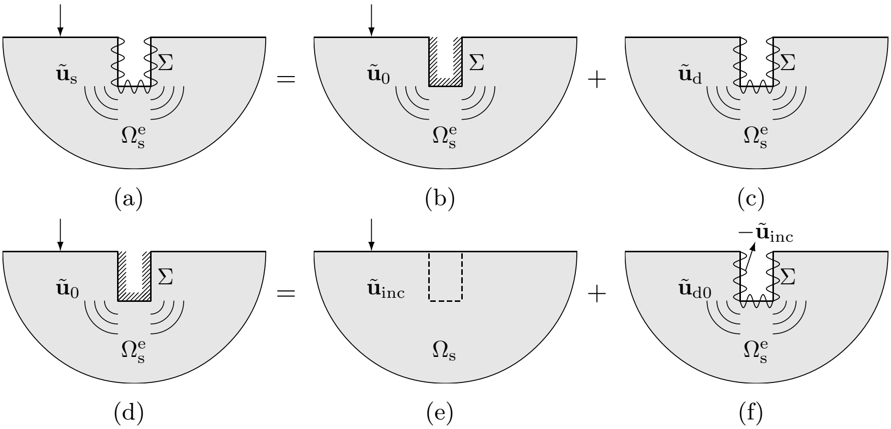
$\tilde{\mathbf{u}}_\mathrm{s}$
Σ
$\Omega_\mathrm{s}^\mathrm{e}$
=
$\tilde{\mathbf{u}}_0$
Σ
$\Omega_\mathrm{s}^\mathrm{e}$
+
$\tilde{\mathbf{u}}_\mathrm{d}$
Σ
$\Omega_\mathrm{s}^\mathrm{e}$
(a)
(b)
(c)
$\tilde{\mathbf{u}}_0$
Σ
$\Omega_\mathrm{s}^\mathrm{e}$
=
$\tilde{\mathbf{u}}_\mathrm{inc}$
Ω_s
+
$-\tilde{\mathbf{u}}_\mathrm{inc}$
$\tilde{\mathbf{u}}_\mathrm{d0}$
Σ
$\Omega_\mathrm{s}^\mathrm{e}$
(d)
(e)
(f)

Figure 6.10: Decomposition of (a) the soil displacement field $\tilde{\mathbf{u}}_\mathrm{s}$ into (b) the wave field $\tilde{\mathbf{u}}_0$ and (c) the diffracted wave field $\tilde{\mathbf{u}}_\mathrm{d}$ and decomposition of (d) the wave field $\tilde{\mathbf{u}}_0$ into (e) the incident wave field $\tilde{\mathbf{u}}_\mathrm{inc}$ and (f) the locally diffracted wavefield $\tilde{\mathbf{u}}_\mathrm{d0}$.

6.3.2 Spatial windowing

Spatial windowing allows taking the finite size of a structure into account [52, 170]. The wave field is approximated by putting a window on the radiated wave field. It should be noted that this technique only allows computing an approximation of the actual wave field due to its inability to account for the modal behaviour of the structure [52, 115].

Reconsider the Fourier transform pair relating $\hat{f}(y)$ and $\tilde{f}(k_y)$:

$$\tilde{f}(k_y) = \int_{-\infty}^{\infty} e^{+\mathrm{i}k_y y} \hat{f}(y)\,\mathrm{d}y \tag{6.14}$$

$$\hat{f}(y) = \frac{1}{2\pi} \int_{-\infty}^{\infty} e^{-\mathrm{i}k_{y0} y} \tilde{f}(k_{y0})\,\mathrm{d}k_{y0} \tag{6.15}$$

The forward Fourier transform is an integral over the longitudinal coordinate y. A structure with a finite length, situated between y_1 and y_2, is only able to contribute to the radiation of waves into the soil domain from y_1 and y_2. The wave field $\tilde{f}_\mathrm{sw}(k_y)$ in the wavenumber domain is therefore obtained by integrating from y_1 to y_2:

$$\tilde{f}^{\mathrm{sw}}\left(k_y\right) = \int\limits_{y_1}^{y_2} e^{+\mathrm{i}k_y y} \hat{f}\left(y\right) \mathrm{d}y \tag{6.16}$$

Introducing the inverse Fourier transform leads to:

$$\begin{aligned} \tilde{f}^{\mathrm{sw}}\left(k_y\right) &= \int\limits_{y_1}^{y_2} e^{+\mathrm{i}k_y y} \left\{ \frac{1}{2\pi} \int\limits_{-\infty}^{\infty} e^{-\mathrm{i}k_{y0} y} \tilde{f}\left(k_{y0}\right) \mathrm{d}k_{y0} \right\} \mathrm{d}y \\ &= \int\limits_{-\infty}^{\infty} \tilde{f}\left(k_{y0}\right) \left\{ \frac{1}{2\pi} \int\limits_{y_1}^{y_2} e^{+\mathrm{i}\left(k_y - k_{y0}\right) y} \mathrm{d}y \right\} \mathrm{d}k_{y0} \end{aligned} \tag{6.17}$$

Elaborating the integrals results in [52]:

$$\begin{aligned} \tilde{f}^{\mathrm{sw}}\left(k_y\right) &= \int\limits_{-\infty}^{\infty} \tilde{f}\left(k_{y0}\right) \left\{ \frac{1}{2\pi} \frac{e^{+\mathrm{i}\left(k_y - k_{y0}\right) y_2}}{\mathrm{i}\left(k_y - k_{y0}\right)} \left[1 - e^{-\mathrm{i}\left(k_y - k_{y0}\right)\left(y_2 - y_1\right)} \right] \right\} \mathrm{d}k_{y0} \\ &= \tilde{f}\left(k_y\right) * \left\{ \frac{1}{2\pi} \frac{e^{+\mathrm{i}k_y y_2}}{\mathrm{i}k_y} \left[1 - e^{-\mathrm{i}k_y\left(y_2 - y_1\right)} \right] \right\} \end{aligned} \tag{6.18}$$

The spatial windowing is now applied to the wave fields $\tilde{\mathbf{u}}_{\mathrm{d}0}$ and $\tilde{\mathbf{u}}_{\mathrm{d}}$ in the subdomain formulation. The locally diffracted wave field $\tilde{\mathbf{u}}_{\mathrm{d}0}$ is calculated by applying a spatial window on the imposed displacements at the interface Σ:

$$\underline{\tilde{\mathbf{u}}}_{\mathrm{d}0}|_{\Sigma} = -\underline{\tilde{\mathbf{u}}}_{\mathrm{inc}}^{\mathrm{sw}}|_{\Sigma} = -\underline{\tilde{\mathbf{u}}}_{\mathrm{inc}} * \left\{ \frac{1}{2\pi} \frac{e^{+\mathrm{i}k_y y_2}}{\mathrm{i}k_y} \left[1 - e^{-\mathrm{i}k_y\left(y_2 - y_1\right)} \right] \right\} \Big|_{\Sigma} \tag{6.19}$$

The diffracted wave field $\tilde{\mathbf{u}}_{\mathrm{d}}$ is calculated from $\tilde{\mathbf{K}}\underline{\tilde{\mathbf{u}}}_{\mathrm{d}} = \underline{\tilde{\mathbf{p}}}_{\Sigma}^{\mathrm{sw}}$, where $\underline{\tilde{\mathbf{p}}}_{\Sigma}^{\mathrm{sw}}$ is calculated as:

$$\underline{\tilde{\mathbf{p}}}_{\Sigma}^{\mathrm{sw}} = \underline{\tilde{\mathbf{p}}}_{\Sigma} * \left\{ \frac{1}{2\pi} \frac{e^{+\mathrm{i}k_y y_2}}{\mathrm{i}k_y} \left[1 - e^{-\mathrm{i}k_y\left(y_2 - y_1\right)} \right] \right\} \tag{6.20}$$

A limitation of the spatial windowing technique is its inability to account for the modal behaviour of the structure [52, 115]. The modal overlap gives an indication of the transition from the lower frequency range where the dynamic response is dominated by resonating behaviour of individual modes to the higher frequency range where the contribution of individual modes can no

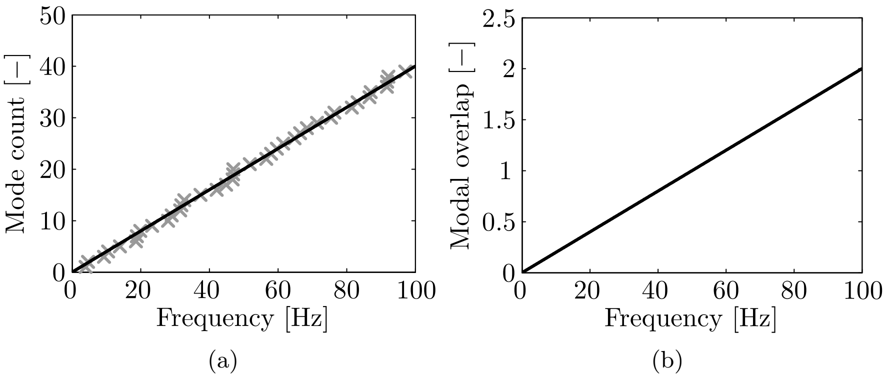

Figure 6.11: (a) Discrete (gray crosses) and fitted (black solid line) mode count $N(f)$ and (b) modal overlap $M(f)$, for the reference design in figure 5.4 with a length of $L_{\mathrm{b}y} = 15\,\mathrm{m}$.

longer be distinguished. It is defined as $M(f) = \eta f n(f)$, where $\eta = 2\beta_{\mathrm{s}}$ is the loss factor [70] and $n(f)$ is the modal density. Figure 6.11a shows the mode count $N(f)$ as a function of the frequency for the reference design in figure 5.4 with a rectangular cross-section of $7.5\,\mathrm{m} \times 1\,\mathrm{m}$ and a length of $L_{\mathrm{b}y} = 15\,\mathrm{m}$. A continuous function is fitted through the discrete curve in figure 6.11a in order to have an estimation of the modal density $n(f) = \mathrm{d}N(f)/\mathrm{d}f$. The modal overlap $M(f) = \eta f n(f)$ for the considered case is then shown in figure 6.11b. Commonly, the value $M(f) = 1$ is chosen as transition between the two frequency ranges [70]. In this case, this corresponds to 50 Hz.

For the calculation of the modal overlap, only material damping is taken into account. As pointed out by Coulier et al. [52], the influence of the resonating behaviour of individual modes in the lower frequency range stays rather limited due to strong dynamic soil-structure interaction and the associated radiation damping in the soil. As Coulier et al. [52] showed that the response at lower frequencies is mostly well estimated by the spatial windowing technique, it is assumed that the resonating behaviour of individual modes only has a limited influence on the response computed for the frequency range $20 - 80\,\mathrm{Hz}$ considered in this section.

6.3.3 Sensitivities

The sensitivities for an objective or constraint function ϕ are computed using equation (6.1). The displacement fields are obtained using the subdomain approach in equation (6.11), in which only the diffracted displacement field $\underline{\tilde{\mathbf{u}}}_{\mathrm{d}k}$ depends on the element densities $\bar{\rho}_e$. These displacement fields are obtained from the set of equilibrium equations $\tilde{\mathbf{K}}_k\underline{\tilde{\mathbf{u}}}_{\mathrm{d}k} = \underline{\tilde{\mathbf{p}}}^{\mathrm{sw}}_{\Sigma k}$, and the sensitivities of the displacements are equal to:

$$\frac{\partial \underline{\tilde{\mathbf{u}}}_k}{\partial \bar{\rho}_e} = \frac{\partial \underline{\tilde{\mathbf{u}}}_{\mathrm{d}k}}{\partial \bar{\rho}_e} = -\tilde{\mathbf{K}}_k^{-1}\frac{\partial \tilde{\mathbf{K}}_k}{\partial \bar{\rho}_e}\underline{\tilde{\mathbf{u}}}_{\mathrm{d}k} \tag{6.21}$$

Introducing this expression into equation (6.1), the sensitivities are obtained as:

$$\frac{\mathrm{d}\phi}{\mathrm{d}\bar{\rho}_e} = \frac{\partial \phi}{\partial \bar{\rho}_e} + 2\sum_{k=1}^{N_k}\mathrm{Re}\left\{\boldsymbol{\lambda}_k^{\mathrm{T}}\frac{\partial \tilde{\mathbf{K}}}{\partial \bar{\rho}_e}\underline{\tilde{\mathbf{u}}}_{\mathrm{d}k}\right\} \tag{6.22}$$

where the vectors $\boldsymbol{\lambda}_k$ are obtained from the adjoint equations:

$$\tilde{\mathbf{K}}_k^{\mathrm{T}}\boldsymbol{\lambda}_k = -\left(\frac{\partial \phi}{\partial \underline{\tilde{\mathbf{u}}}_k}\right)^{\mathrm{T}} \tag{6.23}$$

The optimization procedure is as follows. The design domain is taken as interior domain, while the surrounding domain is considered as the exterior domain. As a pre-processing step, the wave fields $\underline{\tilde{\mathbf{u}}}_{\mathrm{inc}k}$ and $\underline{\tilde{\mathbf{u}}}_{\mathrm{d}0k}$, and the force vectors $\underline{\tilde{\mathbf{p}}}_{\Sigma k}$ on the interface Σ are computed. During the optimization, first the displacement fields $\underline{\tilde{\mathbf{u}}}_{\mathrm{d}k}$ are computed. These are added to the displacement fields $\underline{\tilde{\mathbf{u}}}_{\mathrm{inc}k}$ and $\underline{\tilde{\mathbf{u}}}_{\mathrm{d}0k}$ to obtain the total displacement fields, which are used to calculate the objective function and the set of adjoint equations. The displacement vector $\underline{\tilde{\mathbf{u}}}_{\mathrm{d}k}$ and the adjoint vector $\boldsymbol{\lambda}_k$ are then used to calculate the sensitivities. Note that only equation (6.13) and (6.23) for computing the diffracted wave field $\underline{\tilde{\mathbf{u}}}_{\mathrm{d}k}$ and the adjoint vector $\boldsymbol{\lambda}_k$ need to be computed every iteration. When the pre-processing is disregarded, the computational cost for a finite barrier is therefore similar to the one for an infinite barrier.

6.3.4 Results

The problem considered in subsection 6.2.3 is now reconsidered for a barrier of finite length. A barrier with a length of $L_{\mathrm{b}y} = 15\,\mathrm{m}$ is considered. First, the insertion loss at $(x = 15\,\mathrm{m}, y = 0\,\mathrm{m}, z = 0\,\mathrm{m})$ is minimized at 25 Hz, at 50 Hz, and for the frequency range 20−80 Hz. The resulting designs and corresponding insertion losses as a function of the frequency are shown in figure 6.12. The designs resemble the infinite barrier designs optimized for a point load, for the same reason these designs resemble the ones optimized for a line load: the response at $y = 0\,\mathrm{m}$ dominates the overall response.

The wave fields are plotted in figure 6.13. As pointed out by Coulier et al. [52], due to the finite length of the barrier, waves propagating at angles θ larger than θ_L do not hit the barrier, where θ_L is given by:

$$\sin\theta_L = \frac{L_{\mathrm{b}y}/2}{\sqrt{\left(\Delta_x^{\mathrm{sb}}\right)^2 + \left(L_{\mathrm{b}y}/2\right)^2}} \tag{6.24}$$

with Δ_x^{sb} the distance in the x-direction between the source and the barrier. For the rectangular reference design, this distance is equal to 7 m.

As the waves propagating at angles $\theta > \theta_L$ are not directly affected by the barrier, the insertion loss averaged over a large length L_{rec} decreases. Figure 6.14 shows the designs optimizing the averaged insertion loss for three lengths L_{rec}: 0 m, 10 m, and 40 m. As for the infinite barriers, the designs for $L_{\mathrm{rec}} = 10\,\mathrm{m}$ resemble the ones for $L_{\mathrm{rec}} = 0\,\mathrm{m}$. For $L_{\mathrm{rec}} = 40\,\mathrm{m}$, however, considerably modified designs are obtained. Although the design optimized at 25 Hz looks different for $L_{\mathrm{rec}} = 40\,\mathrm{m}$ (figure 6.14c), the performance has hardly improved: the averaged insertion loss $\hat{\mathrm{IL}}_{40\,\mathrm{m}}$ at 25 Hz is equal to 1.2 dB for the reference design, 1.9 dB for the design optimized for $L_{\mathrm{rec}} = 0\,\mathrm{m}$ (figure 6.14a), and 2.0 dB for the design optimized for $L_{\mathrm{rec}} = 40\,\mathrm{m}$ (figure 6.14c). The design optimized at 50 Hz and for the frequency band $20 - 80\,\mathrm{Hz}$ show a greater improvement. The averaged insertion loss $\hat{\mathrm{IL}}_{40\,\mathrm{m}}$ at 50 Hz is equal to 4.1 dB for the rectangular reference barrier, 8.3 dB for the barrier optimized for $L_{\mathrm{rec}} = 0\,\mathrm{m}$ (figure 6.14d), and 10.3 dB for the one optimized for $L_{\mathrm{rec}} = 40\,\mathrm{m}$ (figure 6.14f). The averaged insertion loss $\overline{\hat{\mathrm{IL}}_{40\,\mathrm{m}}}$, frequency averaged in the range $20 - 80\,\mathrm{Hz}$, is equal to 3.3 dB for the rectangular reference barrier, 4.4 dB for the barrier optimized for $L_{\mathrm{rec}} = 0\,\mathrm{m}$ (figure 6.14g), and 6.4 dB for the one optimized for $L_{\mathrm{rec}} = 40\,\mathrm{m}$ (figure 6.14i).

6.4 A case study

In this section, the methods from the previous sections are applied to a particular problem reducing the vibration levels in a building caused by the passage of a train on a nearby railway line. First, the problem is introduced and the performance of a double wall barrier is studied. Subsequently, two optimization problems are considered. The first optimization problem minimizes the vibration level while a constraint is put on the volume. The second minimizes the volume while reducing the vibrations to a certain level.

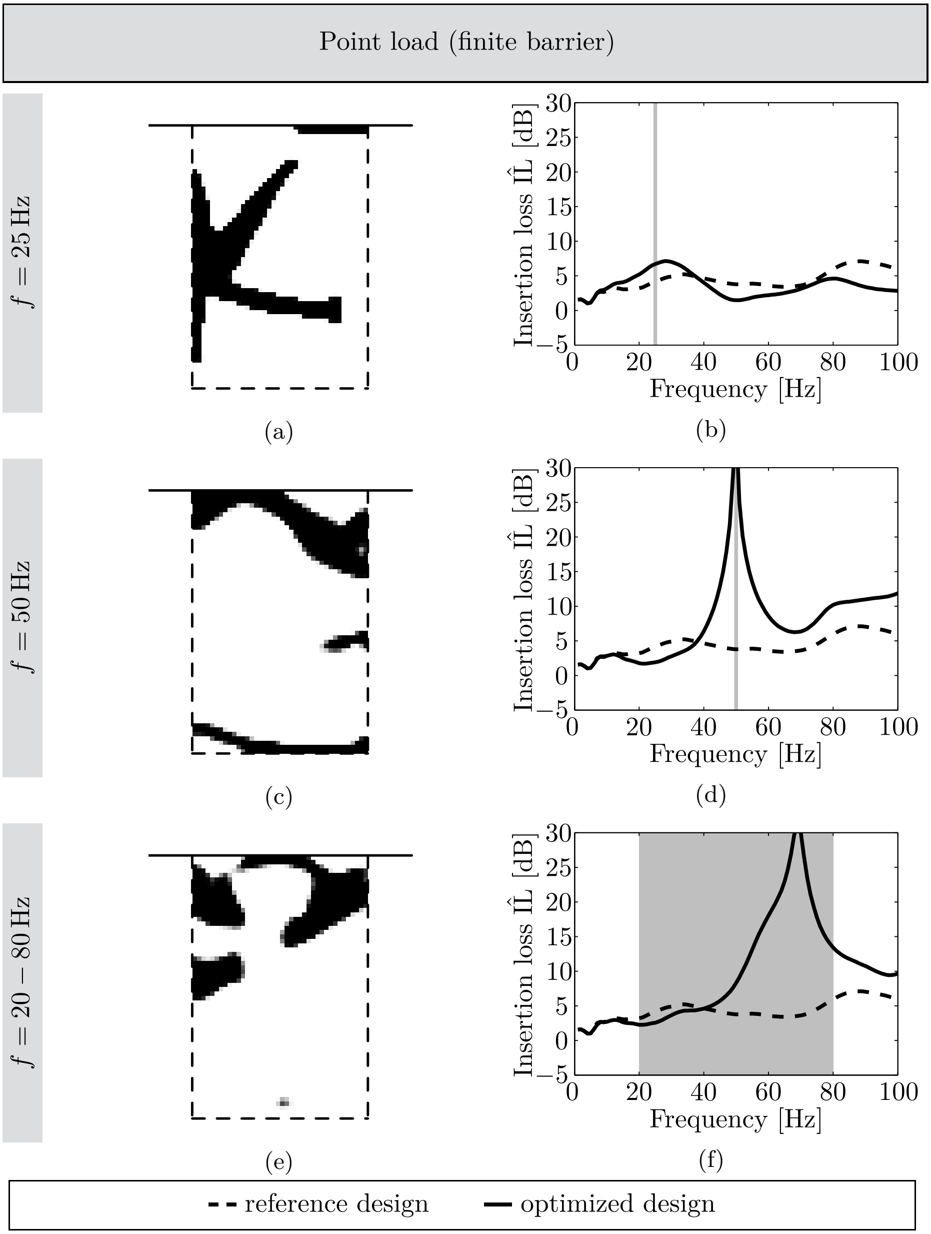

Figure 6.12: Designs with a finite length of $L_{\mathrm{b}y} = 15\,\mathrm{m}$ optimized for a point load (a) at a frequency of 25 Hz, (c) at a frequency of 50 Hz, and (e) for the frequency range $20 - 80\,\mathrm{Hz}$. Resulting insertion loss as a function of the frequency for the reference design in figure 5.4 (dashed line) and the optimized design (solid line) (b) at a frequency of 25 Hz, (d) at a frequency of 50 Hz, and (f) for the frequency range $20 - 80\,\mathrm{Hz}$.

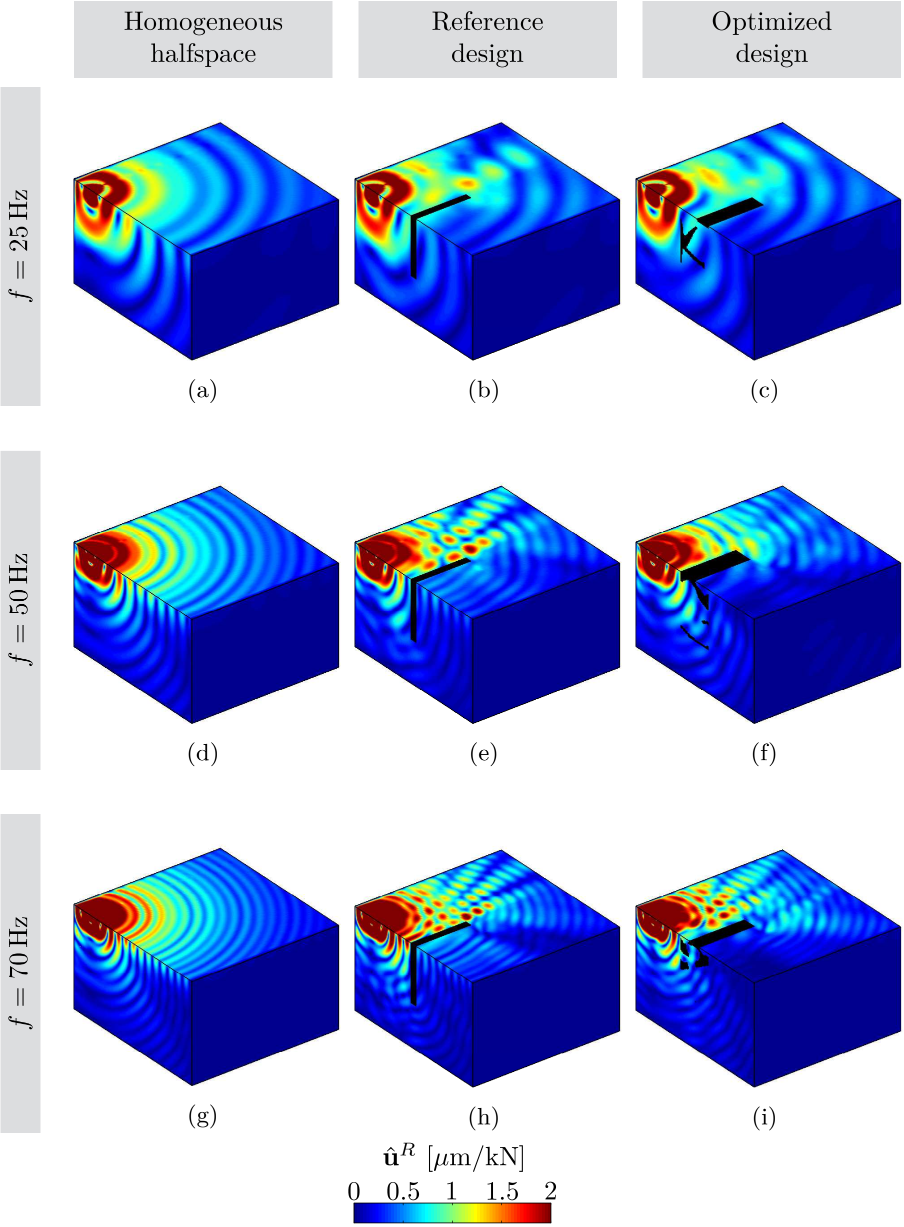
Homogeneous halfspace
Reference design
Optimized design
$f = 25\,\mathrm{Hz}$
$f = 50\,\mathrm{Hz}$
$f = 70\,\mathrm{Hz}$
(a)
(b)
(c)
(d)
(e)
(f)
(g)
(h)
(i)
$\hat{\mathbf{u}}^R$ [μm/kN]
0
0.5
1
1.5
2

Figure 6.13: Real part of the displacement field $\hat{\mathbf{u}}^R$ in the homogeneous halfspace at a frequency f of (a) 25 Hz, (d) 50 Hz, and (g) 70 Hz, with the finite reference design at a frequency f of (b) 25 Hz, (e) 50 Hz, and (h) 70 Hz, and with the finite designs optimized for a receiver at $(x = 15\,\mathrm{m}, y = 0\,\mathrm{m}, z = 0\,\mathrm{m})$ at a frequency of (c) 25 Hz, (f) 50 Hz, and (i) 70 Hz (design optimized for 20 − 80 Hz).

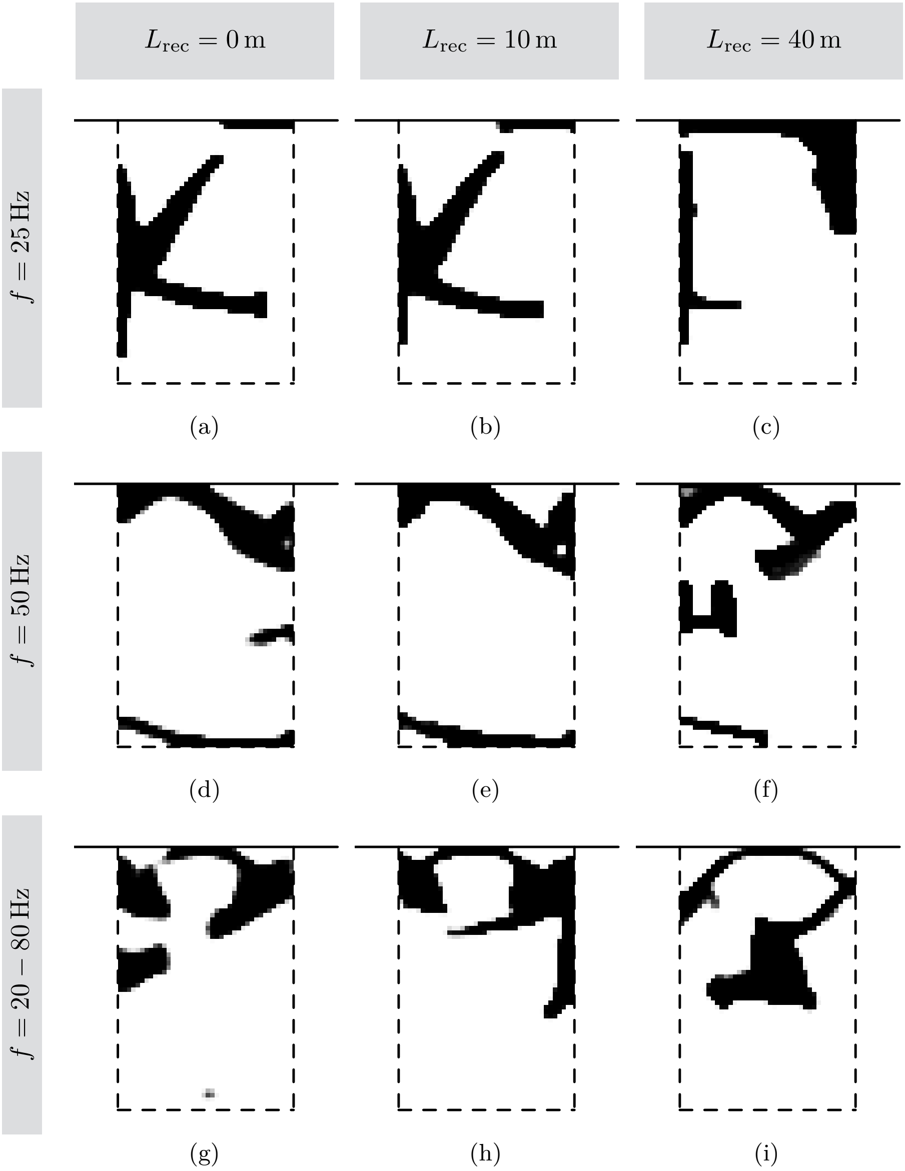
$L_{\mathrm{rec}} = 0\,\mathrm{m}$
$L_{\mathrm{rec}} = 10\,\mathrm{m}$
$L_{\mathrm{rec}} = 40\,\mathrm{m}$
$f = 25\,\mathrm{Hz}$
$f = 50\,\mathrm{Hz}$
$f = 20 - 80\,\mathrm{Hz}$
(a)
(b)
(c)
(d)
(e)
(f)
(g)
(h)
(i)

Figure 6.14: Designs with a finite length of $L_{\mathrm{b}y} = 15\,\mathrm{m}$ optimizing the insertion loss $\hat{\mathrm{IL}}_{0\,\mathrm{m}}$ at a frequency of (a) 25 Hz, (d) 50 Hz, and (g) 20 − 80 Hz. Designs optimizing the averaged insertion loss $\hat{\mathrm{IL}}_{10\,\mathrm{m}}$ for a point load at a frequency of (b) 25 Hz, (e) 50 Hz, and (h) 20 − 80 Hz. Designs optimizing the averaged insertion loss $\hat{\mathrm{IL}}_{40\,\mathrm{m}}$ for a point load at a frequency of (c) 25 Hz, (f) 50 Hz, and (i) 20 − 80 Hz.

6.4.1 Problem description

The problem considered in this case study is shown in figure 6.15. On the surface of a homogeneous halfspace, representing the soil, a building is located close to a railway track. In the building, sensitive equipment is placed, whose operation is disturbed by vibrations resulting from train passages. In order to reduce the transmission of vibrations from the railway track to the building stiffer material is inserted in the soil.

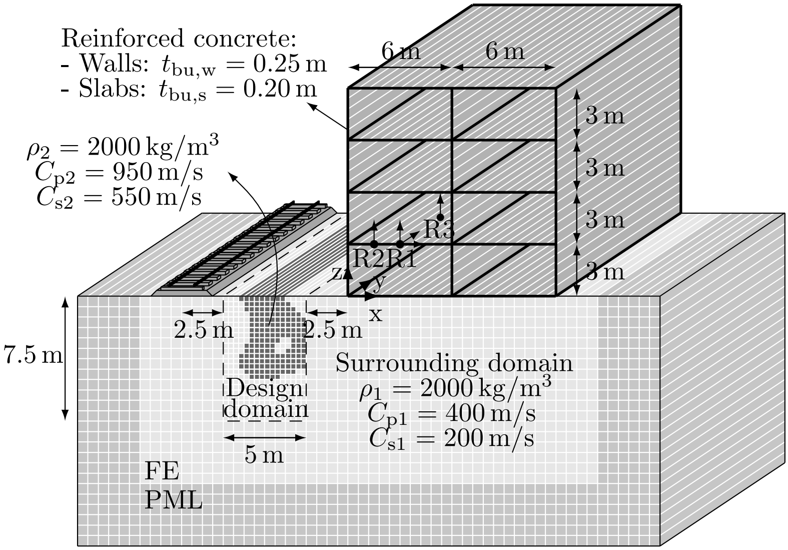
Reinforced concrete:
- Walls: $t_{\mathrm{bu,w}} = 0.25\,\mathrm{m}$
- Slabs: $t_{\mathrm{bu,s}} = 0.20\,\mathrm{m}$
$\rho_2 = 2000\,\mathrm{kg/m^3}$
$C_{\mathrm{p2}} = 950\,\mathrm{m/s}$
$C_{\mathrm{s2}} = 550\,\mathrm{m/s}$
6 m
6 m
3 m
3 m
3 m
3 m
R3
R2
R1
z
y
x
2.5 m
2.5 m
7.5 m
Design domain
5 m
Surrounding domain
$\rho_1 = 2000\,\mathrm{kg/m^3}$
$C_{\mathrm{p1}} = 400\,\mathrm{m/s}$
$C_{\mathrm{s1}} = 200\,\mathrm{m/s}$
FE
PML

Figure 6.15: The longitudinally invariant elastodynamic optimization problem. The mesh is added as illustration only and is not the actual finite element mesh.

The soil is a typical sandy soil having a mass density of $2000\,\mathrm{kg/m^3}$, a dilatational wave velocity of $400\,\mathrm{m/s}$, a shear wave velocity of $200\,\mathrm{m/s}$, and material damping ratios of $\beta_{\mathrm{p}} = \beta_{\mathrm{s}} = 0.025$ for the dilatational waves and the shear waves, respectively. The soil is modeled using two-and-a-half-dimensional four-node volume elements with an element size of 0.25 m, corresponding to ten elements per shear wavelength at a frequency of 80 Hz. At the boundaries, PMLs are added to prevent spurious reflections.

The building is a four-story frame with a raft foundation consisting of four floors and two spans. It has a total width of 12 m and a total height of 12 m. The thickness of the walls is 0.25 m, while the thickness of the slabs is

0.20 m. The walls and slabs are made of reinforced concrete with a mass density of 2500 kg/m^3, a Young's modulus of 30 GPa, and a Poisson's ratio of 0.25. The building is discretized using two-and-a-half-dimensional two-node shell elements with a length of 0.25 m. The mass and stiffness matrices are derived in appendix B. The degrees of freedom not only consist of the displacements in three directions, but also of a rotation for out-of-plane bending.

The railway track is situated at a distance of 10 m from the building ($x = -10\,\mathrm{m}$). The track is a classical ballasted track with sleepers supporting the rails. The model used for the railway track is shown in figure 6.16a. The rails are modeled as Euler-Bernoulli beams, while the rail pads are modeled as continuous spring-damper connections. The sleepers are assumed to be rigid in the plane of the track cross section and are assumed not to contribute to the longitudinal stiffness of the track, so they can be modeled as a uniformly distributed structure over the track length. The ballast is assumed to act as a set of distributed, independent linear springs and dampers. The characteristics of the railway track are taken from Lombaert et al. [119] and are listed in table 6.1.

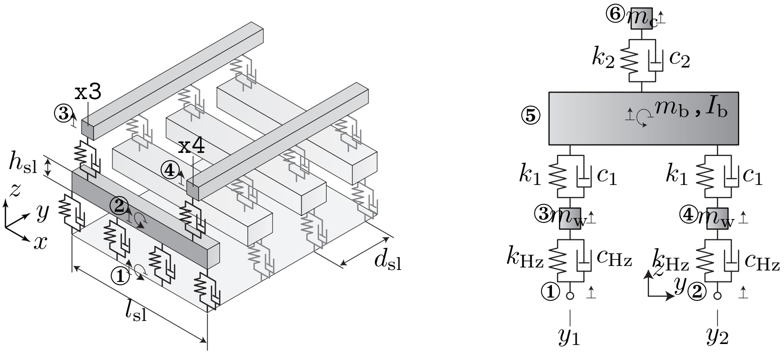

(a) (b)

Figure 6.16: Model of (a) the railway track and (b) half a wagon [122].

The displacement field resulting from a passing train is calculated in a simplified way, applying the dynamic axle loads at fixed positions on the track as a series of incoherent point loads of the same magnitude. Previous studies have indicated that the stationary part of the response can be well approximated in this way (see section 3.4.2). A typical two-car EMU train (according to [129]) at a speed of 160 km/h is considered, with a car length of 26.6 m and a total length of 53.2 m. The bogie center distance is 19 m and the distance between two axles of a bogie is 2.7 m. The center of the train is located at ($x = -10\,\mathrm{m}, y = 0\,\mathrm{m}, z = 0\,\mathrm{m}$). By assuming that both rails have the same unevenness, the train can be

Table 6.1: Characteristics of the railway track [119].

Part	Characteristic	Value	Dimension
Rail	Bending stiffness $E_\mathrm{r}I_\mathrm{r}$	6.4×10^6	Nm^2
	Mass per unit length $\rho_\mathrm{r}A_\mathrm{r}$	60	kg/m
	Position x_3	-10.7175	m
	Position x_4	-9.2825	m
Rail pad	Stiffness k_rp	255.7×10^6	N/m
	Viscous damping c_rp	22.5×10^3	Ns/m
Sleeper	Length l_sl	2.5	m
	Width b_sl	0.235	m
	Height h_sl	0.205	m
	Mass m_sl	300	kg
	Sleeper distance d_sl	0.6	m
Ballast	Height h_b	0.35	m
	Mass density ρ_b	1700	$\mathrm{kg/m}^3$
	Stiffness K_b	156.7×10^6	$\mathrm{N/m}^3$
	Viscous damping C_b	28.6×10^3	$\mathrm{Ns/m}^3$

modeled with a two-dimensional model (figure 6.16b). The characteristics are taken from Mirza et al. [129] and are listed in table 6.2.

Table 6.2: Characteristics of the EMU train [129].

Characteristic	Value	Dimension
Hertzian spring stiffness k_Hz	1.5×10^9	N/m
Hertzian spring damping c_Hz	0	Ns/m
Wheelset mass m_w	1800	kg
Primary spring stiffness k_1	2.4×10^6	N/m
Primary spring damping c_1	30×10^3	Ns/m
Bogie mass m_b	5000	kg
Bogie moment of inertia m_b	6000	kgm^2
Secondary spring stiffness k_2	0.6×10^6	N/m
Secondary spring damping c_2	20×10^3	Ns/m
Train car mass m_c	40000	kg

The dynamic axle loads are obtained by solving a dynamic train-track interaction problem, with rail unevenness as excitation mechanism [119]. The following PSD function is used for the rail unevenness [5]:

$$\tilde{S}_{u_{\mathrm{w/r}}}(k_y) = \frac{A}{2\pi(1 + n/n_0)^3} \tag{6.25}$$

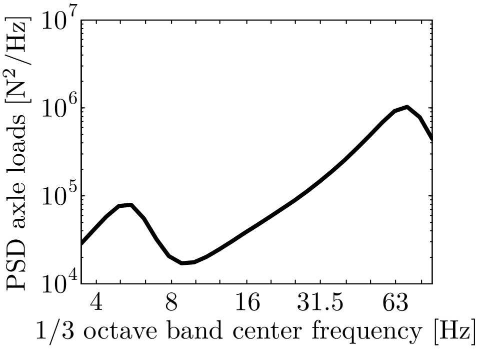

Figure 6.17: PSD function of the dynamic axle loads obtained from the dynamic train-track interaction problem with the PSD function of the rail unevenness given by equation (6.25).

where $n = k_y/2\pi$ is the cyclic frequency, $n_0 = 0.0233$ cycles/m, and A is taken to be equal to $160 \times 10^{-6}\,\mathrm{m}^3$/cycle [5]. The resulting PSD function of the axle loads is shown in figure 6.17.

The vibration levels are evaluated at specific points and directions inside the building, at the locations of sensitive equipment. In this case five receivers are considered on the first floor in the span closest to the source. Their positions are shown in figure 6.15 and are listed in table 6.3. The RMS velocity spectra at the different receivers are shown in figure 6.18 in case of the homogeneous halfspace, i.e. before introducing a wave barrier.

Table 6.3: Receiver positions in the building where the vibration levels are to be reduced.

Label	x [m]	y [m]	z [m]	Direction
R1x	3	0	3	x
R1y	3	0	3	y
R1z	3	0	3	z
R2z	1.5	0	3	z
R3z	3	1.5	3	z

The vibration levels are evaluated with respect to Gordon's generic vibration criteria for sensitive equipment [78]. These criteria are generally denoted as the Vibration Criteria (VC) and are superimposed in figure 6.18. They are specified in terms of the maximum allowable RMS velocity in the one-third octave bands between 4 and 80 Hz. Less stringent vibration limits are

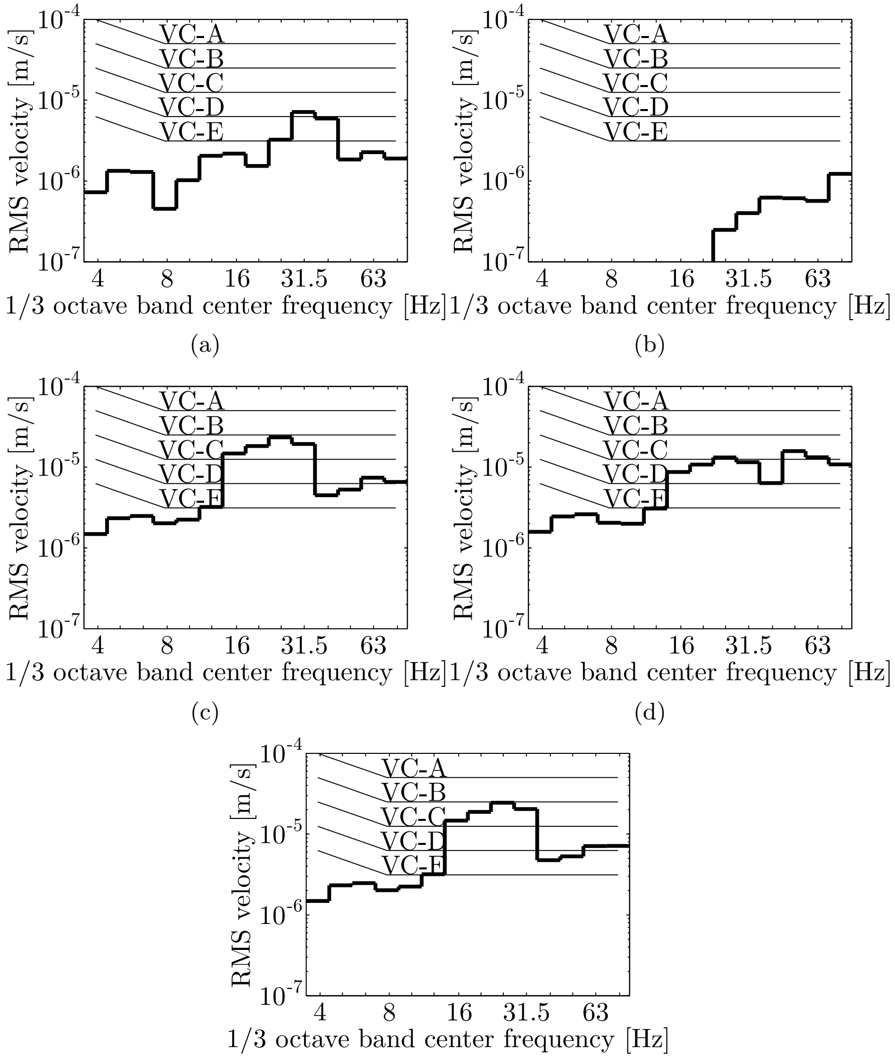

(a)

(b)

(c)

(d)

(e)

Figure 6.18: The one-third octave band RMS spectra of the velocity for the original homogeneous halfspace at receivers (a) `R1x`, (b) `R1y`, (c) `R1z`, (d) `R2z`, (e) `R3z`. Superimposed are Gordon's generic vibration criteria for sensitive equipment [78].

imposed in the frequency range between 4 to 8 Hz, where the limit is that of constant acceleration instead of constant velocity, as this frequency range in most instances lies below the lowest resonance frequency of the equipment components. As a result, relative motions between the components are harder to excite [78].

The RMS velocity spectra in the first two receivers, which are horizontal receivers in the `x`- and `y`-direction, have rather small values compared with the vertical receivers. For receivers `R1z` and `R3z`, for which only the `y`-coordinate differs, the RMS velocity levels are similar. For these receivers, the largest RMS velocity levels are found in the one-third octave bands with a center frequency of 16 Hz, 20 Hz, 25 Hz, and 31.5 Hz. For receiver `R2z`, however, the largest RMS velocity levels are found in the one-third octave bands with a center frequency of 50 Hz and 63 Hz.

The difference in RMS velocity spectra for receivers `R1z` and `R3z` on the one hand, and for receiver `R2z` on the other hand can be explained by their location. Receivers `R1z` and `R3z` are located in the middle of the floor, while receiver `R2z` is located at one fourth of the floor span. The bending modes of the floors, assumed clamped at both sides, are shown in figure 6.19. The first bending mode has a maximum in the middle of the floor, causing higher vibration levels at receivers `R1z` and `R3z` for frequencies around its natural frequency, which is 21 Hz. The second bending mode has a node in the middle of the floor and has a maximum close to one fourth of the floor span, causing higher vibration levels at receiver `R2z` for frequencies around its natural frequency, being 56 Hz. As excitation around the first two natural frequencies results in high vibration levels in the corresponding one-third octave bands, the mitigation measures should mainly reduce the vibration levels in these bands. The performance is evaluated for the maximum RMS velocity spectra over the different receivers, which is shown in figure 6.20 for the homogeneous halfspace.

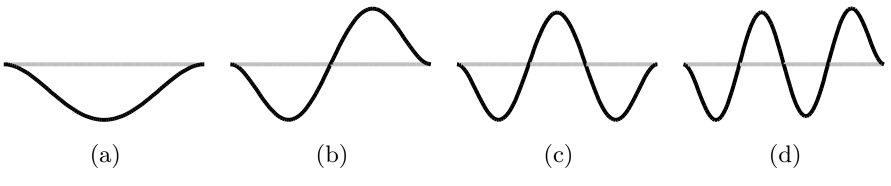

(a) (b) (c) (d)

Figure 6.19: Modes of the clamped building floor at (a) 21 Hz, (b) 56 Hz, (c) 110 Hz, and (d) 183 Hz (values for $k_y = 0\,\mathrm{m}^{-1}$).

In order to reduce the vibration levels at the considered receiver points, a barrier is introduced between the building and the track. The barrier is assumed to be infinitely long and is constructed by jet grouting, which results in a stiffer soil.

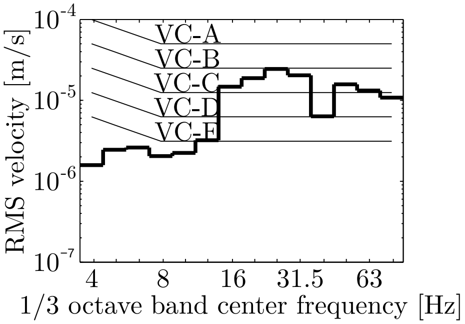

Figure 6.20: The maximum one-third octave band RMS spectra of the velocity over the different receivers for the homogeneous halfspace. Superimposed are Gordon's generic vibration criteria for sensitive equipment [78].

Jet grouting is assumed to be possible in a zone with dimensions $7.5 \times 5\mathrm{m}^2$, the design domain, located between the railway track and the building (figure 6.15). The stiffer material has a mass density of $2000\,\mathrm{kg/m}^3$, a dilatational wave velocity of $950\,\mathrm{m/s}$, a shear wave velocity of $550\,\mathrm{m/s}$, and material damping ratios of $\beta_\mathrm{p} = \beta_\mathrm{s} = 0.025$ for the dilatational waves and the shear waves, respectively.

6.4.2 A double wall barrier

As a reference, a single and double wall barrier are first considered. They both have a depth of 7.5 m. The thickness of the single wall barrier is 1 m, the walls of the double wall barrier are 0.5 m, both corresponding to a volume of 20 % of the design domain shown in figure 6.15. The distance between the two walls of the double wall barrier is equal to 3.5 m, corresponding to the theoretical best-performing distance-thickness relation $k_{\mathrm{R}1}d + k_{\mathrm{R}2}t = n\pi$ for frequencies $25, 50, 75, \ldots$ Hz.

The single wall, the double wall, and the resulting maximum RMS velocity spectra in the different receivers are shown in figure 6.21. For the original homogeneous halfspace, the maximum RMS velocity is situated in the one-third octave band with a center frequency at 25 Hz and is equal to $24.42\,\mu\mathrm{m/s}$, which is close to the VC-B criterion ($25\,\mu\mathrm{m/s}$). By introducing the single wall barrier, the RMS velocity in this one-third octave band is reduced to $15.62\,\mu\mathrm{m/s}$. However, the maximum RMS velocity is now situated in the one-third octave band with a center frequency at 50 Hz and is equal to $19.65\,\mu\mathrm{m/s}$. The double wall barrier results in a lower maximum RMS velocity in the 50 Hz one-third octave band, namely 17.15 μm/s, but also in a slightly higher maximum RMS velocity in the 25 Hz one-third octave band, namely 17.81 μm/s. The overall performance, determined by the maximum of the RMS velocity in all one-third octave bands, is slightly better for the double wall barrier, but the difference is hardly significant (17.81 μm/s instead of 19.65 μm/s).

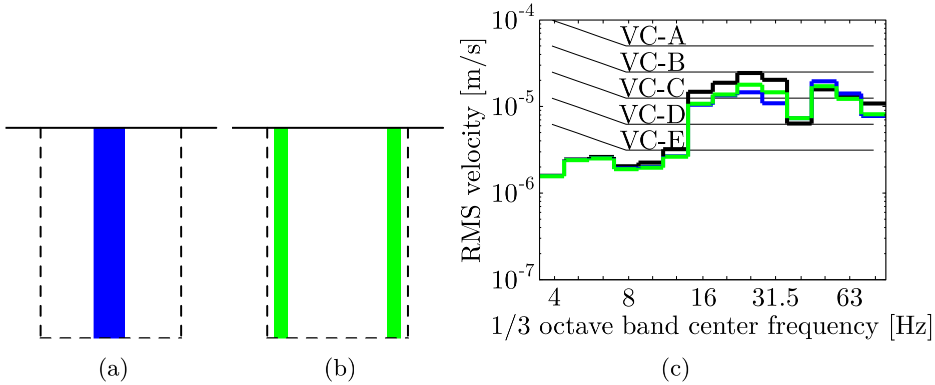

(a) (b) (c)

Figure 6.21: (a) The single wall barrier, (b) the double wall barrier and (c) the maximum one-third octave band RMS spectra of the velocity at the different receivers for the original homogeneous halfspace (black), for the single wall barrier (blue), and for the double wall barrier (blue).

6.4.3 Minimizing the vibration levels

The aim of the first optimization problem is to optimally distribute a given volume of stiffer material in the design domain (indicated in figure 6.15) such that the vibration levels are minimized. The objective function is the maximum RMS velocity in the several frequency bands $m = 1 \ldots N_{\text{band}}$ and at the different receiver points $j = 1 \ldots N_L$. As the vibration criteria for sensitive equipment are not flat over the frequency range considered, weights w_m are introduced (figure 6.22). The optimization problem can therefore mathematically be formulated as:

$$\begin{aligned} \min_{\rho_e} \quad & \max_{m=1\ldots N_{\text{band}}} \left\{ \max_{j=1\ldots N_L} \left[\frac{\hat{v}_{mj}^{\text{RMS}}\left(\bar{\rho}_e\right)}{w_m} \right] \right\} \\ \text{s. t.} \quad & \sum_{e=1}^{N_e} v_e \bar{\rho}_e \leq V^{\max} \\ & 0 \leq \rho_e \leq 1, \qquad\qquad\qquad e = 1 \ldots N_e \end{aligned} \tag{6.26}$$

where $\hat{v}_{mj}^{\mathrm{RMS}}$ is the RMS velocity in the m-th one-third octave band at receiver position j, v_e is the volume of element e, and $V^{\max}$ is the upper limit for the volume of distributed material, here equal to 20 % of the design domain. As this problem is not differentiable, it is reformulated using a bound formulation. The gradient of the RMS velocity $\hat{v}_{mj}^{\mathrm{RMS}}$ is computed with equation (6.3), where the adjoint variables $\boldsymbol{\lambda}_k$ are computed from equation (6.4). The computation time of the optimization is 59 hours.

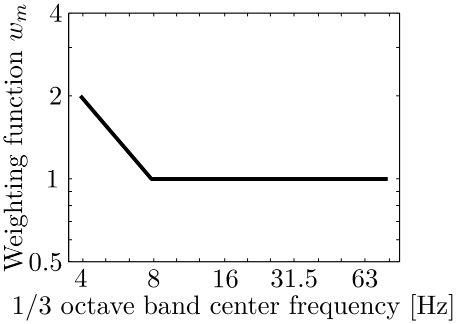

Figure 6.22: The weighting function w_m.

Figure 6.23a shows the topology optimized design, obtained from solving the optimization problem in equation (6.26). The performance of this design is compared with the one of the single wall barrier with a width of 1 m and a depth of 7.5 m, as considered in the previous section. The single wall barrier has therefore the same volume as the optimized design and extends to the bottom of the design domain. For the topology optimized design, the RMS velocity remains under 9.94 μm/s for all one-third octave bands. The maximum RMS velocity level is therefore reduced by 59 % compared to the original halfspace, by 49 % compared to the single wall barrier, and 44 % compared to the double wall barrier, while the single wall barrier, the double wall barrier, and the optimized barrier all have the same volume of material (20 % of the design domain). In contrast to the single and double wall barriers, the VC-C criterion is now satisfied.

The design has two main features: the inclined part, guiding the waves into the soil, away from the surface and the building, and a vertical part. Figure 6.24 shows the influence of the inclined part. When only the inclined part is considered, the RMS velocity is mainly reduced for the one-third octave bands with a center frequency of 16 Hz, 20 Hz, 25 Hz, and 31.5 Hz. The RMS velocity for one-third octave bands with a higher center frequency is almost unaffected as compared to the RMS velocity for the homogeneous halfspace. The inclined part therefore reduces the vibration levels around the lowest natural frequency

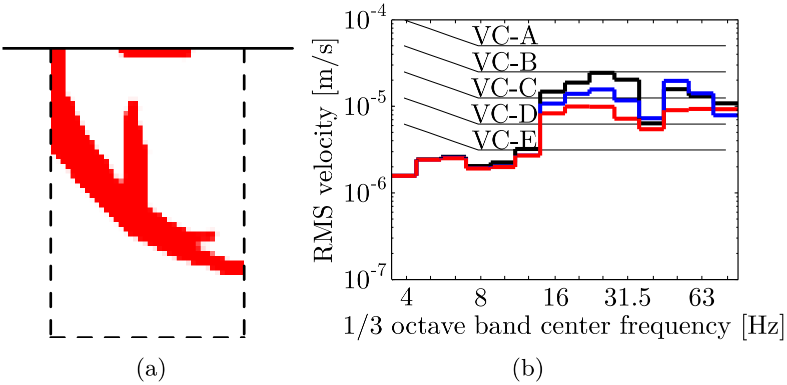

Figure 6.23: (a) The topology optimized design and (b) the maximum one-third octave band RMS spectra of the velocity at the different receivers for the original homogeneous halfspace (black), for the rectangular reference design in figure 6.21a (blue), and for the optimized design (red).

of the building floors, while the vertical and horizontal part at the surface reduce the RMS velocity at higher frequencies.

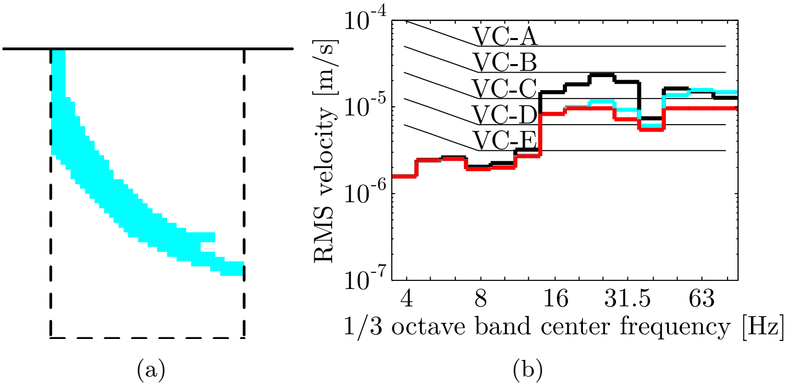

Figure 6.24: (a) The inclined part of the topology optimized design and (b) the maximum one-third octave band RMS spectra of the velocity at the different receivers for the original homogeneous halfspace (black), for the optimized design (red), and for the inclined part of this design (cyan).

The sensitivity with respect to geometric imperfections is evaluated by changing the projection function threshold η in equation (4.11). A dilated ($\eta = 0.25$), intermediate ($\eta = 0.5$), and eroded ($\eta = 0.75$) version of the optimized design are shown in figure 6.25. This figure also shows the influence of the projection threshold on the maximum RMS velocity spectra at the different receivers for the different one-third octave bands. For projection thresholds in the interval $[0.25, 0.75]$, the VC-C criterion is satisfied. The design is therefore simplified manually without first applying a robust optimization. The result of the post-processing is shown in figure 6.26. The maximum RMS velocity level is equal to $11.07\,\mu$m/s, which is only slightly higher than for the optimized design ($9.94\,\mu$m/s).

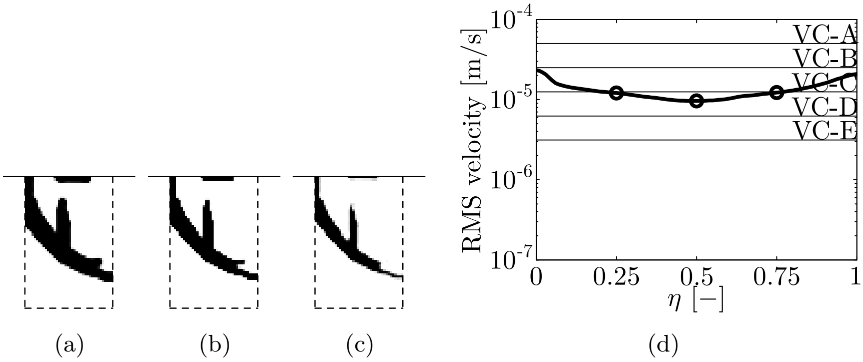

(a) (b) (c) (d)

Figure 6.25: The (a) dilated ($\eta = 0.25$), (b) intermediate ($\eta = 0.5$), and (c) eroded ($\eta = 0.75$) version of the optimized design and (d) the influence of the projection threshold η on the maximum one-third octave band RMS spectra of the velocity at the different receivers.

6.4.4 Minimizing the volume

In many practical cases, the aim is to minimize the costs while reducing the vibration levels in the building such that a certain vibration criterion is satisfied. Both the volume and the feasibility of the barrier influence the cost. In this subsection, only the volume of the barrier is minimized as the feasibility is case-specific and should therefore be evaluated with the contractor. It must be noted, however, that the feasibility has a serious impact on the total cost.

The aim of this optimization problem is thus to minimize the volume of stiffer material in the design domain while satisfying a given vibration criterion in the different frequency bands $m = 1 \ldots N_{\text{band}}$ at the receiver points $j = 1 \ldots N_L$.

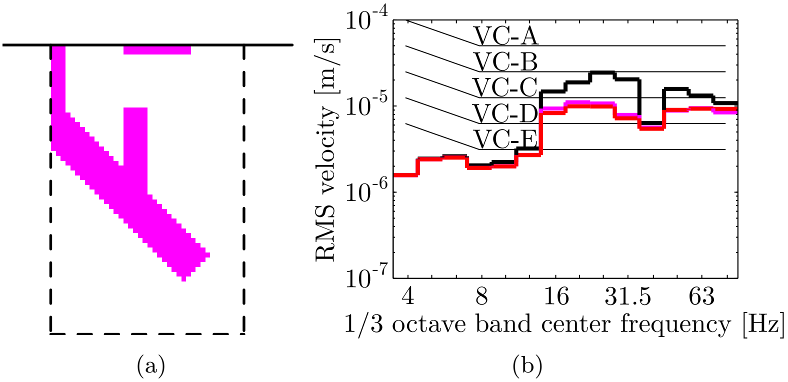

(a) (b)

Figure 6.26: (a) Simplified design after a manual post-processing of the topology optimized design and (b) the maximum one-third octave band RMS spectra of the velocity at the different receivers for the original homogeneous halfspace (black), for the optimized design (red), and for the simplified design (magenta).

This problem is formulated as:

$$\begin{array}{lll} \min & \sum_{e=1}^{N_e} v_e \bar{\rho}_e & \\ \text{s.t.} & \hat{v}_{mj}^{\text{RMS}}\left(\bar{\rho}_e\right) \leq c_m, & m = 1 \ldots N_{\text{band}} \\ & & j = 1 \ldots N_L \\ & 0 \leq \rho_e \leq 1, & e = 1 \ldots N_e \end{array} \tag{6.27}$$

where c_m is the vibration criterion in the mth one-third octave band.

The first optimization problem in the previous section showed that, for an optimized barrier with a volume of only 20% of the design domain, it is possible to reduce the vibration levels such that they satisfy the VC-C criterion. The optimization problem in equation (6.27) is therefore solved for the VC-C criterion. The topology optimized design and the corresponding RMS velocity spectra are shown in figure 6.27. In this case, only 13.3 % of the design domain volume is needed to satisfy the VC-C criterion in all one-third octave bands at all receivers. This is a considerable improvement with respect to the single and double wall barrier, which despite their higher volume of stiffer material (20 % of the design domain) do not reduce the vibration levels to the VC-C criterion.

Figure 6.28 shows the optimized design and the corresponding RMS velocity spectra with the constraint that the vibration levels at the receivers need to satisfy the VC-D criterion. The volume of the optimized design is equal to

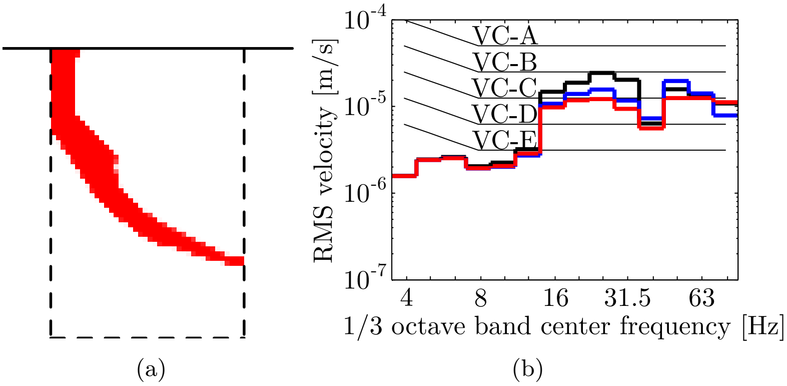

Figure 6.27: (a) The topology optimized design satisfying the VC-C for a minimum volume and (b) the maximum one-third octave band RMS spectra of the velocity at the different receivers for the original homogeneous halfspace (black), for the rectangular reference design in figure 6.21a (blue), and for the optimized design (red).

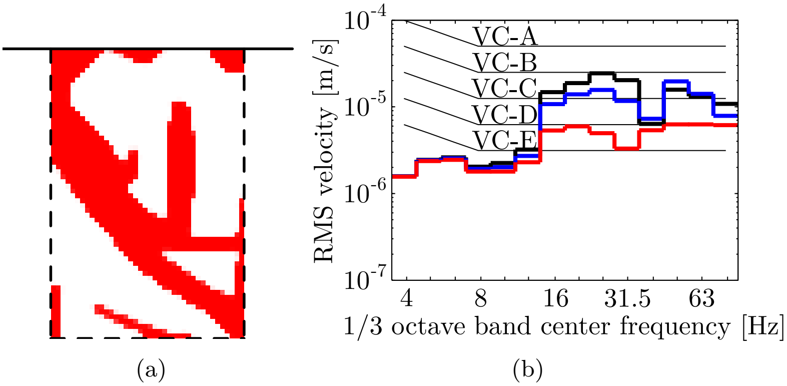

Figure 6.28: (a) The topology optimized design satisfying the VC-D for a minimum volume and (b) the maximum one-third octave band RMS spectra of the velocity at the different receivers for the original homogeneous halfspace (black), for the rectangular reference design in figure 6.21a (blue), and for the optimized design (red).

38.5 % of the design domain volume, and therefore almost twice the volume of the design in figure 6.23. Although the design has the same main features, namely the inclined part going from the left upper corner to the right bottom corner of the design domain and the vertical part in the center of the design domain, these features have become larger and multiple small features have been added to the design, which makes it more complex. This complexity results in an excellent performance, satisfying the VC-D criterion and therefore reducing the vibration levels by 74 % compared to the ones obtained for the original halfspace, but also reduces the feasibility of the design and increases its sensitivity to geometric imperfections.

6.5 Conclusion

In this chapter, topology optimization is applied to design wave barriers which reduce vibration transmission caused by point loads on a surface. A 2.5D FE-PML model is used to obtain the three-dimensional displacement field for problems with invariant cross sections. The sensitivities for the 2.5D model have been derived and are used to solve a number of problems.

First, wave barriers of infinite length have been considered. Two cases were considered: spatially harmonic line loads and point loads. As the design domain projected to the wave front propagation direction becomes larger for higher wavenumbers than the design domain in the xz-plane, the designs are different by exploiting this larger apparent width of the design domain. For the highest wavenumbers, the optimized designs were double (or triple) walls, which are optimal for the quarter wave-stack condition.

Subsequently, point loads were considered, where the equilibrium equations are computed for multiple wavenumbers after which an inverse Fourier transform is applied to obtain the displacements in the spatial domain. The designs were optimized for two harmonic loads (at 25 Hz and 50 Hz) and a broadband source (for frequencies in the interval $20-80$ Hz). Next to a receiver point, also receiver lines were considered. The receiver point and the small receiver lengths result in designs similar to the ones optimized for a line load. For larger receiver lengths, the stiffness of the barrier becomes important. This results in slightly different designs.

To take into account the effect of a finite length of the wave barrier, the spatial windowing technique is applied. This technique in fact puts a window on the radiated wave field. This radiated wave field is computed using the subdomain formulation. By applying spatial windowing, the 2.5D FE-PML method can by applied to compute the displacement fields, and therefore its computational efficiency is maintained.

Finally, a realistic case study is considered, where a building is added to the model. A passing train is modeled as a series of incoherent point sources, whose excitation is caused by railway unevenness. A single wall barrier, a double wall barrier and some optimized wave barriers are compared. It is shown that the optimized wave barriers outperform the former two and that simplifying the design hardly leads to a deterioration of the performance. In practical applications, one might want to minimize the volume, which influences the cost, while satisfying some vibration criteria. Low vibration levels can be obtained with a significant reduction in material use.

Chapter 7

Conclusions and recommendations for further research

In order to reduce environmental ground vibration due to railway traffic, mitigation measures on the transmission path can be applied to impede propagation of ground vibration from source to receiver. Currently, only a limited number of simple design geometries have been investigated. These have mainly been determined by trial and error because of the high cost of numerical simulations. As a result, the performance of current designs is suboptimal which leaves much room for improvement.

The aim of this work is therefore to study novel design geometries which have the potential to improve the current performance and to develop a methodology to optimize the design of mitigation measures. For this purpose, topology optimization is used as it simultaneously optimizes size, shape, and topology of material distribution problems and is therefore particularly suitable for finding novel designs.

This chapter starts by summarizing the main conclusions of this thesis. Additionally, some recommendations for further research are presented.

7.1 Conclusions

Double wall barrier

A double wall barrier is analyzed as mitigation measure for ground vibration transmission. In acoustics, the use of double walls is a well established measure for reducing the sound transmission as it leads to higher sound reduction between the mass-spring-mass resonance and the cavity resonances. For the reduction of ground vibration transmission, however, it is found that the performance of double wall barriers is hardly better than for single wall barriers. Both the bending stiffness of the barrier and the contrast in impedance between the soil and the barrier play a role in the performance of single and double wall barriers. The bending stiffness is the same for a single wall barrier and a double wall barrier with wall thicknesses equal to the half of the single wall barrier thickness. Reflection of incoming waves, however, determined by the contrast in impedance, is different for single and double wall barriers. Equivalent one-dimensional models showed that a maximum reflection and therefore minimum transmission of the surface waves is obtained when the thickness of the walls and the distance between the walls is equal to a quarter of the Rayleigh wavelength. This, however, is mostly not practical as for the frequency interval of interest, it would require large wall thicknesses and a large distance between the walls. For smaller thicknesses and distances, the performance of a double wall barrier is therefore mostly similar to the one of a single wall barrier. For double walls, standing waves moreover occur, further reducing the performance and therefore compensating for the improved reflection capacities.

Topology optimization of wave barriers

Topology optimization is then applied to find novel designs performing better than the previously studied simple designs, such as the single and double wall barrier. The density based approach is applied with the SIMP interpolation for the material properties. Regularization techniques are employed to control the complexity of the final design and to prevent numerical issues. Continuation schemes are used to avoid getting stuck in local minima in an early stage of the optimization. The topology optimization problems are solved using the gradient based algorithm MMA. Topology optimization problems are characterized by a large number of design variables. An efficient computation of the sensitivities is therefore indispensable, and the adjoint method is applied as it only requires one additional computation of an equation, the adjoint equation, which is similar to the forward state equation. The sensitivities are obtained for one-dimensional problems modeled with the direct stiffness method and for two- and two-and-a-half-dimensional problems modeled with finite elements and perfectly matched layers at the boundaries to prevent spurious reflections.

The methodology is first applied to one-dimensional problems, consisting of two halfspaces and an intermediate domain. In this intermediate domain, layers of a different material are optimally distributed to reduce the transmittance of plane waves. For harmonic waves, the optimization leads to periodic layer sequences whose performance is characterized by stopbands, frequency bands where the transmission is attenuated. These result in the lowest transmittance if the thickness of the layers is equal to a quarter of the wavelength. The more periodic cells fit in the intermediate domain, the more pronounced are the stopbands. To reduce the transmittance for larger frequency bands, the optimized design loses its periodicity to create multiple stopbands close to each other.

Topology optimization is then applied to design wave barriers with an invariant cross section in a homogeneous halfspace to optimally reduce the transmission of railway induced ground vibrations. The loading of a train is first approximated by a line load. This allows using a two-dimensional model which is computationally relatively cheap. The obtained optimized barriers reduce the vibration levels at the surface behind the barrier by reflecting the incoming waves or directing them away from the surface. Accounting for the three-dimensional behavior of the wave barrier is, however, crucial, as the stiffness of the barrier prevents the propagation of waves when the trace wavelength of the incoming wave is smaller than the bending wavelength of the barrier. Topology optimization is therefore performed for a point load exciting the surface, as this allows taking this three-dimensional effect into account. The optimized designs for a point load are more or less the same as for a line load when only the responses at small longitudinal distances from the source is taken into account for assessing the performance. Different barriers are obtained when also the response at larger longitudinal distances are taken into account, as the bending stiffness of the barrier will hinder wave transmission for trace wavelengths smaller than the bending wavelength. The finite length of the barrier is modeled by applying spatial windowing to the radiated wave fields. Except for the larger preprocessing step, the optimization is computationally not more expensive than for the infinite barrier.

Robustness and feasibility

The designs obtained with topology optimization may contain small features which makes them difficult to manufacture and which are sensitive to geometric imperfections. By applying a robust design, the sensitivity to geometric imperfections is reduced and the small features are mostly removed. This makes it possible to manually simplify the design with little deterioration of performance. This can be followed by a shape optimization step. Alternatively, the layout of discrete objects can be distributed over the design domain.

An important note should be made regarding the feasibility of the designs presented in this work. Although for example inclined jet-grout injections are possible with current construction techniques [106], the complexity of the design will increase the construction cost of the mitigation measure. It is therefore advised to discuss with the contractor and other stakeholders which designs can be constructed and how the trade-off between the construction cost of the barrier design and its performance should be taken into account.

Case study

The dissertation concludes with a case study applying topology optimization to a more realistic problem setting. A railway track is situated close to a building where sensitive equipment is installed. The axle loads of the passing train are obtained solving a dynamic train-track interaction problem, with rail unevenness as excitation mechanism. The vibration levels in the building are assessed with generic vibration criteria for sensitive equipment. The performance for a single wall barrier, a double wall barrier, and optimized designs are compared with each other. The case study demonstrates the high potential of optimized designs in terms of performance improvement and volume reduction.

7.2 Recommendations for further research

Based on the research presented in this thesis, a number of recommendations for further research are made, which are listed below.

The soil was modeled as a homogeneous halfspace. The soil layering can, however, have an important effect as multiple reflections and refractions occur at the layer interfaces. It is straightforward to adapt the presented models for layered inhomogeneous soils, but a physical interpretation of the response becomes even more challenging.

The two-and-a-half-dimensional approach can be used for invariant cross sections. However, it might be beneficial to have a barrier whose cross section varies along its length:

- Many mitigation measures on the transmission path display a periodicity in the plan geometry. Examples include soft or stiff wave barriers created by rows of piles and heavy masses placed next to the track. For these mitigation measures, a Floquet transform can be used to obtain the solution of the original three-dimensional problem based on the discretization of a single periodic cell. The methodology developed in this text can be extended to these problems. Mitigation measures with a periodicity in plan view lend themselves very well to layout optimization of discrete objects. These discrete objects could be the piles which are optimally distributed in the soil or masses optimally placed on the surface.
- Also three-dimensional models can be used. This, however, results in excessive computational costs, and reducing this cost becomes even more crucial.

Solving the equilibrium equations is computationally the most expensive part of the optimization methodology as presented in this work. First steps were taken to keep the computation cost reasonable, by using the efficient 2.5D methodology, by computing the sensitivities with the adjoint approach, and by splitting the stiffness matrix blocks of the design and surrounding domain. Further research can be conducted for additional cost reduction. This is especially the case when larger problems or three-dimensional models are considered. The following measures are proposed:

- For large-scale problems, iterative procedures can be used for solving the equilibrium and adjoint equations. Preconditioners and multigrid methods can accelerate the convergence of iterative methods. Approaches such as reanalysis techniques [6] can furthermore reduce the computational cost by re-using the factorization of a stiffness matrix to approximate the solution of another linear system involving a similar stiffness matrix.
- Optimizing a design for broadband excitation requires the analysis to be repeated for excitation at multiple frequencies. As the numerical analysis of the problem often has the largest contribution to the computation time in an iteration of the optimization process, solving this problem is rather computationally expensive. Alternatively, the analysis can be performed in the time domain, which makes it possible to perform a single analysis in the time domain by selecting a proper input signal. This has for example been done by Dahl et al. [57] for problems in one dimension, using an implicit Newmark scheme for the time integration of the finite element equations. Also topology optimization of two-dimensional transient wave propagation problems has been considered in a previous study [126]. This methodology can be applied to the problems considered in this work.

An advantage of topology optimization is the large design freedom, allowing for the exploration of a wide variety of designs. This, however, often leads to designs which contain small features and which consist of disconnected features. This undermines the manufacturability of the design. Although some methods were presented to improve the manufacturability, further improvement in this area can be obtained by investigating the following topics:

- More and more research is done on constraints for manufacturability, mostly in the context of novel production techniques such as additive manufacturing. They are mostly based on projection techniques to avoid adding a large number of local constraints. Techniques used in these research areas can help in preventing the complex designs containing small features.
- Instead of considering the volume as a measure for the cost, a better approximation of the actual cost can be made that considers the complexity and the depth of the barrier. A first step can be to add a term to the objective function which is proportional to the depth of the design variables, thereby penalizing the distribution of material at larger depths.

In this thesis, only geometric imperfections were considered as source of uncertainty. Other sources of uncertainties can be considered, as outlined in the introduction. For the problem treated in this text, especially the following uncertainties are expected to influence the results:

- Preliminary studies showed that uncertainty in material parameters influences the performance of the optimized barrier. This includes both the material of the barrier and the surrounding soil. Not only the material parameters are a source of uncertainty, but also the heterogeneity of the material. Random field theory can be applied to deal with this [111].
- Another source of uncertainty to be considered is misplacement of material. This refers to a mismatch between the actual location of the barrier features and the location of the ideal topology optimized design. Misplacement of material can be taken into account by adding a perturbation to the center of the density filter kernel [94].

Appendix A

Properties of the transfer matrix H for a periodic stacking of layers

Recall that the transfer matrix $\mathbf{H}$ of a unit cell is given by equation (2.44):

$$\mathbf{H} = \begin{bmatrix} H_{11} & H_{12} \\ H_{21} & H_{22} \end{bmatrix} \tag{A.1}$$

With:

$$\begin{aligned}
H_{11} &= e^{+\mathrm{i}k_{\mathrm{p}1}L_1}\left[\cos(k_{\mathrm{p}2}L_2) + \frac{\mathrm{i}}{2}\left(K + \frac{1}{K}\right)\sin(k_{\mathrm{p}2}L_2)\right] \\
H_{12} &= e^{-\mathrm{i}k_{\mathrm{p}1}L_1}\left[\frac{\mathrm{i}}{2}\left(K - \frac{1}{K}\right)\sin(k_{\mathrm{p}2}L_2)\right] \\
H_{21} &= e^{+\mathrm{i}k_{\mathrm{p}1}L_1}\left[-\frac{\mathrm{i}}{2}\left(K - \frac{1}{K}\right)\sin(k_{\mathrm{p}2}L_2)\right] \\
H_{22} &= e^{-\mathrm{i}k_{\mathrm{p}1}L_1}\left[\cos(k_{\mathrm{p}2}L_2) - \frac{\mathrm{i}}{2}\left(K + \frac{1}{K}\right)\sin(k_{\mathrm{p}2}L_2)\right]
\end{aligned} \tag{A.2}$$

This matrix has some special properties. In this appendix, the determinant and the trace are calculated and the Chebyshev identity is proven.

A.1 Properties of the transfer matrix

The determinant of the 2×2 transfer matrix is equal to 1:

$$\begin{aligned}
\det(\mathbf{H}) &= H_{11}H_{22} - H_{21}H_{12} \\
&= \left[\cos(k_{\mathrm{p}2}L_2) + \frac{\mathrm{i}}{2}\left(K + \frac{1}{K}\right)\sin(k_{\mathrm{p}2}L_2)\right] \\
&\quad \left[\cos(k_{\mathrm{p}2}L_2) - \frac{\mathrm{i}}{2}\left(K + \frac{1}{K}\right)\sin(k_{\mathrm{p}2}L_2)\right] \\
&\quad - \left[\frac{\mathrm{i}}{2}\left(K - \frac{1}{K}\right)\sin(k_{\mathrm{p}2}L_2)\right]\left[-\frac{\mathrm{i}}{2}\left(K - \frac{1}{K}\right)\sin(k_{\mathrm{p}2}L_2)\right] \\
&= \cos^2(k_{\mathrm{p}2}L_2) + \frac{1}{4}\left(K^2 + 2 + \frac{1}{K^2}\right)\sin^2(k_{\mathrm{p}2}L_2) \\
&\quad - \frac{1}{4}\left(K^2 - 2 + \frac{1}{K^2}\right)\sin^2(k_{\mathrm{p}2}L_2) \\
&= \cos^2(k_{\mathrm{p}2}L_2) + \sin^2(k_{\mathrm{p}2}L_2) \\
&= 1
\end{aligned} \tag{A.3}$$

The trace of the transfer matrix is equal to:

$$\begin{aligned}
\mathrm{Tr}(\mathbf{H}) &= H_{11} + H_{22} \\
&= e^{+\mathrm{i}k_{\mathrm{p}1}L_1}\left[\cos(k_{\mathrm{p}2}L_2) + \frac{\mathrm{i}}{2}\left(K + \frac{1}{K}\right)\sin(k_{\mathrm{p}2}L_2)\right] \\
&\quad + e^{-\mathrm{i}k_{\mathrm{p}1}L_1}\left[\cos(k_{\mathrm{p}2}L_2) - \frac{\mathrm{i}}{2}\left(K + \frac{1}{K}\right)\sin(k_{\mathrm{p}2}L_2)\right] \\
&= \cos(k_{\mathrm{p}2}L_2)\left[e^{+\mathrm{i}k_{\mathrm{p}1}L_1} + e^{-\mathrm{i}k_{\mathrm{p}1}L_1}\right] \\
&\quad + \frac{\mathrm{i}}{2}\left(K + \frac{1}{K}\right)\sin(k_{\mathrm{p}2}L_2)\left[e^{+\mathrm{i}k_{\mathrm{p}1}L_1} - e^{-\mathrm{i}k_{\mathrm{p}1}L_1}\right] \\
&= \cos(k_{\mathrm{p}2}L_2)\left[2\cos(k_{\mathrm{p}1}L_1)\right] \\
&\quad + \frac{\mathrm{i}}{2}\left(K + \frac{1}{K}\right)\sin(k_{\mathrm{p}2}L_2)\left[2\mathrm{i}\sin(k_{\mathrm{p}1}L_1)\right] \\
&= 2\cos(k_{\mathrm{p}1}L_1)\cos(k_{\mathrm{p}2}L_2) - \left(K + \frac{1}{K}\right)\sin(k_{\mathrm{p}1}L_1)\sin(k_{\mathrm{p}2}L_2)
\end{aligned} \tag{A.4}$$

A.2 Derivation of the Chebyshev Identity

The derivation is largely based on appendix B from Yeh et al. [180]. The eigenvalues of the transfer matrix are equal to:

$$e^{\pm \mathrm{i}kL} = \frac{H_{11}+H_{22}}{2} \pm i\sqrt{1-\left(\frac{H_{11}+H_{22}}{2}\right)^2} \tag{A.5}$$

The corresponding eigenvectors are given by:

$$\mathbf{v}_{\pm} = \begin{Bmatrix} \alpha_{\pm} \\ \beta_{\pm} \end{Bmatrix} = \begin{Bmatrix} \dfrac{H_{12}}{\sqrt{H_{12}^2+(e^{\pm \mathrm{i}kL}-H_{11})^2}} \\ \dfrac{e^{\pm \mathrm{i}kL}-H_{11}}{\sqrt{H_{12}^2+(e^{\pm \mathrm{i}kL}-H_{11})^2}} \end{Bmatrix} \tag{A.6}$$

The proof follows from the theorem that the Nth power of a transformed matrix is equal to the transform of the Nth power of the original matrix, or:

$$\left[\mathbf{T}\mathbf{H}\mathbf{T}^{-1}\right]^N = \mathbf{T}\mathbf{H}^N\mathbf{T}^{-1} \tag{A.7}$$

If a matrix $\mathbf{T}$ can be found such that:

$$\mathbf{T}\mathbf{H}\mathbf{T}^{-1} = \begin{bmatrix} e^{\mathrm{i}kL} & 0 \\ 0 & e^{-\mathrm{i}kL} \end{bmatrix} \tag{A.8}$$

then the Nth power of the matrix $\mathbf{H}$ is given by:

$$\mathbf{H}^N = \mathbf{T}^{-1} \begin{bmatrix} e^{\mathrm{i}NkL} & 0 \\ 0 & e^{-\mathrm{i}NkL} \end{bmatrix} \mathbf{T} \tag{A.9}$$

The following matrices $\mathbf{T}$ and $\mathbf{T}^{-1}$ obey equation (A.8):

$$\mathbf{T} = \frac{1}{\sqrt{\alpha_+\beta_- - \alpha_-\beta_+}} \begin{bmatrix} \beta_- & -\alpha_- \\ -\beta_+ & \alpha_+ \end{bmatrix} \tag{A.10}$$

$$\mathbf{T}^{-1} = \frac{1}{\sqrt{\alpha_+\beta_- - \alpha_-\beta_+}} \begin{bmatrix} \alpha_+ & \alpha_- \\ \beta_+ & \beta_- \end{bmatrix} \tag{A.11}$$

The two columns in equation (A.11) are the eigenvectors of the matrix $\mathbf{H}$. Introducing equations (A.10) and (A.11) in equation (A.9) gives:

$$\begin{aligned}
\mathbf{H}^N &= \frac{1}{\alpha_+\beta_- - \alpha_-\beta_+}\begin{bmatrix}\alpha_+ & \alpha_- \\ \beta_+ & \beta_-\end{bmatrix}\begin{bmatrix}e^{\mathrm{i}NkL} & 0 \\ 0 & e^{-\mathrm{i}NkL}\end{bmatrix}\begin{bmatrix}\beta_- & -\alpha_- \\ -\beta_+ & \alpha_+\end{bmatrix} \\
&= \begin{bmatrix}\dfrac{H_{11}\sin(NkL)-\sin((N-1)kL)}{\sin(kL)} & \dfrac{H_{12}\sin(NkL)}{\sin(kL)} \\ \dfrac{H_{21}\sin(NkL)}{\sin(kL)} & \dfrac{H_{22}\sin(NkL)-\sin((N-1)kL)}{\sin(kL)}\end{bmatrix} \\
&= \begin{bmatrix}H_{11}\Psi_{N-1}-\Psi_{N-2} & H_{12}\Psi_{N-1} \\ H_{21}\Psi_{N-1} & H_{22}\Psi_{N-1}-\Psi_{N-2}\end{bmatrix}
\end{aligned} \tag{A.12}$$

with:

$$\Psi_N = \frac{\sin((N+1)kL)}{\sin(kL)} \tag{A.13}$$

Appendix B

2.5D methodology for shell elements

In this chapter, the finite element equations are derived for two-and-a-half dimensional shell elements. For every shell element, a local system of coordinates is used with the local x-axis along the element, the local y-axis in the longitudinal direction and the local z-axis perpendicular to the x-axis and y-axis. The fundamental variables $\mathbf{u}(x, y, z, t)$ are discretized on element level to obtain the element stiffness matrix. In the following subsections, the finite element equations for in-plane shell deformation and bending are derived.

For the bending of shell elements, use is made of the classical Kirchhoff bending theory for thin shells. This theory is based on three base hypotheses. A first hypothesis is that the mid-surface of the shell remains undeformed. Secondly, the stresses perpendicular to the shell ($\hat{\sigma}_z = 0$) are neglected, resulting in plane stress conditions. Third, the sections remains straight after deformation. This Bernoulli's hypothesis corresponds to the fact that the shear deformation ($\hat{\gamma}_{yz} = \hat{\gamma}_{zx} = 0$) is neglected.

B.1 In-plane shell deformation

As plane stress applies ($\sigma_{zz} = \sigma_{yz} = \sigma_{zx} = 0$), the equilibrium equations become:

$$\begin{cases} \dfrac{\partial \hat{\sigma}_{xx}}{\partial x} + \dfrac{\partial \hat{\sigma}_{xy}}{\partial y} = -\omega^2 \rho \hat{u}_x \\ \dfrac{\partial \hat{\sigma}_{xy}}{\partial x} + \dfrac{\partial \hat{\sigma}_{yy}}{\partial y} = -\omega^2 \rho \hat{u}_y \end{cases} \tag{B.1}$$

or:

$$\left(\begin{bmatrix} \frac{\partial}{\partial x} & 0 & 0 \\ 0 & 0 & \frac{\partial}{\partial x} \end{bmatrix} + \begin{bmatrix} 0 & 0 & 1 \\ 0 & 1 & 0 \end{bmatrix} \frac{\partial}{\partial y} \right) \begin{Bmatrix} \hat{\sigma}_{xx} \\ \hat{\sigma}_{yy} \\ \hat{\sigma}_{xy} \end{Bmatrix} = -\omega^2 \rho \begin{Bmatrix} \hat{u}_x \\ \hat{u}_y \end{Bmatrix} \tag{B.2}$$

As this can be written as

$$\left(\mathbf{L}_1^{\mathrm{T}} + \mathbf{L}_2^{\mathrm{T}} \frac{\partial}{\partial y} \right) \hat{\boldsymbol{\sigma}} = -\omega^2 \rho \hat{\mathbf{u}} \tag{B.3}$$

the same procedure as in chapter 3 can be applied, where the stresses are calculated from the constitutive equation:

$$\hat{\boldsymbol{\sigma}} = \begin{Bmatrix} \hat{\sigma}_{xx} \\ \hat{\sigma}_{yy} \\ \hat{\sigma}_{xy} \end{Bmatrix} = \frac{E}{1-\nu^2} \begin{bmatrix} 1 & \nu & 0 \\ \nu & 1 & 0 \\ 0 & 0 & \dfrac{1-\nu}{2} \end{bmatrix} \begin{Bmatrix} \hat{\epsilon}_{xx} \\ \hat{\epsilon}_{yy} \\ \hat{\gamma}_{xy} \end{Bmatrix} = \mathbf{C}\hat{\boldsymbol{\epsilon}} \tag{B.4}$$

and the strains are calculated from:

$$\hat{\boldsymbol{\epsilon}} = \begin{Bmatrix} \hat{\epsilon}_{xx} \\ \hat{\epsilon}_{yy} \\ \hat{\gamma}_{xy} \end{Bmatrix} = \left(\begin{bmatrix} \frac{\partial}{\partial x} & 0 \\ 0 & 0 \\ 0 & \frac{\partial}{\partial z} \end{bmatrix} + \begin{bmatrix} 0 & 0 \\ 0 & 1 \\ 1 & 0 \end{bmatrix} \frac{\partial}{\partial y} \right) \begin{Bmatrix} \hat{u}_x \\ \hat{u}_y \end{Bmatrix} = \left(\mathbf{L}_1 + \mathbf{L}_2 \frac{\partial}{\partial y} \right) \hat{\mathbf{u}} \tag{B.5}$$

The elements are discretized as:

$$\hat{\mathbf{u}}(x, y, z=0, \omega) \approx \mathbf{N}(x) \underline{\hat{\mathbf{u}}}(y, \omega) \tag{B.6}$$

As a result, the discretized strains and stresses become:

$$\hat{\boldsymbol{\epsilon}} = \mathbf{L}_1 \mathbf{N} \underline{\hat{\mathbf{u}}} + \mathbf{L}_2 \mathbf{N} \frac{\partial \underline{\hat{\mathbf{u}}}}{\partial y} = \mathbf{B}_1 \underline{\hat{\mathbf{u}}} + \mathbf{B}_2 \frac{\partial \underline{\hat{\mathbf{u}}}}{\partial y} \tag{B.7}$$

$$\hat{\boldsymbol{\sigma}} = \mathbf{C}\hat{\boldsymbol{\epsilon}} = \mathbf{C}\mathbf{B}_1 \underline{\hat{\mathbf{u}}} + \mathbf{C}\mathbf{B}_2 \frac{\partial \underline{\hat{\mathbf{u}}}}{\partial y} \tag{B.8}$$

The elaboration proceeds analogously as for volume elements (chapter 3), and the resulting finite element equation reads as:

$$\left(-\omega^2 \mathbf{M} + \mathbf{K}^0 - i k_y \mathbf{K}^1 - k_y^2 \mathbf{K}^2 \right) \underline{\tilde{\mathbf{u}}} \left(k_y, \omega \right) = \underline{\tilde{\mathbf{f}}} \left(k_y, \omega \right) \tag{B.9}$$

with:

$$\mathbf{M} = \int_F \mathbf{N}^{\mathrm{T}} \rho \mathbf{N} b \mathrm{d}F \tag{B.10}$$

$$\mathbf{K}^0 = \int_F \mathbf{B}_1^{\mathrm{T}} \mathbf{C} \mathbf{B}_1 b \mathrm{d}F \tag{B.11}$$

$$\mathbf{K}^1 = \int_F \mathbf{B}_1^{\mathrm{T}} \mathbf{C} \mathbf{B}_2 b \mathrm{d}F - \int_F \mathbf{B}_2^{\mathrm{T}} \mathbf{C} \mathbf{B}_1 b \mathrm{d}F \tag{B.12}$$

$$\mathbf{K}^2 = -\int_F \mathbf{B}_2^{\mathrm{T}} \mathbf{C} \mathbf{B}_2 b \mathrm{d}F \tag{B.13}$$

where F is the cross section of the shell elements and b is the shell width.

B.2 Bending of shell elements

The equilibrium for a Kirchhoff plate can be written as:

$$\frac{\partial^2 \hat{m}_{xx}}{\partial x^2} + 2\frac{\partial^2 \hat{m}_{xy}}{\partial x \partial y} + \frac{\partial^2 \hat{m}_{yy}}{\partial y^2} = -\omega^2 \rho b \hat{u}_z \tag{B.14}$$

where the moments per unit length are given by:

$$\begin{cases} \hat{m}_{xx} = \int\limits_{-b/2}^{b/2} \hat{\sigma}_{xx} z \mathrm{d}z \\ \hat{m}_{yy} = \int\limits_{-b/2}^{b/2} \hat{\sigma}_{yy} z \mathrm{d}z \\ \hat{m}_{xy} = \int\limits_{-b/2}^{b/2} \hat{\sigma}_{xy} z \mathrm{d}z \end{cases} \tag{B.15}$$

The equilibrium equation can be written as:

$$\left(\begin{bmatrix} \frac{\partial^2}{\partial x^2} & 0 & 0 \end{bmatrix} + \begin{bmatrix} 0 & 0 & 2\frac{\partial}{\partial x} \end{bmatrix} \frac{\partial}{\partial y} + \begin{bmatrix} 0 & 1 & 0 \end{bmatrix} \frac{\partial^2}{\partial y^2} \right) \begin{Bmatrix} \hat{m}_{xx} \\ \hat{m}_{yy} \\ \hat{m}_{xy} \end{Bmatrix} = -\omega^2 \rho b \hat{u}_z \tag{B.16}$$

Or:

$$\left(\mathbf{L}_1^{\mathrm{T}} + \mathbf{L}_2^{\mathrm{T}} \frac{\partial}{\partial y} + \mathbf{L}_3^{\mathrm{T}} \frac{\partial^2}{\partial y^2} \right) \hat{\boldsymbol{m}} = -\omega^2 \rho b \hat{u}_z \tag{B.17}$$

Neumann boundary conditions $\hat{\boldsymbol{m}} \cdot \mathbf{n} = \hat{\boldsymbol{m}}^{\mathrm{n}} = \bar{\boldsymbol{m}}^{\mathrm{n}}$ are applied with $\mathbf{n}$ the unit outward normal vector of the boundary Ξ_t. The equilibrium equations and the

Neumann boundary conditions are formulated in a weak form by considering a virtual displacement field $\hat{v}$ on the domain Γ:

$$\begin{aligned}&\int_\Gamma \hat{v}\left[\left(\mathbf{L}_1^{\mathrm{T}} + \mathbf{L}_2^{\mathrm{T}}\frac{\partial}{\partial y} + \mathbf{L}_3^{\mathrm{T}}\frac{\partial^2}{\partial y^2}\right)\hat{\boldsymbol{m}}\right]\mathrm{d}\Gamma + \omega^2\int_\Gamma \hat{v}\rho b\hat{u}_z\mathrm{d}\Gamma \\ &\quad - \int_{\Xi_t}\hat{v}\left(\hat{\boldsymbol{m}}^{\mathrm{n}} - \bar{\boldsymbol{m}}^{\mathrm{n}}\right)\mathrm{d}\Xi = 0\end{aligned} \tag{B.18}$$

Integration by parts and application of the divergence theorem leads to:

$$\begin{aligned}&\int_\Xi \hat{v}\hat{\boldsymbol{m}}^{\mathrm{n}}\mathrm{d}\Xi - \int_\Gamma\left[\left(\mathbf{L}_1 + \mathbf{L}_2\frac{\partial}{\partial y} + \mathbf{L}_3\frac{\partial^2}{\partial y^2}\right)\hat{v}\right]^{\mathrm{T}}\hat{\boldsymbol{m}}\mathrm{d}\Gamma + \omega^2\int_\Gamma \hat{v}\rho b\hat{u}_z\mathrm{d}\Gamma \\ &\quad - \int_{\Xi_t}\hat{v}\left(\hat{\boldsymbol{m}}^{\mathrm{n}} - \bar{\boldsymbol{m}}^{\mathrm{n}}\right)\mathrm{d}\Xi = 0\end{aligned} \tag{B.19}$$

Since $\Xi = \Xi_t + \Xi_u$ with Ξ_u the part of Ξ on which homogeneous Dirichlet conditions are applied, and as the virtual displacement field $\hat{v}$ is chosen to satisfy the Dirichlet conditions on the boundary Ξ_u, this equation becomes:

$$-\omega^2\int_\Gamma \hat{v}\rho b\hat{u}_z\mathrm{d}\Gamma + \int_\Gamma\left[\left(\mathbf{L}_1 + \mathbf{L}_2\frac{\partial}{\partial y} + \mathbf{L}_3\frac{\partial^2}{\partial y^2}\right)\hat{v}\right]^{\mathrm{T}}\hat{\boldsymbol{m}}\mathrm{d}\Gamma = \int_{\Xi_t}\hat{v}\bar{\boldsymbol{m}}^{\mathrm{n}}\mathrm{d}\Xi \tag{B.20}$$

The moments per unit length $\hat{\boldsymbol{m}}$ can be calculated from the curvatures $\hat{\boldsymbol{\kappa}}$:

$$\hat{\boldsymbol{m}} = \begin{Bmatrix}\hat{m}_{xx}\\ \hat{m}_{yy}\\ \hat{m}_{xy}\end{Bmatrix} = \frac{Eb^3}{12(1-\nu^2)}\begin{bmatrix}1 & \nu & 0\\ \nu & 1 & 0\\ 0 & 0 & \frac{1-\nu}{2}\end{bmatrix}\begin{Bmatrix}\kappa_{xx}\\ \kappa_{yy}\\ \kappa_{xy}\end{Bmatrix} = \mathbf{C}_{\mathrm{b}}\hat{\boldsymbol{\kappa}} \tag{B.21}$$

The strains are related to the displacement in the z-direction and to the curvatures $\hat{\boldsymbol{\kappa}}$:

$$\begin{cases}\epsilon_{xx} = \dfrac{\partial\hat{u}_x}{\partial x} = \dfrac{\partial}{\partial x}\left(-z\dfrac{\partial\hat{u}_z}{\partial x}\right) = -z\dfrac{\partial^2\hat{u}_z}{\partial x^2} = z\kappa_{xx}\\ \epsilon_{yy} = \dfrac{\partial\hat{u}_y}{\partial y} = \dfrac{\partial}{\partial y}\left(-z\dfrac{\partial\hat{u}_z}{\partial y}\right) = -z\dfrac{\partial^2\hat{u}_z}{\partial y^2} = z\kappa_{yy}\\ \gamma_{xy} = \dfrac{\partial\hat{u}_x}{\partial y} + \dfrac{\partial\hat{u}_y}{\partial x} = \dfrac{\partial}{\partial y}\left(-z\dfrac{\partial\hat{u}_z}{\partial x}\right) + \dfrac{\partial}{\partial x}\left(-z\dfrac{\partial\hat{u}_z}{\partial y}\right) = -2z\dfrac{\partial^2\hat{u}_z}{\partial x\partial y} = z\kappa_{xy}\end{cases} \tag{B.22}$$

These curvatures are therefore related to the displacements:

$$\begin{aligned}\hat{\boldsymbol{\kappa}} = \begin{Bmatrix}\kappa_x\\ \kappa_y\\ \kappa_{xy}\end{Bmatrix} &= -\left(\begin{bmatrix}\frac{\partial^2}{\partial x^2}\\ 0\\ 0\end{bmatrix} + \begin{bmatrix}0\\ 0\\ 2\frac{\partial}{\partial x}\end{bmatrix}\frac{\partial}{\partial y} + \begin{bmatrix}0\\ 1\\ 0\end{bmatrix}\frac{\partial^2}{\partial y^2}\right)\hat{u}_z \\ &= -\left(\mathbf{L}_1 + \mathbf{L}_2\frac{\partial}{\partial y} + \mathbf{L}_3\frac{\partial^2}{\partial y^2}\right)\hat{u}_z\end{aligned} \tag{B.23}$$

The domain is discretized using finite elements. As the domain is longitudinally invariant, the displacement vector $\hat{u}_z$ is discretized as:

$$\hat{u}_z(x, y, z = 0, \omega) \approx \mathbf{N}(x)\underline{\hat{\mathbf{u}}}(y, \omega) \tag{B.24}$$

where $\mathbf{N}(x)$ are the shape functions defined over the cross section and $\underline{\hat{\mathbf{u}}}(y, \omega)$ is the discretized displacement vector which is a function of the longitudinal coordinate y and the frequency ω. The vector contains the degrees of freedom at all nodes of the 2D cross section mesh. As a result, the discretized curvatures and moments per unit length become:

$$\hat{\boldsymbol{\kappa}} = -\mathbf{L}_1\mathbf{N}\underline{\hat{\mathbf{u}}} - \mathbf{L}_2\mathbf{N}\frac{\partial\underline{\hat{\mathbf{u}}}}{\partial y} - \mathbf{L}_3\mathbf{N}\frac{\partial^2\underline{\hat{\mathbf{u}}}}{\partial y^2} = \mathbf{B}_1\underline{\hat{\mathbf{u}}} + \mathbf{B}_2\frac{\partial\underline{\hat{\mathbf{u}}}}{\partial y} + \mathbf{B}_3\frac{\partial^2\underline{\hat{\mathbf{u}}}}{\partial y^2} \tag{B.25}$$

$$\hat{\boldsymbol{m}} = \mathbf{C}_\mathrm{b}\hat{\boldsymbol{\kappa}} = \mathbf{C}_\mathrm{b}\mathbf{B}_1\underline{\hat{\mathbf{u}}} + \mathbf{C}_\mathrm{b}\mathbf{B}_2\frac{\partial\underline{\hat{\mathbf{u}}}}{\partial y} + \mathbf{C}_\mathrm{b}\mathbf{B}_3\frac{\partial^2\underline{\hat{\mathbf{u}}}}{\partial y^2} \tag{B.26}$$

with $\mathbf{B}_1 = -\mathbf{L}_1\mathbf{N}$, $\mathbf{B}_2 = -\mathbf{L}_2\mathbf{N}$, and $\mathbf{B}_3 = -\mathbf{L}_3\mathbf{N}$.

A standard Galerkin procedure is followed, where the same approximation is used for the virtual displacement vector $\hat{v}$ as for the displacement vector $\hat{u}_z$:

$$\hat{v}(x, y, z = 0, \omega) \approx \mathbf{N}(x)\underline{\hat{\mathbf{v}}}(y, \omega) \tag{B.27}$$

The virtual work formulation therefore becomes:

$$\begin{aligned}&-\omega^2\int_\Gamma \underline{\hat{\mathbf{v}}}^\mathrm{T}\mathbf{N}^\mathrm{T}\rho b\mathbf{N}\underline{\hat{\mathbf{u}}}\mathrm{d}\Gamma + \int_\Gamma\left[\left(\underline{\hat{\mathbf{v}}}^\mathrm{T}\mathbf{B}_1^\mathrm{T} + \left(\frac{\partial\underline{\hat{\mathbf{v}}}}{\partial y}\right)^\mathrm{T}\mathbf{B}_2^\mathrm{T} + \left(\frac{\partial^2\underline{\hat{\mathbf{v}}}}{\partial y^2}\right)^\mathrm{T}\mathbf{B}_3^\mathrm{T}\right)\right. \\ &\left.\mathbf{C}_\mathrm{b}\left(\mathbf{B}_1\underline{\hat{\mathbf{u}}} + \mathbf{B}_2\frac{\partial\underline{\hat{\mathbf{u}}}}{\partial y} + \mathbf{B}_3\frac{\partial^2\underline{\hat{\mathbf{u}}}}{\partial y^2}\right)\right]\mathrm{d}\Gamma = \int_{\Xi_t}\underline{\hat{\mathbf{v}}}^\mathrm{T}\mathbf{N}^\mathrm{T}\bar{\boldsymbol{m}}^\mathrm{n}\mathrm{d}\Xi\end{aligned} \tag{B.28}$$

This equation is further elaborated, rewriting the surface integrals as an integral over the longitudinal coordinate y and the cross section F:

$$\begin{aligned}
&-\omega^2 \int_y \underline{\hat{\mathbf{v}}}^{\mathrm{T}} \left(\int_F \mathbf{N}^{\mathrm{T}} \rho \mathbf{N} b \mathrm{d}F \right) \underline{\hat{\mathbf{u}}} \mathrm{d}y \\
&+ \int_y \underline{\hat{\mathbf{v}}}^{\mathrm{T}} \left(\int_F \mathbf{B}_1^{\mathrm{T}} \mathbf{C}_{\mathrm{b}} \mathbf{B}_1 \mathrm{d}F \right) \underline{\hat{\mathbf{u}}} \mathrm{d}y \\
&+ \int_y \underline{\hat{\mathbf{v}}}^{\mathrm{T}} \left(\int_F \mathbf{B}_1^{\mathrm{T}} \mathbf{C}_{\mathrm{b}} \mathbf{B}_2 \mathrm{d}F \right) \frac{\partial \underline{\hat{\mathbf{u}}}}{\partial y} \mathrm{d}y \\
&+ \int_y \underline{\hat{\mathbf{v}}}^{\mathrm{T}} \left(\int_F \mathbf{B}_1^{\mathrm{T}} \mathbf{C}_{\mathrm{b}} \mathbf{B}_3 \mathrm{d}F \right) \frac{\partial^2 \underline{\hat{\mathbf{u}}}}{\partial y^2} \mathrm{d}y \\
&+ \int_y \left(\frac{\partial \underline{\hat{\mathbf{v}}}}{\partial y} \right)^{\mathrm{T}} \left(\int_F \mathbf{B}_2^{\mathrm{T}} \mathbf{C}_{\mathrm{b}} \mathbf{B}_1 \mathrm{d}F \right) \underline{\hat{\mathbf{u}}} \mathrm{d}y \\
&+ \int_y \left(\frac{\partial \underline{\hat{\mathbf{v}}}}{\partial y} \right)^{\mathrm{T}} \left(\int_F \mathbf{B}_2^{\mathrm{T}} \mathbf{C}_{\mathrm{b}} \mathbf{B}_2 \mathrm{d}F \right) \frac{\partial \underline{\hat{\mathbf{u}}}}{\partial y} \mathrm{d}y \\
&+ \int_y \left(\frac{\partial \underline{\hat{\mathbf{v}}}}{\partial y} \right)^{\mathrm{T}} \left(\int_F \mathbf{B}_2^{\mathrm{T}} \mathbf{C}_{\mathrm{b}} \mathbf{B}_3 \mathrm{d}F \right) \frac{\partial^2 \underline{\hat{\mathbf{u}}}}{\partial y^2} \mathrm{d}y \\
&+ \int_y \left(\frac{\partial^2 \underline{\hat{\mathbf{v}}}}{\partial y^2} \right)^{\mathrm{T}} \left(\int_F \mathbf{B}_3^{\mathrm{T}} \mathbf{C}_{\mathrm{b}} \mathbf{B}_1 \mathrm{d}F \right) \underline{\hat{\mathbf{u}}} \mathrm{d}y \\
&+ \int_y \left(\frac{\partial^2 \underline{\hat{\mathbf{v}}}}{\partial y^2} \right)^{\mathrm{T}} \left(\int_F \mathbf{B}_3^{\mathrm{T}} \mathbf{C}_{\mathrm{b}} \mathbf{B}_2 \mathrm{d}F \right) \frac{\partial \underline{\hat{\mathbf{u}}}}{\partial y} \mathrm{d}y \\
&+ \int_y \left(\frac{\partial^2 \underline{\hat{\mathbf{v}}}}{\partial y^2} \right)^{\mathrm{T}} \left(\int_F \mathbf{B}_3^{\mathrm{T}} \mathbf{C}_{\mathrm{b}} \mathbf{B}_3 \mathrm{d}F \right) \frac{\partial^2 \underline{\hat{\mathbf{u}}}}{\partial y^2} \mathrm{d}y \\
&= \int_y \underline{\hat{\mathbf{v}}}^{\mathrm{T}} \left(\int_{X_t} \mathbf{N}^{\mathrm{T}} \bar{\boldsymbol{m}}^{\mathrm{n}} \mathrm{d}s \right) \mathrm{d}y
\end{aligned} \tag{B.29}$$

where X_t is the intersection of the surface Ξ_t with the plane $y = 0$.

Integration by parts on the terms containing derivatives to y leads to:

$$\begin{aligned}
&-\omega^2 \int_y \underline{\hat{\mathbf{v}}}^{\mathrm{T}} \left(\int_F \mathbf{N}^{\mathrm{T}} \rho \mathbf{N} b \mathrm{d}F \right) \underline{\hat{\mathbf{u}}} \mathrm{d}y + \int_y \underline{\hat{\mathbf{v}}}^{\mathrm{T}} \left(\int_F \mathbf{B}_1^{\mathrm{T}} \mathbf{C}_{\mathrm{b}} \mathbf{B}_1 \mathrm{d}F \right) \underline{\hat{\mathbf{u}}} \mathrm{d}y \\
&\quad + \int_y \underline{\hat{\mathbf{v}}}^{\mathrm{T}} \left(\int_F \mathbf{B}_1^{\mathrm{T}} \mathbf{C}_{\mathrm{b}} \mathbf{B}_2 \mathrm{d}F \right) \frac{\partial \underline{\hat{\mathbf{u}}}}{\partial y} \mathrm{d}y + \int_y \underline{\hat{\mathbf{v}}}^{\mathrm{T}} \left(\int_F \mathbf{B}_1^{\mathrm{T}} \mathbf{C}_{\mathrm{b}} \mathbf{B}_3 \mathrm{d}F \right) \frac{\partial^2 \underline{\hat{\mathbf{u}}}}{\partial y^2} \mathrm{d}y \\
&\quad - \int_y \hat{\mathbf{v}}^{\mathrm{T}} \left(\int_F \mathbf{B}_2^{\mathrm{T}} \mathbf{C}_{\mathrm{b}} \mathbf{B}_1 \mathrm{d}F \right) \frac{\partial \underline{\hat{\mathbf{u}}}}{\partial y} \mathrm{d}y - \int_y \hat{\mathbf{v}}^{\mathrm{T}} \left(\int_F \mathbf{B}_2^{\mathrm{T}} \mathbf{C}_{\mathrm{b}} \mathbf{B}_2 \mathrm{d}F \right) \frac{\partial^2 \underline{\hat{\mathbf{u}}}}{\partial y^2} \mathrm{d}y \\
&\quad - \int_y \hat{\mathbf{v}}^{\mathrm{T}} \left(\int_F \mathbf{B}_2^{\mathrm{T}} \mathbf{C}_{\mathrm{b}} \mathbf{B}_3 \mathrm{d}F \right) \frac{\partial^3 \underline{\hat{\mathbf{u}}}}{\partial y^3} \mathrm{d}y + \int_y \hat{\mathbf{v}}^{\mathrm{T}} \left(\int_F \mathbf{B}_3^{\mathrm{T}} \mathbf{C}_{\mathrm{b}} \mathbf{B}_1 \mathrm{d}F \right) \frac{\partial^2 \underline{\hat{\mathbf{u}}}}{\partial y^2} \mathrm{d}y \\
&\quad + \int_y \hat{\mathbf{v}}^{\mathrm{T}} \left(\int_F \mathbf{B}_3^{\mathrm{T}} \mathbf{C}_{\mathrm{b}} \mathbf{B}_2 \mathrm{d}F \right) \frac{\partial^3 \underline{\hat{\mathbf{u}}}}{\partial y^3} \mathrm{d}y + \int_y \hat{\mathbf{v}}^{\mathrm{T}} \left(\int_F \mathbf{B}_3^{\mathrm{T}} \mathbf{C}_{\mathrm{b}} \mathbf{B}_3 \mathrm{d}F \right) \frac{\partial^4 \underline{\hat{\mathbf{u}}}}{\partial y^4} \mathrm{d}y \\
&\quad = \int_y \underline{\hat{\mathbf{v}}}^{\mathrm{T}} \left(\int_{X_t} \mathbf{N}^{\mathrm{T}} \bar{\boldsymbol{m}}^{\mathrm{n}} \mathrm{d}s \right) \mathrm{d}y
\end{aligned} \tag{B.30}$$

Since this equation holds for any virtual displacement $\underline{\hat{\mathbf{v}}}$, it is equivalent to:

$$\begin{aligned}
&-\omega^2 \mathbf{M} \underline{\hat{\mathbf{u}}}(y,\omega) + \mathbf{K}^0 \underline{\hat{\mathbf{u}}}(y,\omega) + \mathbf{K}^1 \frac{\partial \underline{\hat{\mathbf{u}}}(y,\omega)}{\partial y} + \mathbf{K}^2 \frac{\partial^2 \underline{\hat{\mathbf{u}}}(y,\omega)}{\partial y^2} \\
&\quad + \mathbf{K}^3 \frac{\partial^3 \underline{\hat{\mathbf{u}}}(y,\omega)}{\partial y^3} + \mathbf{K}^4 \frac{\partial^4 \underline{\hat{\mathbf{u}}}(y,\omega)}{\partial y^4} = \underline{\hat{\mathbf{f}}}(y,\omega)
\end{aligned} \tag{B.31}$$

with:

$$\mathbf{M} = \int_F \mathbf{N}^{\mathrm{T}} \rho \mathbf{N} b \mathrm{d}F \tag{B.32}$$

$$\mathbf{K}^0 = \int_F \mathbf{B}_1^{\mathrm{T}} \mathbf{C}_{\mathrm{b}} \mathbf{B}_1 \mathrm{d}F \tag{B.33}$$

$$\mathbf{K}^1 = \int_F \mathbf{B}_1^{\mathrm{T}} \mathbf{C}_{\mathrm{b}} \mathbf{B}_2 \mathrm{d}F - \int_F \mathbf{B}_2^{\mathrm{T}} \mathbf{C}_{\mathrm{b}} \mathbf{B}_1 \mathrm{d}F \tag{B.34}$$

$$\mathbf{K}^2 = \int_F \mathbf{B}_1^{\mathrm{T}} \mathbf{C}_{\mathrm{b}} \mathbf{B}_3 \mathrm{d}F - \int_F \mathbf{B}_2^{\mathrm{T}} \mathbf{C}_{\mathrm{b}} \mathbf{B}_2 \mathrm{d}F + \int_F \mathbf{B}_3^{\mathrm{T}} \mathbf{C}_{\mathrm{b}} \mathbf{B}_1 \mathrm{d}F \tag{B.35}$$

$$\mathbf{K}^3 = -\int_F \mathbf{B}_2^{\mathrm{T}} \mathbf{C}_{\mathrm{b}} \mathbf{B}_3 \mathrm{d}F + \int_F \mathbf{B}_3^{\mathrm{T}} \mathbf{C}_{\mathrm{b}} \mathbf{B}_2 \mathrm{d}F \tag{B.36}$$

$$\mathbf{K}^4 = \int_F \mathbf{B}_3^{\mathrm{T}} \mathbf{C}_{\mathrm{b}} \mathbf{B}_3 \mathrm{d}F \tag{B.37}$$

In the frequency-wavenumber domain, this equation is written as:

$$\left(-\omega^2\mathbf{M} + \mathbf{K}^0 - ik_y\mathbf{K}^1 - k_y^2\mathbf{K}^2 + ik_y^3\mathbf{K}^3 + k_y^4\mathbf{K}^4\right)\underline{\tilde{\mathbf{u}}}\left(k_y, \omega\right) = \underline{\tilde{\mathbf{f}}}\left(k_y, \omega\right) \quad \text{(B.38)}$$

The combination of equations (B.9) and (B.31) describes the general 2.5D finite element formulation for shell elements.

B.3 Shape functions for two-node shell elements

For the in-plane degrees of freedom, the displacement vector is discretized as:

$$\begin{aligned}\hat{\mathbf{u}}(x, y, z = 0, \omega) &\approx \mathbf{N}(x)\underline{\hat{\mathbf{u}}}(y, \omega)\\ &= \begin{bmatrix} N_1 & 0 & | & N_2 & 0 \\ 0 & N_1 & | & 0 & N_2 \end{bmatrix} \begin{Bmatrix} \underline{\hat{u}}_{1x} \\ \underline{\hat{u}}_{1y} \\ --- \\ \underline{\hat{u}}_{2x} \\ \underline{\hat{u}}_{2y} \end{Bmatrix}\end{aligned} \quad \text{(B.39)}$$

with

$$\begin{cases} N_1(x) = 1 - \dfrac{x}{l} \\ N_2(x) = \dfrac{x}{l} \end{cases} \quad \text{(B.40)}$$

where l is the length of the element considered.

For the out-plane degree of freedom, the displacement vector is discretized as:

$$\begin{aligned}\hat{u}_z(x, y, z = 0, \omega) &\approx \mathbf{N}(x)\underline{\hat{\mathbf{u}}}(y, \omega)\\ &= \begin{bmatrix} N_1 & N_2 & | & N_3 & N_4 \end{bmatrix} \begin{Bmatrix} \underline{\hat{u}}_{1z} \\ \underline{\hat{\phi}}_{1x} \\ --- \\ \underline{\hat{u}}_{2z} \\ \underline{\hat{\phi}}_{2x} \end{Bmatrix}\end{aligned} \quad \text{(B.41)}$$

with

$$\begin{cases} N_1(x) = \dfrac{2x^3}{l^3} - \dfrac{3x^2}{l^2} + 1 \\ N_2(x) = -\dfrac{x^3}{l^2} + \dfrac{2x^2}{l} - x \\ N_3(x) = \dfrac{2x^3}{l^3} + \dfrac{3x^2}{l^2} + 1 \\ N_4(x) = -\dfrac{x^3}{l^2} + \dfrac{x^2}{l} \end{cases} \quad \text{(B.42)}$$

Appendix C

Dispersion relations for a beam

To obtain the dispersion relations for the longitudinal mode, the bending-shear mode, and the torsion mode analytically, multiple methods can be used. In this report, Hamilton's principle is applied.

Hamilton's principle states that, in the absence of external loads, the dynamics of the system are determined by the following expression [135]:

$$\delta \int_t (\Pi - \mathcal{T})\,\mathrm{d}t = 0 \tag{C.1}$$

where $\mathcal{T}$ the kinetic energy, Π is the potential energy, and the integration is done over time t. The kinetic energy and the potential are given by the following expressions:

$$\mathcal{T} = \frac{1}{2}\int_\Omega \rho \left[\left(\frac{\partial u_x}{\partial t}\right)^2 + \left(\frac{\partial u_y}{\partial t}\right)^2 + \left(\frac{\partial u_z}{\partial t}\right)^2\right] \mathrm{d}\Omega \tag{C.2}$$

$$\Pi = \frac{1}{2}\int_\Omega \left(\sigma_{xx}\epsilon_{xx} + \sigma_{yy}\epsilon_{yy} + \sigma_{zz}\epsilon_{zz} + \sigma_{xy}\gamma_{xy} + \sigma_{yz}\gamma_{yz} + \sigma_{zx}\gamma_{zx}\right) \mathrm{d}\Omega \tag{C.3}$$

where Ω is the volume and ρ is the mass density of the beam.

C.1 Longitudinal mode

Displacements, strains, and stresses Consider first the longitudinal motion of a beam (figure C.1). The displacement is only different from zero in the direction parallel to the beam axis. Therefore, the displacements are given by:

$$\begin{cases} u_x = 0 \\ u_y = u_y(y,t) \\ u_z = 0 \end{cases} \tag{C.4}$$

where u_x, u_y, and u_z are the displacements of the beam in the x, y, and z direction.

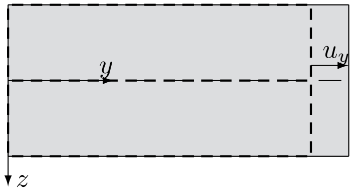

Figure C.1: Element with longitudinal deformation.

The strains can be derived by differentiating these displacements:

$$\begin{cases} \epsilon_{xx} = \dfrac{\partial u_x}{\partial x} = 0 \\ \epsilon_{yy} = \dfrac{\partial u_y}{\partial y} \\ \epsilon_{zz} = \dfrac{\partial u_z}{\partial z} = 0 \\ \gamma_{xy} = \dfrac{\partial u_x}{\partial y} + \dfrac{\partial u_y}{\partial x} = 0 \\ \gamma_{yz} = \dfrac{\partial u_y}{\partial z} + \dfrac{\partial u_z}{\partial y} = 0 \\ \gamma_{zx} = \dfrac{\partial u_z}{\partial x} + \dfrac{\partial u_x}{\partial z} = 0 \end{cases} \tag{C.5}$$

The stresses follow then from the constitutive relations:

$$\begin{cases} \sigma_{xx} = \dfrac{E}{(1+\nu)(1-2\nu)}\left((1-\nu)\epsilon_{xx} + \nu\epsilon_{yy} + \nu\epsilon_{zz}\right) \\ \qquad = \dfrac{E\nu}{(1+\nu)(1-2\nu)}\dfrac{\partial u_y}{\partial y} \approx 0 \\ \sigma_{yy} = \dfrac{E}{(1+\nu)(1-2\nu)}\left(\nu\epsilon_{xx} + (1-\nu)\epsilon_{yy} + \nu\epsilon_{zz}\right) \\ \qquad = \dfrac{E(1-\nu)}{(1+\nu)(1-2\nu)}\dfrac{\partial u_y}{\partial y} \approx E\dfrac{\partial u_y}{\partial y} \\ \sigma_{zz} = \dfrac{E}{(1+\nu)(1-2\nu)}\left(\nu\epsilon_{xx} + \nu\epsilon_{yy} + (1-\nu)\epsilon_{zz}\right) \\ \qquad = \dfrac{E\nu\phi}{(1+\nu)(1-2\nu)}\dfrac{\partial u_y}{\partial y} \approx 0 \\ \tau_{xy} = G\gamma_{xy} = 0 \\ \tau_{yz} = G\gamma_{yz} = 0 \\ \tau_{zx} = G\gamma_{zx} = 0 \end{cases} \tag{C.6}$$

where E and ν are the Young's modulus and the Poisson coefficient.

Hamilton's principle The kinetic energy $\mathcal{T}$ can be expressed as:

$$\begin{aligned} \mathcal{T} &= \frac{1}{2}\int_\Omega \rho\left[\left(\frac{\partial u_x}{\partial t}\right)^2 + \left(\frac{\partial u_y}{\partial t}\right)^2 + \left(\frac{\partial u_z}{\partial t}\right)^2\right]\mathrm{d}\Omega \\ &= \frac{1}{2}\int_y\int_A \rho\left(\frac{\partial u_y}{\partial t}\right)^2 \mathrm{d}A\mathrm{d}y \end{aligned} \tag{C.7}$$

Therefore, the variation of the kinetic energy $\mathcal{T}$ is given by:

$$\delta\mathcal{T} = \int_y\int_A \rho\frac{\partial u_y}{\partial t}\frac{\partial \delta u_y}{\partial t}\mathrm{d}A\mathrm{d}y = \int_y \rho A\frac{\partial u_y}{\partial t}\frac{\partial \delta u_y}{\partial t}\mathrm{d}y \overset{\mathrm{PI}}{=} -\int_y \rho A\frac{\partial^2 u_y}{\partial t^2}\delta u_y \mathrm{d}y \tag{C.8}$$

where partial integration (PI) or integration by parts was used.

The strain energy Π can be expressed as:

$$\begin{aligned}\Pi &= \frac{1}{2}\int_{\Omega} \left(\sigma_{xx}\epsilon_{xx} + \sigma_{yy}\epsilon_{yy} + \sigma_{zz}\epsilon_{zz} + \tau_{xy}\gamma_{xy} + \tau_{yz}\gamma_{yz} + \tau_{zx}\gamma_{zx}\right) \mathrm{d}\Omega \\ &= \frac{1}{2}\int_{y}\int_{A} E\left(\frac{\partial u_y}{\partial y}\right)^2 \mathrm{d}A\mathrm{d}y\end{aligned} \tag{C.9}$$

Therefore, the variation of the strain energy Π is given by:

$$\begin{aligned}\delta\Pi = \int_{y}\int_{A} E\frac{\partial u_y}{\partial y}\frac{\partial \delta u_y}{\partial y}\mathrm{d}A\mathrm{d}y &= \int_{y} EA\frac{\partial u_y}{\partial y}\frac{\partial \delta u_y}{\partial y}\mathrm{d}y \\ &\overset{\text{PI}}{=} EA\frac{\partial u_y}{\partial y}\delta u_y\bigg|_0^l - \int_{y} EA\frac{\partial^2 u_y}{\partial y^2}\delta u_y \mathrm{d}y\end{aligned} \tag{C.10}$$

By applying Hamilton's principle in Eq. (C.1), the following differential equation is obtained:

$$EA\frac{\partial^2 u_y}{\partial y^2} = \rho A\frac{\partial^2 u_y}{\partial t^2} \tag{C.11}$$

Dispersion curve In the frequency-wavenumber domain, equation (C.11) becomes:

$$\left[Ek_y^2 - \rho\omega^2\right]\tilde{u}_y = 0 \tag{C.12}$$

This leads to the following dispersion relation:

$$Ek_y^2 - \rho\omega^2 = 0 \tag{C.13}$$

The (positive) solution of this equation for k_y is:

$$k_y = \sqrt{\frac{\rho}{E}}\omega \tag{C.14}$$

This corresponds to a constant slowness:

$$p_y = \frac{k_y}{\omega} = \sqrt{\frac{\rho}{E}} \tag{C.15}$$

C.2 Bending-shear modes

Displacements, strains, and stresses In the Timoshenko beam theory [162, 163], shear deformation is taken into account (figure C.2), and the displacements are given by:

$$\begin{cases} u_x = 0 \\ u_y = -z\chi(y,t) \\ u_z = u_z(y,t) \end{cases} \tag{C.16}$$

where $\chi = \dfrac{\partial u_z}{\partial y} - \beta$ in which β is the shear angle.

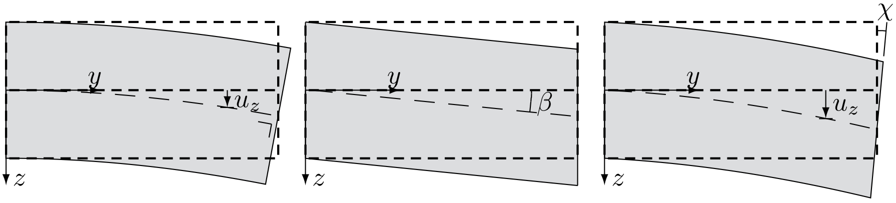

(a) (b) (c)

Figure C.2: Element with (a) only bending deformation, (b) only shear deformation, and (c) total bending-shear deformation (Timoshenko's Theory).

This leads to the following strains:

$$\begin{cases} \epsilon_{xx} = \dfrac{\partial u_x}{\partial x} = 0 \\ \epsilon_{yy} = \dfrac{\partial u_y}{\partial y} = -z\dfrac{\partial \chi}{\partial y} \\ \epsilon_{zz} = \dfrac{\partial u_z}{\partial z} = 0 \\ \gamma_{xy} = \dfrac{\partial u_x}{\partial y} + \dfrac{\partial u_y}{\partial x} = 0 \\ \gamma_{yz} = \dfrac{\partial u_y}{\partial z} + \dfrac{\partial u_z}{\partial y} = -\chi + \dfrac{\partial u_z}{\partial y} \\ \gamma_{zx} = \dfrac{\partial u_z}{\partial x} + \dfrac{\partial u_x}{\partial z} = 0 \end{cases} \tag{C.17}$$

and stresses:

$$\left\{\begin{aligned} \sigma_{xx} &= \frac{E}{(1+\nu)(1-2\nu)}\left((1-\nu)\epsilon_{xx}+\nu\epsilon_{yy}+\nu\epsilon_{zz}\right)\\ &= \frac{-zE\nu}{(1+\nu)(1-2\nu)}\frac{\partial\chi}{\partial y}\approx 0\\ \sigma_{yy} &= \frac{E}{(1+\nu)(1-2\nu)}\left(\nu\epsilon_{xx}+(1-\nu)\epsilon_{yy}+\nu\epsilon_{zz}\right)\\ &= \frac{-zE(1-\nu)}{(1+\nu)(1-2\nu)}\frac{\partial\chi}{\partial y}\approx -zE\frac{\partial\chi}{\partial y}\\ \sigma_{zz} &= \frac{E}{(1+\nu)(1-2\nu)}\left(\nu\epsilon_{xx}+\nu\epsilon_{yy}+(1-\nu)\epsilon_{zz}\right)\\ &= \frac{-zE\nu\phi}{(1+\nu)(1-2\nu)}\frac{\partial\chi}{\partial y}\approx 0\\ \tau_{xy} &= G\gamma_{xy}=0\\ \tau_{yz} &= G\gamma_{yz}=G\left(\frac{\partial u_z}{\partial y}-\chi\right)\\ \tau_{zx} &= G\gamma_{zx}=0 \end{aligned}\right. \tag{C.18}$$

Hamilton's principle The kinetic energy $\mathcal{T}$ can be expressed as:

$$\begin{aligned} \mathcal{T} &= \frac{1}{2}\int_y\int_A \rho\left[\left(\frac{\partial u_x}{\partial t}\right)^2+\left(\frac{\partial u_y}{\partial t}\right)^2+\left(\frac{\partial u_z}{\partial t}\right)^2\right]\mathrm{d}A\mathrm{d}y\\ &= \frac{1}{2}\int_y\int_A \rho z^2\left(\frac{\partial\chi}{\partial t}\right)^2\mathrm{d}A\mathrm{d}y+\frac{1}{2}\int_y\int_A\rho\left(\frac{\partial u_z}{\partial t}\right)^2\mathrm{d}A\mathrm{d}y \end{aligned} \tag{C.19}$$

Therefore, the variation of the kinetic energy $\mathcal{T}$ is given by:

$$\begin{aligned} \delta\mathcal{T} &= \int_y\int_A \rho z^2\frac{\partial\chi}{\partial t}\frac{\partial\delta\chi}{\partial t}\mathrm{d}A\mathrm{d}y+\int_y\int_A\rho\frac{\partial u_z}{\partial t}\frac{\partial\delta u_z}{\partial t}\mathrm{d}A\mathrm{d}y\\ &= \int_y \rho I_z\frac{\partial\chi}{\partial t}\frac{\partial\delta\chi}{\partial t}\mathrm{d}y+\int_y\rho A\frac{\partial u_z}{\partial t}\frac{\partial\delta u_z}{\partial t}\mathrm{d}y\\ &\overset{\mathrm{PI}}{=} -\int_y\rho I_z\frac{\partial^2\chi}{\partial t^2}\delta\chi\mathrm{d}y-\int_y\rho A\frac{\partial^2 u_z}{\partial t^2}\delta u_z\mathrm{d}y \end{aligned} \tag{C.20}$$

with

$$I_z=\int_A z^2\mathrm{d}A \tag{C.21}$$

The strain energy Π can be expressed as:

$$\begin{aligned}\Pi &= \frac{1}{2}\int_y\int_A \left(\sigma_{xx}\epsilon_{xx} + \sigma_{yy}\epsilon_{yy} + \sigma_{zz}\epsilon_{zz} + \tau_{xy}\gamma_{xy} + \tau_{yz}\gamma_{yz} + \tau_{zx}\gamma_{zx}\right)\mathrm{d}A\mathrm{d}y \\ &= \frac{1}{2}\int_y\int_A Ez^2\left(\frac{\partial\chi}{\partial y}\right)^2\mathrm{d}A\mathrm{d}y + \frac{1}{2}\int_y\int_A G\left(\frac{\partial u_z}{\partial y} - \chi\right)^2\mathrm{d}A\mathrm{d}y\end{aligned} \tag{C.22}$$

Therefore, the variation of the strain energy Π is given by:

$$\begin{aligned}\delta\Pi &= \int_y\int_A Ez^2\frac{\partial\chi}{\partial y}\frac{\partial\delta\chi}{\partial y}\mathrm{d}A\mathrm{d}y + \int_y\int_A G\left(\frac{\partial u_z}{\partial y} - \chi\right)\left(\frac{\partial\delta u_z}{\partial y} - \delta\chi\right)\mathrm{d}A\mathrm{d}y \\ &= \int_y EI_z\frac{\partial\chi}{\partial y}\frac{\partial\delta\chi}{\partial y}\mathrm{d}y + \int_y GA\left(\frac{\partial u_z}{\partial y} - \chi\right)\left(\frac{\partial\delta u_z}{\partial y} - \delta\chi\right)\mathrm{d}y \\ &\overset{\text{PI}}{=} EI_z\frac{\partial\chi}{\partial y}\delta\chi\bigg|_0^l - \int_y EI_z\frac{\partial^2\chi}{\partial y^2}\delta\chi\mathrm{d}y + GA\left(\frac{\partial u_z}{\partial y} - \chi\right)\delta u_z\bigg|_0^l \\ &\quad - \int_y GA\left(\frac{\partial^2 u_z}{\partial y^2} - \frac{\partial\chi}{\partial y}\right)\delta u_z\mathrm{d}y - \int_y GA\left(\frac{\partial u_z}{\partial y} - \chi\right)\delta\chi\mathrm{d}y\end{aligned} \tag{C.23}$$

By applying Hamilton's principle in equation (C.1), the following differential equations are obtained:

$$GA\left(\frac{\partial^2 u_z}{\partial y^2} - \frac{\partial\chi}{\partial y}\right) = \rho A\frac{\partial^2 u_z}{\partial t^2} \tag{C.24}$$

$$EI_z\frac{\partial^2\chi}{\partial y^2} + GA\left(\frac{\partial u_z}{\partial y} - \chi\right) = \rho I_z\frac{\partial^2\chi}{\partial t^2} \tag{C.25}$$

The next step is to combine equations (C.24) and (C.25) by eliminating the variable u_z or χ and therefore to get a differential equation that only depends on χ or u_z. The variable χ can be eliminated from equation (C.25) since from equation (C.24) we get:

$$\frac{\partial\chi}{\partial y} = \frac{\partial^2 u_z}{\partial y^2} - \frac{\rho}{G}\frac{\partial^2 u_z}{\partial t^2} \tag{C.26}$$

which can be inserted in equation (C.25) after differentiating to y:

$$\begin{aligned} &EI_z \frac{\partial^4 u_z}{\partial y^4} - \frac{\rho E I_z}{G} \frac{\partial^4 u_z}{\partial y^2 \partial t^2} + GA \frac{\partial^2 u_z}{\partial y^2} - GA \frac{\partial^2 u_z}{\partial y^2} + \rho A \frac{\partial^2 u_z}{\partial t^2} \\ &\quad = \rho I_z \frac{\partial^4 u_z}{\partial y^2 \partial t^2} - \frac{\rho^2 I_z}{G} \frac{\partial^4 u_z}{\partial t^4} \end{aligned} \tag{C.27}$$

Rearranging this equation results in:

$$\rho A \frac{\partial^2 u_z}{\partial t^2} + EI_z \frac{\partial^4 u_z}{\partial y^4} - \rho I_z \left(1 + \frac{E}{G}\right) \frac{\partial^4 u_z}{\partial y^2 \partial t^2} + \frac{\rho^2 I_z}{G} \frac{\partial^4 u_z}{\partial t^4} = 0 \tag{C.28}$$

The shear coefficient To control the asymptotes for bending waves with decreasing wavelength, a non-dimensional parameter κ is added:

$$\rho A \frac{\partial^2 u_z}{\partial t^2} + EI_z \frac{\partial^4 u_z}{\partial y^4} - \rho I_z \left(1 + \frac{E}{\kappa G}\right) \frac{\partial^4 u_z}{\partial y^2 \partial t^2} + \frac{\rho^2 I_z}{\kappa G} \frac{\partial^4 u_z}{\partial t^4} = 0 \tag{C.29}$$

The parameter κ is called the shear coefficient. For solid rectangular beams, the shear coefficient κ is equal to 5/6 according to Timoshenko [163]. Several authors have tried to improve this expression for κ, since its dependence on ν. According to Cowper [54], the shear coefficient can be written as:

$$\kappa = \frac{10(1+\nu)}{12 + 11\nu} \tag{C.30}$$

Dispersion curves In the frequency-wavenumber domain, equation (C.29) becomes:

$$\left[-\rho A \omega^2 + EI_z k_y^4 - \rho I_z \left(1 + \frac{E}{\kappa G}\right) \omega^2 k_y^2 + \frac{\rho^2 I_z}{\kappa G} \omega^4\right] \tilde{u}_z = 0 \tag{C.31}$$

This leads to the following dispersion relation:

$$EI_z k_y^4 - \rho I_z \left(1 + \frac{E}{\kappa G}\right) \omega^2 k_y^2 + \left[-\rho A \omega^2 + \frac{\rho^2 I_z}{\kappa G} \omega^4\right] = 0 \tag{C.32}$$

with (positive) solutions:

$$k_y = \frac{1}{\sqrt{2}} \sqrt{\left(\frac{1}{\kappa G} + \frac{1}{E}\right) \rho \omega^2 \pm \sqrt{\left(\frac{1}{\kappa G} - \frac{1}{E}\right)^2 \rho^2 \omega^4 + 4 \frac{\rho A}{E I_z} \omega^2}} \tag{C.33}$$

or:

$$p_y = \frac{1}{\sqrt{2}}\sqrt{\left(\frac{1}{\kappa G}+\frac{1}{E}\right)\rho \pm \sqrt{\left(\frac{1}{\kappa G}-\frac{1}{E}\right)^2 \rho^2 + 4\frac{\rho A}{E I_z \omega^2}}} \tag{C.34}$$

The asymptotes for $\omega \to \infty$ are equal to:

$$p_{y1} = \sqrt{\frac{\rho}{\kappa G}} \tag{C.35}$$

$$p_{y2} = \sqrt{\frac{\rho}{E}} \tag{C.36}$$

C.3 Torsion mode

Displacements, strains, and stresses In the classical theory, Saint-Venant's theory [58], the torsion angle per unit length is assumed to be constant. In a more general theory, Barr's theory [15, 154], the torsion angle per unit length ψ is dependent on the position y and the time t and not equal to the derivative of the in-plane angle θ. The displacements are therefore given by:

$$\begin{cases} u_x = z\theta(y,t) \\ u_y = \phi(x,z)\psi(y,t) \\ u_z = -x\theta(y,t) \end{cases} \tag{C.37}$$

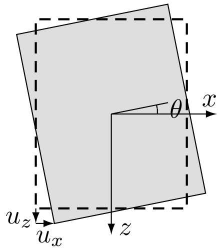

Figure C.3: Element with torsion deformation.

This leads to the following strains:

$$\begin{cases} \epsilon_{xx} = \dfrac{\partial u_x}{\partial x} = 0 \\ \epsilon_{yy} = \dfrac{\partial u_y}{\partial y} = \phi\dfrac{\partial \psi}{\partial y} \\ \epsilon_{zz} = \dfrac{\partial u_z}{\partial z} = 0 \\ \gamma_{xy} = \dfrac{\partial u_x}{\partial y} + \dfrac{\partial u_y}{\partial x} = z\dfrac{\partial \theta}{\partial y} + \dfrac{\partial \phi}{\partial x}\psi \\ \gamma_{yz} = \dfrac{\partial u_y}{\partial z} + \dfrac{\partial u_z}{\partial y} = \dfrac{\partial \phi}{\partial z}\psi - x\dfrac{\partial \theta}{\partial y} \\ \gamma_{zx} = \dfrac{\partial u_z}{\partial x} + \dfrac{\partial u_x}{\partial z} = 0 \end{cases} \tag{C.38}$$

and stresses:

$$\begin{cases} \sigma_{xx} = \dfrac{E}{(1+\nu)(1-2\nu)}\left((1-\nu)\epsilon_{xx} + \nu\epsilon_{yy} + \nu\epsilon_{zz}\right) \\ \qquad = \dfrac{E\nu\phi}{(1+\nu)(1-2\nu)}\dfrac{\partial\psi}{\partial y} \approx 0 \\ \sigma_{yy} = \dfrac{E}{(1+\nu)(1-2\nu)}\left(\nu\epsilon_{xx} + (1-\nu)\epsilon_{yy} + \nu\epsilon_{zz}\right) \\ \qquad = \dfrac{E(1-\nu)\phi}{(1+\nu)(1-2\nu)}\dfrac{\partial\psi}{\partial y} \approx E\phi\dfrac{\partial\psi}{\partial y} \\ \sigma_{zz} = \dfrac{E}{(1+\nu)(1-2\nu)}\left(\nu\epsilon_{xx} + \nu\epsilon_{yy} + (1-\nu)\epsilon_{zz}\right) \\ \qquad = \dfrac{E\nu\phi}{(1+\nu)(1-2\nu)}\dfrac{\partial\psi}{\partial y} \approx 0 \\ \tau_{xy} = G\gamma_{xy} = Gz\dfrac{\partial\theta}{\partial y} + G\dfrac{\partial\phi}{\partial x}\psi \\ \tau_{yz} = G\gamma_{yz} = G\dfrac{\partial\phi}{\partial z}\psi - Gx\dfrac{\partial\theta}{\partial y} \\ \tau_{zx} = G\gamma_{zx} = 0 \end{cases} \tag{C.39}$$

Hamilton's principle The kinetic energy $\mathcal{T}$ can be expressed as:

$$\begin{aligned} \mathcal{T} &= \frac{1}{2}\int_\Omega \rho\left[\left(\frac{\partial u_x}{\partial t}\right)^2 + \left(\frac{\partial u_y}{\partial t}\right)^2 + \left(\frac{\partial u_z}{\partial t}\right)^2\right]\mathrm{d}\Omega \\ &= \frac{1}{2}\int_y\int_A \rho\left[\phi^2\left(\frac{\partial\psi}{\partial t}\right)^2\right]\mathrm{d}A\mathrm{d}y + \frac{1}{2}\int_y\int_A \rho\left[z^2\left(\frac{\partial\theta}{\partial t}\right)^2 + x^2\left(\frac{\partial\theta}{\partial t}\right)^2\right]\mathrm{d}A\mathrm{d}y \\ &= \mathcal{T}_1 + \mathcal{T}_2 \end{aligned} \tag{C.40}$$

The variation of integral $\mathcal{T}_1$ is equal to:

$$\begin{aligned} \delta\mathcal{T}_1 &= \int_y\int_A \rho\left[\phi\delta\phi\left(\frac{\partial\psi}{\partial t}\right)^2 + \phi^2\left(\frac{\partial\psi}{\partial t}\right)\left(\frac{\partial\delta\psi}{\partial t}\right)\right]\mathrm{d}A\mathrm{d}y \\ &\overset{\text{PI}}{=} \int_y\int_A \rho\left(\frac{\partial\psi}{\partial t}\right)^2\phi\delta\phi\mathrm{d}A\mathrm{d}y - \int_y \rho I_\phi\frac{\partial^2\psi}{\partial t^2}\delta\psi\mathrm{d}y \end{aligned} \tag{C.41}$$

with

$$I_\phi = \int_A \phi^2 \mathrm{d}A \tag{C.42}$$

The variation of integral $\mathcal{T}_2$ is equal to:

$$\begin{aligned}\delta\mathcal{T}_2 = \int_y \int_A \rho\left(x^2+z^2\right)\frac{\partial\theta}{\partial t}\frac{\partial\delta\theta}{\partial t}\mathrm{d}A\mathrm{d}y &= \int_y \rho I_\mathrm{p}\frac{\partial\theta}{\partial t}\frac{\partial\delta\theta}{\partial t}\mathrm{d}y \\ &\overset{\mathrm{PI}}{=} -\int_y \rho I_\mathrm{p}\frac{\partial^2\theta}{\partial t^2}\delta\theta\mathrm{d}y\end{aligned} \tag{C.43}$$

with

$$I_\mathrm{p} = \int_A \left(x^2+z^2\right)\mathrm{d}A \tag{C.44}$$

Therefore, the variation of kinetic energy $\mathcal{T}$ is given by:

$$\delta\mathcal{T} = -\int_y \rho I_\phi \frac{\partial^2\psi}{\partial t^2}\delta\psi\mathrm{d}y - \int_y \rho I_\mathrm{p}\frac{\partial^2\theta}{\partial t^2}\delta\theta\mathrm{d}y + \int_y\int_A \rho\left(\frac{\partial\psi}{\partial t}\right)^2\phi\delta\phi\mathrm{d}A\mathrm{d}y \tag{C.45}$$

The strain energy Π can be expressed as:

$$\begin{aligned}\Pi &= \frac{1}{2}\int_\Omega \left(\sigma_{xx}\epsilon_{xx}+\sigma_{yy}\epsilon_{yy}+\sigma_{zz}\epsilon_{zz}+\tau_{xy}\gamma_{xy}+\tau_{yz}\gamma_{yz}+\tau_{zx}\gamma_{zx}\right)\mathrm{d}\Omega \\ &= \frac{1}{2}\int_y\int_A\left[E\left(\phi\frac{\partial\psi}{\partial y}\right)^2\right]\mathrm{d}A\mathrm{d}y + \frac{1}{2}\int_y\int_A\left[G\left(z\frac{\partial\theta}{\partial y}+\frac{\partial\phi}{\partial x}\psi\right)^2\right]\mathrm{d}A\mathrm{d}y \\ &\quad + \frac{1}{2}\int_y\int_A\left[G\left(\frac{\partial\phi}{\partial z}\psi - x\frac{\partial\theta}{\partial y}\right)^2\right]\mathrm{d}A\mathrm{d}y \\ &= \Pi_1+\Pi_2+\Pi_3\end{aligned} \tag{C.46}$$

The variation of integral Π_1 is equal to:

$$\begin{aligned}\delta\Pi_1 &= \int_y\int_A\left[E\phi\delta\phi\left(\frac{\partial\psi}{\partial y}\right)^2\right]\mathrm{d}A\mathrm{d}y + \int_y\int_A\left[E\phi^2\frac{\partial\psi}{\partial y}\frac{\partial\delta\psi}{\partial y}\right]\mathrm{d}A\mathrm{d}y \\ &= \int_y\int_A\left[E\left(\frac{\partial\psi}{\partial y}\right)^2\phi\delta\phi\right]\mathrm{d}A\mathrm{d}y + \int_y\left[EI_\phi\frac{\partial\psi}{\partial y}\frac{\partial\delta\psi}{\partial y}\right]\mathrm{d}y \\ &\overset{\mathrm{PI}}{=} \int_y\int_A\left[E\left(\frac{\partial\psi}{\partial y}\right)^2\phi\delta\phi\right]\mathrm{d}A\mathrm{d}y + EI_\phi\frac{\partial\psi}{\partial y}\delta\psi\Big|_0^l - \int_y\left[EI_\phi\frac{\partial^2\psi}{\partial y^2}\delta\psi\right]\mathrm{d}y\end{aligned} \tag{C.47}$$

The variation of integral Π_2 is equal to:

$$\begin{aligned}
\delta\Pi_2 = &\int_y\int_A \left[G\left(\frac{\partial\phi}{\partial x}\psi + z\frac{\partial\theta}{\partial y}\right)\left(\frac{\partial\phi}{\partial x}\delta\psi + \frac{\partial\delta\phi}{\partial x}\psi + z\frac{\partial\delta\theta}{\partial y}\right)\right]\mathrm{d}A\mathrm{d}y \\
\overset{\text{PI}}{=}& G\left\{\int_y\int_A \left(\frac{\partial\phi}{\partial x}\psi + z\frac{\partial\theta}{\partial y}\right)\frac{\partial\phi}{\partial x}\delta\psi\mathrm{d}A\mathrm{d}y\right. \\
&+\int_y\int_z \left(\frac{\partial\phi}{\partial x}\psi + z\frac{\partial\theta}{\partial y}\right)\psi\delta\phi\bigg|_{-b/2}^{b/2}\mathrm{d}z\mathrm{d}y \\
&-\int_y\int_A \frac{\partial^2\phi}{\partial x^2}\psi^2\delta\phi\mathrm{d}A\mathrm{d}y + \int_A \left(\frac{\partial\phi}{\partial x}\psi + z\frac{\partial\theta}{\partial y}\right)z\delta\theta\bigg|_0^l\mathrm{d}A \\
&\left.-\int_y\int_A \left(z\frac{\partial\phi}{\partial x}\frac{\partial\psi}{\partial y} + z^2\frac{\partial^2\theta}{\partial y^2}\right)\delta\theta\mathrm{d}A\mathrm{d}y\right\}
\end{aligned} \tag{C.48}$$

The variation of integral Π_3 is equal to:

$$\begin{aligned}
\delta\Pi_3 = &\int_y\int_A \left[G\left(\frac{\partial\phi}{\partial z}\psi - x\frac{\partial\theta}{\partial y}\right)\left(\frac{\partial\phi}{\partial z}\delta\psi + \frac{\partial\delta\phi}{\partial z}\psi - x\frac{\partial\delta\theta}{\partial y}\right)\right]\mathrm{d}A\mathrm{d}y \\
\overset{\text{PI}}{=}& G\left\{\int_y\int_A \left(\frac{\partial\phi}{\partial z}\psi - x\frac{\partial\theta}{\partial y}\right)\frac{\partial\phi}{\partial z}\delta\psi\mathrm{d}A\mathrm{d}y\right. \\
&+\int_y\int_x \left(\frac{\partial\phi}{\partial z}\psi - x\frac{\partial\theta}{\partial y}\right)\psi\delta\phi\bigg|_{-h/2}^{h/2}\mathrm{d}x\mathrm{d}y \\
&-\int_y\int_A \frac{\partial^2\phi}{\partial z^2}\psi^2\delta\phi\mathrm{d}A\mathrm{d}y + \int_A \left(\frac{\partial\phi}{\partial z}\psi - x\frac{\partial\theta}{\partial y}\right)x\delta\theta\bigg|_0^l\mathrm{d}A \\
&\left.+\int_y\int_A \left(x\frac{\partial\phi}{\partial z}\frac{\partial\psi}{\partial y} - x^2\frac{\partial^2\theta}{\partial y^2}\right)\delta\theta\mathrm{d}A\mathrm{d}y\right\}
\end{aligned} \tag{C.49}$$

Therefore, the variation of the strain energy Π is given by:

$$\begin{aligned}
\delta\Pi = & \int_y \left[-EI_\phi \frac{\partial^2 \psi}{\partial y^2} + G \int_A \left(\left(\frac{\partial \phi}{\partial x} \right)^2 \psi + z \frac{\partial \phi}{\partial x} \frac{\partial \theta}{\partial y} + \left(\frac{\partial \phi}{\partial z} \right)^2 \psi - x \frac{\partial \phi}{\partial z} \frac{\partial \theta}{\partial y} \right) \mathrm{d}A \right] \delta\psi \mathrm{d}y \\
& + \int_y \left[G \int_A \left(-z \frac{\partial \phi}{\partial x} \frac{\partial \psi}{\partial y} - z^2 \frac{\partial^2 \theta}{\partial y^2} + x \frac{\partial \phi}{\partial z} \frac{\partial \psi}{\partial y} - x^2 \frac{\partial^2 \theta}{\partial y^2} \right) \mathrm{d}A \right] \delta\theta \mathrm{d}y \\
& + \int_A \left[\int_y \left(E \left(\frac{\partial \psi}{\partial y} \right)^2 \phi - G \frac{\partial^2 \phi}{\partial x^2} \psi^2 - G \frac{\partial^2 \phi}{\partial z^2} \psi^2 \right) \mathrm{d}y \right] \delta\phi \mathrm{d}A \\
= & \int_y \left[-EI_\phi \frac{\partial^2 \psi}{\partial y^2} + GD\psi + GL \frac{\partial \theta}{\partial y} \right] \delta\psi \mathrm{d}y + \int_y \left[-GL \frac{\partial \psi}{\partial y} - GI_\mathrm{p} \frac{\partial^2 \theta}{\partial y^2} \right] \delta\theta \mathrm{d}y \\
& + \int_A \left[E\phi \int_y \left(\frac{\partial \psi}{\partial y} \right)^2 \mathrm{d}y - G\nabla^2 \phi \int_y \psi^2 \mathrm{d}y \right] \delta\phi \mathrm{d}A
\end{aligned} \tag{C.50}$$

with

$$D = \int_A \left[\left(\frac{\partial \phi}{\partial x} \right)^2 + \left(\frac{\partial \phi}{\partial z} \right)^2 \right] \mathrm{d}A \tag{C.51}$$

$$L = \int_A \left[z \frac{\partial \phi}{\partial x} - x \frac{\partial \phi}{\partial z} \right] \mathrm{d}A \tag{C.52}$$

$$\nabla^2 \phi = \frac{\partial^2 \phi}{\partial x^2} + \frac{\partial^2 \phi}{\partial z^2} \tag{C.53}$$

By applying Hamilton's principle in Eq. (C.1), the following differential equations are obtained:

$$EI_\phi \frac{\partial^2 \psi}{\partial y^2} - GD\psi - GL \frac{\partial \theta}{\partial y} = \rho I_\phi \frac{\partial^2 \psi}{\partial t^2} \tag{C.54}$$

$$GL \frac{\partial \psi}{\partial y} + GI_\mathrm{p} \frac{\partial^2 \theta}{\partial y^2} = \rho I_p \frac{\partial^2 \theta}{\partial t^2} \tag{C.55}$$

$$E\phi \int_y \left(\frac{\partial \psi}{\partial y} \right)^2 \mathrm{d}y - G\nabla^2 \phi \int_y \psi^2 \mathrm{d}y = \rho\phi \int_y \left(\frac{\partial \psi}{\partial t} \right)^2 \mathrm{d}y \tag{C.56}$$

Often the last equation is simplified to:

$$\nabla^2 \phi = 0 \tag{C.57}$$

The next step is to combine equations (C.54) and (C.55) to eliminate the variable ψ or θ and therefore to get a differential equation that only depends on θ or ψ. The variable ψ can be eliminated from equation (C.54) since from equation (C.55) we get:

$$\frac{\partial \psi}{\partial y} = -\frac{I_\mathrm{p}}{L}\frac{\partial^2 \theta}{\partial y^2} + \frac{\rho I_\mathrm{p}}{GL}\frac{\partial^2 \theta}{\partial t^2} \tag{C.58}$$

which can be inserted in equation (C.54) after differentiating to y:

$$\begin{aligned} &-\frac{EI_\phi I_\mathrm{p}}{L}\frac{\partial^4 \theta}{\partial y^4} + \frac{\rho E I_\phi I_\mathrm{p}}{GL}\frac{\partial^4 \theta}{\partial y^2 \partial t^2} + \frac{GDI_\mathrm{p}}{L}\frac{\partial^2 \theta}{\partial y^2} - \frac{\rho D I_\mathrm{p}}{L}\frac{\partial^2 \theta}{\partial t^2} - GL\frac{\partial^2 \theta}{\partial y^2} \\ &= -\frac{\rho I_\phi I_\mathrm{p}}{L}\frac{\partial^4 \theta}{\partial y^2 \partial t^2} + \frac{\rho^2 I_\phi I_\mathrm{p}}{GL}\frac{\partial^4 \theta}{\partial t^4} \end{aligned} \tag{C.59}$$

Rearranging this equation results in:

$$\begin{aligned} &G\left(L - \frac{DI_\mathrm{p}}{L}\right)\frac{\partial^2 \theta}{\partial y^2} + \frac{\rho D I_\mathrm{p}}{L}\frac{\partial^2 \theta}{\partial t^2} + \frac{EI_\phi I_\mathrm{p}}{L}\frac{\partial^4 \theta}{\partial y^4} \\ &- \frac{\rho I_\phi I_\mathrm{p}}{L}\left(1 + \frac{E}{G}\right)\frac{\partial^4 \theta}{\partial y^2 \partial t^2} + \frac{\rho^2 I_\phi I_\mathrm{p}}{GL}\frac{\partial^4 \theta}{\partial t^4} = 0 \end{aligned} \tag{C.60}$$

This can be simplified by using the relation $D = -L = I_\mathrm{p} - I_\mathrm{t}$. Equation (C.60) becomes:

$$\begin{aligned} &GI_\mathrm{t}\frac{\partial^2 \theta}{\partial y^2} - \rho I_\mathrm{p}\frac{\partial^2 \theta}{\partial t^2} - \frac{EI_\phi I_\mathrm{p}}{I_\mathrm{p} - I_\mathrm{t}}\frac{\partial^4 \theta}{\partial y^4} + \frac{\rho I_\phi I_\mathrm{p}}{I_\mathrm{p} - I_\mathrm{t}}\left(1 + \frac{E}{G}\right)\frac{\partial^4 \theta}{\partial y^2 \partial t^2} \\ &- \frac{\rho^2 I_\phi I_\mathrm{p}}{G\left(I_\mathrm{p} - I_\mathrm{t}\right)}\frac{\partial^4 \theta}{\partial t^4} = 0 \end{aligned} \tag{C.61}$$

This corresponds to the expression found by Barr [15]. To control the asymptotes for torsional waves with decreasing wavelength, a non-dimensional parameter κ' is added, analogous to the added parameter κ in the dispersion relation for shear-bending waves:

$$\begin{aligned} &GI_\mathrm{t}\frac{\partial^2 \theta}{\partial y^2} - \rho I_\mathrm{p}\frac{\partial^2 \theta}{\partial t^2} - \frac{E\kappa' I_\phi I_\mathrm{p}}{I_\mathrm{p} - I_\mathrm{t}}\frac{\partial^4 \theta}{\partial y^4} + \frac{\rho I_\phi I_\mathrm{p}}{I_\mathrm{p} - I_\mathrm{t}}\left(\kappa' + \frac{E}{G}\right)\frac{\partial^4 \theta}{\partial y^2 \partial t^2} \\ &- \frac{\rho^2 I_\phi I_\mathrm{p}}{G\left(I_\mathrm{p} - I_\mathrm{t}\right)}\frac{\partial^4 \theta}{\partial t^4} = 0 \end{aligned} \tag{C.62}$$

Dispersion curve In the frequency-wavenumber domain, equation (C.62) becomes:

$$\begin{aligned}\Bigg[-GI_{\mathrm{t}}k_y^2 + \rho I_{\mathrm{p}}\omega^2 - \frac{E\kappa' I_\phi I_{\mathrm{p}}}{I_{\mathrm{p}} - I_{\mathrm{t}}}k_y^4 + \frac{\rho I_\phi I_{\mathrm{p}}}{I_{\mathrm{p}} - I_{\mathrm{t}}}\left(\kappa' + \frac{E}{G}\right)\omega^2 k_y^2 \\ - \frac{\rho^2 I_\phi I_{\mathrm{p}}}{G\left(I_{\mathrm{p}} - I_{\mathrm{t}}\right)}\omega^4\Bigg]\tilde{\theta} = 0\end{aligned} \tag{C.63}$$

This leads to the following dispersion relation:

$$\begin{aligned}-\frac{E\kappa' I_\phi I_{\mathrm{p}}}{I_{\mathrm{p}} - I_{\mathrm{t}}}k_y^4 + \left[\frac{\rho I_\phi I_{\mathrm{p}}}{I_{\mathrm{p}} - I_{\mathrm{t}}}\left(\kappa' + \frac{E}{G}\right)\omega^2 - GI_{\mathrm{t}}\right]k_y^2 + \\ \left[\rho I_{\mathrm{p}}\omega^2 - \frac{\rho^2 I_\phi I_{\mathrm{p}}}{G\left(I_{\mathrm{p}} - I_{\mathrm{t}}\right)}\omega^4\right] = 0\end{aligned} \tag{C.64}$$

or

$$Ak_y^4 + Bk_y^2 + C = 0 \tag{C.65}$$

with (positive) solutions:

$$k_y = \sqrt{\frac{-B \pm \sqrt{B^2 - 4AC}}{2A}} = \frac{1}{\sqrt{2}}\sqrt{-\frac{B}{A} \pm \sqrt{\left(\frac{B}{A}\right)^2 - \frac{4C}{A}}} \tag{C.66}$$

or:

$$p_y = \frac{1}{\omega\sqrt{2}}\sqrt{-\frac{B}{A} \pm \sqrt{\left(\frac{B}{A}\right)^2 - \frac{4C}{A}}} \tag{C.67}$$

The asymptotes for $\omega \to \infty$ are:

$$\begin{aligned}p_y &= \frac{1}{\sqrt{2}}\sqrt{\frac{\rho}{E\kappa'}\left(\kappa' + \frac{E}{G}\right) \pm \sqrt{\left[\frac{-\rho}{E\kappa'}\left(\kappa' + \frac{E}{G}\right)\right]^2 - \frac{4\rho^2}{E\kappa' G}}} \\ &= \frac{1}{\sqrt{2}}\sqrt{\left(\frac{1}{E} + \frac{1}{\kappa' G}\right)\rho \pm \sqrt{\left(\frac{\rho^2}{E^2} + \frac{2\rho^2}{E\kappa' G} + \frac{\rho^2}{\kappa'^2 G^2}\right) - \frac{4\rho^2}{E\kappa' G}}} \\ &= \frac{1}{\sqrt{2}}\sqrt{\left(\frac{1}{E} + \frac{1}{\kappa' G}\right)\rho \pm \sqrt{\left(\frac{1}{E^2} - \frac{2}{E\kappa' G} + \frac{1}{\kappa'^2 G^2}\right)\rho^2}} \\ &= \frac{1}{\sqrt{2}}\sqrt{\left(\frac{1}{E} + \frac{1}{\kappa' G}\right)\rho \pm \sqrt{\left(\frac{1}{E} - \frac{1}{\kappa' G}\right)^2 \rho^2}}\end{aligned} \tag{C.68}$$

with solutions:

$$p_{y1} = \sqrt{\frac{\rho}{\kappa' G}} \tag{C.69}$$

$$p_{y2} = \sqrt{\frac{\rho}{E}} \tag{C.70}$$

For $\omega \to \infty$, p_{y1} should go to p_{R} [154]. Therefore:

$$p_{y1} = \sqrt{\frac{\rho}{\kappa' G}} = p_{\mathrm{R}} = \frac{1}{C_{\mathrm{R}}} \Leftrightarrow \kappa' = \frac{\rho C_{\mathrm{R}}^2}{G} = \frac{\rho C_{\mathrm{R}}^2}{\rho C_{\mathrm{s}}^2} = \frac{C_{\mathrm{R}}^2}{C_{\mathrm{s}}^2} \tag{C.71}$$

Bibliography

[1] Abe, K., Fujiu, T., and Koro, K. Shape optimization with topological derivative and its application to noise barrier for railway viaducts. In *Proceedings of the 11th International Conference of Advances in Boundary Element Techniques XI* (2010), C. Zhang, M. Aliabadi, and M. Schanz, Eds., pp. 7–12.

[2] Achenbach, J. *Wave propagation in elastic solids*, vol. 16 of *North-Holland Series in Applied Mathematics and Mechanics.* North-Holland, Amsterdam, The Netherlands, 1973.

[3] Adam, D., Vogel, A., and Zimmermann, A. Ground improvement techniques beneath existing rail tracks. *Proceedings of the Institution of Civil Engineers-Ground Improvement 11*, 4 (2007), 229–235.

[4] Ahmad, S., and Al-Hussaini, T. Simplified design for vibration screening by open and in-filled trenches. *Journal of Geotechnical Engineering, Proceedings of the ASCE 117*, 1 (1991), 67–88.

[5] Alias, J. *La voie ferrée: techniques de construction et d'entretien.* Eyrolles, Paris, France, 1984.

[6] Amir, O., Sigmund, O., Lazarov, B., and Schevenels, M. Efficient reanalysis techniques for robust topology optimization. *Computer Methods in Applied Mechanics and Engineering 245* (2012), 217–231.

[7] Andersen, L., Frigaard, P., and Augustesen, A. Mitigation of ground vibration by double sheet-pile walls. In *The International Congress on Advances in Civil Engineering* (2008), Eastern Mediterranean University Press, pp. 247–254.

[8] Andersen, L., and Jones, C. Coupled boundary and finite element analysis of vibration from railway tunnels - a comparison of two-and

three-dimensional models. *Journal of Sound and Vibration 293*, 3 (2006), 611–625.

[9] Andersen, L., and Nielsen, S. Reduction of ground vibration by means of barriers or soil improvement along a railway track. *Soil Dynamics and Earthquake Engineering 25* (2005), 701–716.

[10] Arnout, S., Firl, M., and Bletzinger, K.-U. Parameter free shape and thickness optimisation considering stress response. *Structural and Multidisciplinary Optimization 45*, 6 (2012), 801–814.

[11] Asadpoure, A., Tootkaboni, M., and Guest, J. Robust topology optimization of structures with uncertainties in stiffness–application to truss structures. *Computers & Structures 89*, 11 (2011), 1131–1141.

[12] Aubry, D., and Clouteau, D. A subdomain approach to dynamic soil-structure interaction. In *Recent advances in Earthquake Engineering and Structural Dynamics*, V. Davidovici and R. Clough, Eds. Ouest Editions/AFPS, Nantes, 1992, pp. 251–272.

[13] Ausilio, E., and Conte, E. Soil compaction by vibro-replacement: a case study. *Ground Improvement 11*, 3 (2007), 117–126.

[14] Bahrekazemi, M., Bodare, A., Andréasson, B., and Smekal, A. Mitigation of train-induced ground vibrations; lessons from the Ledsgård project. In *Proceedings of the 5th International Conference on Case Histories in Geotechnical Engineering* (New York, USA, April 2004), Missouri University of Science and Technology.

[15] Barr, A. Torsional waves in uniform rods of non-circular section. *Journal of Mechanical Engineering Sciences 4*, 2 (1962), 127–135.

[16] Basu, U. Explicit finite element perfectly matched layer for transient three-dimensional elastic waves. *International Journal for Numerical Methods in Engineering 77* (2009), 151–176.

[17] Basu, U., and Chopra, A. Perfectly matched layers for time-harmonic elastodynamics of unbounded domains: theory and finite-element implementation. *Computer Methods in Applied Mechanics and Engineering 192*, 11 (2003), 1337–1375.

[18] Bécache, E., Bonnet-Ben Dhia, A., and Legendre, G. Perfectly matched layers for the convected helmholtz equation. *SIAM Journal on Numerical Analysis 42*, 1 (2004), 409–433.

[19] Bellido, J., and Donoso, A. An optimal design problem in wave propagation. *Journal of Optimization Theory and Applications 134*, 2 (2007), 339–352.

[20] Ben-Tal, A., and Nemirovski, A. Robust truss topology design via semidefinite programming. *SIAM Journal on Optimization 7*, 4 (1997), 991–1016.

[21] Bendickson, J., Dowling, J., and Scalora, M. Analytic expressions for the electromagnetic mode density in finite, one-dimensional, photonic band-gap structures. *Physical Review E 53*, 4 (1996), 4107–4121.

[22] Bendsøe, M. Optimal shape design as a material distribution problem. *Structural Optimization 1*, 4 (1989), 193–202.

[23] Bendsøe, M., and Sigmund, O. *Topology optimization: theory, methods and applications.* Springer, Berlin, Germany, 2003.

[24] Beranek, L., and Work, G. Sound transmission through multiple structures containing flexible blankets. *The Journal of the Acoustical Society of America 21*, 4 (1949), 419–428.

[25] Bérenger, J. A perfectly matched layer for the absorption of electromagnetic waves. *Journal of Computational Physics 114*, 2 (1994), 185–200.

[26] Bérenger, J. Application of the CFS PML to the absorption of evanescent waves in waveguides. *IEEE Microwave and Wireless Components Letter 12*, 6 (2002), 218–220.

[27] Beskos, D., Dasgupta, B., and Vardoulakis, I. Vibration isolation using open or filled trenches. Part I: 2-D homogeneous soil. *Computational Mechanics 1* (1986), 43–63.

[28] Bettess, P. Infinite elements. *International Journal for Numerical Methods in Engineering 11*, 1 (1977), 53–64.

[29] Borel, P., Harpøth, A., Frandsen, L., Kristensen, M., Shi, P., Jensen, J., and Sigmund, O. Topology optimization and fabrication of photonic crystal structures. *Optics Express 12*, 9 (2004), 1996–2001.

[30] Bourdin, B. Filters in topology optimization. *International Journal for Numerical Methods in Engineering 50*, 9 (2001), 2143–2158.

[31] Boyd, S., and Vandenberghe, L. *Convex optimization*, 7th ed. Cambridge University Press, Cambridge, UK, 2009.

[32] Braibant, V., and Fleury, C. Shape optimal design using B-splines. *Computer Methods in Applied Mechanics and Engineering 44* (1984), 247–267.

[33] Brenner, S., and Scott, R. *The mathematical theory of finite element methods*, vol. 15. Springer Science & Business Media, 2007.

[34] Brillouin, L. *Wave propagation in periodic structures: electric filters and crystal lattices.* Dover Phoenix, New York, USA, 2003.

[35] Brittain, K., Silva, M., and Tortorelli, D. Minmax topology optimization. *Structural and Multidisciplinary Optimization 45*, 5 (2012), 657–668.

[36] Bruns, T., and Tortorelli, D. Topology optimization of non-linear elastic structures and compliant mechanisms. *Computer Methods in Applied Mechanics and Engineering 190*, 26–27 (2001), 3443–3459.

[37] Camley, R., Djafari-Rouhani, B., Dobrzynski, L., and Maradudin, A. Transverse elastic waves in periodically layered infinite and semi-infinite media. *Physical Review B 27*, 12 (1983), 7318–7329.

[38] Chebli, H., Othman, R., Clouteau, D., Arnst, M., and Degrande, G. 3D periodic BE-FE model for various transportation structures interacting with soil. *Computers and Geotechnics 35* (2008).

[39] Chen, S., Chen, W., and Lee, S. Level set based robust shape and topology optimization under random field uncertainties. *Structural and Multidisciplinary Optimization 41*, 4 (2010), 507.

[40] Chew, W., Jin, J., and Michielssen, E. Complex coordinate stretching as a generalized absorbing boundary condition. *Microwave and Optical Technology Letters 15*, 6 (1997), 363–369.

[41] Chew, W., and Weedon, W. A 3D perfectly matched medium from modified Maxwell's equations with stretched coordinates. *Microwave and Optical Technology Letters 7*, 13 (1996), 599–604.

[42] Choi, K., and Kim, N. *Structural sensitivity analysis and optimization, Volume 1. Linear systems.* Springer, New York, 2005.

[43] Christensen, P. W., and Klarbring, A. *An introduction to structural optimization*, vol. 153 of *Solid mechanics and its applications.* Springer Science & Business Media, 2008.

[44] Christiansen, R., Lazarov, B., Jensen, J., and Sigmund, O. Creating geometrically robust designs for highly sensitive problems using topology optimization. *Structural and Multidisciplinary Optimization 52*, 4 (2015), 737–754.

[45] Christiansen, R., Sigmund, O., and Fernandez-Grande, E. Experimental validation of a topology optimized acoustic cavity. *The Journal of the Acoustical Society of America 138*, 6 (2015), 3470–3474.

[46] Clouteau, D., Elhabre, M., and Aubry, D. Periodic BEM and FEM-BEM coupling: application to seismic behaviour of very long structures. *Computational Mechanics 25* (2000), 567–577.

[47] Cook, R., Malkus, D., Plesha, M., and Witt, R. *Concepts and applications of finite element analysis*, fourth ed. John Wiley & Sons, 2002.

[48] Cooley, J., and Tukey, J. An algorithm for the machine calculation of complex Fourier series. *Mathematics of Computation 19*, 90 (1965), 297–301.

[49] Costa, P., Calçada, R., and Cardoso, A. Ballast mats for the reduction of railway traffic vibrations. Numerical study. *Soil Dynamics and Earthquake Engineering 42* (2012), 137–150.

[50] Coulier, P., Cuéllar, V., Degrande, G., and Lombaert, G. Experimental and numerical evaluation of the effectiveness of a stiff wave barrier in the soil. *Soil Dynamics and Earthquake Engineering 77* (2015), 238–253.

[51] Coulier, P., Degrande, G., Dijckmans, A., Houbrechts, J., Lombaert, G., Rücker, W., Auersch, L., Plaza, M., Cuéllar, V., Thompson, D., Ekblad, A., and Smekal, A. Scope of the parametric study on mitigation measures on the transmission path. RIVAS project SCP0-GA-2010-265754, Deliverable D4.1, Report to the EC, October 2011.

[52] Coulier, P., Dijckmans, A., François, S., Degrande, G., and Lombaert, G. A spatial windowing technique to account for finite dimensions in 2.5D dynamic soil–structure interaction problems. *Soil Dynamics and Earthquake Engineering 59* (2014), 51–67.

[53] Coulier, P., François, S., Degrande, G., and Lombaert, G. Subgrade stiffening next to the track as a wave impeding barrier for railway induced vibrations. *Soil Dynamics and Earthquake Engineering 48* (2013), 119–131.

[54] Cowper, G. The shear coefficient in Timoshenko's beam theory. *Journal of Applied Mechanics 33*, 2 (1966), 335–340.

[55] Cremer, L. Theorie der Schalldämmung dünner Wände bei schrägem Einfall. *Akustische Zeitschrift 7* (1942), 81–104.

[56] Cremer, L., Heckl, M., and Petersson, B. *Structure-borne sound: Structural vibrations and sound radiation at audio frequencies*, 3rd ed. Springer, Berlin, Germany, 2005.

[57] Dahl, J., Jensen, J., and Sigmund, O. Topology optimization for transient wave propagation problems in one dimension. *Structural and Multidisciplinary Optimization 36*, 6 (2008), 585–595.

[58] de Saint-Venant, B. Mémoire sur les vibrations tournantes des verges élastiques. *Comptes Rendus 28* (1849), 69–72.

[59] Deaton, J., and Grandhi, R. A survey of structural and multidisciplinary continuum topology optimization: post 2000. *Structural and Multidisciplinary Optimization 49*, 1 (2013), 1–38.

[60] Degrande, G. *H02Z8A Seismic wave propagation course notes.* Department of Civil Engineering, KU Leuven, 2008.

[61] Diehl, M. *Script for Numerical Optimization Course B–KUL–H03E3A.* VTK, Leuven, Belgium, 2013.

[62] Dijckmans, A., Coulier, P., Degrande, G., Lombaert, G., Ekblad, A., Smekal, A., RodrÃŋguez Plaza, M., AndrÃľs-Alguacil, ., CuÃľllar, V., Keil, J., and Vukotic, G. Mitigation measures on the transmission path: results of field tests. RIVAS project SCP0-GA-2010-265754, Deliverable D4.5, Report to the EC, December 2013.

[63] Dijckmans, A., Coulier, P., Jiang, J., Toward, M., Thompson, D., Degrande, G., and Lombaert, G. Mitigation of railway induced ground vibration by heavy masses next to the track. *Soil Dynamics and Earthquake Engineering 75* (2015), 158–170.

[64] Dijckmans, A., Ekblad, A., Smekal, A., Degrande, G., and Lombaert, G. Efficacy of a sheet pile wall as a wave barrier for railway induced ground vibration. *Soil Dynamics and Earthquake Engineering 84* (2016), 55–69.

[65] Dijckmans, A., Jiang, J., Toward, M., Lombaert, G., Degrande, G., and Thompson, D. Numerical study of vibration mitigation

measures in the transmission path. RIVAS project SCP0-GA-2010-265754, Deliverable D4.4, Report to the EC, December 2013.

[66] Duhamel, P., and Vetterli, M. Fast fourier transforms: a tutorial review and a state of the art. *Signal processing 19*, 4 (1990), 259–299.

[67] Dühring, M., Jensen, J., and Sigmund, O. Acoustic design by topology optimization. *Journal of Sound and Vibration 317*, 3 (2008), 557–575.

[68] Dunning, P., Kim, H., and Mullineux, G. Introducing loading uncertainty in topology optimization. *AIAA Journal 49*, 4 (2011), 760–768.

[69] Dykstra, C., Mathijssen, F., and Molenkamp, F. Settlement predictions of embankments on organic soils in engineering practice. In *Proceedings of the Second International Workshop on Geotechnics of Soft Soils* (Glasgow, Scotland, September 2008), pp. 13–21.

[70] Fahy, F., and Gardonio, P. *Sound and structural vibration: radiation, transmission and response*, 2nd ed. Academic Press, Oxford, UK, 2007.

[71] Fourier, J. *Théorie analytique de la chaleur*. Firmin Didot, Paris, 1822.

[72] François, S., Schevenels, M., Lombaert, G., and Degrande, G. A 2.5D displacement based PML for elastodynamic wave propagation. *International Journal for Numerical Methods in Engineering 90*, 7 (2012), 819–837.

[73] François, S., Schevenels, M., Lombaert, G., Galvín, P., and Degrande, G. A 2.5D coupled FE-BE methodology for the dynamic interaction between longitudinally invariant structures and a layered halfspace. *Computer Methods in Applied Mechanics and Engineering 199*, 23-24 (2010), 1536–1548.

[74] François, S., Schevenels, M., Thyssen, B., Borgions, J., and Degrande, G. Design and efficiency of a vibration isolating screen in the soil. *Soil Dynamics and Earthquake Engineering 39* (2012), 113–127.

[75] Galvín, P., François, S., Schevenels, M., Bongini, E., Degrande, G., and Lombaert, G. A 2.5D coupled FE-BE model for the prediction of railway induced vibrations. *Soil Dynamics and Earthquake Engineering 30*, 12 (2010), 1500–1512.

[76] Gavrić, L. Finite element computation of dispersion properties of thin-walled waveguides. *Journal of Sound and Vibration 173*, 1 (1994), 113–124.

[77] Gavrić, L. Computation of propagative waves in free rail using finite element technique. *Journal of Sound and Vibration 183*, 3 (1995), 531–543.

[78] Gordon, C. Generic vibration criteria for vibration-sensitive equipment. In *Proceedings of the SPIE Conference on Vibration Control and Metrology* (San Jose, California, USA, November 1991), vol. 1619, pp. 71–85.

[79] Greiner, D., Aznárez, J., Maeso, O., and Winter, G. Single- and multi-objective shape design of Y-noise barriers using evolutionary computation and boundary elements. *Advances in Engineering Software 41*, 2 (2010), 368–378.

[80] Guest, J. A projection-based topology optimization approach to distributing discrete features in structures and materials. In *9th World Congress on Structural and Multidisciplinary Optimization* (Shizuoka, Japan, June 2011), pp. 13–17.

[81] Guest, J. Optimizing the layout of discrete objects in structures and materials: A projection-based topology optimization approach. *Computer Methods in Applied Mechanics and Engineering 283* (2015), 330–351.

[82] Guest, J., Prevost, J., and Belytschko, T. Achieving minimum length scale in topology optimization using nodal design variables and projection functions. *International Journal for Numerical Methods in Engineering 61*, 2 (2004), 238–254.

[83] Guest, J., and Smith Genut, L. Reducing dimensionality in topology optimization using adaptive design variable fields. *International Journal for Numerical Methods in Engineering 81*, 8 (2010), 1019–1045.

[84] Gupta, S., Hussein, M., Degrande, G., Hunt, H., and Clouteau, D. A comparison of two numerical models for the prediction of vibrations from underground railway traffic. *Soil Dynamics and Earthquake Engineering 27*, 7 (2007), 608–624.

[85] Haftka, R., and Grandhi, R. Structural shape optimization – a survey. *Computer Methods in Applied Mechanics and Engineering 57* (1986), 91–106.

[86] Haftka, R., and Gürdal, Z. *Elements of structural optimization*, vol. 11 of *Solid mechanics and its applications.* Kluwer Academic Publishers, Dordrecht, The Netherlands, 1992.

[87] Haskell, N. The dispersion of surface waves on multilayered media. *Bulletin of the Seismological Society of America 73* (1953), 17–43.

[88] Hildebrand, R. Effect of soil stabilization on audible band railway ground vibration. *Soil Dynamics and Earthquake Engineering 24*, 5 (2004), 411–424.

[89] Hinze, M., Pinnau, R., Ulbrich, M., and Ulbrich, S. *Optimization with PDE constraints*, vol. 23 of *Mathematical modelling: theory and applications*. Springer, Berlin, Germany, 2009.

[90] Huang, X., and Xie, Y. *Evolutionary topology optimization of continuum structures: methods and applications*. John Wiley & Sons, Chichester, UK, 2010.

[91] Hussein, M., Hamza, K., Hulbert, G., Scott, R., and Saitou, K. Multiobjective evolutionary optimization of periodic layered materials for desired wave dispersion characteristics. *Structural and Multidisciplinary Optimization 31*, 1 (2006), 60–75.

[92] Hussein, M., Hulbert, G., and Scott, R. Dispersive elastodynamics of 1D banded materials and structures: Analysis. *Journal of Sound and Vibration 289*, 4 (2006), 779–806.

[93] Hussein, M., Hulbert, G., and Scott, R. Dispersive elastodynamics of 1D banded materials and structures: Design. *Journal of Sound and Vibration 307*, 3 (2007), 865–893.

[94] Jansen, M., Lombaert, G., Diehl, M., Lazarov, B., Sigmund, O., and Schevenels, M. Robust topology optimization accounting for misplacement of material. *Structural and Multidisciplinary Optimization 47* (2013), 317–333.

[95] Jansen, M., Lombaert, G., Schevenels, M., and Sigmund, O. Topology optimization of fail-safe structures using a simplified local damage model. *Structural and Multidisciplinary Optimization 49*, 4 (2014), 657–666.

[96] Jensen, J. Topology optimization problems for reflection and dissipation of elastic waves. *Journal of Sound and Vibration 301* (2007), 319–340.

[97] Jensen, J., and Sigmund, O. Topology optimization of photonic crystal structures: a high-bandwidth low-loss T-junction waveguide. *Journal of the Optical Society of America B 22*, 6 (2005), 1191–1198.

[98] Jensen, J., and Sigmund, O. Topology optimization for nano-photonics. *Laser & Photonics Reviews 5*, 2 (2011), 308–321.

[99] Joannopoulos, J., Johnson, S., Winn, J., and Meade, R. *Photonic crystals: molding the flow of light.* Princeton university press, Princeton, USA, 2008.

[100] Jones, C., Thompson, D., and Andreu-Medina, J. Initial theoretical study of reducing surface-propagating vibration from trains using earthworks close to the track. In *Proceedings of the 8th International Conference on Structural Dynamics, EURODYN 2011* (2011), pp. 684–691.

[101] Karlström, A., and Boström, A. Efficiency of trenches along railways for trains moving at sub- or supersonic speeds. *Soil Dynamics and Earthquake Engineering 27* (2007), 625–641.

[102] Kattis, S., Polyzos, D., and Beskos, D. Modelling of pile wave barriers by effective trenches and their screening effectiveness. *Soil Dynamics and Earthquake Engineering 18* (1999), 1–10.

[103] Kausel, E. *Fundamental solutions in elastodynamics: a compendium.* Cambridge University Press, New York, 2006.

[104] Kausel, E., and Roesset, J. Stiffness matrices for layered soils. *Bulletin of the Seismological Society of America 71* (1981), 1743–1761.

[105] Kawamoto, A., Matsumori, T., Yamasaki, S., Nomura, T., Kondoh, T., and Nishiwaki, S. Heaviside projection based topology optimization by a pde-filtered scalar function. *Structural and Multidisciplinary Optimization 44*, 1 (2011), 19–24.

[106] Keller. The Soilcrete® - jet grouting process. Brochure 67-03E.

[107] Kim, M., Lee, P., Kim, D., and Kwon, H. Vibration isolation using flexible rubber chip barriers. In *Proceedings of the International Workshop Wave 2000, Wave propagation, Moving load, Vibration reduction* (2000), G. Schmid and N. Chouw, Eds., A.A Balkema, Amsterdam, pp. 289–298.

[108] Kook, J., Koo, K., Hyun, J., Jensen, J., and Wang, S. Acoustical topology optimization for Zwicker's loudness model – Application to noise barriers. *Computer Methods in Applied Mechanics and Engineering 237* (2012), 130–151.

[109] Kristensen, S. Topology optimization for damping of ground vibration. Master's thesis, DTU, 2012.

[110] Krylov, V. Scattering of Rayleigh waves by heavy masses as method of protection against traffic-induced ground vibrations. In *Environmental vibrations. Prediction, monitoring, mitigation and evaluation* (2005), H. Takemiya, Ed., Taylor and Francis Group, London, pp. 393–398.

[111] Lazarov, B., Schevenels, M., and Sigmund, O. Topology optimization considering material and geometric uncertainties using stochastic collocation methods. *Structural and Multidisciplinary Optimization 46*, 4 (2012), 597–612.

[112] Lazarov, B., and Sigmund, O. Filters in topology optimization based on Helmholtz-type differential equations. *International Journal for Numerical Methods in Engineering 86*, 6 (2011), 765–781.

[113] Le, C., Bruns, T., and Tortorelli, D. A gradient-based, parameter-free approach to shape optimization. *Computer Methods in Applied Mechanics and Engineering 200*, 9 (2011), 985–996.

[114] Lee, J., Kim, E., Kim, Y., Kim, J., and Kang, Y. Optimal poroelastic layer sequencing for sound transmission loss maximization by topology optimization method. *The Journal of the Acoustical Society of America 122*, 4 (2007), 2097–2106.

[115] Legault, J., Mejdi, A., and Atalla, N. Vibro-acoustic response of orthogonally stiffened panels: The effects of finite dimensions. *Journal of Sound and Vibration 330*, 24 (2011), 5928–5948.

[116] Liu, Z., Zhang, X., Mao, Y., Zhu, Y., Yang, Z., Chan, C., and Sheng, P. Locally resonant sonic materials. *Science 289* (2000), 1734–1736.

[117] Lombaert, G., Degrande, G., and Clouteau, D. Numerical modelling of free field traffic induced vibrations. *Soil Dynamics and Earthquake Engineering 19*, 7 (2000), 473–488.

[118] Lombaert, G., Degrande, G., François, S., and Thompson, D. Ground-borne vibration due to railway traffic. In *Proceedings of the 11th International Workshop on Railway Noise IWRN11* (Uddevalla, Sweden, September 2013), J. Nielsen, D. Anderson, P. de Vos, P.-E. Gautier, M. Iida, J. Nelson, T. Tielkes, D. Thompson, and D. Towers, Eds., pp. 266–301.

[119] Lombaert, G., Degrande, G., Kogut, J., and François, S. The experimental validation of a numerical model for the prediction of railway induced vibrations. *Journal of Sound and Vibration 297*, 3–5 (2006), 512–535.

[120] Lombaert, G., Degrande, G., Vanhauwere, B., Vandeborght, B., and François, S. The control of ground borne vibrations from railway traffic by means of continuous floating slabs. *Journal of Sound and Vibration 297*, 3-5 (2006), 946–961.

[121] Lombaert, G., Dijckmans, A., Coulier, P., Degrande, G., Smekal, A., Ekblad, A., Thompson, D., Jiang, J., Toward, M., Rücker, W., Keil, J., Vukotic, G., Rodríguez Plaza, M., Andrés, A., Cuéllar, V., Garburg, R., and Müller, R. Design guide and technology assessment of the transmission mitigation measures. RIVAS project SCP0-GA-2010-265754, Deliverable D4.6, Report to the EC, December 2013.

[122] Lombaert, G., François, S., and Degrande, G. Traffic: Matlab toolbox for traffic induced vibrations. Report BWM-2012-10, Department of Civil Engineering, KU Leuven, November 2012.

[123] Loy, H. Mitigating vibration using under-sleeper pads. *Railway Gazette International 168*, 4 (2012), 40–43.

[124] Lysmer, J., and Kuhlemeyer, R. Finite dynamic model for infinite media. *Journal of the Engineering Mechanics Division 95*, 4 (1969), 859–878.

[125] Massarsch, K. Vibration isolation using gas-filled cushions. In *Proceedings of the Geo-Frontiers 2005 Congress* (Austin, Texas, January 2005), American Society of Civil Engineers, pp. 1–20.

[126] Matzen, R., Jensen, J., and Sigmund, O. Transient topology optimization of two-dimensional elastic wave propagation. In *Proceedings of the 9th International Conference on Computational Structures Technology* (Stirlingshire, Scotland, September 2008), B. Topping and M. Papadrakakis, Eds., Civil-Comp Press.

[127] Maute, K., and Frangopol, D. Reliability-based design of MEMS mechanisms by topology optimization. *Computers & Structures 81*, 8–11 (2003), 813–824.

[128] Mead, D. Wave propagation in continuous periodic structures: research contributions from Southampton, 1964–1995. *Journal of Sound and Vibration 190*, 3 (1996), 495–524.

[129] Mirza, A., Frid, A., Nielsen, J., and Jones, C. Ground vibrations induced by railway traffic - the influence of vehicle parameters. In *Proceedings of the 10th International Workshop on Railway Noise IWRN10*, B. Schulte-Werning, D. Thompson, P.-E. Gautier, C. Hanson,

B. Hemsworth, J. Nelson, T. Maeda, and P. de Vos, Eds., vol. 118 of *Notes on Numerical Fluid Mechanics and Multidisciplinary Design*. Springer, Nagahama, Japan, October 2012, pp. 259–266.

[130] Moseley, M., and Kirsch, K. *Ground improvement*. CRC Press, New York, USA, 2004.

[131] Nelson, J. Recent developments in ground-borne noise and vibration control. *Journal of Sound and Vibration 193*, 1 (1996), 367–376.

[132] Nocedal, J., and Wright, S. *Numerical optimization*. Springer, New York, USA, 1999.

[133] Papadopoulos, M., François, S., Degrande, G., and Lombaert, G. Analysis of stochastic dynamic soil-structure interaction problems by means of coupled finite elements-perfectly matched layers. In *Proceedings of the European Congress on Computational Methods in Applied Sciences and Engineering 2016* (Crete, Greece, June 2016), M. Papadrakakis, V. Papadopoulos, G. Stefanou, and P. V., Eds., pp. 6172–6185.

[134] Peplow, A., Jones, C., and Petyt, M. Surface vibration propagation over a layered halfspace with an inclusion. *Applied Acoustics 56* (1999), 283–296.

[135] Rao, S. *Vibration of continuous systems*. John Wiley & Sons, Hoboken, New Jersey, USA, 2007.

[136] Read, W. Stress analysis for compressible viscoelastic materials. *Journal of Applied Physics 21* (1950), 671–674.

[137] Rizzo, F., and Shippy, D. An application of the correspondence principle of linear viscoelasticity theory. *SIAM Journal on Applied Mathematics 21*, 2 (1971), 321–330.

[138] Rozvany, G. A critical review of established methods of structural topology optimization. *Structural and Multidisciplinary Optimization 37*, 3 (2009), 217–237.

[139] Rozvany, G., Zhou, M., and Birker, T. Generalized shape optimization without homogenization. *Structural Optimization 4*, 3–4 (1992), 250–252.

[140] Rupp, C. *Topology optimization for wave propagation and vibration phenomena in elastic and piezoelectric solids*. PhD thesis, University of Colorado, 2009.

[141] Saleh, B., and Teich, M. *Fundamentals of photonics.* John Wiley & Sons, New York, USA, 1991.

[142] Schevenels, M., François, S., and Degrande, G. EDT: An ElastoDynamics Toolbox for MATLAB. *Computers & Geosciences 35*, 8 (2009), 1752–1754.

[143] Schevenels, M., Lazarov, B., and Sigmund, O. Robust topology optimization accounting for spatially varying manufacturing errors. *Computer Methods in Applied Mechanics and Engineering 200*, 49 (2011), 3613–3627.

[144] Sheng, X., Jones, C., and Thompson, D. Modelling ground vibrations from railways using wavenumber finite- and boundary-element methods. *Proceedings of the Royal Society A: Mathematical, Physical and Engineering Sciences 461* (2005), 2043–2070.

[145] Sheng, X., Jones, C., and Thompson, D. Prediction of ground vibration from trains using the wavenumber finite and boundary element methods. *Journal of Sound and Vibration 293*, 3 (2006), 575–586.

[146] Sigmund, O. Morphology-based black and white filters for topology optimization. *Structural and Multidisciplinary Optimization 33*, 4–5 (2007), 401–424.

[147] Sigmund, O. Manufacturing tolerant topology optimization. *Acta Mechanica Sinica 25*, 2 (2009), 227–239.

[148] Sigmund, O. On the usefulness of non-gradient approaches in topology optimization. *Structural and Multidisciplinary Optimization 43*, 5 (2011), 589–596.

[149] Sigmund, O., and Jensen, J. Systematic design of phononic band-gap materials and structures by topology optimization. *Philosophical Transactions of the Royal Society of London Series A: Mathematical, Physical and Engineering Sciences 361*, 1806 (2003), 1001–1019.

[150] Sigmund, O., and Petersson, J. Numerical instabilities in topology optimization: A survey on procedures dealing with checkerboards, mesh-dependencies and local minima. *Structural and Multidisciplinary Optimization 16*, 1 (1998), 68–75.

[151] Sommerfeld, A. *Partial differential equations in physics*, vol. 1. Academic press, 1949.

[152] Sprung, D., Wu, H., and Martorell, J. Scattering by a finite periodic potential. *American Journal of Physics 61*, 12 (1993), 1118–1123.

[153] Stamos, A., and Beskos, D. 3-D seismic response analysis of long lined tunnels in half-space. *Soil Dynamics and Earthquake Engineering 15* (1996), 111–118.

[154] Stephen, N. Comparison of dynamic torsion theories for beams of elliptical cross-section. *Journal of Sound and Vibration 100*, 1 (1985), 1–6.

[155] Svanberg, K. The method of moving asymptotes – a new method for structural optimization. *International Journal for Numerical Methods in Engineering 24*, 2 (1987), 359–373.

[156] Svanberg, K. Some modelling aspects for the Matlab implementation of MMA, 2004.

[157] Takemiya, H. Field vibration mitigation by honeycomb WIB for pile foundations of a high-speed train viaduct. *Soil Dynamics and Earthquake Engineering 24* (2004), 69–87.

[158] Takemiya, H., and Fujiwara, A. Wave propagation/impediment in a stratum and wave impeding block (WIB) measured for SSI response reduction. *Soil Dynamics and Earthquake Engineering 13* (1994), 49–61.

[159] Talbot, J., and Hunt, H. A generic model for evaluating the performance of base-isolated buildings. *Journal of Low Frequency Noise, Vibration and Active Control 22*, 3 (2003), 149–160.

[160] Thanedar, P., and Vanderplaats, G. Survey of discrete variable optimization for structural design. *Journal of Structural Engineering 121*, 2 (1995), 301–306.

[161] Thomson, W. Transmission of elastic waves through a stratified solid medium. *Journal of Applied Physics 21* (1950), 89–93.

[162] Timoshenko, S. On the correction for shear of the differential equation for the transverse vibrations of prismatic bars. *Philosophical Magazine 41* (1921), 744–746.

[163] Timoshenko, S. On the transverse vibrations of bars of uniform cross section. *Philosophical Magazine 43* (1922), 125–131.

[164] Tisseur, F., and Meerbergen, K. The quadratic eigenvalue problem. *SIAM review 43*, 2 (2001), 235–286.

[165] Titchmarsh, E. *Introduction to the theory of Fourier integrals.* Oxford University, Clarendon Press, London, UK, 1986.

[166] Ungless, R. *Infinite finite element.* PhD thesis, University of British Columbia, 1973.

[167] Van hoorickx, C., Sigmund, O., Schevenels, M., Lazarov, B., and Lombaert, G. Topology optimization of two-dimensional elastic wave barriers. *Journal of Sound and Vibration 376* (2016), 95–111.

[168] Van Mellaert, R., Lombaert, G., and Schevenels, M. Global size optimization of statically determinate trusses considering displacement, member, and joint constraints. *ASCE Journal of Structural Engineering 142*, 2 (2016), 040151201–0401512013.

[169] Verbraken, H., Lombaert, G., and Degrande, G. Verification of an empirical prediction method for railway induced vibrations by means of numerical simulations. *Journal of Sound and Vibration 330*, 8 (2011), 1692–1703.

[170] Villot, M., Guigou, C., and Gagliardini, L. Predicting the acoustical radiation of finite size multi-layered structures by applying spatial windowing on infinite structures. *Journal of Sound and Vibration 245*, 3 (2001), 433–455.

[171] Wadbro, E., and Berggren, M. Topology optimization of an acoustic horn. *Computer Methods in Applied Mechanics and Engineering 196* (2006), 420–436.

[172] Wang, F., Lazarov, B., and Sigmund, O. On projection methods, convergence and robust formulations in topology optimization. *Structural and Multidisciplinary Optimization 43*, 6 (2011), 767–784.

[173] Wein, F., Kaltenbacher, M., Kaltenbacher, B., Leugering, G., Bänsch, E., and Schury, F. On the effect of self-penalization of piezoelectric composites in topology optimization. *Structural and Multidisciplinary Optimization 43*, 3 (2011), 405–417.

[174] Woods, R. Screening of surface waves in soils. *Journal of the Soil Mechanics and Foundation Division, Proceedings of the ASCE 94*, SM4 (1968), 951–979.

[175] Xie, Y., and Steven, G. A simple evolutionary procedure for structural optimization. *Computers & Structures 49*, 5 (1993), 885–896.

[176] Yang, X., Xei, Y., Steven, G., and Querin, O. Bidirectional evolutionary method for stiffness optimization. *AIAA Journal 37*, 11 (1999), 1483–1488.

[177] Yang, Y., and Hung, H. A 2.5D finite-infinite element approach for modelling visco-elastic bodies subjected to moving loads. *International Journal for Numerical Methods in Engineering 51* (2001), 1317–1336.

[178] Yang, Y., Liang, X., Hung, H., and Wu, Y. Comparative study of 2D and 2.5D responses of long underground tunnels to moving train loads. *Soil Dynamics and Earthquake Engineering 97* (2017), 86–100.

[179] Yariv, A., and Yeh, P. *Optical waves in crystals.* John Wiley & Sons, New York, USA, 1984.

[180] Yeh, P., Yariv, A., and Hong, C. Electromagnetic propagation in periodic stratified media. I. General theory. *Journal of the Optical Society of America 67*, 4 (1977), 423–438.

[181] Yoon, G., Jensen, J., and Sigmund, O. Topology optimization of acoustic–structure interaction problems using a mixed finite element formulation. *International Journal for Numerical Methods in Engineering 70*, 9 (2007), 1049–1075.

[182] Zienkiewicz, O., and Campbell, J. Shape optimization and sequential linear programming. In *Optimum structural design*, R. Gallagher and O. Zienkiewicz, Eds. Wiley, New York, 1973, ch. 7, pp. 109–126.

[183] Zoccali, P., Cantisani, G., and Loprencipe, G. Ground-vibrations induced by trains: filled trenches mitigation capacity and length influence. *Construction and Building Materials 74* (2015), 1–8.

Curriculum vitae

Cédric Van hoorickx
°1 November 1990, Duffel, Belgium

Education

2013 – 2017
PhD in Engineering, Department of Civil Engineering, KU Leuven

2011 – 2013
MSc in Civil Engineering, KU Leuven

2008 – 2011
BSc in Civil Engineering, KU Leuven

2002 – 2008
Secondary education (Greek-mathematics), Sint-Jozefcollege, Turnhout

Professional experience

2013 – present
PhD fellow FWO, Department of Civil Engineering, KU Leuven

2013 – present
Teaching assistant, Department of Civil Engineering, KU Leuven
  BSc Engineering: Exercises *Strength of Materials 1*
  BSc Civil & Architectural Engineering: Exercises *Strength of Materials 2*
  BSc Civil & Architectural Engineering: Exercises *Strength of Materials 3*
  MSc Civil & Architectural Engineering: Exercises *Finite Elements, part 1*
  MSc Civil Engineering: Project Work *Clean Room*
  Thesis advisor for MSc Civil & Architectural Engineering students

Research visits abroad

August 2014 – October 2014
Visiting researcher at the Department of Mechanical Engineering, Technical University of Denmark (DTU), Lyngby, Denmark, in collaboration with Prof. Ole Sigmund

Grants and awards

2013 – 2017
PhD fellowship of the Research Foundation Flanders (FWO - Vlaanderen).

2015 – 2016
Gouden Krijtje for best Teaching Assistant 3rd BSc Architectural Engineering.

September 2016
Best Poster Award at the 12th International Workshop on Railway Noise (IWRN12), held in Terrigal, Australia from 12 to 16 September 2016.

Publications

Papers published in ISI journals

[1] C. Van hoorickx, M. Schevenels, and G. Lombaert. Double wall barriers for the reduction of ground vibration transmission. *Soil Dynamics and Earthquake Engineering*, 97:1-13, 2017.

[2] E. Reynders, C. Van hoorickx, and A. Dijckmans. Sound transmission through finite rib-stiffened and orthotropic plates. *Acta Acustica united with Acustica*, 102(6):999-1010, 2016.

[3] C. Van hoorickx, O. Sigmund, M. Schevenels, B.S. Lazarov, and G. Lombaert. Topology optimization of two-dimensional elastic wave barriers. *Journal of Sound and Vibration*, 376:95-111, 2016.

Papers published or accepted for publication in proceedings of international conferences

[1] C. Van hoorickx, M. Schevenels, and G. Lombaert. Double wall barriers as mitigation measures for ground vibration transmission. In *Proceedings of the 10th International Conference on Structural Dynamics, EURODYN 2017*, Rome, Italy, September 2017. Accepted for publication.

[2] C. Van hoorickx, M. Schevenels, and G. Lombaert. Topology optimization of elastic wave barriers using a two-and-a-half dimensional finite element methodology. In K.-U. Bletzinger, S. Fiebig, K. Muate, A. Schumacher, and T. Vieter, editors, *Proceedings of the 12th World Congress of Structural and Multidisciplinary Optimisation, WCSMO 12*, Braunschweig, Germany, June 2017.

[3] C. Van hoorickx, M. Schevenels, and G. Lombaert. Optimal design of wave barriers for the reduction of vibration levels. In D. Anderson, P.-E. Gautier, J.C.O. Nielsen, M. Iida, J.T. Nelson, D. Thompson, T. Tielkes, D.A. Towers, and P. de Vos, editors, *Proceedings of the 12th International Workshop on Railway Noise, IWRN 12*, pages 130-137, Terrigal, Australia, September 2016.

[4] C. Van hoorickx, M. Schevenels, and G. Lombaert. Topology optimization of wave barriers for railway induced vibrations in buildings. In M. Papadrakakis, V. Papadopoulos, G. Stefanou, and V. Plevris, editors, *Proceedings of the 7th European Congress on Computational Methods in Applied Sciences and Engineering, ECCOMAS 2016*, pages 3461–3472, Crete Island, Greece, June 2016.

[5] E. Reynders, C. Van hoorickx, and A. Dijckmans. Semi-discrete coincidence in the mid-frequency sound transmission through rib-stiffened panels. In M. Papadrakakis, V. Papadopoulos, G. Stefanou, and V. Plevris, editors, *Proceedings of the 7th European Congress on Computational Methods in Applied Sciences and Engineering, ECCOMAS 2016*, pages 7620–7627, Crete Island, Greece, June 2016.

[6] C. Van hoorickx, O. Sigmund, M. Schevenels, B.S. Lazarov, and G. Lombaert. Topology optimization of two-dimensional wave barriers for the reduction of ground vibration transmission. In M. Papadrakakis, V. Papadopoulos, and V. Plevris, editors, *Proceedings of the 5th International Conference On Computational Methods in Structural Dynamics and Earthquake Engineering, COMPDYN 2015*, pages 3309–3319, Crete Island, Greece, May 2015.

[7] C. Van hoorickx, M. Schevenels, and G. Lombaert. Topology optimization of one-dimensional wave impeding barriers. In P. Sas, D. Moens, and H. Denayer, editors, *Proceedings of 26th International Conference on Noise and Vibration Engineering, ISMA 2014*, pages 3557-3571, Leuven, Belgium, September 2014.

[8] E. Reynders and C. Van hoorickx. An investigation into the sound insulation of finite-sized rib-stiffened plates. In *Proceedings of 7th Forum Acusticum*, Kraków, Poland, September 2014.

Other contributions at international conferences

[1] C. Van hoorickx, M. Schevenels, and G. Lombaert. A robust topology optimization approach to the design of elastic wave barriers. 4th European Conference on Computational Optimization, EUCCO 2016, Leuven, Belgium, September 2016.

[2] C. Van hoorickx, M. Schevenels, and G. Lombaert. Topology optimization of two-dimensional wave barriers. Engineering Mechanics Institute Conference, EMI 2015, Stanford, USA, June 2015.

Other contributions at national conferences and meetings

[1] C. Van hoorickx, M. Schevenels, and G. Lombaert. Topology optimization of wave barriers. KU Leuven OPTEC Retreat, Spa, Belgium, November 2015.

[2] C. Van hoorickx, M. Schevenels, and G. Lombaert. Topology optimization of wave barriers. OPTEC WG4 meeting, KU Leuven, Leuven, Belgium, December 2014.

[3] C. Van hoorickx, O. Sigmund, M. Schevenels, B.S. Lazarov, and G. Lombaert. Topology optimization of two-dimensional wave barriers. TopOpt meeting, DTU, Lyngby, Denmark, October 2014.

[4] C. Van hoorickx and E. Reynders. Modelling the vibro-acoustic behaviour of stiffened plates using model updating and a hybrid FE-SEA approach. 2nd ABAV PhD and Young Acousticians Day, Liège, February 2014.

[5] E. Reynders, J. Legault, R.S. Langley, C. Van hoorickx, A. Dijckmans, and G. Vermeir. Robust sound transmission modelling with hybrid FE-SEA. 2nd ABAV PhD and Young Acousticians Day, Liège, February 2014.

Internal reports

[1] C. Van hoorickx, K. Maes, and G. Degrande. Site vibration evaluation at the Corelab 1B research facility of KU Leuven for the installation of an electron microscope. Report BWM-2017-14, Department of Civil Engineering, KU Leuven, September 2017.

[2] K. Kuo, K. Maes, C. Van hoorickx, S. François, and G. Degrande. Vibration measurements in Corelab 1B during truck and bus passages. Report BWM-2017-07, Department of Civil Engineering, KU Leuven, May 2017.

[3] C. Van hoorickx and G. Degrande. Site vibration evaluation at the FAB3 clean room of IMEC. Report BWM-2017-04, Department of Civil Engineering, KU Leuven, May 2017.

[4] C. Van hoorickx and G. Degrande. Trillingsmetingen voor de installatie van een elektronenmicroscopie-cluster in het gebouw Onderwijs en Navorsing 5 op de Campus Gasthuisberg. Report BWM-2016-09, Department of Civil Engineering, KU Leuven, June 2016.

[5] C. Van hoorickx, K. Kuo, and G. Degrande. Site vibration evaluation in the technical area of IMEC I. Report BWM-2016-08, Department of Civil Engineering, KU Leuven, April 2016.

[6] C. Van hoorickx and G. Degrande. Trillingsmetingen in IMEC I. Report BWM-2016-03, Department of Civil Engineering, KU Leuven, April 2016.

[7] C. Van hoorickx, M. Schevenels, and G. Lombaert. Analysis and topology optimization of a one-dimensional wave barrier. Report BWM-2014-04, Department of Civil Engineering, KU Leuven, May 2014.

[8] C. Van hoorickx, K. Maes, and G. Degrande. Site vibration evaluation at building 331-60 S.E.G.-Agricultural Sciences for the installation of a mass spectrometer. Report BWM-2014-01, Department of Civil Engineering, KU Leuven, January 2014.

Master's thesis

C. Van hoorickx. Vibro-akoestische modellering van verstijfde vloerplaten. Master's thesis, Department of Civil Engineering, KU Leuven, 2013.